Project No. 09-819

Testing of Performance of Optical Fibers Under Irradiation in Intense Radiation Fields When Subjected to High Temperature

Reactors Concept RD&D

Dr. Thomas Blue
The Ohio State University

In collaboration with:
Luna Innovations, Inc.

Frances Marshall, Technical POC
Sue Lesica, Federal POC

NEUP Nuclear Energy University Programs
U.S. Department of Energy

FINAL REPORT

Project Title: Testing of Performance of Optical Fibers Under Irradiation in Intense Radiation Fields when Subjected to High Temperature

Project Number: NEUP 09-346

Covering Period: October 1, 2009 through October 31, 2012

Principle Investigators:

Dr. Thomas E. Blue (OSU)
(614) 292-0629
blue.1@osu.edu

Dr. Wolfgang Windl (OSU)
windl.1@osu.edu

Organization:

The Ohio State University
Nuclear Engineering Program
201 West 19th Avenue
Columbus, OH 43210

Industrial Collaborator:

Luna Innovations, Inc.
Dr. Bryan Dickerson
dickersonb@lunainnovations.com

Project Objective: The primary objective of this project was to measure, model and understand, by comparison of measured and modeled results, the performance of optical fibers under irradiation in intense radiation fields, when they are subjected to very high temperatures. This research will pave the way for future testing of fiber optics and optically-based sensors under conditions expected in future high temperature gas cooled reactors.

THE OHIO STATE UNIVERSITY

NEUP Nuclear Energy University Programs

U.S. Department of Energy

Abstract

Distributed measurements made with fiber optic instrumentation have the potential to revolutionize data collection for facility monitoring and process control in industrial environments. Dozens of sensors etched into a single optical fiber can be used to instrument equipment and structures so that dozens of spatially distributed temperature measurements, for example, can be made quickly using one optical fiber. Optically based sensors are commercially available to measure temperature, strain, and other physical quantities that can be related to strain, such as pressure and acceleration. Other commercially available technology eliminates the need to etch discrete sensors into an optical fiber and allows temperature measurements to be made along the length of an ordinary silica fiber. Distributed sensing with optical instrumentation is commonly used in the petroleum industry to measure the temperature and pressure profiles in down hole applications.

The U.S. Department of Energy is interested in extending the distributed sensing capabilities of optical instrumentation to high temperature reactor radiation environments. For this technology extension to be possible, the survivability of silica optical fibers needed to be determined in this environment. In this work, radiation damage to silica was investigated computationally and radiation damage to single and multi-mode silica optical fibers was investigated experimentally.

In the computational portion of this project, molecular dynamics (MD) simulations and first-principles electronic structure calculations were used to model and analyze the structural changes in glass fibers in radiation environments and the corresponding changes in the electronic structure and optical properties. Besides the characterization of optically active defect structures in terms of vacancies or mis-coordinated atoms, a number of approaches for identifying and analyzing structural changes upon heating and irradiation in the amorphous system were analyzed. First-principles electronic structure calculations were used to correlate the structural properties of the defect structures to the resulting optical activity and to the resulting total attenuation. For this purpose, the Vienna Ab-initio Simulation Package (VASP) was used with HSE hybrid functional potentials, which allow accurate prediction of correct band gaps and optical properties.

In the experimental portion of this project, optical attenuation added to silica optical fiber exposed simultaneously to reactor radiation and temperatures to 1000°C was determined. Optical transmission measurements were made in-situ from 400nm-2300nm. For easy visualization, all of the multimode transmission results generated in this work were processed into movies that are available publicly [1]. Silica optical fibers were shown to survive optically and mechanically in a reactor radiation environment to 1000°C. For the combined high temperature reactor irradiation experiments completed in this investigation, the maximum attenuation increase in the low-OH optical fibers was around 0.5db/m at 1550nm and 0.6dB/m at 1300nm. The radiation induced optical attenuation primarily affected wavelengths less than 1000nm and this attenuation cannot be avoided in silica.

Thermal effects dominated the increase in attenuation at wavelengths above 1000nm and it may be possible to mitigate these effects. Fortuitously, commercial optical instrumentation typically utilizes wavelengths centered around 1300nm and 1550nm where the radiation induced attenuation was minimal. The maximum continuous use temperature of silica optical fiber may be limited to 900°C with intermittent use to 1000°C. The silica optical fibers tested in this project are inexpensive and commercially available. An optical fiber, used as a sensor, was interrogated by Luna Innovations' OBR to experimentally determine its performance in a high temperature radiation environment. Development and testing of other radiation hard optical sensors is recommended as future work.

Table of Contents

Abstract ii

Table of Contents iii

List of Tables vii

List of Figures viii

List of Equations xii

Publications and Information Released xiii

Chapter 1. Introduction [2] 2

1.1 Introduction to Optical Fiber 2
1.2 Telecommunications vs. Engineering Measurements 4
1.3 Introduction to Optically Based Sensors 5
1.4 Introduction to Amorphous Silicon Dioxide 5
1.5 Optical Attenuation 7
1.6 Geometric Attenuation in Silica Optical Fibers 8
1.7 Intrinsic Material Attenuation in Silica Optical Fibers 9
1.7.1 Rayleigh Scattering at Low and High Temperatures 10
1.7.2 Brillouin Scattering at Low and High Temperatures 15
1.7.3 UV Absorption at Low and High Temperatures 16
1.8 Impurity, Defect and Radiation Induced Attenuation 17
1.8.1 Defects in Silica Optical Fiber 20
1.8.2 Impurities in Silica Optical Fiber 27
1.8.3 Interaction between Defects and Impurities in Silica Optical Fiber 32
1.8.4 Crystallization (Devitrification) of Silica Optical Fiber 33
1.8.5 Radiation Induced Attenuation in Silica 34
1.9 Optical Attenuation caused by Radiation 35
1.10 Summary 35

Chapter 2. Task A [10] 37

2.1 Deliverable 37
2.2 Introduction 37
2.3 Ring-Order Distribution 37
2.4 Coordination Number Variation 38
2.5 Pair-Correlation Functions 40
2.6 Structure Factor 40
2.7 X-Ray Diffraction 41
2.8 Potential Energy & DSC 43

Chapter 3. Task B/G 44

3.1 Deliverable 44
3.2 MCNP Modeling 44
3.3 Neutron Flux Spectra in the OSURR Fiber Irradiation Test Facility 45
3.4 Characterization of the Radiation Field in the OSURR in Standard Terms 48
3.5 Dosimetric Characterization of Radiation Field in Irradiation Test Rig in ULORR 52

Chapter 4. Task C 53

4.1 Deliverable 53
4.2 Modeling of PKAs using TRIM/SRIM 53
4.3 Calculation of Production of Defects using TRIM/SRIM 53

Chapter 5. Task D [10] 54

5.1 Deliverable 54
5.2 Damage Evolution Model for Silica at High Temperatures 54
5.2.1 Coordination Number 54
5.2.2 Displacement of Recoil Atoms 55
5.2.3 Variation in the Structure Factor as a Function of Irradiation Damage 56
5.2.4 Ring-Order Variation 57
5.2.5 XRD Simulation Analysis 59
5.2.6 Isolation of Defects in Irradiated Silica 60
5.3 First-Principles Electronic Structure Calculations of Defects in Silica 61
5.3.1 Previous Electronic Structure Calculations of Point Defects in SiO_2 61
5.3.2 Simulation of Electronic Structure Properties of SiO_2 using VASP 61
5.3.3 Band-Structure and Density of States of Perfect- SiO_2 62
5.3.4 Calculation of Absorption Coefficient of Perfect SiO_2 63
5.3.5 Absorption Coefficients of Defective ODC Configurations 64
5.3.6 Calculations of Charged Defect Configurations 64
5.3.7 Optical Properties of Oxygen Interstitial Configurations in Silica 66

Chapter 6. Task E [2] [97] 71

6.1 Deliverable 71
6.2 Identification of Wavelengths to Test 71
6.3 Identification of Fiber Types 71
6.4 Purchase of Broadband Fiber Transmission Light Source 72

Chapter 7. Task F [2] 73

7.1 Deliverable 73
7.2 Introduction 73
7.3 High-Temperature Furnaces 73
7.3.1 Reactor Irradiation Furnace 74
7.3.2 Gamma Irradiation Furnace 80
7.3.3 Molybdenum di-Silicide Tube Furnace 80

7.4 Neutron Activation Analysis 81
7.5 Power Supply and Safety System 82
7.5.1 Power Supply 83
7.5.2 Safety System 86

Chapter 8. Task H [2] [97] 89

8.1 Deliverable 89
8.2 Broadband Optical Transmission Measurement System [2] 89
8.2.1 Spectrometers 90
8.2.2 Multiplexers 91
8.2.3 Power Meter 92
8.2.4 Light Source 92
8.3 Software Used for Setup & Data Collection [2] 93
8.4 Optical Fiber Spooling Mechanism [2] 95
8.5 Setup of Thermal-Only Multimode Experiments without Radiation 96
8.5.1 Second High Temperature Experiment without Radiation 97
8.5.2 Third High Temperature Experiment without Radiation 99
8.5.3 Fourth High Temperature Experiment without Radiation 99
8.6 Results from Thermal-Only Multimode Experiments without Radiation 100
8.6.1 Results from Heated Experiments up to 900°C 101
8.6.2 Results from Heated Experiments at 1000°C 105
8.7 High Temperature OBR Experiments without Radiation [97] 107
8.8 Summary of Heated Experiments 109

Chapter 9. Task I [2] [97] 111

9.1 Deliverable 111
9.2 Introduction [2] 111
9.2.1 Data Processing Methods for Multimode Attenuation Data 112
9.2.2 Example Optical Instrumentation Application 114
9.3 High Temperature Multimode Experiments with Radiation [2] 115
9.4 High Temperature Multimode Experiments in the Co-60 Irradiator [2] 115
9.4.2 Results from the Multimode Heated Gamma Irradiation Experiment 117
9.5 High Temperature OBR Experiment in the Co-60 Irradiator [97] 119
9.6 Summary of Gamma Experiments 121
9.7 Experiments in a High Temperature Reactor Radiation Environment 122
9.7.1 Setup of Reactor Experiments 122
9.7.2 First Reactor Experiment 124
9.7.3 Second Reactor Experiment 125
9.7.4 Third Reactor Experiment 126
9.8 Results for Multimode Fiber Irradiations in the OSU Research Reactor [2] 128
9.8.1 Reactor Irradiation at Room Temperature 128
9.8.2 Results from the Heated Reactor Irradiation Experiment 129
9.8.3 Sources of Experimental Error in Multimode Measurements 132
9.9 Results for OBR Experiments in the OSU Research Reactor [97] 133

Chapter 10. Task J 136

10.1 Deliverable 136
10.2 Data Processing 136
10.3 Comparison of Experimental Results with Calculations 136
10.3.1 Griscom's Fractal Kinetics Model 136
10.3.2 Parameter Matching 138
10.3.3 Problems with Griscom's Fractal Kinetics Model 139

Chapter 11. Conclusions & Future Work 141

11.1 Conclusions from Reactor Experiments 141
11.1.1 Multimode Transmission Conclusion 141
11.1.2 OBR Conclusion 142
11.2 Future Work 142

Bibliography 144

List of Tables

Table 1: Parameter values for Equation 9 (Godmanis [33], Saito [32]) 16
Table 2: Position & Intensities of OH & OH+SiO_4 Absorption Bands in Silica [34] 29
Table 3: DPA Rate at 450kW for Calculated & Measured Neutron Spectra in 7" Dry Tube 47
Table 4: PKA Rates at Different Heights in Furnace 51
Table 5: DPA Estimate Comparison using MCNP and SPECTER-ANL 51
Table 6: TRIM Results Calculated at Core Centerline 53
Table 7: Comparison of calculated defects with variation in PKA energy 55
Table 8: Comparison of unirradiated & irradiated defect concentration amorphous SiO_2 55
Table 9: Multi-Mode Optical Fibers Investigated 72
Table 10: High Temperature Fiber Experiments (no radiation) 96
Table 11: List of Multimode Optical Fiber Degradation Experiments 115

List of Figures

Figure 1: Cross-Section View of Single-Mode and Multi-Mode Optical Fibers 3
Figure 2: Bound (top) & Leaky (bottom) Ray in a Planar Step-Index Waveguide 4
Figure 3: Two SiO_2 Tetrahedra Shown Sharing an Oxygen Atom [10] 6
Figure 4: 2D Representation of Quartz (left) and Fused Silica (right) 6
Figure 5: Absolute Attenuation for Low-OH (left) & High-OH (right) Fibers [12] 8
Figure 6: Mechanisms Leading to Attenuation in Silica 9
Figure 7: Thermally Induced Attenuation for Low-OH Silica Fiber 10
Figure 8: Temperature Dependence of the Index of Refraction of Silica 12
Figure 9: Temperature Dependence of Rayleigh Attenuation for T_f=1600°C 13
Figure 10: Cooling Rate and OH Concentration Dependencies of the Glass Transition Temperature and Fictive Temperature of Silica Glass [16] 14
Figure 11: Effect of OH Impurity on the Scattering Intensity of Fused Silica [16]. 14
Figure 12: Rayleigh Scattering Dependence on Fictive Temperature 14
Figure 13: Temperature Dependence of Brillouin Attenuation 16
Figure 14: Temperature dependent attenuation caused by Urbach absorption 17
Figure 15: Refractive Index Profile for a Step-Index Optical Fiber 18
Figure 16: Conversion between Photon Energy, Wavelength & Frequency 20
Figure 17: Common Intrinsic Defect Structures in Fused Silica 21
Figure 18: Optical Absorption Bands of Common Structural Defects in Silica [36] 22
Figure 19: Absolute Attenuation for Low-OH Polymicro Optical Fiber 23
Figure 20: Absolute Attenuation for High-OH Polymicro Optical Fiber 23
Figure 21: Diffusion Coefficients for Silicon & Oxygen in Fused Silica [42] [43] 24
Figure 22: Equilibrium Defect Concentration in Stoichiometric Silica 25
Figure 23: Equilibrium Defect Concentration in Oxygen-Excess Silica 25
Figure 24: Equilibrium Defect Concentration in Oxygen-Deficient Silica 26
Figure 25: Stoichiometry Dependent Equilibrium Defects in Silica at 1000°C 27
Figure 26: Common Hydrogen Impurity Configurations in Silica 28
Figure 27: Formation of Si-OH & Si-H from Intrinsic Defects & H or H_2 28
Figure 28: Intrinsic Vibrational Absorption in High-OH Polymicro Fiber 29
Figure 29: Intrinsic Vibrational Absorption in Low-OH Polymicro Fiber 30
Figure 30: Loss at 1390nm in Silica Fiber Heated with Polymer Coating [44] 31
Figure 31: Diffusion of Germanium (left) and Fluorine (right) in Silica at 1000°C 32
Figure 32: Nucleation and Growth of Crystal Grains on a Silica Optical Fiber [27] 33
Figure 33: Presence of 3, 4, 5 and 6-membered rings 38
Figure 34: Ring-order variation of amorphous silica with temperature & radiation damage 38
Figure 35: Potential Energy/Oxygen atom Distribution with O1, O2 and O3 coordination of amorphous silica at room-temperature 39
Figure 36: Potential Energy/ Oxygen atom Distribution with O1, O2 and O3 coordination of irradiated silica, increase in the number of O1 coordinated atoms 39
Figure 37: Variation of pair-correlation function with temperature evolution 40
Figure 38: Experimental Structure factor distribution of amorphous silica at room-temperature 41
Figure 39: Comparison of structure factor for unirradiated and irradiated SiO_2 41
Figure 40: XRD simulation using Crystal Diffract for SiO_2 42
Figure 41: Experimental XRD spectrum of amorphous SiO_2 [68]. 42
Figure 42: Schematic DSC curve 43
Figure 43: MCNP Model of OSURR Including 7" Dry-Tube 44

Figure 44: Spectrum Comparison in 7" Dry Tube, Calculated with MCNP 45
Figure 45: Initial and Revised Fiber Holder Design 46
Figure 46: Neutron flux spectrum in the fibers with varying axial position (z-axis) 46
Figure 47: Total neutron flux vs distance (Z) from core horizontal midplane in cm 47
Figure 48: Comparison of Calculated & Measured Flux in 7" Dry Tube 48
Figure 49: Normalized absorbed dose rate vs axial position (z-axis) in cm 49
Figure 50: Revised MCNP model in the XZ plane, dashed box is enlarged on right 49
Figure 51: Revised MCNP model in the XY plane at two heights 50
Figure 52: PKA Spectrum in the Fiber Holder at the Bottom of the Furnace at 450kW 52
Figure 53: Variation of coordination number in amorphous silica with PKA energy 54
Figure 54: Maximum displacement of atoms in the silica structure as a function of PKA energies 56
Figure 55: Average displacement of atoms in the silica structure as a function of PKA energies 56
Figure 56: Comparison of structure factor for unirradiated and irradiated SiO_2 57
Figure 57: Snapshot from Materials Studio of amorphous silica structure at 300K 58
Figure 58: Variation of percentage of ring-sizes in vitreous silica with temperature and irradiation with a PKA energy of 3.5 keV 58
Figure 59: XRD simulation using Crystal Diffract for SiO_2 59
Figure 60: Experimental XRD spectrum of amorphous SiO_2 [68]. 60
Figure 61: Density of States of 48-atom cell perfect β-cristobalite silica 62
Figure 62: Band structure of 48-atom cell perfect β-cristobalite SiO2 63
Figure 63: Plot of absorption coefficient (cm-1) vs Energy (eV) of perfect SiO_2 63
Figure 64: Comparison of absorption coefficient of SiO_2 with ODC (red-line) with perfect SiO_2 64
Figure 65: Energetically favorable mechanism of defect production 65
Figure 66: Formation energy calculations of charged defect configurations of O vacancies in SiO_2 65
Figure 67: Absorption coefficients of +1 and +2 charged Oxygen Vacancy configurations 66
Figure 68: Oxygen Interstitial configurations in silica 66
Figure 69: Formation energy calculations of interstitial configurations in SiO_2 67
Figure 70: DOS of Double-bridged configuration with neutral charge, q=0 68
Figure 71: DOS of Double-bridged configuration with charge, q=+2 68
Figure 72: DOS of Double-bridged configuration with charge, q=-2 69
Figure 73: Absorption coefficients of neutral Oxygen interstitial configurations in SiO_2 70
Figure 74: Absorption coefficients of charged, double-bridged O interstitials in SiO_2 70
Figure 75: StellarNet Model SL1 Broadband Tungsten Light Source 72
Figure 76: $MoSi_2$ Furnace (L), Reactor Furnace (C), Gamma Furnace (R) 74
Figure 77: Components of Reactor Irradiation Furnace 75
Figure 78: Features of a SiC Cartridge Heater [101] 76
Figure 79: Fiber Holder CAD (L), Quartz Assembly with Fiber(C) & with 5 TCs(R) 77
Figure 80: Quartz Fiber Holder Ring 78
Figure 81: Assembly of Quartz Fiber Holders into Reactor Irradiation Furnace 78
Figure 82: Electrical Connections and Lifting Lugs on SiC Furnace 79
Figure 83: Co-60 Gamma Irradiation Furnace 80
Figure 84: Molybdenum di-Silicide Furnace 81
Figure 85: Block Diagram of the Power Supply & Safety System 83
Figure 86: Front Panel of the Power Supply & Safety System 83
Figure 87: Top View of Assembled Power Supply & Safety System 84
Figure 88: 5kVA Dongan Transformer with 24/48VAC Switch 85
Figure 89: Metal Oxide Varistor for Surge Suppression 85
Figure 90: Example of Alarming Conditions for the CAS200 87

Figure 91: Diagram of Supplemental Safety Logic Circuit 87
Figure 92: Supplemental Safety Logic Circuit with Labels 88
Figure 93: Truth Table for Supplementary Safety Circuit 88
Figure 94: Block Diagram of Experimental Setup 89
Figure 95: Broadband Optical Measurement Equipment 90
Figure 96: CCD Sensitivity in UV-vis-NIR [109](L) & NIRX (R) Spectrometers 90
Figure 97: Hysteresis Reduction in Modified vs Unmodified Multiplexers 91
Figure 98: Spectral Sensitivity of Power Meter [111] 92
Figure 99: Normalized Emission from a 2800K Black Body Emitter 93
Figure 100: Block Diagram of Optical Data Acquisition Program Execution 94
Figure 101: Hardware Setup Tab in Optical Data Acquisition Application 94
Figure 102: Spectrometer Setup & Preview in Data Acquisition Application 95
Figure 103: Run Experiment Tab in in Optical Data Acquisition Application 95
Figure 104: Fiber Spooling Mechanism 96
Figure 105: Temperature Profile for Second Thermal-Only Experiment 97
Figure 106: Equipment Setup for Second Thermal-Only Experiment 98
Figure 107: Equipment Setup for Third Thermal-Only Experiment 98
Figure 108: Temperature Profile for Third Thermal-Only Experiment 99
Figure 109: Temperature Profile for Fourth Thermal-Only Experiment 100
Figure 110: Broadband Thermal Attenuation in Low-OH Polymicro Fiber 101
Figure 111: Time Dependent Thermal Attenuation in Low-OH Polymicro Fiber 102
Figure 112: Broadband Thermal Attenuation at 900°C in Low-OH Polymicro 103
Figure 113: Broadband Thermal Attenuation in Low-OH CeramOptec Fiber 104
Figure 114: Time Dependent Thermal Attenuation in Low-OH CeramOptec Fiber 104
Figure 115: Broadband Thermal Attenuation in High-OH Polymicro Fiber 105
Figure 116: Broadband Thermal Attenuation at 1000°C in Low-OH Polymicro 106
Figure 117: Broadband Thermal Attenuation at 1000°C in High-OH Polymicro 106
Figure 118: Average optical power returned from single-mode OBR fiber [97] 108
Figure 119: Reprocessed OBR Thermal-Only Experiment Data 108
Figure 120: Additional Thermal-Only OBR Results 109
Figure 121: Optical Instrumentation for Distributed Measurements with FBGs 111
Figure 122: Block Diagram of Optical Connections 113
Figure 123: Conversion between Percent Transmission and Attenuation in dB 113
Figure 124: Loss Analysis for Example Optical Measurement System 114
Figure 125: Temperature and Dose Profile for Heated Gamma Experiment 117
Figure 126: Broadband Thermal & Co-60 Gamma Attenuation in Low-OH 118
Figure 127: Thermal & Co-60 Gamma Attenuation in Low-OH CeramOptec Fiber 118
Figure 128: Broadband Thermal & Co-60 Gamma Attenuation in High-OH Fiber 119
Figure 129: Singlemode fiber spooled on a fiber holder 120
Figure 130: Dose Rate and Temperature Profile for OBR Gamma Experiment 120
Figure 131: Average Amplitude (dB) for Channel 2 in OBR Gamma Irradiation Experiment 121
Figure 132: Reactor Irradiation Position 123
Figure 133: Neutron Energy Spectrum at Fiber Holders in Reactor Furnace [118] 123
Figure 134: Temperature & Reactor Power for 1st Reactor Experiment 124
Figure 135: Temperature & Fast Neutron Fluence for 1st Reactor Experiment 125
Figure 136: Temperature & Reactor Power for 2nd Reactor Experiment 126
Figure 137: Temperature & Fast Neutron Fluence for 2nd Reactor Experiment 126
Figure 138: Temperature & Reactor Power for 3rd Reactor Experiment 127

Figure 139: Temperature & Fast Neutron Fluence for 3rd Reactor Experiment 127
Figure 140: Broadband Reactor Radiation Induced Attenuation in Low-OH Poly- 128
Figure 141: Broadband Reactor Radiation Induced Attenuation in Low-OH 129
Figure 142: Broadband Thermal & 10% Power Irradiation Attenuation in Low-OH 130
Figure 143: Thermal & Reactor Radiation Induced Attenuation in Low-OH Poly- 131
Figure 144: Thermal & Reactor Radiation Induced Attenuation in Low-OH Ceram- 131
Figure 145: Thermal & Reactor Radiation Induced Attenuation in High-OH Poly- 132
Figure 146: Average Amplitude (dB) for Channel 2 in OBR Reactor Irradiation Experiment 134
Figure 147: OBR Reactor Experiment Data Reprocessed for Temperature 134
Figure 148: Attenuation at Specified times for high-OH Polymicro Fiber in Gamma Experiment .. 138
Figure 149: Plot of μ vs. Inverse Temperature for Parameter Fitting 138
Figure 150: Attenuation Fit at 600nm for α=0.67, β=1.35, E_a=0.35, $\nu\varepsilon^{(\beta-1)/\alpha}$=27.86 139

List of Equations

Equation 1: Definition of Critical Angle 3
Equation 2: Attenuation Mechanisms 7
Equation 3: Change in Optical Intensity 7
Equation 4: Calculation of Change in Optical Attenuation 8
Equation 5: Rayleigh Scattering Coefficient 11
Equation 6: Isotropic Photoelastic (Pockels) Coefficient [19] [22] 11
Equation 7: Temperature Dependent Index of Refraction for Fused Silica [23] 12
Equation 8: Brillouin Scattering Coefficient 15
Equation 9: Urbach Absorption Coefficient 17
Equation 10: Conversion between Photon Energy, Frequency & Wavelength 19
Equation 11: Fluorine [52] & Germanium [53] Diffusion Coefficients in Silica 31
Equation 12: Conversion of a Si-Si Bond into an E' and E'γ Center (E'γ is charged) 35
Equation 13: Griscom's Fractal Kinetics Model for Radiation Induced Attenuation 137
Equation 14 137
Equation 15 137

Publications and Information Released

- Hawn, Petrie, Blue & Windl. "In-Situ Performance of Optical Fibers Heater to 600°C during Gamma Irradiation." American Nuclear Society Transactions. Vol. 106, p. 614-615, 2012.
- Petrie, Hawn, Blue & Windl. "In-Situ Performance of Optical Fibers Heated to 1000°C." American Nuclear Society Transactions. Vol. 106, p. 616-617, 2012.
- D. P. Hawn, Ph.D. dissertation: "The Effects of High Temperature and Nuclear Radiation on the Optical Transmission of Silica Optical Fibers," The Ohio State University, Columbus, 2012.
- B. P. Blake. MS thesis: "Initial Testing of Single-Mode Optical Fibers Interrogated with an Optical Backscatter Reflectometer at High Temperatures and in Radiation Environments for Advanced Instrumentation in Nuclear Reactors," The Ohio State University, Columbus, 2012.
- H. Govindarajan. MS thesis: "Atomic-Scale Modeling of the Effects of Irradiation on Silica Optical Fibers," The Ohio State University, Columbus, 2011.
- Govindarajan, Harish. Poster presentation: "Atomic-scale modeling of the effects of Irradiation on Silica Optical Fibers." 2011 OSU Institute for Materials Research Conference. Columbus, Ohio.
- D. P. Hawn. Presentation: "High-Temperature Low-Activation Optical Fiber Irradiation Facility." 2011 Test, Research, & Training Reactors Annual Meeting.
- Hawn, Blake, Petrie, & Blue. "Initial Testing of a High-Temperature Low-Activation Furnace." American Nuclear Society Transactions. Vol. 104, p. 309-309, 2011.
- C. M. Petrie, T. E. Blue and J. A. Kulisek, "Modeling High Temperature Radiation Damage to Optical Fibers," *Transactions of the American Nuclear Society,* vol. 104, pp. 269-270, 2011.
- Govindarajan, Mishra, & Windl. "Atomic-Scale Modeling of the Effects of Irradiation on the Optical Properties of Silica Glass Fibers." *Transactions of the American Nuclear Society,* vol. 104, pp. 33-34, 2011.
- Hawn, Petrie, Blue, & Winningham. "Design and Analysis of a High-Temperature Low-Activation Furnace." American Nuclear Society Transactions. Vol. 103, p. 302-303, 2010.

Harish

Chapter 1. Introduction [2]

Optical fibers allowing high-bandwidth, low-loss, secure data transmission have revolutionized the telecommunications industry. Compared to traditional copper wire, optical fibers exhibit lower loss, have higher bandwidth, are not affected by electromagnetic interference, are smaller in diameter, and are lighter. The telecommunications industry uses optical fibers for long-distance, high-bandwidth data transmission. Optically based instrumentation has developed in parallel with optical data transmission and, despite serving different purposes, has benefited from technologies developed for the telecommunications industry. Optical instrumentation has the potential to revolutionize the way engineering measurements are made in both mundane and harsh environments.

Optically based instrumentation includes optical sensors connected with optical fibers to readout instrumentation. Optical sensors encode the measured quantity as an optical signal and are commercially available to measure temperature, strain, acceleration, pressure, etc. Depending on the type of optical sensor, the optical signal transmitted to the readout equipment can be independent of the transmitted light intensity. Multiple intrinsic optical sensors can be integrated into a single optical fiber for distributed measurements, or a single intrinsic or extrinsic optical sensor can be used for point measurements at the end of a fiber. Optical fibers transmitting sensor signals are similar to telecommunication fibers and also are unaffected by electromagnetic interference, exhibit low loss and have small diameters.

The benefits associated with optical instrumentation have created interest in extending optical instrumentation to high temperature radiation environments as a high resolution tool for materials and fuels research [3] and for future reactor instrumentation [4]. Optical sensors and optical fibers, however, must be able to survive the harsh environment for this technology extension to be possible. The color changing effect that radiation has on glass has been investigated since its first observation by Roentgen [5]. More recently, the effects of neutron and gamma radiation on silica optical fibers have been investigated. The effects of high temperature on bulk silica and silica optical fibers have also been researched. A summary of the relevant literature is presented in a following chapter.

The previous experimental work on silica optical fiber has included some combinations of gamma and neutron irradiation with ex-situ or in-situ optical measurements and active or passive temperature control. An experimental investigation combining reactor irradiation with in-situ optical measurements and in-situ heating had not been previously completed and has been accomplished in this project. The purpose of this work is to experimentally investigate the change in attenuation in silica optical fibers in a high temperature reactor radiation environment.

To explain the change in attenuation demonstrated experimentally, individual attenuation mechanisms have been modeled that are dependent on temperature, gamma irradiation and neutron irradiation. The individual mechanisms can cause permanent or transient changes to the attenuation. Mostly reversible attenuation mechanisms associated with the intrinsic material properties of silica are described in this chapter. This chapter also includes an overview of optical fiber, optical instrumentation, silica, and calculation of optical attenuation as well as permanent and transient attenuation associated with intrinsic defects in the silica and radiation induced changes.

1.1 Introduction to Optical Fiber

Optical fibers are waveguides that propagate light signals along a very long, thin, flexible fiber. Cross-sectional views of typical single-mode and multi-mode step-index optical fibers are shown in Figure 1. These fibers are manufactured with glass, polymer, or combinations of glass and polymer layers. The light signal is propagated in the core of the optical fiber and reflections at the core-clad interface keep the signal in the core. Dopants in the core and/or the clad reduce the

refractive index of the clad compared to the core ($\eta_{co}>\eta_{cl}$) and create a total internal reflection condition at the boundary of those layers.

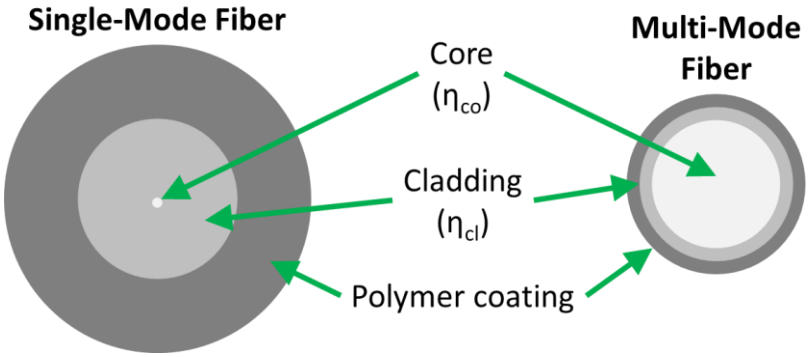

Figure 1: Cross-Section View of Single-Mode and Multi-Mode Optical Fibers (to scale for SMF28 & FIP100120140)

The behavior of a light ray at the core-clad interface is described by Snell's Law. If a ray is incident on the core-clad interface with an angle (θ_z) that is less than the critical angle (θ_c), total internal reflection occurs as shown in Figure 2 (top). This type of ray is called a bound ray and in a straight, non-absorbing waveguide, will propagate indefinitely. The critical angle is a function of the refractive indices of the core and the clad and is defined in Equation 1. If a ray is incident on the core-clad interface with an angle greater than the critical angle, part of the optical power of the ray will leak out of the core at each partial reflection, as shown in Figure 2 (bottom). Leaky rays will not be propagated for a great distance and this loss mechanism will be described in more detail in a following section.

$$\theta_c = \cos^{-1}\left(\frac{n_{cl}}{n_{co}}\right)$$

where:

θ_c = critical angle for total internal reflection

n_{cl} = refractive index of clad

n_{co} = refractive index of core

Equation 1: Definition of Critical Angle

The compositions of both single-mode and multi-mode optical fibers are optimized to reduce the material attenuation of the fiber. A polymer coating is applied outside the clad during manufacture to improve the mechanical properties of the fiber and to protect the optical fiber from environmental contamination. After the polymer coating has been removed, the bare optical fiber is fragile and additional mechanical deformation will cause the fiber to break.

Bound Ray in a Planar Step-Index Waveguide:

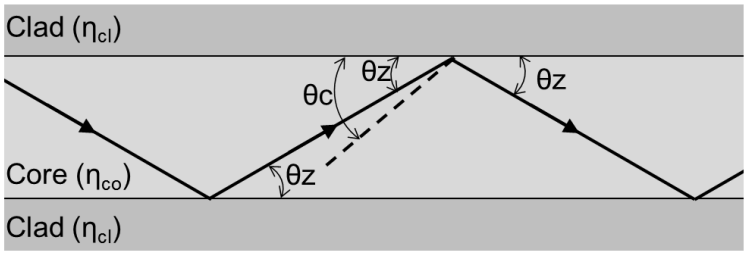

Leaky Ray in a Planar Step-Index Waveguide:

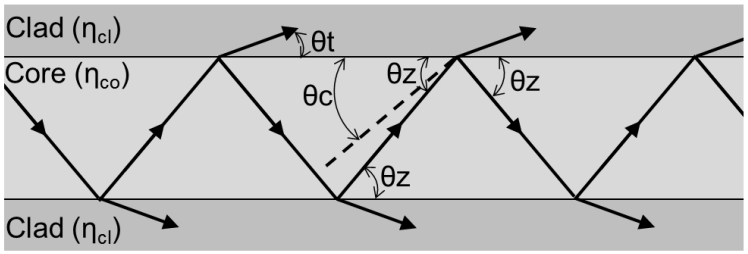

Figure 2: Bound (top) & Leaky (bottom) Ray in a Planar Step-Index Waveguide

As shown in Figure 1, the core diameter of multi-mode fiber is large compared to the core diameter of a single-mode fiber. The larger core diameter and larger numeric aperture (NA) allows multi-mode fibers to easily accept and propagate photons incident on the cross-section, compared to single-mode fibers. The large acceptance cone simplifies the coupling of light sources to the fiber allowing LEDs and white light sources to be used without rigorous alignment. This property of multi-mode fibers is beneficial in cases where application of laser sources is cost prohibitive or when a broadband photon spectrum is needed. Multi-mode fibers suffer a drawback because photons with a distributed angle of incidence (θ_z) entering the waveguide at the same time can travel different optical distances and exit the optical fiber at slightly different times. This effect is called dispersion and reduces the data transfer rate through the waveguide. The propagation of light through multi-mode waveguides can be sufficiently described using ray tracing and geometric optics and wave effects are negligible in most cases [6]. For the purposes of this work, equations derived from classical geometric optics will be used and wave effects will only be considered when necessary.

The geometry of single-mode optical fiber is optimized to minimize the dispersion for a narrow range of transmission wavelengths. Minimizing the dispersion increases the data transfer rate through the fiber and is especially important for long transmission lengths. Unfortunately, the dispersion is minimized by reducing the core diameter and the NA of the fiber which also makes it difficult to couple light sources to the fiber. A carefully aligned photon source with a narrow wavelength range is needed and laser sources are typically used.

1.2 Telecommunications vs. Engineering Measurements

The primary customer for optical fibers is the telecommunications industry which is interested in high bandwidth communication over very large distances—gigabytes per second over many kilometers. Because of this, much of the optical fiber and associated technology is focused on single mode fibers optimized for one of the two primary telecommunications wavelengths, 1300nm and 1550nm. For scientific or engineering measurements, however, high bandwidth is less

important and the transmission distances are typically much shorter. In addition, the expense of the equipment necessary to use single mode fiber often precludes its use.

To minimize dispersion and maximize bandwidth, single-mode optical fibers coupled to laser sources are typical used in the telecommunications industry. Optical fibers used for optically based instrumentation can be multi-mode or single-mode but because high bandwidth is less of a priority, multimode fibers can be used. Less expensive light sources with a range of wavelengths can be coupled to multimode fibers.

Standard telecommunication wavelengths are based on available and economic laser and detector technologies cross-referenced with the low attenuation regions of commercially available optical fibers. For engineering measurements, however, the wavelength or wavelengths of interest may or may not be dependent on the fundamental physics of the measurement. Because of this, it might not be possible to choose wavelengths that exist in the low attenuating regions of a waveguide.

Optically based transducers can utilize several mechanisms to encode measurements of physical phenomenon into a photon based signal. The information encoded in the optical signal is interrogated at the termination of the waveguide which can be a significant distance away from the measurement location. Despite the differences in purpose between optical communications and optical instrumentation, technologies developed for the telecommunications industry can be repurposed in optical instrumentation to reduce development costs.

1.3 Introduction to Optically Based Sensors

Optical sensors provide new measurement techniques that allow data to be taken in harsh environments where electrically based sensors do not perform acceptably. For one subset of optical sensors, the measured reading is a function of the light intensity coming from the optical fiber. This subset includes remote pyrometers, and sensors based on fluorescence or absorbance. Degradation of the optical fiber directly affects the measurement from these types of sensors. Another subset of optical sensors uses interferometric techniques to determine the measured quantity. Interferometric sensors are commercially available to measure temperature, strain, displacement, acceleration [7], and products from mainstream instrumentation companies [8] are making this technology less of a niche product. With interferometric sensors, the measurement is independent of the light intensity and the measurement is not affected by increased attenuation in the optical fiber until the sensitivity of the measurement equipment is reached. While the research conducted for this project is generally applicable to either sensor type, it is anticipated that interferometric sensors will be more suited for application in nuclear reactors.

1.4 Introduction to Amorphous Silicon Dioxide

Silica optical fibers are composed of amorphous, synthetic silicon dioxide, commonly called fused silica. The properties of fused silica make it an ideal choice for optical waveguides. Silica has good transmission characteristics over a broad range of wavelengths from the near-infrared (NIR) to the ultra-violet (UV). The raw materials for silica are abundant and inexpensive, and extremely pure fibers with tight tolerances can be produced for about a dollar per meter. Fabrication techniques, fiber coatings, and the mechanical properties of silica make the fibers strong and flexible. Silica is also a high temperature material and the maximum continuous use temperature for silica fibers is close to 1000°C [9].

The basic building block of both amorphous silica and crystalline quartz is a tetrahedron with an oxygen atom at each corner and a silicon atom in the center, as shown in Figure 3. In the absence of defects and impurities, each of the corner oxygen atoms are shared by neighboring silicon atoms so that the ratio of oxygen to silicon is 2 to 1.

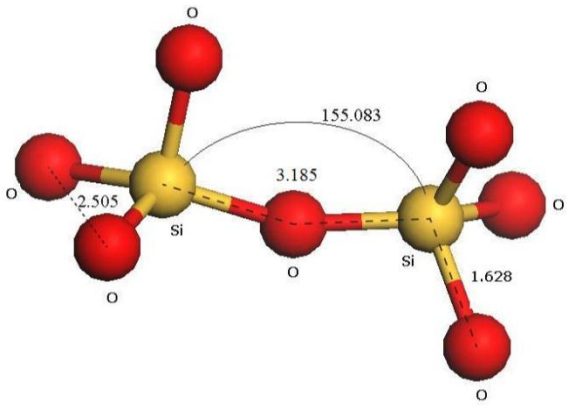

Figure 3: Two SiO_2 Tetrahedra Shown Sharing an Oxygen Atom [10]
Copyright 2011, Govindarajan.

If SiO_2 is cooled slowly during manufacture, one of several crystalline forms of SiO_2 would be formed. If SiO_2 is cooled from the liquid state quickly, crystallization does not occur, there is no long-range order, and an amorphous material results. Figure 4 shows a two-dimensional representation of quartz and silica [11]. The bond angles for the quartz structure are identical and the number of oxygen atoms in a closed loop, in this example, is always 6. The bond angles for the silica structure vary and the number of oxygen atoms in a closed loop, in this example, varies from 4 to 6. The bond angle and ring order distributions are dependent on manufacturing processes and affect the material properties. Figure 4 is a simplified two-dimensional representation of complicated three-dimensional structures. In addition to the complexity added by the third dimension, structural defects that exist in silica are not shown in Figure 4 but are described in Section 1.8.1.

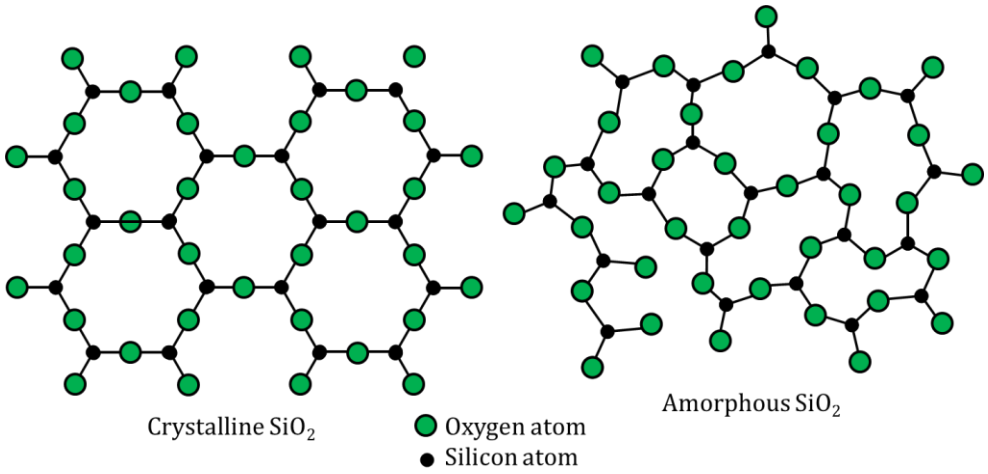

Figure 4: 2D Representation of Quartz (left) and Fused Silica (right)

The bond angle and ring order distribution in the silica network cause local density fluctuations in the material that reduce optical transmission through Rayleigh scattering. In addition, structural defects in the silica contribute to density fluctuation and also absorb photons at energies characteristic to the type of structural defect.

1.5 Optical Attenuation

Light incident on the cross-section of an optical fiber can be accepted into the waveguide and propagated along the fiber. The design and fabrication of optical fibers has been optimized to maximize transmission for a broad range of wavelengths. The composition of optical fibers can even be tailored to improve transmission in a specific wavelength range, usually at the expense of decreased transmission at other wavelengths. Regardless, not all of the optical power accepted into the fiber actually reaches the detection equipment at the opposite end of the fiber. Absorption, scattering, and leakage of light contribute to the total attenuation in the optical fiber. Absorption and scattering are attenuation mechanisms related to the material properties of the waveguide. Leakage of unbound rays from the fiber core and losses at fiber couplings are geometric attenuation mechanisms. A wavelength (energy) dependent total attenuation coefficient can be determined by summing individual attenuation contributions as is shown in Equation 2. The total attenuation coefficient can be used to calculate the wavelength dependent optical intensity transmitted through an attenuating medium as shown in Equation 3. The time dependence of the attenuation coefficient in Equation 3 indicates that attenuation can change depending on degradation in the optical fiber with time.

$$\alpha_{Total}(\lambda) = \alpha_{material}(\lambda) + \alpha_{geometry}(\lambda)$$
$$\alpha_{geometry} = \alpha_{leakage} + \alpha_{connector}$$
$$\alpha_{material} = \alpha_{scattering} + \alpha_{absorption}$$
$$\alpha_{scattering} = \alpha_{Rayleigh} + \alpha_{Brillouin} + \alpha_{Mie}$$
$$\alpha_{absorption} = \alpha_{impurity} + \alpha_{SiO_2}$$

Equation 2: Attenuation Mechanisms

$$I(\lambda,t) = I(\lambda,0)\exp\left[-\alpha_T(\lambda,t)L\right]$$

where:

$I(\lambda,t)$ = linear intensity (unitless)

$\alpha_T(\lambda,t)$ = total attenuation coefficient (1/m)

λ = wavelength (nm or eV)

L = length of fiber (m)

t = time relative to start of experiment

Equation 3: Change in Optical Intensity

High temperature and ionizing radiation cause changes in material properties that affect optical transmission. In the experimental component of this work, optical attenuation is calculated from optical transmission measurements and changes in material properties are inferred. Change in optical attenuation is calculated from experimental measurements as shown in Equation 4. The terms in Equation 4 is described in more detail in [2]. The absolute attenuation cannot be directly measured in this experiment and only changes in attenuation can be calculated from transmission measurements, as shown in Equation 4. Fortunately, the fiber manufacturers provide absolute attenuation measurements for their products [12], as shown in Figure 5. The manufacturer-provided initial absolute attenuation data can be combined with the experimentally determined

changes in attenuation to calculate the absolute attenuation as a function of time, temperature and radiation environment.

$$A_M(t,\lambda) = \frac{-10}{L} Log_{10}\left(\frac{I_{CM}(\lambda,t)}{I_{CM}(\lambda,0)}\right)$$

where:

$A_M(t,\lambda)$ = change in attenuation for channel M (dB/m)

$I_{CM}(t,\lambda)$ = corrected intensity for channel M

L = length of fiber under test for channel M (meters)

λ = wavelength (nm or eV)

t = time from beginning of experiment

Equation 4: Calculation of Change in Optical Attenuation

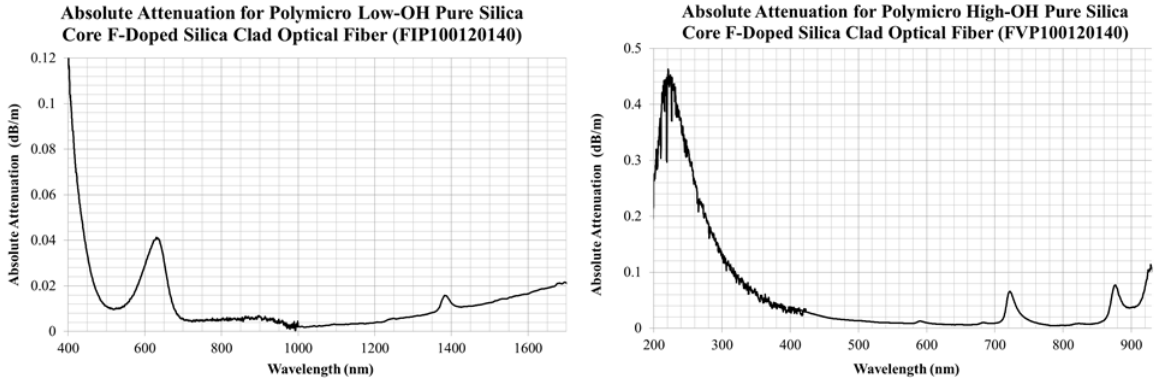

Figure 5: Absolute Attenuation for Low-OH (left) & High-OH (right) Fibers [12]

Figure 5 shows manufacturer supplied absolute attenuation measurements for two commercially available optical fibers studied in this work, one with an intentionally low-OH concentration (left) and the other with an intentionally high concentration of OH (right). Low-OH optical fibers have low attenuation over a broad range and are intended to be used for visible to near-infrared (380-2400nm) applications [13]. Absorption peaks caused by vibrational modes of silica tetrahedra limit the use of low-OH fiber above 2400nm. High-OH silica fibers are intended to be used for UV to near-infrared (180-1150nm) applications [13]. High-OH optical fibers have significant Si-OH absorption peaks limiting its use to 1150nm. The intentional inclusion of OH impurities, however, enables high-OH fiber to be used in the UV range down to 180nm.

1.6 Geometric Attenuation in Silica Optical Fibers

Geometric attenuation is only discussed briefly because the effects of these mechanisms were minimized in the experiment. Leaky light rays ($\theta_z > \theta_c$) are propagated, but refraction occurs at the core-clad interface, as shown schematically in Figure 2 (bottom). Some of the optical power is lost at each partial reflection until all of power from the leaky ray has been lost from the core. For a perfectly straight, non-absorbing optical fiber, leaky rays would be lost from the fiber after a short distance and all bound rays ($\theta_z < \theta_c$) would be propagated indefinitely [6].

Optical fibers of any reasonable length always include bent portions, as is the case in this experiment. In a bent waveguide, there are no bound rays and all rays lose some power as they

propagate [6]. The power lost due to a bend is a function of the bend radius, the radius of the fiber core, and the length of the bent section. By minimizing the fiber core diameter and maximizing the bend diameter, power loss per unit length of bent fiber is minimized [14]. The diameter of the coiled optical fibers is constrained in this experiment and the bend loss should be constant.

Significant optical losses occur at mechanical connections between optical fibers, between an optical fiber and a light source, and between an optical fiber and optical instrumentation. These losses have been minimized by using repeatable mechanical connectors and by never disturbing optical connections during an experiment. In addition, all of the optical connections exist in an environment that remains at room temperature, in a low-radiation field, throughout the experiment. As long as the optical connections are not disturbed during an experiment, it is assumed that these losses are constant.

1.7 Intrinsic Material Attenuation in Silica Optical Fibers

Temperature dependent intrinsic material attenuation mechanisms for silica optical fibers in the absence of radiation are described in this section. Intrinsic material attenuation is caused by scattering and absorption of light by the silica. Figure 6 generically depicts several contributions to the total material attenuation in silica optical fibers. Rayleigh scattering, Brillouin scattering, and Urbach (UV) absorption primarily contribute to broadband attenuation at lower wavelengths. Defect structures in the silica network, such as non-bridging oxygen hole centers (NBOHCs), cause attenuation around wavelengths characteristic to the defect and are discussed in Section 1.8.1. Characteristic attenuation associated with Si-OH impurity is also discussed in Section 1.8.2, but because the OH concentration can affect intrinsic attenuation mechanisms, broadband effects of OH impurity are first mentioned here.

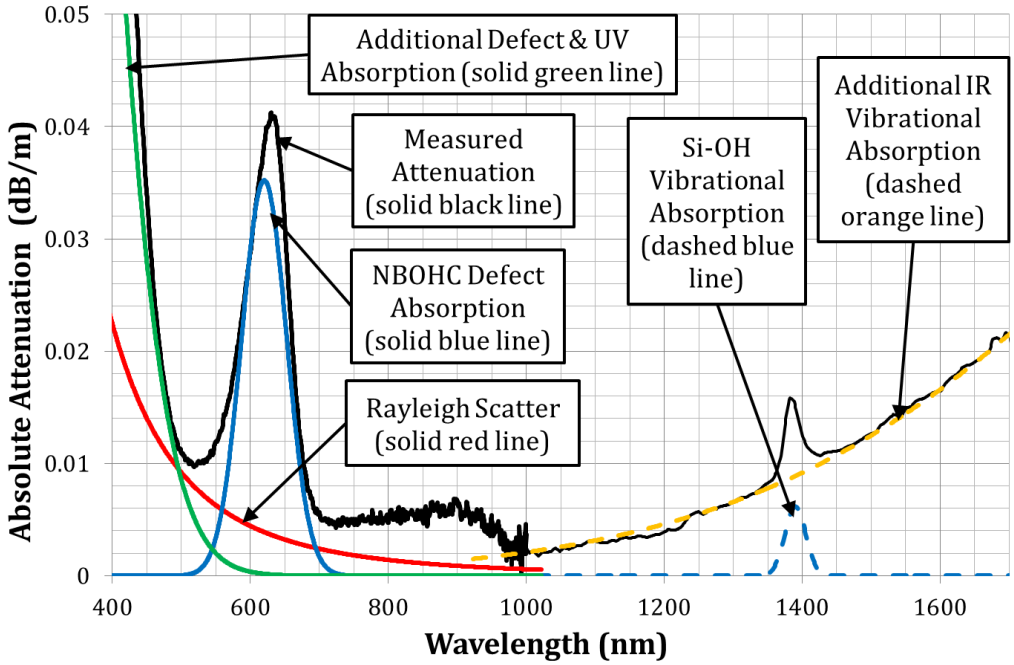

Figure 6: Mechanisms Leading to Attenuation in Silica

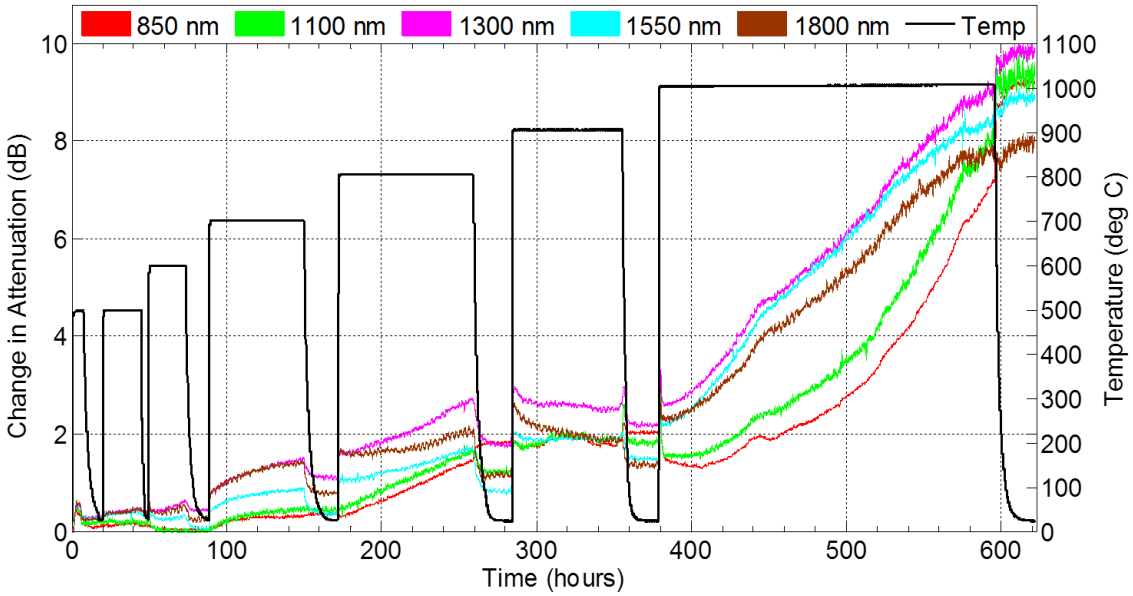

Figure 7: Thermally Induced Attenuation for Low-OH Silica Fiber (Polymicro FIP100120140, heated length = 7.39m±0.3m) [15]

Figure 7 shows an example of the experimental data quantifying the attenuation added by operating silica optical fibers up to 1000°C in the absence of radiation. Figure 7 is shown to illustrate the reversible and permanent components of thermally induced attenuation that is observed during high temperature operation. At 1300nm, for example, the total attenuation at 900°C was on the order of 0.3dB per meter which includes a permanent change in attenuation and a small component that is reversible when the fiber is returned to room temperature. Additional experimental results are presented and discussed in Chapter 8 and Chapter 9.

1.7.1 Rayleigh Scattering at Low and High Temperatures

Rayleigh scattering is elastic scattering of photons from local density fluctuations frozen into the silica network during manufacture. Previously bound photons can be lost from the fiber if they are scattered in a direction that exceeds the critical angle for total internal reflection for the optical fiber. Photons scattered out of the fiber, or in the backwards direction, contribute to the total Rayleigh attenuation. For optical transmission through pure fused silica glass, attenuation caused by Rayleigh scattering creates a fundamental minimum achievable attenuation below ~1500nm, as shown in Figure 6. Reduction of Rayleigh scattering through doping and thermal treatment is a topic of current research [16]. Backward Rayleigh scattering can occur such that the photons continue to be propagated in the fiber but in the direction toward the light source. Luna's Optical Backscatter Reflectometer, for example, uses Rayleigh backscattered photons from intrinsic or extrinsic density fluctuations in an optical fiber to make measurements [17].

A thorough background on Rayleigh scattering, including forms with angular dependence, can be found in [18] and [19]. An attenuation coefficient for the transmission losses through an optical fiber caused by Rayleigh scattering has been derived by Pinnow et al. [20] and is shown in Equation 5 with the isotropic photoelastic coefficient calculated as shown in Equation 6. The temperature dependence of Rayleigh scattering was investigated in an attempt to explain the temperature dependent absorption tail affecting the visible spectrum.

As shown in Equation 5, Rayleigh attenuation is strongly dependent on wavelength and increases for shorter wavelength photons. The refractive index of silica is slightly temperature

dependent, but because the refractive index appears in Equation 5 to the eighth power, the contribution of this effect was investigated. The Rayleigh scattering coefficient is calculated at the fictive temperature (T_f) and not at the absolute temperature of the silica fiber. For pure fused silica with low concentration of impurities, the fictive temperature is the same as the glass transition temperature (T_g). The fictive temperature, however, is affected by the thermal history of the glass and by intentional or unintentional impurities in the glass [16] [21]. The idea that the fictive temperature represents a physically meaningful temperature is a dated concept. The fictive temperature should be considered as a parameter representing the structural disorder of the silica network that is dependent on the glass transition temperature, impurity concentration, and thermal history of the glass.

$$\alpha_{scat,\,R} = \frac{8\pi^3}{3\lambda^4} n^8 p^2 k_B T_f \beta_T$$

where:

$\alpha_{scat,\,R}$ = Rayleigh scattering coefficient (1/m)

λ = photon wavelength (m)

$n(T)$ = index of refraction (unitless)

$p(T)$ = average photoelastic coefficient (unitless)

k_B = Boltzmann's constant ($\mathrm{N \cdot m/K}$)

$T_f(T)$ = fictive temperature (K)

β_T = isothermal compressibility at T_f ($\mathrm{m^2/N}$)

Equation 5: Rayleigh Scattering Coefficient

$$p = \frac{p_{11} + 2p_{12}}{3}$$

where:

p = isotropic photoelastic (Pockels) coefficient

p_{11} = longitudinal photoelastic coefficient

p_{12} = transverse photoelastic coefficient

Equation 6: Isotropic Photoelastic (Pockels) Coefficient [19] [22]

$$n(\lambda,T)^2 = A + \frac{B}{1-\frac{C}{\lambda^2}} + \frac{D}{1-\frac{E}{\lambda^2}}$$

where:

$n(\lambda,T)$ = index of refraction (unitless)

λ = wavelength (μm)

T = Temperature (°C)

$A = 6.90754E-6\times T + 1.31552$ $\quad$ $B = 2.35835E-5\times T + 0.788404$

$C = 5.84758E-7\times T + 1.10199E-2$ $\quad$ $D = 5.48368E-7\times T + 0.91316$

$E = 100$

Equation 7: Temperature Dependent Index of Refraction for Fused Silica [23]

The wavelength and temperature dependent index of refraction for silica has been experimentally determined over a wide temperature range [24]. Ghosh et al. have combined refractive index data from several sources into a convenient form as shown in Equation 7 [23]. Figure 8 shows the temperature dependence of the refractive index of silica at 26°C, 471°C and 828°C and compares experimental data with the curve fit provided in Equation 7. Keeping the fictive temperature constant at 1600°C [25], the attenuation caused by Rayleigh scattering is plotted at 20°C and 1000°C in Figure 9. As is shown in Figure 9, the change in attenuation because of Rayleigh scattering is negligible when the fictive temperature is kept constant and the index of refraction is corrected for temperature. It is likely, however, that the fictive temperature changes as a result of heating the fiber to high temperatures.

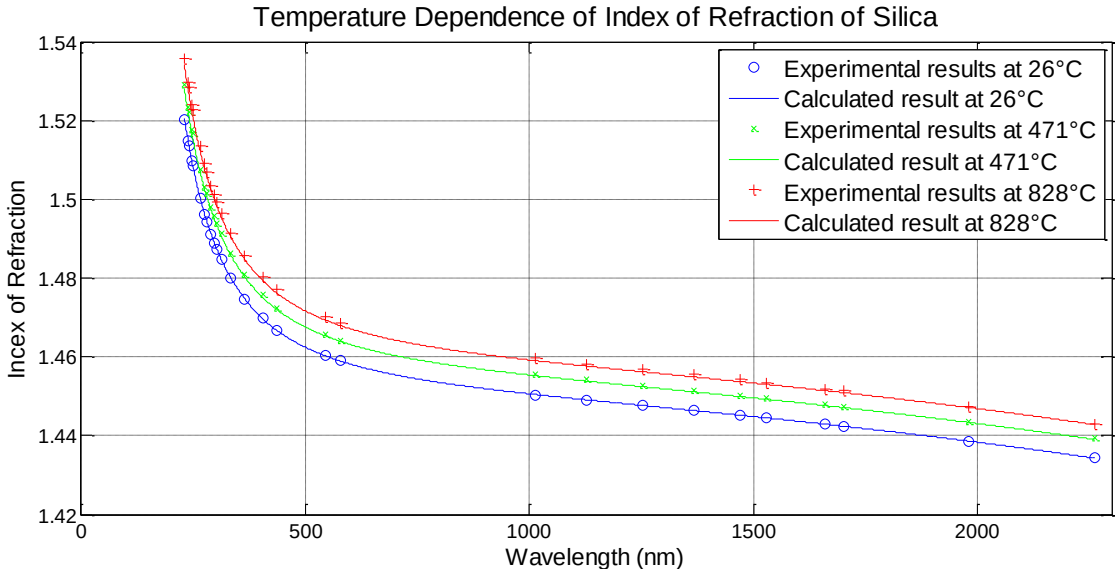

Figure 8: Temperature Dependence of the Index of Refraction of Silica (experimental results from [24], calculated results using Equation 7)

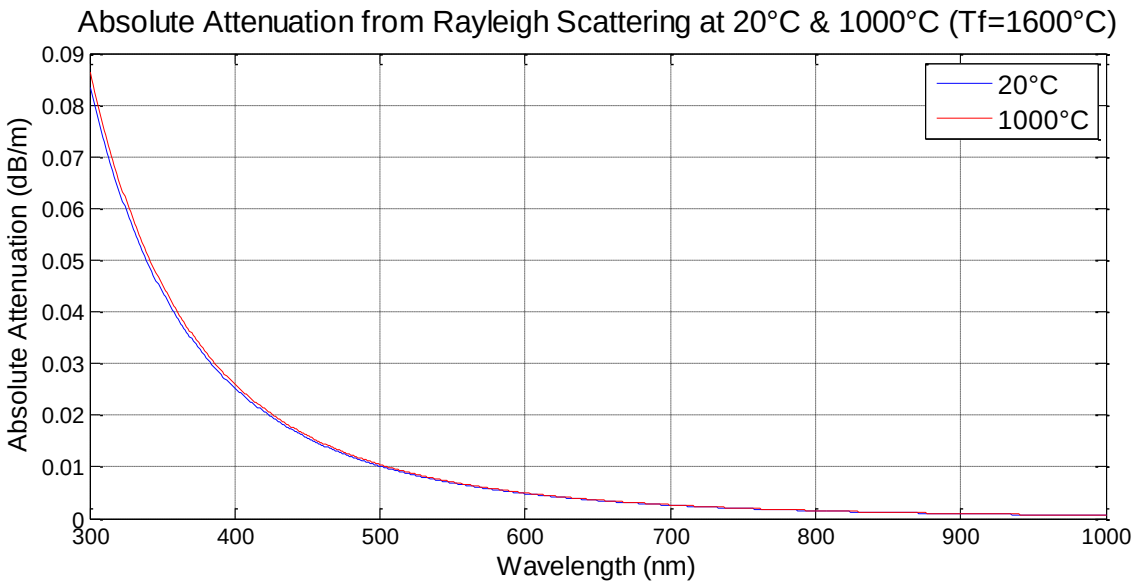

Figure 9: Temperature Dependence of Rayleigh Attenuation for T_f=1600°C

As SiO_2 is cooled from a liquid to a solid, the SiO_2 tetrahedra rearrange and bond to form structures like those shown in Figure 4. As the liquid cools the gradually increasing viscosity inhibits structural rearrangement and the cooling rate determines the time allowed for rearrangement. Qualitatively, the glass transition temperature is the temperature at which additional rearrangement is not possible and the liquid structure is frozen into a glass. The glass transition temperature is dependent on the cooling rate and is greater for faster cooling rates, as is shown in Figure 10 [16]. Because of the small geometry of an optical fiber, the cooling rate, and therefore the glass transition temperature, can be much higher than for larger silica components.

For pure silica glass the fictive temperature and the glass transition temperature are equal. The OH concentration in silica can be increased, either intentionally or unintentionally, to reduce the fictive temperature below the glass transition temperature. The OH impurity promotes structural relaxation and reduces the disorder in the silica below what would be expected based on the glass transition temperature of a sample. The decrease in fictive temperature reduces the Rayleigh scattering as shown in Figure 11 from Ikushima et al. [16]. For silica glass with OH impurities, the glass transition temperature and the fictive temperature are both dependent on the cooling rate of the material and the OH concentration as shown in Figure 10. The attenuation caused by Rayleigh scattering in silica at room temperature for fictive temperatures of 1150°C and 1300°C is shown in Figure 12.

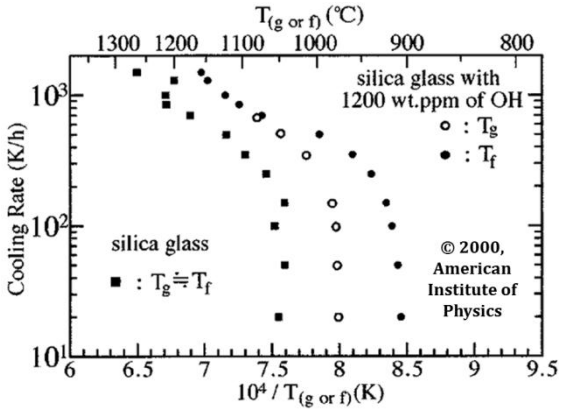

Figure 10: Cooling Rate and OH Concentration Dependencies of the Glass Transition Temperature and Fictive Temperature of Silica Glass [16].
Copyright 2000, American Institute of Physics

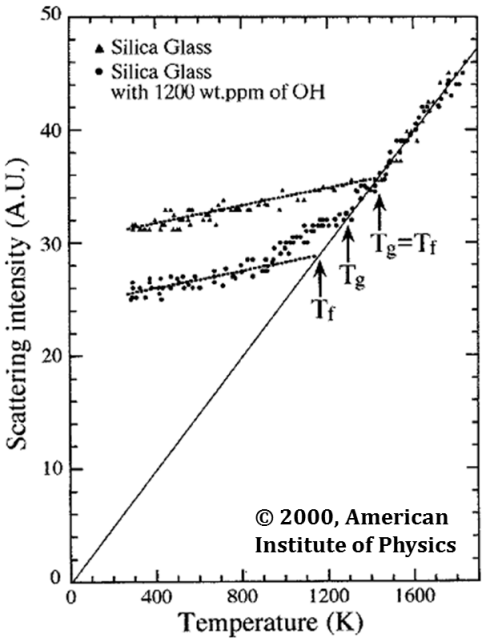

Figure 11: Effect of OH Impurity on the Scattering Intensity of Fused Silica [16].
Copyright 2000, American Institute of Physics

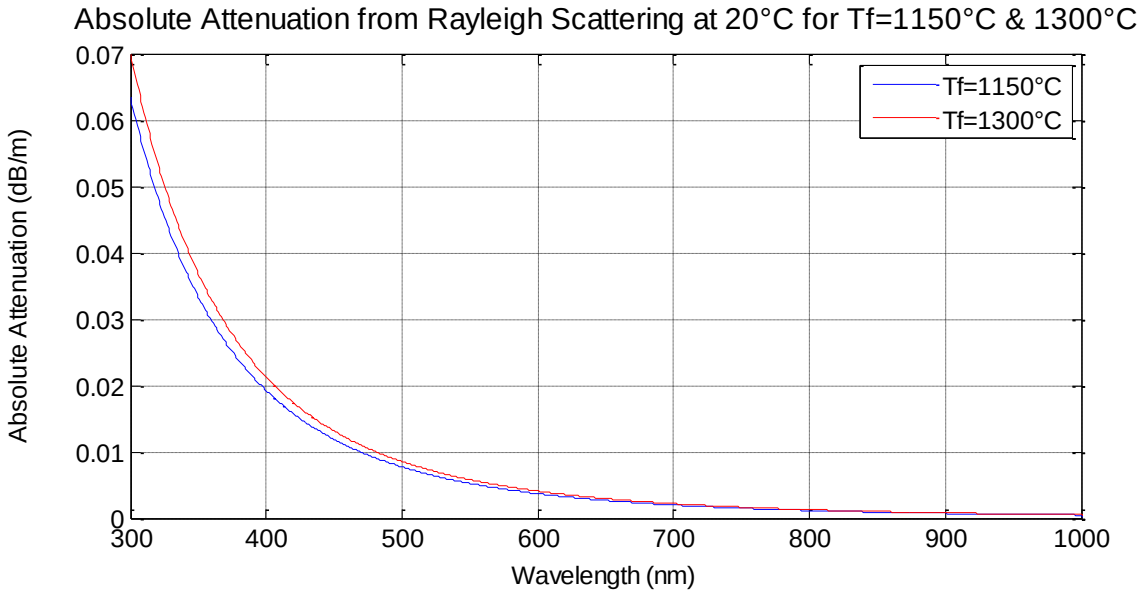

Figure 12: Rayleigh Scattering Dependence on Fictive Temperature

Hydrogen is mobile in silica at temperatures below the glass transition temperature [26]. If silica optical fibers are exposed to a high temperature environment and hydrogen is available, the hydrogen can diffuse into the silica and bond with pre-existing non-bridging oxygen hole centers (NBOHCs) forming ≡Si-OH. The additional OH concentration promotes structural relaxation, reducing the disorder of the silica and reducing the fictive temperature [16]. NBOHCs are structural

defects in the silica network that will be described in greater detail in 1.8. Sources of hydrogen in the environment include the polymer coating on the optical fiber and ambient humidity [27]. Because of the mobility of hydrogen in silica at modest temperatures, the fictive temperature, and therefore the Rayleigh attenuation, is dependent on the thermal and environmental history of the glass.

1.7.2 Brillouin Scattering at Low and High Temperatures

Brillouin scattering is inelastic scattering of photons interacting with temperature dependent vibrations of atoms or molecules in a material. As with Rayleigh scattering, Brillouin scattering can cause previously bound photons can be scattered out of the optical fiber causing attenuation. An attenuation coefficient for the transmission losses through an optical fiber caused by Brillouin scattering has been derived by Rich et al. [28] and is shown in Equation 8. The temperature dependence of Brillouin scattering was also investigated in an attempt to explain the temperature dependent absorption tail affecting the visible spectrum.

The temperature (T) shown in Equation 8 is the absolute temperature of the material and several other parameters in this equation are also temperature dependent. The temperature dependent photoelastic coefficients for silica were taken from Bucaro and Dardy [29] who experimentally determined this coefficient for silica from room temperature to 1300°C. The temperature dependent refractive index was calculated as shown in Equation 7. The longitudinal acoustic velocity for silica was experimentally determined by Polian et al. from room temperature to 2000°C [30]. The temperature dependent density was calculated based on temperature dependent linear thermal expansion coefficients for silica [31].

Figure 13 shows the attenuation caused by Brillouin scattering in silica at 20°C and 1000°C. While the Brillouin scattering increases with temperature, the magnitude of the increased attenuation is small.

$$\alpha_{scat,\,B} = \frac{8\pi^3}{3\lambda^4} k_B T \frac{n^8 p_{12}^2}{\rho V^2}$$

where:

$\alpha_{scat,\,B}$ = Brillouin scattering coefficient (1/m)

λ = photon wavelength (m)

$n(T)$ = index of refraction (unitless)

$p_{12}(T)$ = longitudinal photoelastic (Pockels) coefficient (unitless)

k_B = Boltzmann's constant ($\mathrm{N \cdot m/K}$)

T = temperature (K)

$\rho(T)$ = density ($\mathrm{kg/m^3}$)

$V(T)$ = longitudinal mode acoustic velocity (m/sec)

Equation 8: Brillouin Scattering Coefficient

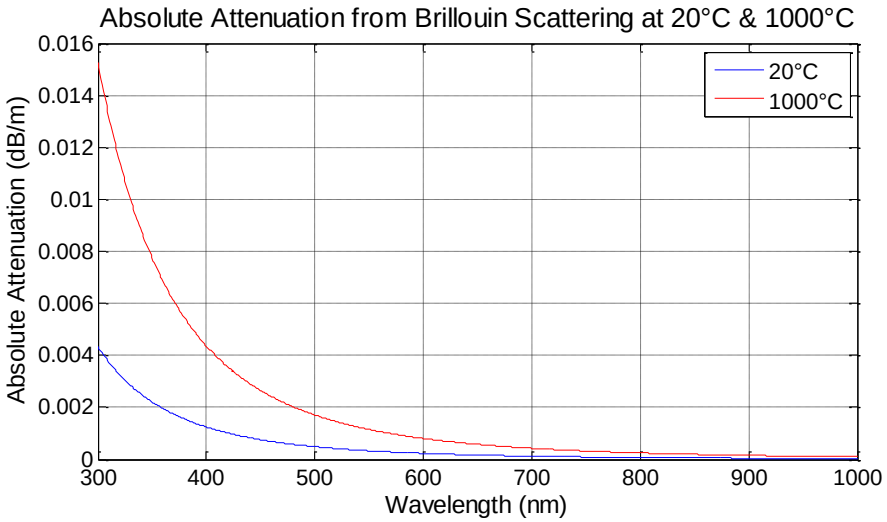

Figure 13: Temperature Dependence of Brillouin Attenuation

1.7.3 UV Absorption at Low and High Temperatures

Silica has good transmission characteristics over a broad range of wavelengths, 180nm (6.7ev) to 2400nm (0.5eV), because it is a wide band gap material. Higher energy (lower wavelength) photons can cause electron transitions across the gap and are absorbed in the process. The UV spectrum is not currently used for optically based instrumentation but the temperature dependence of the UV absorption was investigated in an attempt to explain the temperature dependent absorption tail affecting the visible spectrum. UV absorption in silica glasses increases exponentially with increasing photon energy and also increases with increasing temperature.

The disorder of amorphous silica creates a decreasing distribution, or tail, of energy states above the valence band and also below the conduction band compared to the band structure of perfectly ordered crystalline quartz [32]. The absorption associated with these additional states is described by the Urbach coefficient, as shown in Equation 9. For most amorphous materials, the Urbach coefficient is not temperature dependent and a different form of the Urbach coefficient is used. Amorphous silica, however, has been experimentally shown to follow the temperature dependent Urbach rule shown in Equation 9 [33].

Using the coefficients provided by Godmanis, shown in Table 1, the absolute Urbach absorption in silica at 20°C, 500°C, and 1000°C is plotted in Figure 14. The attenuation is certainly dependent on temperature as shown in Figure 14. However, the magnitude of the temperature dependent attenuation contributed by Urbach absorption is negligible in the wavelengths of interest for this project.

Parameter	Value from		Units
	Godmanis et al.	Saito et al.	
α_0	$10^{5.5}$	--	cm^{-1}
σ_0	0.54	0.66	unitless
$\hbar\omega_0$	0.058	0.079	eV
E_0	8.7	8.52	eV

Table 1: Parameter values for Equation 9 (Godmanis [33], Saito [32])

$$\alpha_U(E,T) = \alpha_0 \exp\left[\frac{\sigma(E - E_0)}{k_B T}\right]$$

where:

α_U = Urbach absorption coefficient (1/cm)

$\sigma = \sigma_0 \frac{2k_B T}{\hbar\omega_0} \tanh \frac{\hbar\omega_0}{2k_B T}$

α_0 = material dependent parameter (1/cm)

E = incident photon energy (eV)

E_0 = material dependent parameter related to peak exciton absorption band (eV)

k_B = Boltzmann constant (eV/K)

T = absolute temperature (K)

σ_0 = material dependent parameter related to exciton-phonon coupling (unitless)

$\hbar\omega_0$ = material dependent parameter related to exciton-phonon energy (eV)

Equation 9: Urbach Absorption Coefficient

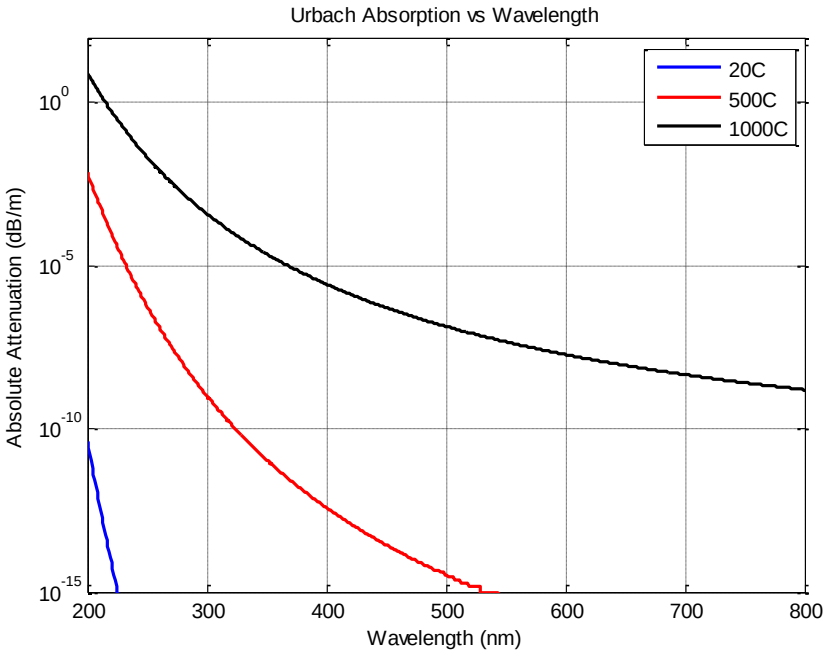

Figure 14: Temperature dependent attenuation caused by Urbach absorption

1.8 Impurity, Defect and Radiation Induced Attenuation

Pure fused silica is a wide band gap insulator that has good transmission characteristics over a broad range of wavelengths from infrared (IR) to ultra-violet (UV). In 0, attenuation contributions from Rayleigh scattering, Brillouin scattering, and Urbach absorption were discussed. These three attenuation mechanisms would exist in silica even in the absence of the defects, impurities, and radiation induced attenuation that are discussed in this chapter.

Impurities and defects in silica can increase absorption at wavelengths characteristic to the impurity type or defect. OH impurities, for example, increase absorption with peaks centered at 1383nm, 1246nm, and 943nm [34] [35]. The OH absorption is caused by vibrational excitations of the OH molecule. Low-OH optical fibers are manufactured in a hydrogen poor environment resulting in a low OH concentration. High-OH optical fibers are manufactured in a hydrogen rich environment resulting in a high OH concentration. Exposure to high temperature enables hydrogen migration in either fiber type which can unintentionally change the OH concentration in the fiber. Modern manufacturing methods have reduced or eliminated unintentional impurities other than the hydrogen related impurities which are described in this chapter [36].

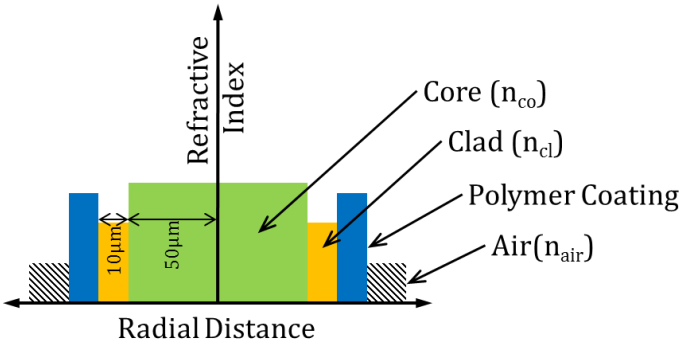

Figure 15: Refractive Index Profile for a Step-Index Optical Fiber

Fluorine and germanium are intentional impurities used to dope the clad and core, respectively, to reduce the index of refraction of the clad (n_{cl}) with respect to the core (n_{co}). The index of refraction of the clad, for example, is linearly related to the fluorine concentration in the clad. Step-index fibers were used in this project, meaning the refractive index of the core is uniform and a step change in the refractive index occurs between the clad and the core. The refractive index profile of a step-index optical fiber is shown schematically in Figure 15. Diffusion of the intentional dopants causes changes to the original refractive index profile potentially resulting in a less effective waveguide. The broadband attenuation increase associated with diffusion of intentional dopants is described in this chapter.

Silica is amorphous because the material was cooled quickly during manufacture. Subsequent exposure to high temperature allows structural rearrangement and with sufficient time at high temperature, the silica could crystalize. Crystallization of a long and thin geometry, such as an optical fiber, would result in a polycrystalline material. Reflections and scattering at crystal grain interfaces would make a polycrystalline fiber ineffective as a waveguide. The relatively low temperatures used in this experiment are unlikely to promote crystal nucleation in the core of the fiber. Crystal grains can, however, nucleate on the surface of the clad or at the interface between the clad and the core [27]. With continued exposure to high temperature, these crystal grains can grow into the fiber and increase optical scattering. The broadband attenuation increase associated with scattering as a result of crystallization is described in this chapter.

Silicon and oxygen atoms existing in configurations other than SiO_4 tetrahedra are considered defects and create electronic states in the band gap of silica. Most of the electronic states create attenuation with peaks centered at wavelengths in the UV region, but some of the defects create attenuation affecting the visible region [37]. The concentration of defects in an unirradiated fiber is a complicated function of the silica stoichiometry, the hydrogen concentration, and the thermal history of the fiber. Exposure to ionizing radiation, additional heating, and hydrogen migration causes changes in the defect concentration.

The differential change in the magnitude of the attenuation caused by a defect or impurity is proportional to the differential change in the concentration of the defect or impurity. Initially it was hoped that changes in defect concentrations could be quantified by measuring changes in optical attenuation. Many researchers have worked to correlate optical attenuation with specific defects and impurities in silica by combining optical spectroscopy with other measurement techniques and a good review of this work is provided by Skuja [37] [36]. Unfortunately Skuja indicates that most defects in silica cannot be determined using optical spectra alone. A description of the difficulties related to this is provided in this chapter.

A description of the common defects in silica is presented in this chapter qualitatively and not quantitatively for two reasons. First, as the optical attenuation measurements made in this project were analyzed, it became apparent that quantifying defect concentrations with the available data was not possible. Second, the attenuation created by these defects primarily affects wavelengths below 700nm which is below the wavelengths of interest for commercially available optical instrumentation. For these reasons, common defects in silica and the dependence of those defects on temperature are described qualitatively with an emphasis on defects causing attenuation in the visible and IR.

To preclude any confusion associated with the units used in this chapter, photon energies are typically displayed with units of nanometers (nm). In some cases, however, it is more appropriate to list the photon energy in electron-volts (eV) or the photon frequency in THz. These units are interchangeable as shown in Figure 16 and Equation 10.

$$E = \frac{h\nu}{10^{-12}} = \frac{10^{9} hc}{\lambda}$$

where: E = photon energy in eV

ν = photon frequency in THz

λ = photon wavelength in nm

c = speed of light in vacuum (3×10^{8}m/sec)

h = Planck constant (4.136×10^{-15}eVsec)

Equation 10: Conversion between Photon Energy, Frequency & Wavelength

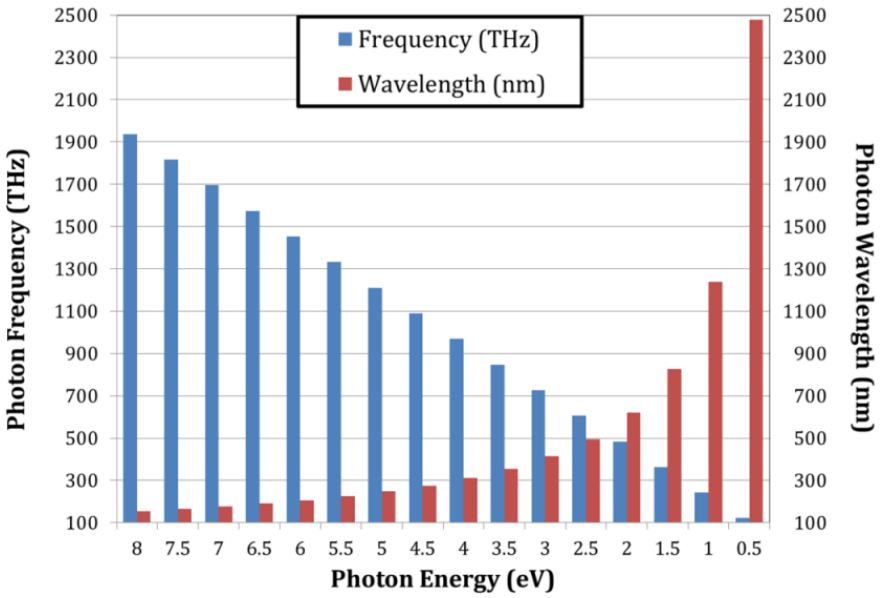

Figure 16: Conversion between Photon Energy, Wavelength & Frequency

1.8.1 Defects in Silica Optical Fiber

Silicon and oxygen atoms existing in configurations other than SiO_4 tetrahedra are considered intrinsic defects and cause optical attenuation in silica. The defects and impurities in silica fibers are dependent on the manufacturing processes involved. Cylindrical rods, or preforms, are produced using chemical vapor deposition techniques and have separate doped regions for the clad and the core. In a common production method, oxygen and a silicon rich precursor gas are injected into a rotating silica tube. The tube material eventually becomes the clad layer of the optical fiber. A high temperature (1300°C to 1600°C) source oxidizes the silicon precursor and the silicon dioxide deposits as a glassy layer on the inner diameter of the tube [38]. The mass flow rates of the silicon precursor and the oxygen are chosen and do not necessarily result in a ratio of two oxygen atoms to one silicon atom. The stoichiometric ratio of silicon and oxygen affects the concentration of intrinsic defects and the creation of new defects when exposed to high temperature or radiation [39] [37].

After a sufficient thickness of core material has been deposited, the hollow preform is heated to approximately 1900°C causing the diameter of the preform to shrink until the axial void is eliminated. The finished preform is mounted vertically in a drawing machine and the bottom of the preform is heated to 2000°C-2300°C for drawing. Fiber is drawn from the heated region, a polymer coating is applied, and the fiber is collected on a spool [38]. The thermal and mechanical processes involved in drawing optical fiber introduce additional intrinsic defects [39] [40].

Fibers produced with variations of these processes have intrinsic defect concentrations that are dependent on the oxygen excess or deficiency, the thermal history, and the intentional or unintentional inclusion of impurities. Despite this, manufacturers can produce silica optical fibers that have low intrinsic attenuation over a broad range of wavelengths. In this section specific defect configurations are described qualitatively. The intrinsic attenuation of the low-OH and high-OH Polymicro fiber used in this project are shown. The effect of temperature on defect concentrations is qualitatively described, assuming negligible variation of hydrogen. Hydrogen concentration has a substantial effect on the concentration of some defects, and the interaction between defects and hydrogen is discussed later.

Intrinsic Defect Configurations in Fused Silica

Two-dimensional representations of several common defect structures are depicted in Figure 17. Silicon atoms have fourteen electrons and oxygen atoms have eight. Ideally, each oxygen atom forms two covalent bonds to fill its 2p orbitals and each silicon atom forms four covalent bonds to fill its 3p orbitals. Fragments of two perfect silica tetrahedra are shown in Figure 17A. Interstitials and vacancies lead to incorrect bonds or dangling bonds as shown in Figure 17B-H.

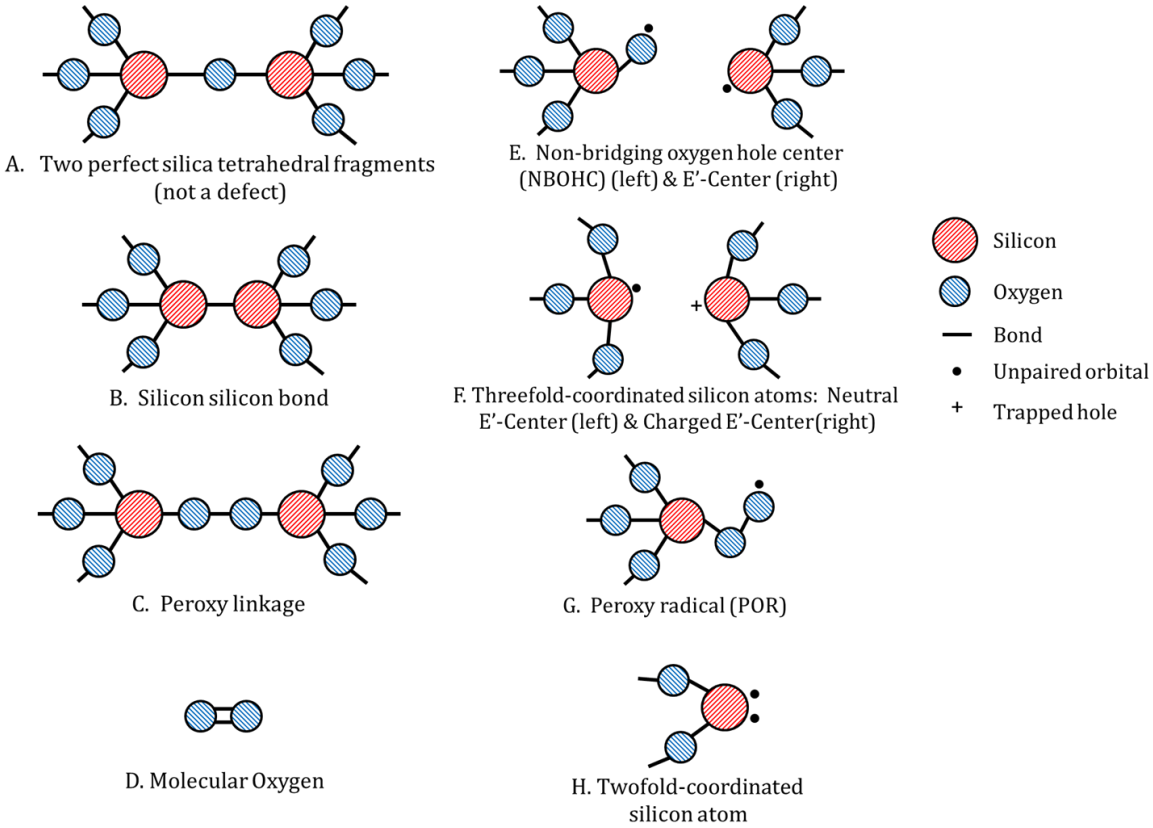

Figure 17: Common Intrinsic Defect Structures in Fused Silica

Silicon-silicon bonds (oxygen vacancy, ≡Si-Si≡), threefold-coordinated silicon atoms (E'-center, ≡Si•), and twofold-coordinated silicon atoms (=Si:) appear in large concentrations in oxygen deficient silica. Non-bridging oxygen hole centers (NBOHCs, ≡Si-O•), peroxy linkages (interstitial oxygen, ≡Si-O-O-Si≡), peroxy radicals (POR, ≡Si-O-O•), and molecular oxygen (O_2) appear in large concentrations in oxygen excess silica [39]. Oxygen deficient defects still appear in silica prepared with oxygen excess, but in smaller concentrations. Similarly, small concentrations of oxygen excess defects appear in silica prepared with an oxygen deficit [39]. In this notation, (≡) indicates three normal bonds, (=) indicates two normal bonds, (•) indicates an unpaired electron, and (:) indicates two unpaired electrons.

The defect structures shown in Figure 17 add electronic states to the silica band gap with most optical absorption peaks centered at wavelengths below 400nm, as shown pictorially in Figure 18 [36]. The exception is the NBOHC which has at least one peak in the UV (258nm, 4.8eV) and one peak in the visible (620nm, 2eV) [37]. The charged E'-center at 215nm and the NBOHC peak at 258nm are strong absorbers and even though the peaks are centered in the UV, the absorption tails from these defects can affect the visible spectrum. It should also be noted that the

optical absorption bands associated with several structural defects are contentious in the literature. Regardless, defects with absorption peaks below 400nm cannot be definitively identified in this work because of the limitations with the optical measurement equipment used. This limitation is unfortunate, but from a practical standpoint the UV absorption caused by these defects has a limited effect on commercial optical instrumentation operating at 850nm, 1300nm or 1550nm.

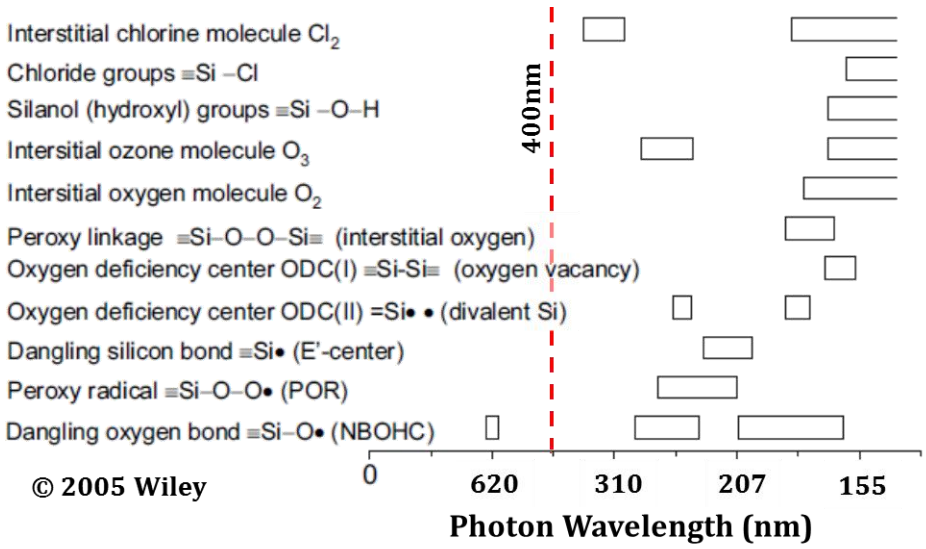

Figure 18: Optical Absorption Bands of Common Structural Defects in Silica [36] Copyright 2005, Wiley.

The simple two dimensional representations of the common defect structures depicted in Figure 17 neglect some details that are important to the formation of defects. Silica is an amorphous three dimensional structure and the distributions of bond lengths and bond angles are affected by manufacturing processes. The fiber drawing process creates defects [41] and also results in bonds that are strained in angle and length. Strained bonds are more easily broken by ionizing radiation, mechanical stresses, and chemical processes. When bonds are broken, the local bond angles and bond lengths can relax and spatially separate the previously bonded atoms. This process creates two complementary defects, such as an NBOHC and an E'-center, in close proximity. Recombination of the defects is inhibited by the spatial separation of the relaxed structure resulting in dangling bonds or creation of other bonds.

Defect Concentration in As-Manufactured Silica Optical Fibers

Figure 19 and Figure 20 show the intrinsic attenuation in the Polymicro fibers used in this project. The manufacturer provided the data in these figures [12], but was unwilling or unable to provide additional details of the stoichiometry or manufacturing processes. Figure 19 shows the absolute attenuation for the low-OH silica fiber with an identifiable NBOHC peak at 620nm, probably indicating that the silica has excess oxygen. The sharp increase in attenuation below 400nm is probably caused by the 258nm NBOHC peak, although this cannot be explicitly determined with this data. Regardless of which defect or defects are to blame, attenuation in the low-OH fiber increases substantially for wavelengths less than 400nm.

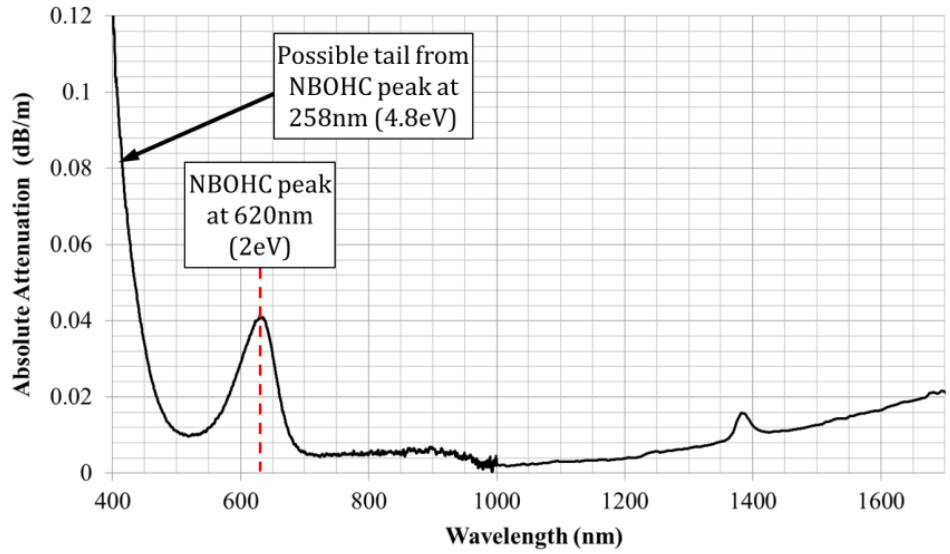

Figure 19: Absolute Attenuation for Low-OH Polymicro Optical Fiber (Pure Silica Core, F-Doped Silica Clad, FIP100120140)

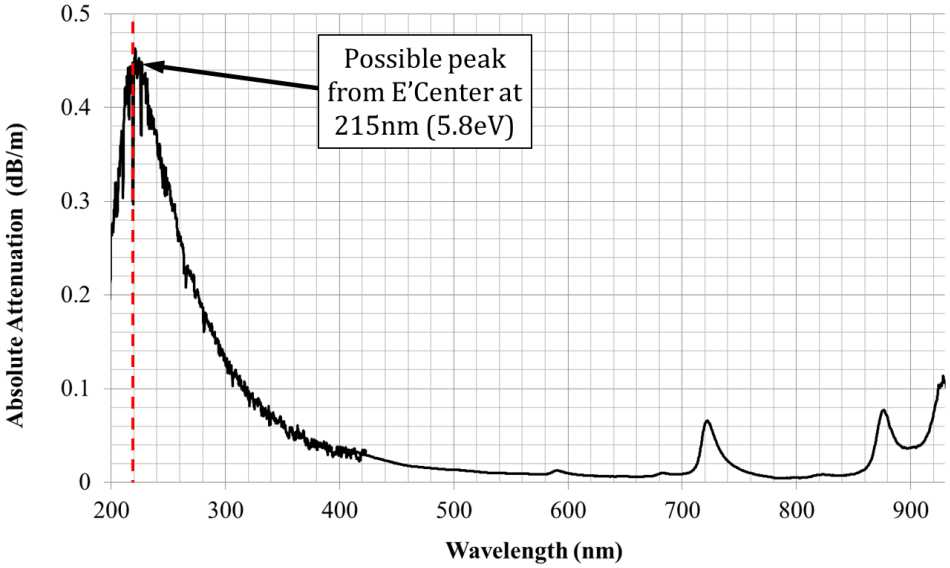

Figure 20: Absolute Attenuation for High-OH Polymicro Optical Fiber (Pure Silica Core, F-Doped Silica Clad, FVP100120140)

Figure 20 shows the intrinsic attenuation in the high-OH Polymicro fiber. The dangling bonds associated with the NBOHCs present in the low-OH fiber are passivized by bonding with hydrogen atoms. The intentionally large hydrogen concentration reduces the concentration of NBOHCs and the optical attenuation associated with that defect. The NBOHC attenuation peak at 620nm in the low-OH fiber (Figure 19) is not present in the high-OH fiber (Figure 20). In addition, the dramatic increase in attenuation at wavelengths below 400nm is not present in the high-OH fiber. Instead, the high-OH fiber has an attenuation peak centered around 220nm that could be attributed to the E'-center defect.

Intentionally increasing the hydrogen concentration is a method used to reduce the optical attenuation in the UV region of oxygen excess silica. The reduced UV attenuation in the high-OH fiber is sometimes incorrectly attributed to a reduction in the fictive temperature causing a decrease in the Rayleigh scattering. While the Rayleigh scattering may be reduced, the primary reduction in the UV attenuation is caused by passivation of the NBOHC defects through formation of ≡Si-OH. Unfortunately increasing the concentration of ≡Si-OH also causes an increase in attenuation in the IR range and this is discussed later in this chapter.

Temperature Dependent Defect Concentration

The concentration of structural defects in a silica optical fiber is dependent on the stoichiometry of the silicon and oxygen, the presence of impurities, and the thermal history during manufacturing. Because of the small geometry, the silica fiber cools quickly after it is drawn from the preform. The drawing process introduces structural defects and strained bonds in the silica and rearrangement of atoms is inhibited by the fast cooling rate. The fast cooling rate effectively freezes the defects into the amorphous structure.

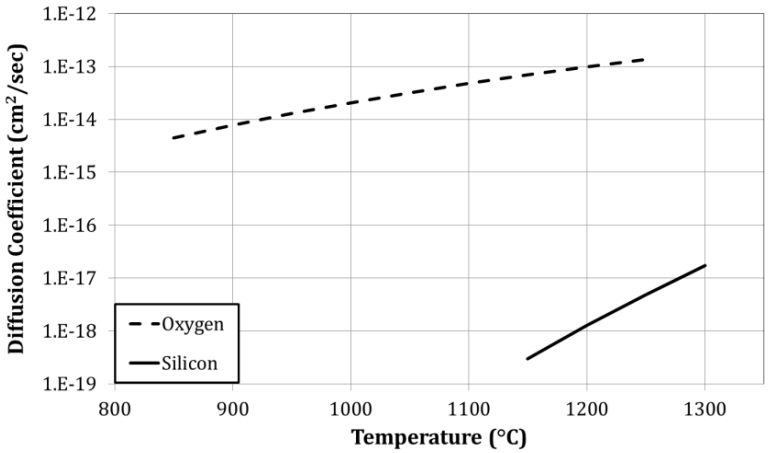

Figure 21: Diffusion Coefficients for Silicon & Oxygen in Fused Silica [42] [43]

Increasing the temperature of the silica increases atomic mobility by increasing the diffusion coefficient and enabling bond rearrangements through chemical reactions. Temperature dependent diffusion coefficients for silicon and oxygen in fused silica are shown in Figure 21 [42] [43]. It is clear from Figure 21 that oxygen is substantially more mobile in silica than silicon.

For a particular silica composition and temperature, there is a preferred equilibrium defect concentration to minimize the free energy of the system. The defect concentration in as-manufactured silica fibers may or may not have reached equilibrium during drawing (around 2000°C) and an equilibrium condition was probably not reached after drawing because of the rapid cooling. Exposing silica to temperatures allowing diffusion on a reasonable time scale enables restructuring of the silica toward the equilibrium defect concentration.

Silin and Lace developed a model that predicts the equilibrium defect concentration in fused silica based on the stoichiometry and temperature [39]. This model considers eight defects including NBOHCs, E'-centers, molecular oxygen, atomic oxygen, peroxy linkages, peroxy radicals, ≡Si-Si≡ bonds, and twofold-coordinated silicon atoms. The concentrations predicted by this model assume the chemical reactions reach equilibrium and are not diffusion limited. In reality, diffusion rates prevent the predicted equilibrium concentrations below 1100K on a reasonable time scale [39]. This model does not include hydrogen impurities and does not account for changes in the

silica composition resulting from out-gassing or absorption of oxygen from the environment. Despite these limitations, the results of this model are useful in understanding the qualitative behavior of fused silica at high temperatures.

Figure 22 shows equilibrium concentrations of defects in fused silica with a stoichiometric ratio of silicon and oxygen. Fused silica has a density of 2.2g/cm^3 and the concentration of regular SiO_2 tetrahedra is $2.21 \times 10^{22} cm^{-3}$. As the temperature increases the concentration of each defect increases, slightly reducing the concentration of perfect SiO_2 tetrahedra. The most prevalent defects are NBOHCs, E'-centers, twofold-coordinated silicon atoms and ≡Si-Si≡ bonds, in that order.

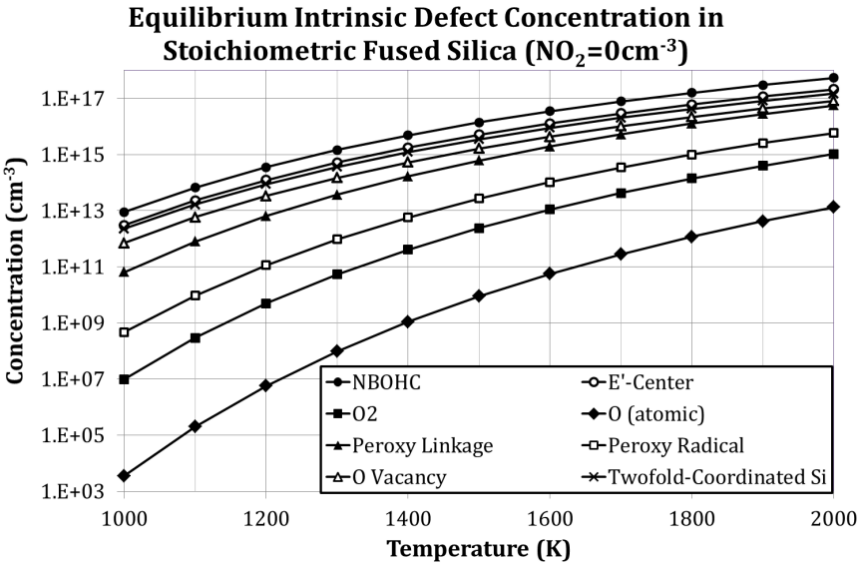

Figure 22: Equilibrium Defect Concentration in Stoichiometric Silica

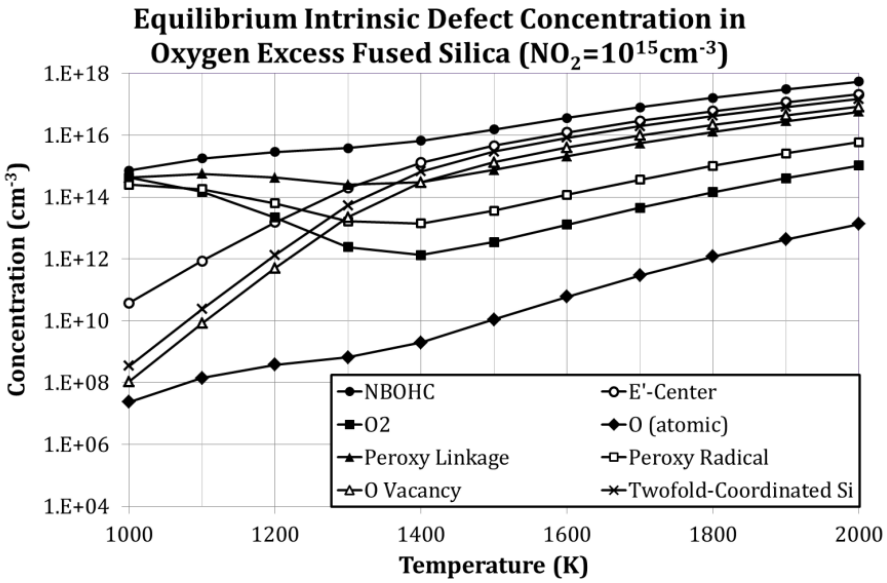

Figure 23: Equilibrium Defect Concentration in Oxygen-Excess Silica

Figure 23 shows the equilibrium concentration of defects in fused silica with a $10^{15}cm^{-3}$ molecular oxygen excess ($2.21x10^{22}cm^{-3}$ + $10^{15}cm^{-3}$). Compared to the stoichiometric case, the additional oxygen causes a decrease in oxygen deficient defects and an increase in oxygen excess defects below 1400K. Above 1400K, the defect concentrations in silica with a $10^{15}cm^{-3}$ O_2 excess are on the same order of magnitude as the corresponding defect concentrations in the stoichiometric case.

Figure 24 shows the equilibrium concentration of defects in fused silica with a $10^{15}cm^{-3}$ molecular oxygen deficiency ($2.21x10^{22}cm^{-3}$ - $10^{15}cm^{-3}$). Compared to the stoichiometric case, the oxygen deficiency causes an increase in oxygen deficient defects and a decrease in oxygen excess defects below 1400K. As with the oxygen excess case, above 1400K the defect concentrations in the oxygen deficient case are similar to the concentrations in the stoichiometric case.

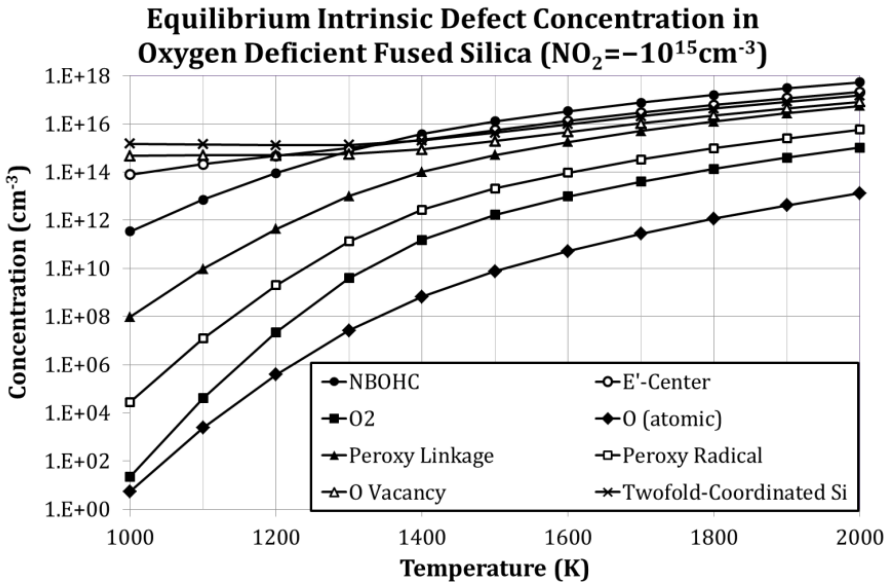

Figure 24: Equilibrium Defect Concentration in Oxygen-Deficient Silica

The equilibrium concentrations of defects at 1000°C for oxygen deficiency and excess concentrations varying from $-10^{20}cm^{-3}$ to $10^{20}cm^{-3}$ are shown in Figure 25. As the oxygen deficit is increased the concentration of oxygen deficient defects increases proportionally and the concentration of oxygen excess defects decreases proportionally. As the oxygen surplus is increased, the defect concentrations do not change proportionally.

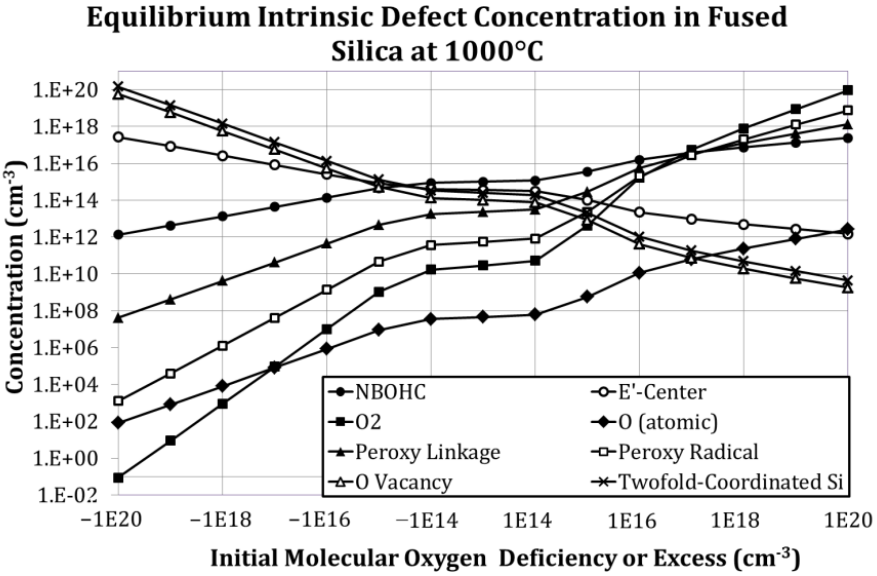

Figure 25: Stoichiometry Dependent Equilibrium Defects in Silica at 1000°C

1.8.2 Impurities in Silica Optical Fiber

Manufacturing techniques for optical fibers have improved such that most unintentional impurities that affect the useful spectrum of silica are either excluded or exist in concentrations too low to detect [36]. Exceptions to this are hydrogen and, to some extent, chlorine. Silica optical fibers are intentionally manufactured to have either a high or a low concentration of hydrogen, resulting in different intrinsic attenuation profiles. Low-OH optical fibers are usable between 380-2400nm and high-OH fibers are usable between 180-1150nm [13]. Chlorine can be introduced during the manufacturing process to remove hydrogen from the preform material and significantly reduce the OH concentration [35]. In this drying process, however, some molecular chlorine unintentionally remains in the silica and is an impurity. Hydrogen is mobile in silica even at room temperature [36] [26] and the original OH concentration in a silica fiber can change depending on the temperature and the availability of hydrogen [44] [45].

For a glass fiber to act as a waveguide, the refractive index of the core must be greater than the refractive index of the clad. Fluorine and germanium are intentional impurities commonly used to decrease or increase, respectively, the refractive index of the silica in optical fibers [35]. These intentional dopants can migrate at high temperature, changing the original refractive index profile of the optical fiber.

Si-OH and Si-H Impurities in Unheated Silica Optical Fibers

Hydrogen intentionally or unintentionally incorporated into silica forms Si-OH and Si-H bonds at NBOHCs and E'-Centers as shown pictorially in Figure 26 and in the reactions listed in Figure 27. In general, pairs or groups of atoms can be vibrationally excited when perturbed at frequencies characteristic to the molecule. The vibrational modes of a molecule depend on the number and type of atoms in the molecule and the bond configuration. The ≡Si-O-Si≡ bridge in pure silica, for example, has a stretching mode with a fundamental frequency around 34THz [46]. Photons at the fundamental frequency (8928nm) are strongly absorbed in silica. In addition to the fundamental frequency, there is also substantial absorption of photons with wavelengths at integer multiples of the fundamental frequency (overtones). Optical absorption peaks also occur around combinations of fundamental modes and overtones of different molecules.

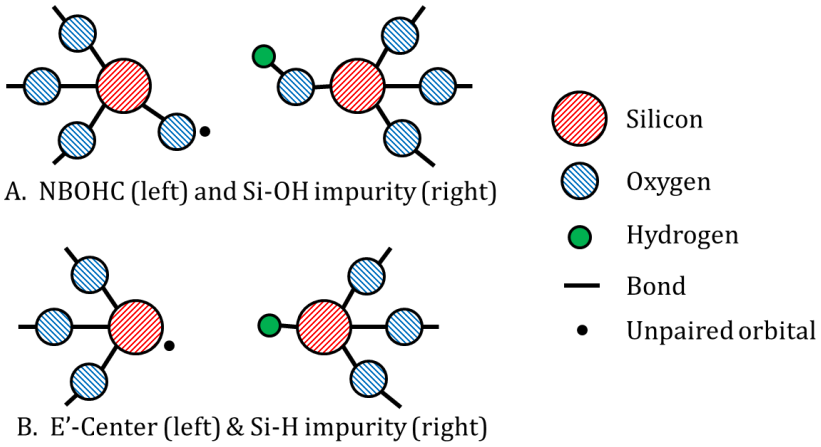

Figure 26: Common Hydrogen Impurity Configurations in Silica

$$\equiv \text{Si-O}^{\bullet} + \text{H}_2 \rightarrow \equiv \text{Si-O-H} + \text{H}^{\bullet}$$

$$\equiv \text{Si-O}^{\bullet} + \text{H}^{\bullet} \rightarrow \equiv \text{Si-O-H}$$

$$\equiv \text{Si}^{\bullet} + \text{H}_2 \rightarrow \equiv \text{Si-H} + \text{H}^{\bullet}$$

$$\equiv \text{Si}^{\bullet} + \text{H}^{\bullet} \rightarrow \equiv \text{Si-H}$$

Figure 27: Formation of Si-OH & Si-H from Intrinsic Defects & H or H_2

The OH molecule is essentially two-thirds of a water molecule and the OH stretching mode is similar for H_2O and Si-OH. Because of this similarity, silica is frequently described as wet or dry, referring to high-OH or low-OH content, respectively. The fundamental and overtone absorption bands of ≡Si-OH and combinations of ≡Si-OH and ≡Si-O-Si≡ stretching modes are listed in Table 2 [34].

The absorption coefficients listed in the last column of Table 2 were measured by several authors and compiled by Humbach et al [34]. Variations in the silica preparation and measurement techniques by the different authors cause disparity in the listed absorption coefficients making comparison of the relative absorption intensities difficult. The relative absorption values listed in the fourth column of Table 2 were systematically measured by Humbach and can be directly compared [34]. The absorption of the fundamental ≡Si-OH mode is substantially larger than the absorption of higher order and combination modes.

The fundamental ≡Si-H stretching mode is around 4440nm [46] putting the fundamental and first overtone of ≡Si-H beyond the measurement capability of the equipment used in this project. The third overtone of the Si-H vibration should be around 1520nm [44], although this overtone may be difficult to distinguish because of its small magnitude compared to the 1383nm ≡Si-OH overtone.

Absorption Band	Wavelength (nm)	Frequency (THz)	Relative Absorption	Reported Absorption Coefficients (dB/(km ppm))
OH	2722	110	10000	10000, 10030
OH + SiOSi	2212	136	201	206.5, 195
OH + 2 x SiOSi	1894	158	0.84	
2 x OH	1383	217	62.7	50.4, 61.9, 60.6
2 x OH + SiOSi	1246	241	2.7	2.6, 2.63
2 x OH + 2 x SiOSi	1139	263	0.07	0.059
3 x OH	943	318	1.6	1.25, 0.83, 1.26, 2
3 x OH + SiOSi	878	341	0.08	0.115, 0.075
3 x OH + 2 x SiOSi	825	363	0.0038	0.014, 0.003
4 x OH	724	414	0.078	0.111, 0.058
4 x OH + SiOSi	685	438	0.0044	0.016, 0.0033
4 x OH + 2 x SiOSi	651	461	0.00028	0.0008
5 x OH	593	506	0.0064	0.009, 0.005

Table 2: Position & Intensities of OH & OH+SiO_4 Absorption Bands in Silica [34]

Figure 28 and Figure 29 have the ≡Si-OH and ≡Si-O-Si≡ related absorption peaks identified on the as-manufactured absorption spectra of the Polymicro fibers studied in this project [12]. Several of the higher order overtone and combination peaks are identifiable in the high-OH fiber. The 943nm, 1246nm and 1383nm bands create substantial absorption making the fiber unusable above 1200nm. Two higher order vibrational modes are identifiable in the low-OH fiber, as shown in Figure 29.

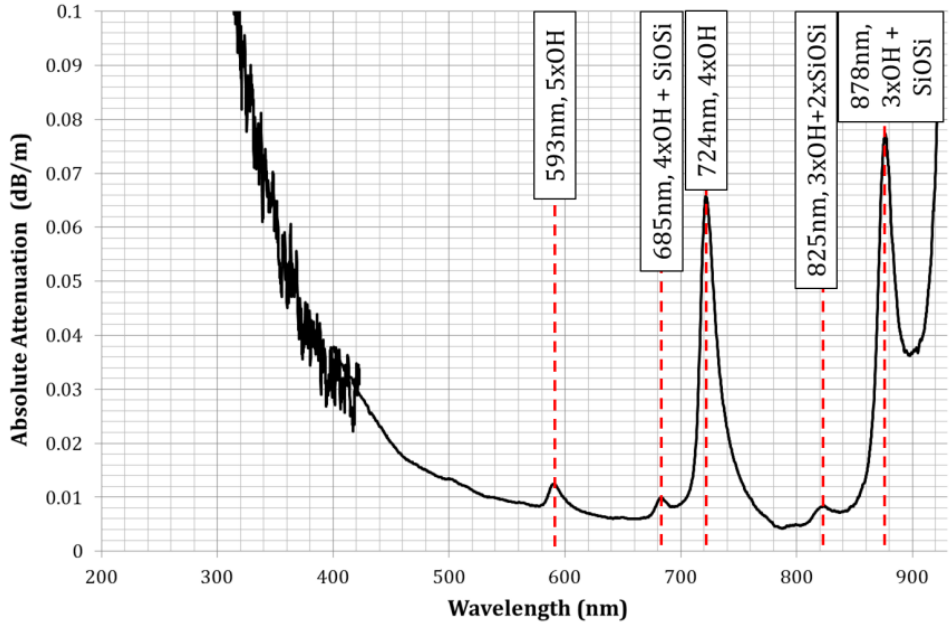

Figure 28: Intrinsic Vibrational Absorption in High-OH Polymicro Fiber (FVP100120140)

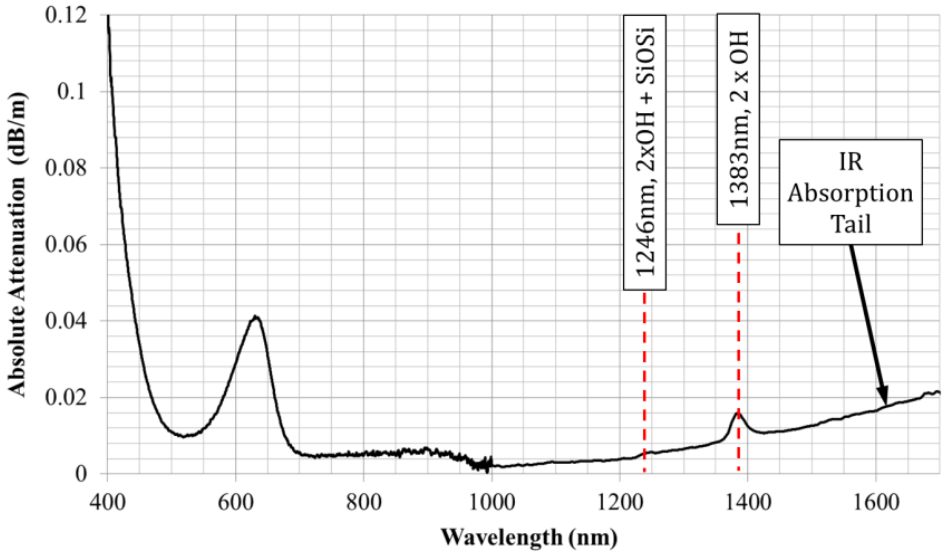

Figure 29: Intrinsic Vibrational Absorption in Low-OH Polymicro Fiber (FIP100120140)

The absorption peaks identified in Figure 28 and Figure 29 are broad because the vibrating molecules interact with other atoms in the silica. The amorphous silica has a distribution of parameters defining the local structure which leads to a distribution of absorption frequencies. In contrast, the OH peaks in the absorption spectra of an isolated water vapor molecule would be sharp [47]. The peaks at 724nm and 878nm in Figure 28 also illustrate that the absorption peaks are inhomogeneously broad. The inhomogeneity is caused by several different bonding configurations for the OH molecules in the silica [48] [49]. The IR absorption tail identified in Figure 29 is caused by overtones and combinations of fundamental SiO_4 vibration modes in addition to the ≡Si-OH impurity absorption. The IR tail shown in Figure 29 has a peak intensity on the order of 1E+7dB/m around 9000nm in undoped fused silica [50].

Temperature Dependent Concentration of Hydrogen Impurities

Atomic and molecular hydrogen are both mobile in silica at relatively low temperatures and the mobility of both increases with increasing temperature [26]. The solubility of hydrogen in silica is dependent on the concentration of NBOHC and E'-center defects which provide dangling bonds that can form ≡Si-OH and ≡Si-H, respectively. The concentration of NBOHCs and E'-centers is dependent on temperature and stoichiometry, as described in a previous section. The concentration of ≡Si-OH in silica is therefore dependent on the thermal history and stoichiometry of the silica in addition to the availability of hydrogen in the environment around the silica.

The silica optical fibers used in this work were manufactured with a polyimide coating. At temperatures below 400°C, this polymer coating provides environmental and mechanical protection. Above 400°C this coating starts to decompose and becomes a source of hydrogen for diffusion into the silica [44]. After the coating has been thermally removed, hydrogen in the environment can readily diffuse into the fiber.

Rose and Bruno heated a short length of polymer coated low-OH silica optical fiber from room temperature to 1200°C and observed a substantial increase in ≡Si-OH related absorption. The researchers repeated the experiment with a length of fiber that had the polymer coating chemically removed prior to heating. An increase in ≡Si-OH absorption was not observed when the polymer

coating was removed prior to heating [44]. In both of these experiments the optical fibers were heated in ambient atmosphere.

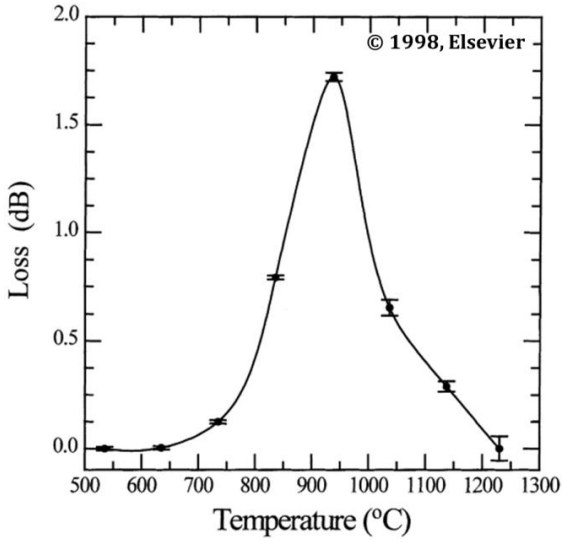

Figure 30: Loss at 1390nm in Silica Fiber Heated with Polymer Coating [44]
Copyright 1998, Elsevier [44].

In addition, the researchers observed that the increased ≡Si-OH attenuation peaked around 950°C and then decreased at higher temperatures, as shown in Figure 30 [44]. Dissociation of the ≡Si-OH bonds at high temperature would reduce the ≡Si-OH attenuation and increase the physically dissolved hydrogen in the silica. If the hydrogen concentration increased beyond its physical solubility in the silica, hydrogen would diffuse out of the silica, assuming the hydrogen concentration in the ambient environment was lower than the hydrogen concentration in the silica. Outgassing of H_2 from high-OH silica heated in vacuum has been reported by Morimoto et al with peak H_2 outgassing around 900°C [51].

Diffusion of Intentional Impurities

The Polymicro fibers tested in this project had a fluorine doped silica clad and a pure silica core. The CeramOptec fiber tested in this project had a fluorine doped silica clad and a germanium doped silica core. Exposing silica optical fibers to high temperatures could result in diffusion of fluorine or germanium. Temperature dependent diffusion coefficients for fluorine and germanium in silica are shown in Equation 11. Diffusion of the intentional dopants would change the as-manufactured refractive index profile and could reduce the effectiveness of the waveguide.

$$D_F = 1.74 \exp\left(\frac{-4.61\times10^4}{T}\right)\frac{\text{cm}^2}{\text{sec}}$$

$$D_{Ge} = 7250 \exp\left(\frac{-6.6\times10^4}{T}\right)\frac{\text{cm}^2}{\text{sec}}$$

$$with: \quad T = \text{temperature in Kelvin}$$

Equation 11: Fluorine [52] & Germanium [53] Diffusion Coefficients in Silica

COMSOL was used to calculate the fluorine and germanium distributions in silica after 100, 200, and 1000 hours at 1000°C, as shown in Figure 31. The geometry and initial dopant distribution for a 50µm radius core, 60µm radius clad, step-index optical fiber was used in the model. The COMSOL model was validated against experimental results published by Hermann et al [54]. In Figure 31, the core-clad interface is at a radial position of 50µm, the clad-air interface is at a radial position of 60µm, and the dopant concentrations were normalized to the initial dopant concentration. Fluorine is more mobile than germanium in silica at 1000°C and the change in the germanium distribution is probably negligible compared to variability introduced in manufacturing. After 1000 hours at 1000°C, fluorine has diffused from the clad into the core so that the change in refractive index occurs gradually over 2µm. This change in refractive index profile is not necessarily detrimental to the waveguide since graded-index (opposed to step-index) optical fibers are intentionally manufactured with similar refractive index profiles [6].

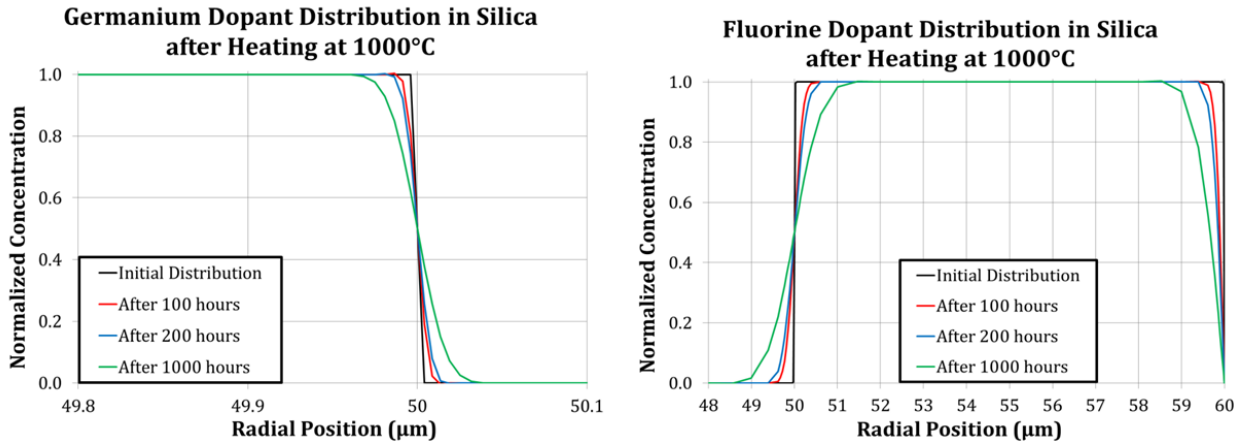

Figure 31: Diffusion of Germanium (left) and Fluorine (right) in Silica at 1000°C

Despite these calculations and despite the fact that fluorine doped silica fibers are manufactured at much higher temperatures, Gibson et al. have reported fluorine migration out of the clad of a silica optical fiber at much lower temperatures [55]. After 70 hours at 670°C the thickness of the fluorine doped region had reduced from 5µm to 3.5µm. After 70 hours at 970°C the thickness of the fluorine doped region had reduced from 5µm to 2.5µm. The paper does not explain the physical mechanism of the fluorine mobility and the author has not yet determined the mechanism [56]. The reduced cladding thickness results in the waveguide being more leaky to longer wavelength photons and appears as broadband attenuation increase with more attenuation in the IR [57].

1.8.3 Interaction between Defects and Impurities in Silica Optical Fiber

Silica components can be intentionally doped with hydrogen by exposing the component to a hydrogen rich atmosphere at elevated temperatures. As discussed previously, NBOHC and E'-center defects are common in silica fibers and create attenuation in the UV range. Atomic or molecular hydrogen in silica readily bonds with these defects according to the reactions listed in Figure 27. Doping silica with hydrogen reduces UV-range absorption by reducing the concentration of NBOHC and E'-center defects. The reduction in UV attenuation in high-OH silica can be observed by comparing the attenuation spectra of the low-OH and high-OH Polymicro fibers, shown in Figure 19 and Figure 20.

Passivating the NBHOC and E'-center dangling bonds with hydrogen forms ≡Si-OH and ≡Si-H, reducing the absorption of the original defects by electronic excitations. Increasing the ≡Si-OH and ≡Si-H concentration, however, increases absorption in the IR range through vibrational excitations, as shown in Table 2. Using hydrogen doping to improve transmission in the UV is done at the cost of decreased IR transmission. The fiber type chosen for an application should be based on the transmission spectra for the as-manufactured product. If low IR attenuation is needed in an application where hydrogen contamination of the fiber is possible, using a fiber produced with an oxygen deficit should inhibit Si-OH formation.

1.8.4 Crystallization (Devitrification) of Silica Optical Fiber

Fused silica is an amorphous form of SiO_2 but several forms of crystalline SiO_2 also exist. When silica is exposed to high temperatures, crystalline SiO_2 can nucleate on the surface of the silica, as shown in Figure 32A [27]. The nucleation rate increases exponentially with temperature and is also dependent on the composition and surface condition of the glass. After nucleation, crystal grains grow along the surface and into the bulk material. The growth rate is also temperature dependent and grain growth can continue at temperatures below that required for grain nucleation [58]. Figure 32B&C show the result of grain growth on the surface of an optical fiber [27]. According to Rose, the transmission at 1287nm for the fiber in Figure 32A was reduced by 50% after eight hours [27], although sources of attenuation other than crystallization were not discussed by the author. The fibers in Figure 32B&C suffered an 80% and 100% transmission loss, respectively.

Crystal grain nucleation creates broadband scattering that increases as crystallization progresses [44]. In addition to optical attenuation, crystallization of silica fibers decreases their strength, increasing the likelihood of a mechanical failure. Nucleation and growth rates are exponential functions of temperature and optical fibers can be used at temperatures where the crystallization rate is negligible.

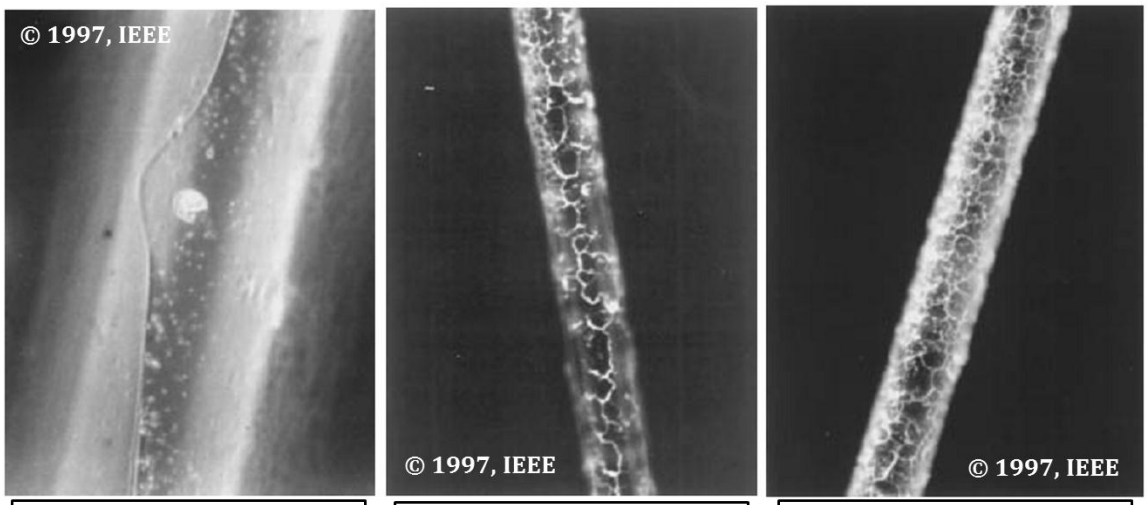

Figure 32: Nucleation and Growth of Crystal Grains on a Silica Optical Fiber [27] Copyright 1997, IEEE [27].

1.8.5 Radiation Induced Attenuation in Silica

The mechanisms that cause increased optical attenuation in silica as a result of exposure to radiation are briefly reviewed in this section. For an in-depth review of radiation induced damage in silica, the reader is referred to a thesis by Govindarajan who also worked on this project [10]. In addition to a providing a good background, Govindarajan also investigated radiation damage in silica using molecular dynamics and ab-initio simulations.

In the context of this work, radiation is defined as gamma radiation and the mixed neutron and gamma radiation produced by nuclear fission. Radiation interaction with silica causes damage that affects the material properties. The two primary results of radiation interaction with glass are ionization and atomic displacements. Gamma radiation mainly results in ionization, although atomic displacements are possible. Fast neutron radiation directly results in atomic displacements but indirectly causes substantial ionization.

Ionization results in electron-hole pairs that are mobile in the material. Some of the electron-hole pairs can become trapped at dangling bonds on the defect structures, described previously in this chapter, causing additional optical attenuation [5]. Atomic displacements disrupt the short range order of the silica and increase the concentration of structural defects.

Neutron Interactions

Neutrons are uncharged particles that interact directly with the nuclei of atoms. Elastic scattering of a neutron with a nucleus results in kinetic energy being transferred from the neutron to the nucleus. The amount of kinetic energy imparted to the nucleus is dependent on the mass of the nucleus, the energy of the incident neutron, and the angle through which the neutron is scattered. If enough kinetic energy is imparted to a nucleus, the nucleus is removed from its original position in the glass matrix and moves through the matrix colliding with other atoms. Removal of the initial nucleus (primary knock on atom or PKA) creates a vacancy and subsequent collisions between the PKA and other atoms can cause additional atomic displacements. The atoms displaced during this damage cascade form interstitial defects in the glass matrix. Displacement damage accumulates in silica at room temperature. In addition to creating displacement damage, fast neutrons indirectly cause ionization as nuclei lose some or all of their electrons when displaced. Also, PKA can cause ionization as they slow down.

Less energy is needed to displace an oxygen atom from the silica network than a silicon atom [59]. A threshold energy needed to create a displacement in silica is assumed to be 25eV. The maximum percent of a neutron's kinetic energy that can be transferred to a silicon or oxygen atom in a single elastic collision is 13.3% and 22.1%, respectively. The distribution of neutron energies at the experimental location used in this project is shown in Figure 133, but only the fast neutrons are capable of creating displacement damage.

Lower energy neutrons cannot cause displacement damage but these neutrons can be absorbed by nuclei, increasing the atomic mass and possibly resulting in an unstable nucleus that would decay into a different element. Silicon has three naturally occurring stable isotopes: Si-28, Si-29 and Si-30. The isotopic abundances of Si-28, Si-29 and Si-30 are 92.23%, 4.67%, and 3.1%, respectively. Neutron capture by this isotope would result in Si-29, which is stable. Neutron capture by Si-30 results in Si-31 which is unstable and decays to P-31 with a half-life of 157 minutes [60]. The small isotopic abundance and the small thermal neutron capture cross section of Si-31 results in a slow production rate of phosphorus in silica produced with naturally occurring silicon. In the irradiations for this dissertation, the concentration of P-31 in the silica at the end of the experiments was on the order of parts per trillion by weight.

The situation is similar for the three naturally occurring stable isotopes of oxygen: O-16, O-17, and O-18. The abundances of O-16, O-17 and O-18 are 99.7%, 0.038% and 0.2%, respectively. O-

19 decays into F-19 with a half-life of 27 seconds, but the small abundance of O-19 causes the ingrowth of fluorine to be negligible.

Gamma Interactions

Gamma radiation interacts with the electrons in a material. Because silicon and oxygen are relatively low atomic number elements, the main photon interaction in silica is Compton scattering [61]. Compton scattering is elastic scattering of a photon by an electron. In this interaction the incident photon loses energy and changes direction, while the struck electron gains kinetic energy and is ejected from the atom. Compton electrons create additional ionization in the material and can cause short range atomic displacements [5]. The atoms displaced as a result of gamma radiation usually recombine, but broken strained bonds can enable structural relaxation that inhibits recombination of closely located complementary defects [37] [62].

1.9 Optical Attenuation caused by Radiation

Displacement damage creates additional structural defects in the silica. The increased concentration of some defects contributes directly to optical attenuation and some defects contribute indirectly by providing additional traps for charge carriers. Accumulation of displacement damage can also lead to extended defects in the silica [41]. At fast neutron fluences around 2E20n/cm^2, neutron irradiated silica approaches a metamict state with an increased density [63].

The structural defects described previously in this chapter were assumed to be electrically neutral dangling bonds. Electrons and holes can be trapped at dangling bonds creating charged defects and additional optical attenuation. E'-centers, for example, must trap a hole and become positively charged to cause optical absorption. NBOHCs, however, cause optical attenuation in the electrically neutral state. The initial displacement event that causes a structural defect leaves the defect in a charged state, with an example shown in Equation 12 [40]. Different types of charged E'-centers exist and the classification of the different centers in the literature is confusing and sometimes contentious. Regardless, charged E'-centers collectively create optical attenuation around 215nm (5.7eV).

The bond broken in Equation 12 can eventually reform, but structural relaxation may inhibit the recombination. Charge carriers can also be trapped at existing dangling bonds without additional creation of broken bonds. Ionization caused by X-rays, for example, can populate dangling bonds with charge carriers but cannot cause additional displacement damage [40].

$$\equiv Si - Si \equiv \xrightarrow{\gamma \text{ or } n} \equiv Si^{\bullet} + {}^{+}\text{Si} \equiv + e^{-}$$

Equation 12: Conversion of a Si-Si Bond into an E' and E'γ Center (E'γ is charged)

The concentration of trapped carriers is dependent on the recombination rate and the creation rate with the latter being dependent on the irradiation conditions. Trapped carriers are more stable at low temperatures and de-trapping of charged E'-centers, for example, occurs at room temperature and with an additional 90% reduction in E_γ'-centers after a few minutes at 200°C [40].

1.10 Summary

Silica optical fibers are commercially available with minimal intrinsic material attenuation in the UV-NIR range in mundane environments. These fibers were developed primarily for data transmission in the telecommunications industry, but some of the technology has been repurposed for optical instrumentation. In the experimental portion of this project, the attenuation in

commercially available multimode silica optical fibers is investigated at temperatures up to 1000°C in a reactor radiation environment. The functionality of the OBR by Luna Innovations using a singlemode silica optical fiber is also investigated experimentally. The effect of radiation damage on fused silica is investigated computationally. Other optical sensors are not being investigated in this project but the results of this work will hopefully be used to assess the longevity of optical instrumentation in high temperature radiation environments.

Chapter 2. Task A [10]

2.1 Deliverable

A validated multi-scale model for the effects of operation at high temperatures on glass fibers including recrystallization.

2.2 Introduction

Identification and classification of structural defects in a crystalline structure is typically straightforward and unambiguous because of the long range order. Identification and classification of defect structures in an amorphous material, such as silica, was difficult because of the lack of long range order. A large number of approaches were considered based on information in the literature and methods known from experimentation until a solution satisfactory for our purposes had been found.

The final goal was to identify optically active defect structures in terms of vacancies or miscoordinated atoms. More generally, however, we were interested in quantities that gave useful information about structural changes in the silica, including crystallization, as a result of heating and irradiation. We have identified a set of techniques that allow us to analyze the data from Molecular Dynamics (MD) simulations and also to connect the findings to experimental results.

These methods are summarized in the following. An optimized amorphous silica model and the Tersoff-Munetoh inter-atomic potential validated from previous results were used for the analysis. MD simulations using the GULP MD code were used with a constant pressure, Nose-Hoover thermostat to simulate the temperature evolution of the structure within the full operating range of nuclear reactors (300K – 1400K). Furthermore, preliminary simulations for knock-on events with energies ~10 keV were performed. For the latter, an adiabatic heat sink was defined over the skin of the simulation box to control the temperature within the irradiated system. A silicon atom at the center of the simulation cell was chosen as the PKA atom and provided with a velocity. After sufficient time evolution, the irradiated structure was quenched to analyze the structure.

In post-processing, a number of structural parameters were used to characterize the structure, including ring-order distribution, coordination number variation correlated with potential energy, pair-correlation (radial distribution) functions, structure factor and finally XRD diffraction data.

2.3 Ring-Order Distribution

A ring was defined to be the shortest closed loop of Si-O bonds, calculated using the "Depth-First Traversal" algorithm, assuming that stable Si-O bonds have bond lengths smaller than 2 Angstroms (Figure 33). Rings of order 3, 4, 5 and 6 were observed in the structure with the ring distribution centered at 6-ordered rings at room temperature [64]. Within the 1400K temperature range, there was a slight increase in the percentage of 3 and 4 member rings followed by a slight decrease in the percentage of 6 member rings (Figure 34). The preliminary irradiation analysis indicated a higher increase in the percentage of 3 and 4 member rings and a decrease in the percentage of 6 member rings. 3 member rings are very close to planar rings and correspond to the vibration frequencies of D1 and D2 lines detected by Raman Spectroscopy [65], which thus allow experimental validation.

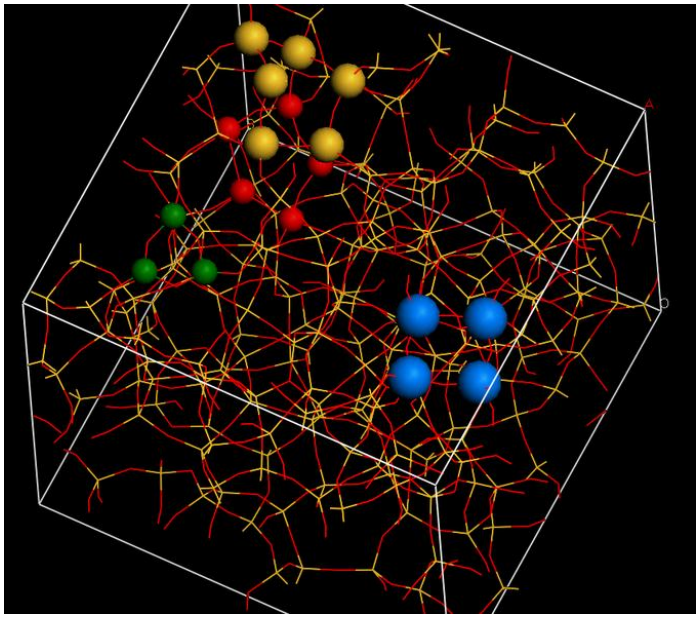

Figure 33: Presence of 3, 4, 5 and 6-membered rings

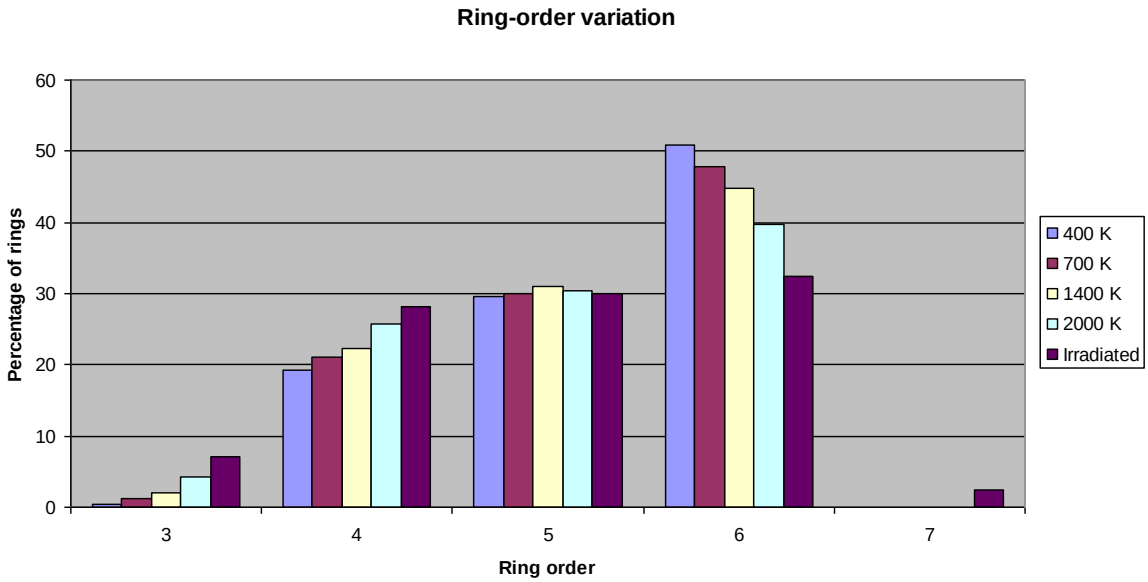

Figure 34: Ring-order variation of amorphous silica with temperature & radiation damage

2.4 Coordination Number Variation

In defining the coordination numbers, a cutoff radius of 2 Å was used between the first and second nearest neighbor distance. Perfectly coordinated oxygen, excess-coordinated oxygen and oxygen with coordination one were binned based on their potential energies (Figure 35 & Figure 36). There was an increase in the number of single coordinated oxygen atoms in the irradiated silica structure when compared to the structure held at 300K. The variation of stable defects with various initial energies of PKA atoms were analyzed subsequently and correlated to literature [66].

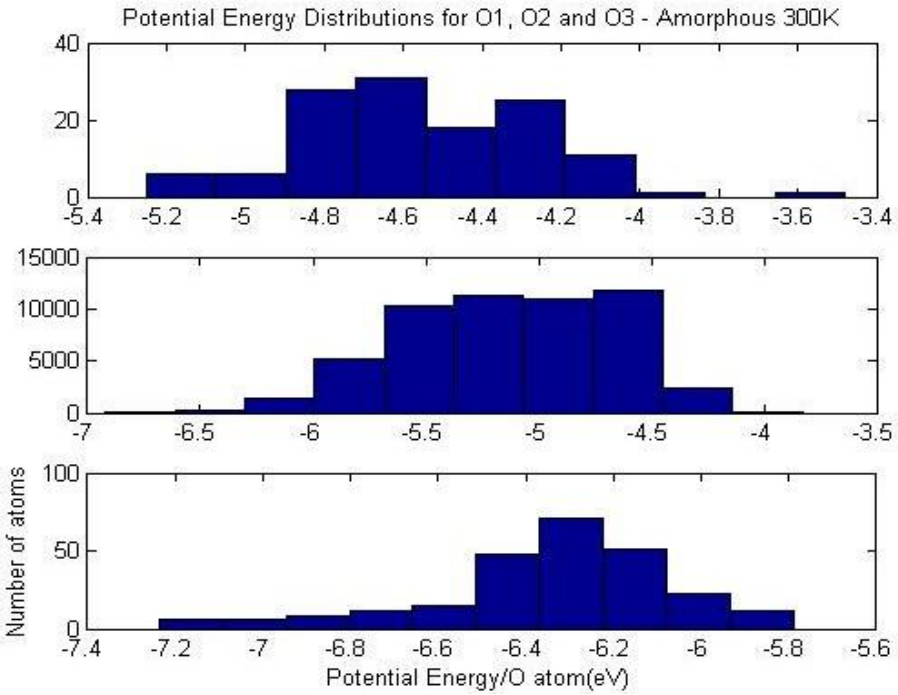

Figure 35: Potential Energy/Oxygen atom Distribution with O1, O2 and O3 coordination of amorphous silica at room-temperature

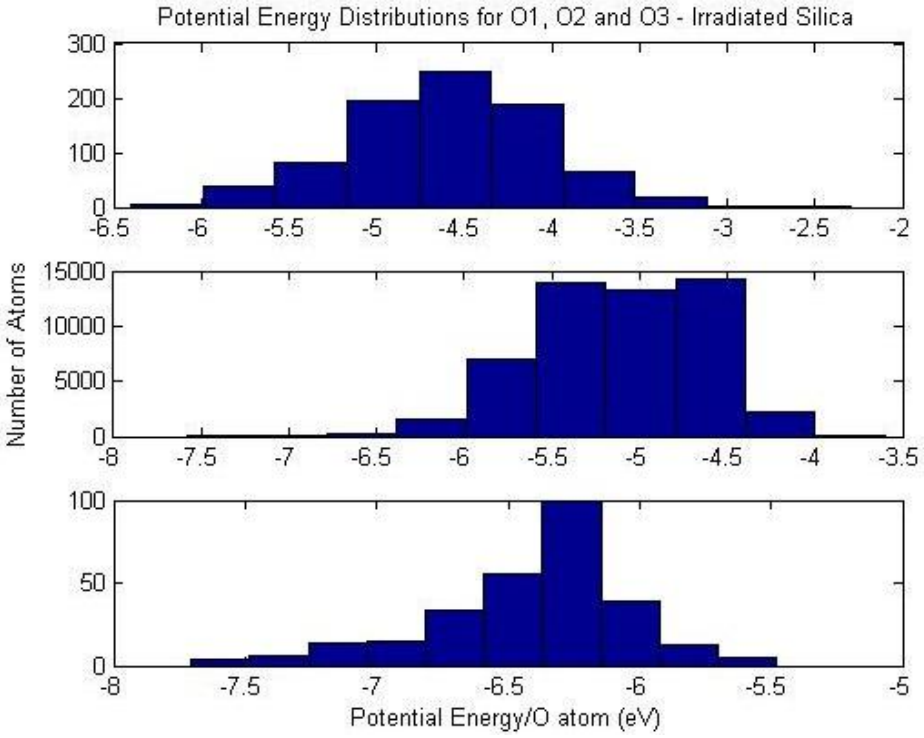

Figure 36: Potential Energy/ Oxygen atom Distribution with O1, O2 and O3 coordination of irradiated silica, increase in the number of O1 coordinated atoms

2.5 Pair-Correlation Functions

Pair-correlation functions of Si-Si, O-O, and Si-O pairs were obtained and compared with increasing temperature. There was a slight decrease in the height of peaks obtained with rise in temperature (Figure 37). From literature [67], the positive thermal expansion of amorphous silica was attributed not to the variation in the lengths of nearest neighbor bonds but to the deformation of network-forming rings described earlier.

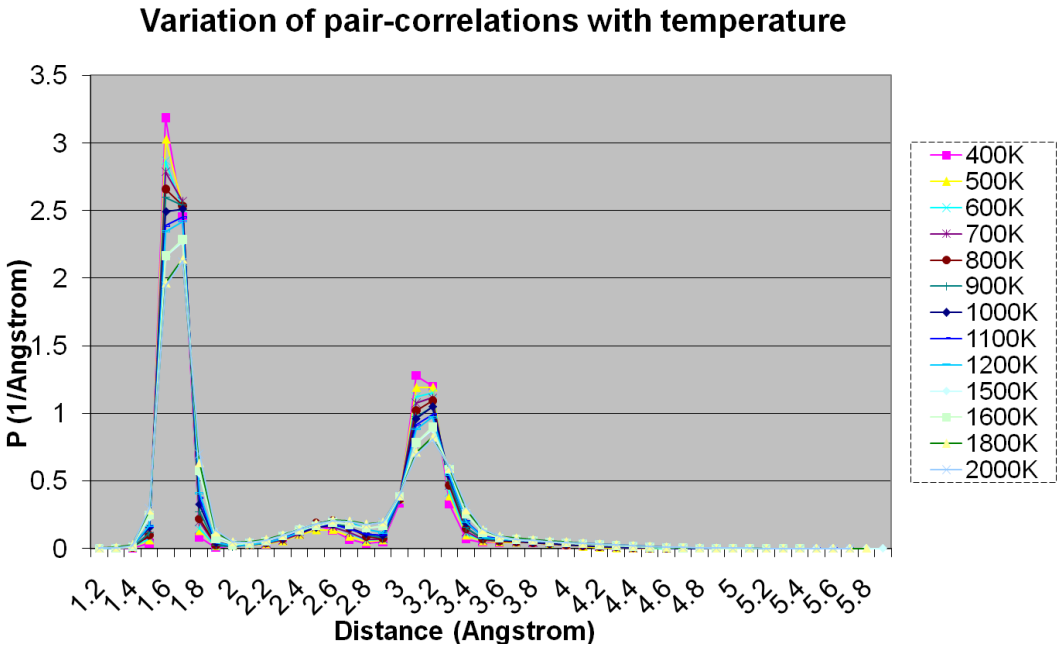

Figure 37: Variation of pair-correlation function with temperature evolution

2.6 Structure Factor

The structure factor, obtained as a function of the Fourier transform of the radial distribution function was computed and compared between the irradiated structure and the structure at room temperature. The structure factor provides information about the medium range order of amorphous materials and can be measured experimentally through x-ray or neutron diffraction. The comparison of structure factor of the irradiated structure and the relaxed structure revealed a relative decrease in the height of the peaks obtained (Figure 38 & Figure 39). The value of the structure factor is an indicator of the ordering prevalent in a structure. The relative decrease in structure factor and the increase in percentage of small member (3 & 4 member) rings with irradiation motivated us to explore the possibility of re-cyrstallization in the material with irradiation.

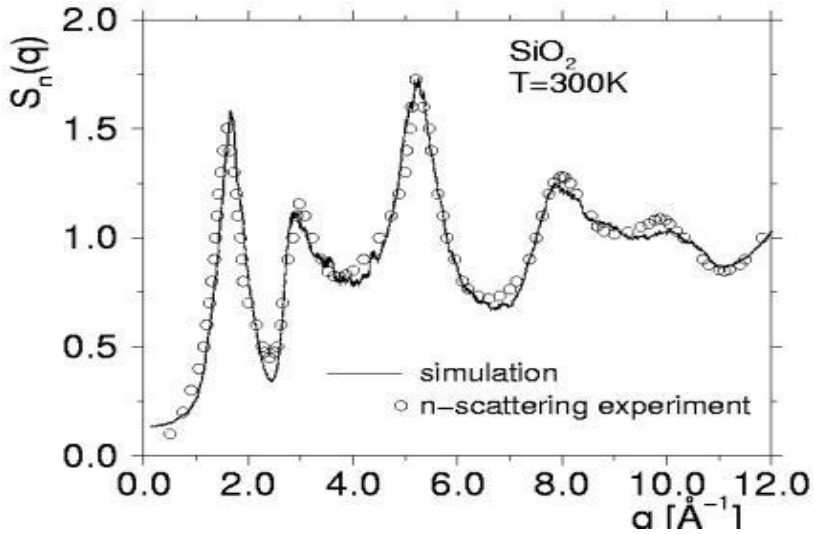

Figure 38: Experimental Structure factor distribution of amorphous silica at room-temperature

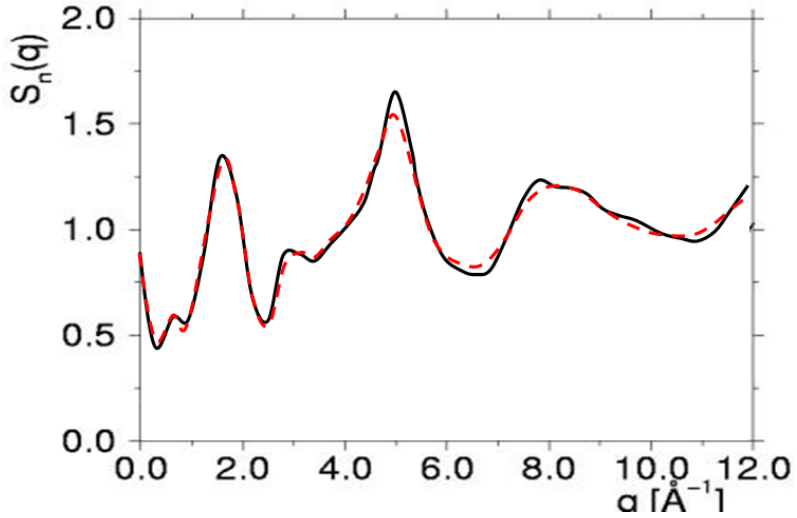

Figure 39: Comparison of structure factor for unirradiated and irradiated SiO_2 Initial amorphous structure (black solid line) and MD simulations of irradiated structure using PKA energy of 3.5keV (dashed line)

2.7 X-Ray Diffraction

The Crystal Diffract tool in the Crystal Maker package was used to perform an XRD analysis of the structures. A Gaussian interpolation was used to plot the diffraction data where the symmetry and shape of the peaks give an indication of the relative crystallization of the structure. The instrumental broadening parameter was kept at the default value of 9.509°. XRD spectra were obtained for Beta-Crystobalite silica, amorphous silica at room-temperature and irradiated silica quenched to room temperature (Figure 40 & Figure 41). From the XRD data of Crystalline Beta-Cristobalite, a number of distinct peaks was observed corresponding to the planes producing reflections. The amorphous silica structure at room temperature produced a near-symmetrical peak at around 21° with a slight hump at 9.5°. The irradiated structure when analyzed produced a second characteristic peak at 44° in addition to the peak at 21° which may correspond to the peaks

seen in the crystobalite spectrum and could indicate a partial crystallization of the structure. Thus, x-ray or electron diffraction, both available at OSU, can be used to examine crystallization effects.

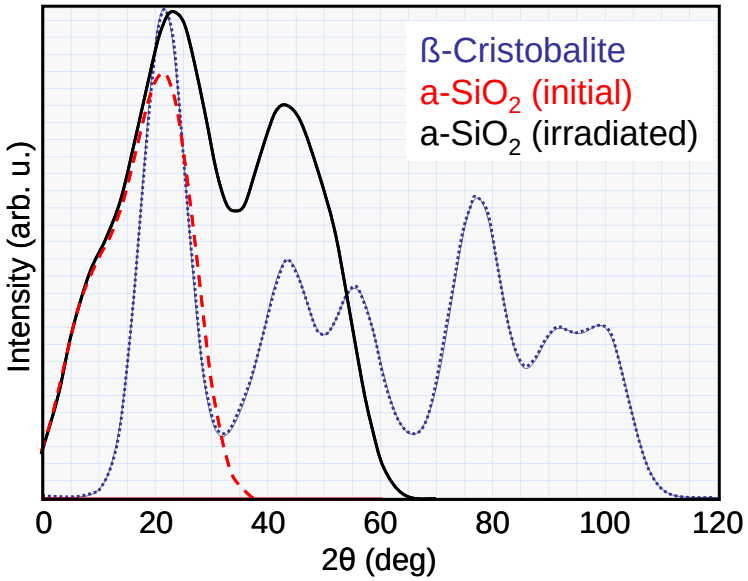

Figure 40: XRD simulation using Crystal Diffract for SiO_2
Crystalline beta-cristobalite (blue dotted line), amorphous SiO_2 before (red dashed line), and after a 3.5 keV knock-on event (black solid line).

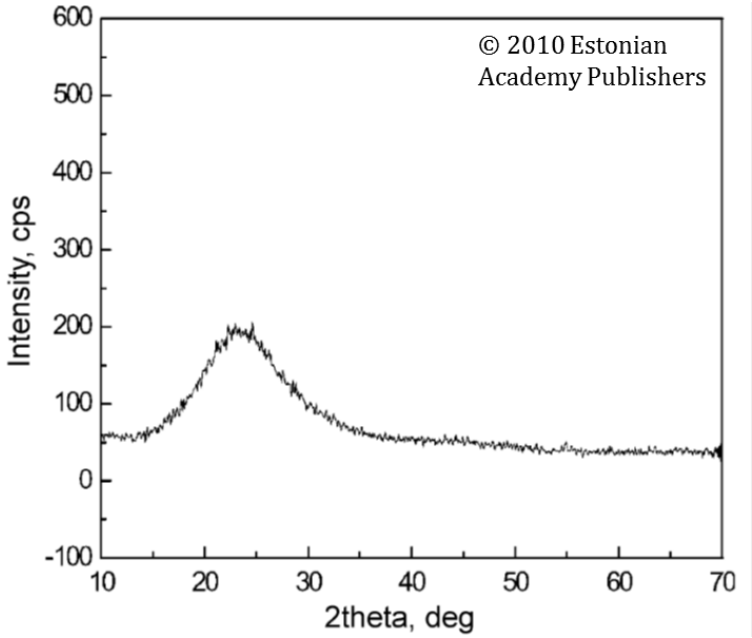

Figure 41: Experimental XRD spectrum of amorphous SiO_2 [68].
Peak near 21° matches calculated XRD spectra.
Copyright 2010, Estonian Academy Publishers [68].

2.8 Potential Energy & DSC

In differential scanning calorimetry (DSC), the difference in the amount of heat required to increase the temperature of a sample and reference is measured as a function of temperature. From that, glass transition, recrystallization, and other phase transitions can be determined. A DSC system is available at OSU.

Figure 42 shows a schematic curve for a glass as an example. In case the enthalpies for crystal and glass are known, an energy intermediate to those can be interpreted as a partially crystalline system, with the degree of crystallization approximated by a linear mixture rule.

In order to further probe the presence of crystallization pockets in the simulated system after irradiation, the energy of the perfectly crystalline and the energy of the 'perfectly' amorphous structures were compared with the energy of the irradiated structure. We observed that the potential energy of the irradiated structure lies between the energy range of the crystalline and amorphous material with the energy difference to the initial amorphous structure corresponding to 14% of the energy difference between fully amorphous and crystalline structure, indicating the possibility of a partial crystallization of the same amount.

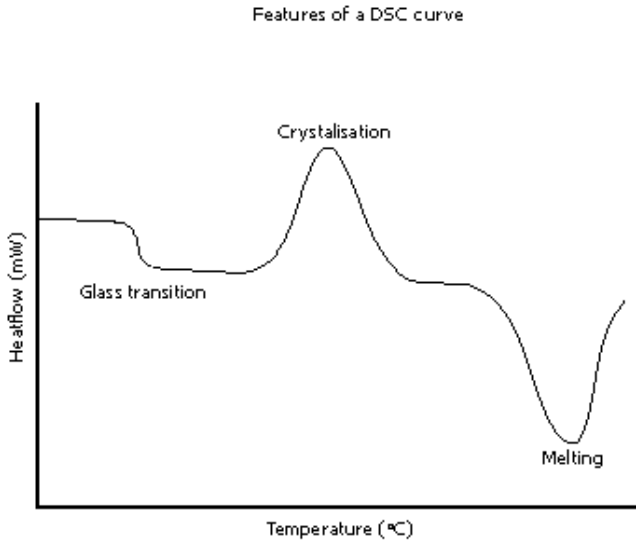

Figure 42: Schematic DSC curve

Chapter 3. Task B/G

3.1 Deliverable

An MCNP model of the radiation field for the fiber irradiation test facility in the ULORR; Calculated neutron flux energy spectra in the ULORR fiber irradiation test facility and its comparison with measurement; Characterization of the radiation field in the ULORR in standard terms, such as the displacement damage rate; Prediction of Primary Knock-On Atom (PKA) source term using MCNP. Dosimetric characterization of radiation field in irradiation test rig in ULORR.

3.2 MCNP Modeling

The radiation field on the periphery of a subvolume near the axial center of the core within the 7" dry tube (Figure 43) was obtained by running a whole core MCNP model of the Ohio State University Research Reactor (OSURR) with a Surface Source Write (SSW) card setup to surround the subvolume. With the assumption that the fiber irradiation furnace, when placed in the subvolume, does not significantly perturb the neutron flux energy distribution from that for a void within the subvolume, a separate, faster running MCNP model was created to determine the radiation field in the reactor irradiation furnace. This faster running MCNP model includes only the subvolume and the fiber irradiation facility test rig within the subvolume. The calculated surface source is specified on the boundary of the subvolume in this MCNP model. Figure 44 compares the neutron flux energy distribution with the fiber rig design model in the subvolume and with the subvolume as a void and shows that the flux is not significantly perturbed.

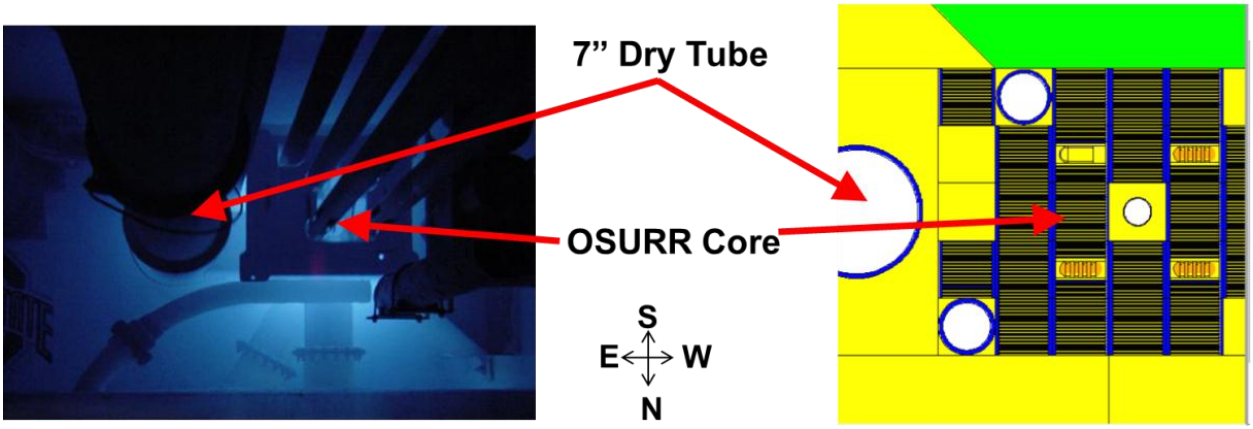

Figure 43: MCNP Model of OSURR Including 7" Dry-Tube

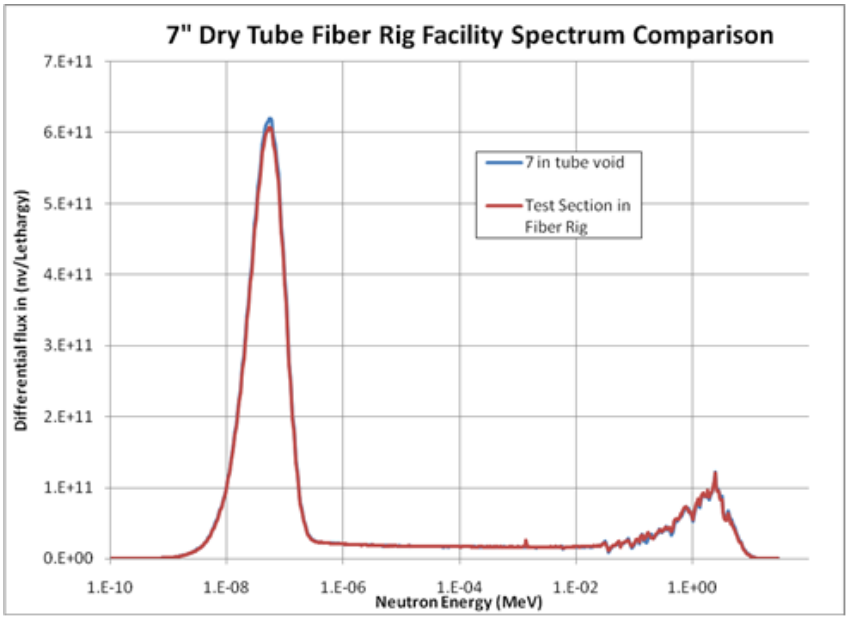

Figure 44: Spectrum Comparison in 7" Dry Tube, Calculated with MCNP

3.3 Neutron Flux Spectra in the OSURR Fiber Irradiation Test Facility

The CAD model that was developed for the fiber experiment, Figure 45, was approximated in an MCNP model in order to determine the flux spectrum in the fibers. Since the actual fiber geometry is a complex helical coil wrapped around the fiber holders, an approximation was made where the fibers were assumed to be a thin cylinder located on the inside surface of the fiber holders. An equivalent thickness of the cylinder was chosen based on the circular cross-sectional area of the fibers. Since the fiber cylinder extends the length of the insulated region in the experimental facility, results will be scaled by the amount of fiber eventually loaded into the facility.

In order to determine whether the flux spectrum is varying with axial position (the Z direction), an additional model was created to determine the flux spectrum in 14 cells with equal volume spaced one inch apart along the Z axis in the model. Figure 46 shows the flux spectra for varying positions relative to the core centerline. The group flux produced by MCNP for each energy bin was divided by bin width. Since the abscissa was plotted on a log scale, the ordinate was multiplied by product of the mid-point energy of the bin and the natural log of ten, so that the area under the curve is meaningful. Figure 47 shows the total neutron flux integrated over all energies with varying distance from the core horizontal midplane. (Z=0 cm). The region in which fibers are to be tested is approximately -15 cm to +15 cm where the top of the core is in the positive Z direction.

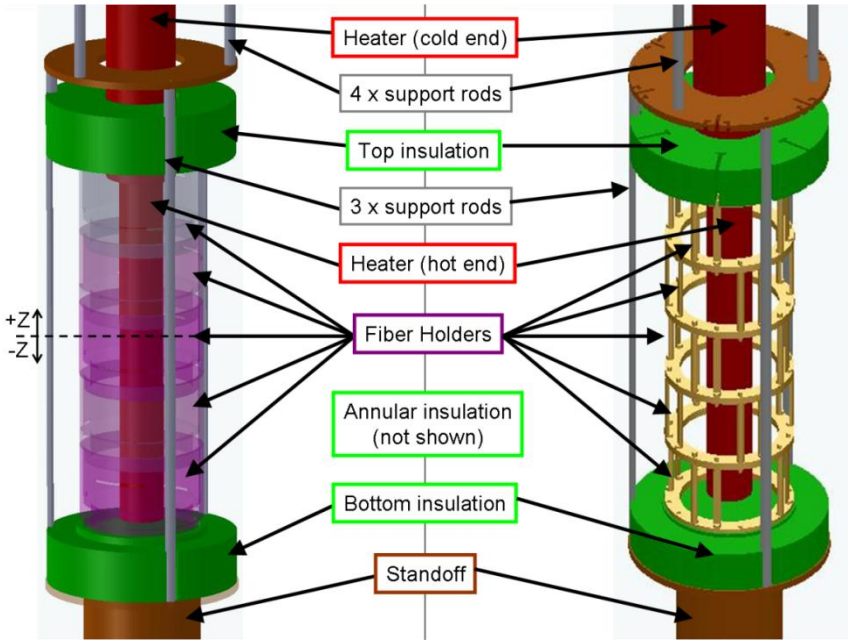

Figure 45: Initial and Revised Fiber Holder Design

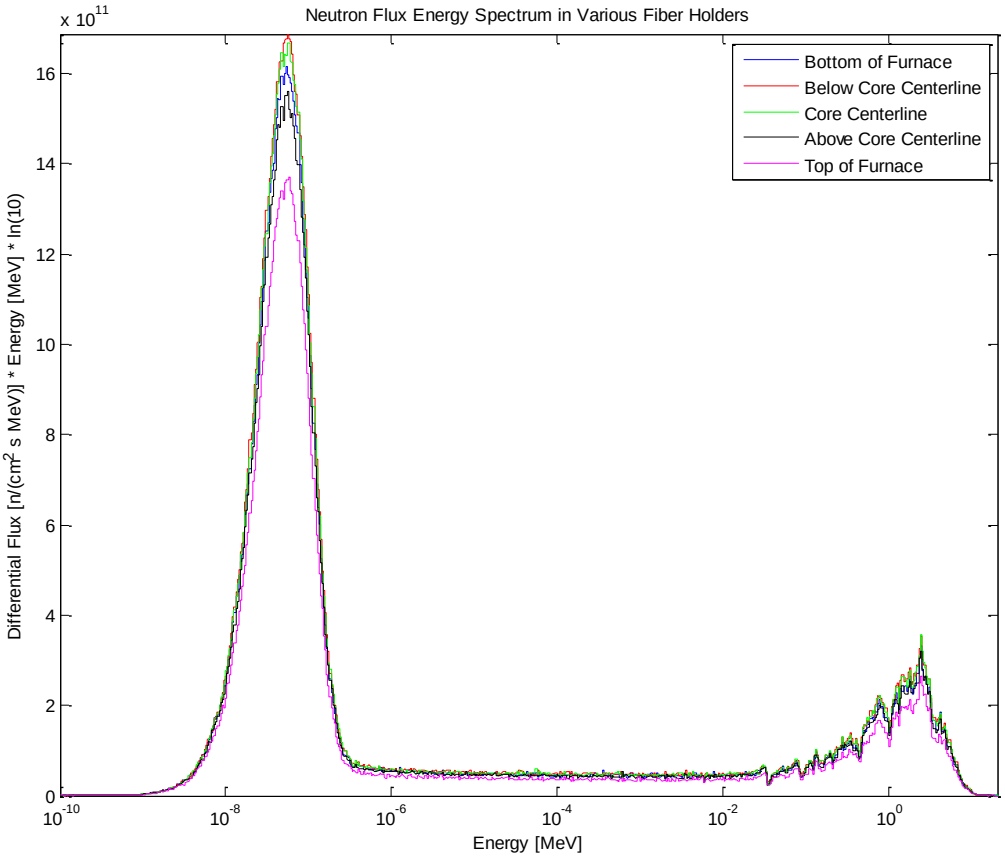

Figure 46: Neutron flux spectrum in the fibers with varying axial position (z-axis)

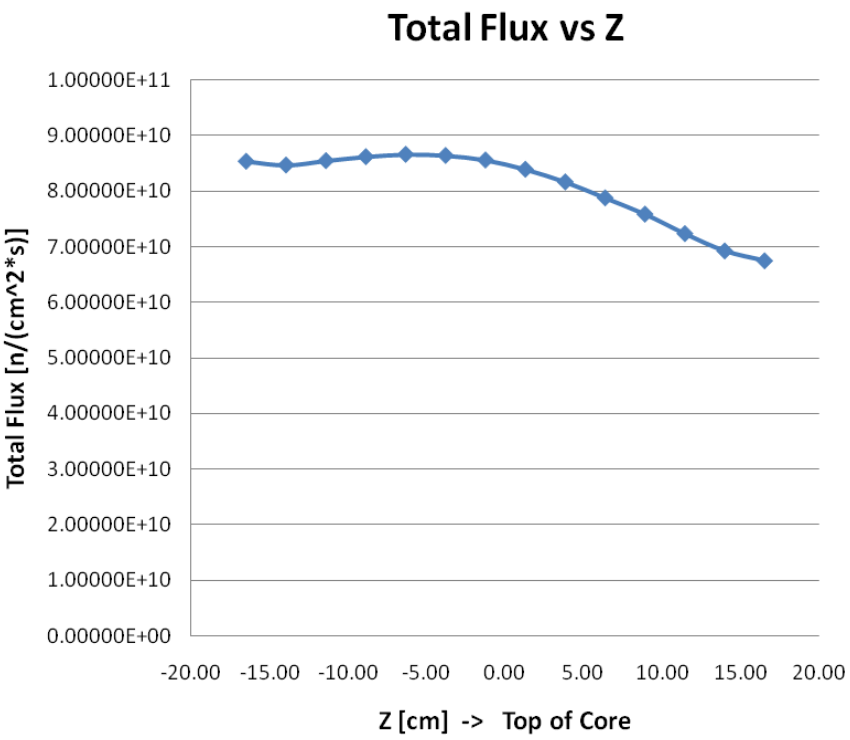

Figure 47: Total neutron flux vs distance (Z) from core horizontal midplane in cm

The neutron flux spectrum in the fiber irradiation test facility, as calculated with MCNP, was compared against a foil activation experiment in the 7" dry tube without the furnace. The foils used were titanium, iron, gold, cobalt, and copper. Two sets of five foils were used in the experiment and one set of foils was covered with cadmium and the other set was uncovered. The neutron flux energy spectrum was unfolded using the SAND-II code and a comparison of the results is shown in Figure 48. Weighting the calculated and measured flux by displacement damage kerma factors for Si and O shows that the two spectra give similar values for displacements per atom (DPA), as shown in Table 3. The neutron flux spectrum calculated with MCNP and with the SAND-II unfolding were in good agreement.

Calculation	DPA/s at 450 kW
MCNP Group Flux in Voided Tube Weighted by Kerma Factors at Room Temperature	3.14e-010
SAND-II Group Flux in Tube Weighted by Kerma Factors at Room Temperature	2.82e-010

Table 3: DPA Rate at 450kW for Calculated & Measured Neutron Spectra in 7" Dry Tube

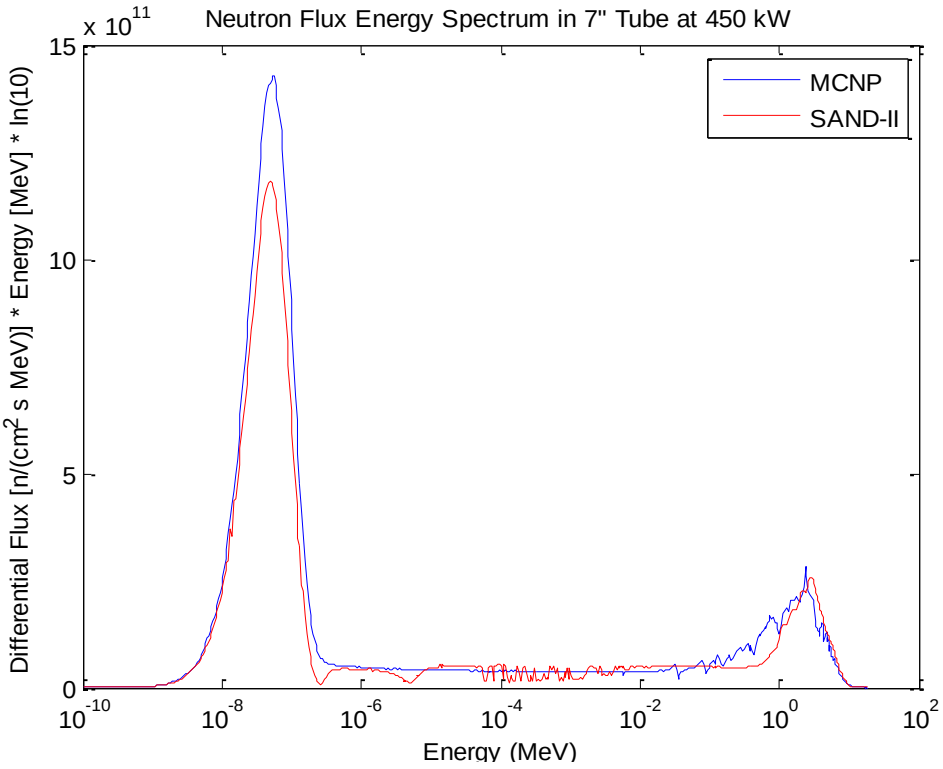

Figure 48: Comparison of Calculated & Measured Flux in 7" Dry Tube

3.4 Characterization of the Radiation Field in the OSURR in Standard Terms

Since a large contribution to this neutron flux spectrum is in the thermal energy range, an energy deposition tally was used in MCNP to determine the neutron absorbed dose in silica with varying distance from the core horizontal midplane. Figure 49 shows the normalized absorbed dose rate in SiO_2 from neutrons at varying distances from the core horizontal midplane. The absorbed dose rates at the various locations are normalized by the maximum absorbed dose rate in the fibers, and consequently the normalized absorbed dose rate at this location is one.

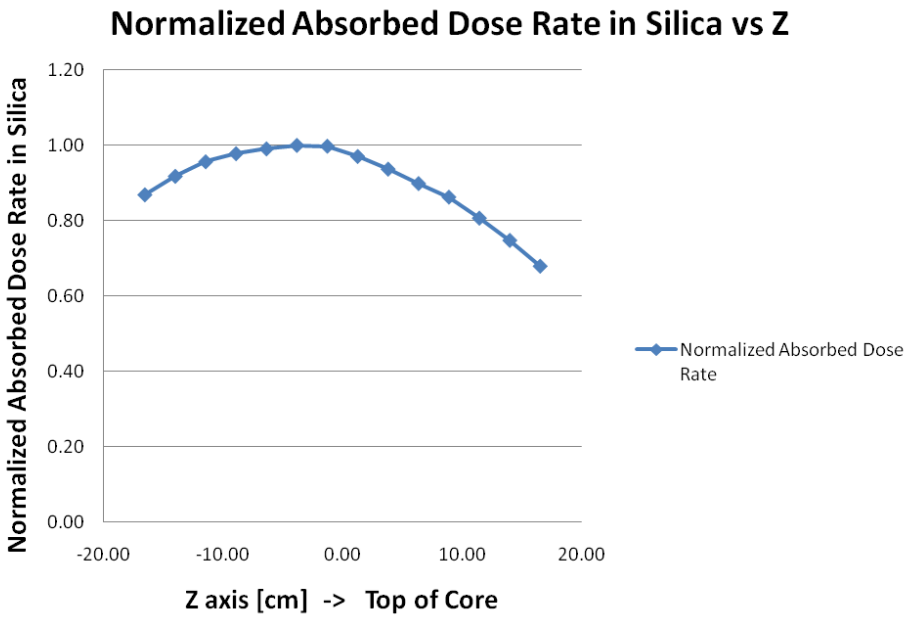

Figure 49: Normalized absorbed dose rate vs axial position (z-axis) in cm

The design change to the fiber holder components, shown in Figure 45, was modeled explicitly in MCNP to avoid having to determine whether this design change would significantly affect the neutron flux energy spectrum in the fibers. Four fiber cells were created so that the neutron flux spectrum and damage rate in the fibers could be compared at varying locations within the irradiation test facility. Vised output showing the model geometry is shown in Figure 50 and Figure 51. Figure 50 shows the facility in the XZ plane with an enlarged view showing the fiber cell on the right side. Figure 51 shows the facility in the XY plane. The top view is a cross-section showing the ends of one of the fiber holders. The bottom left view is a cross-section showing the fiber contained between the silica "posts" that are part of the fiber holders, and the bottom right view is this same view enlarged to show the fiber cell.

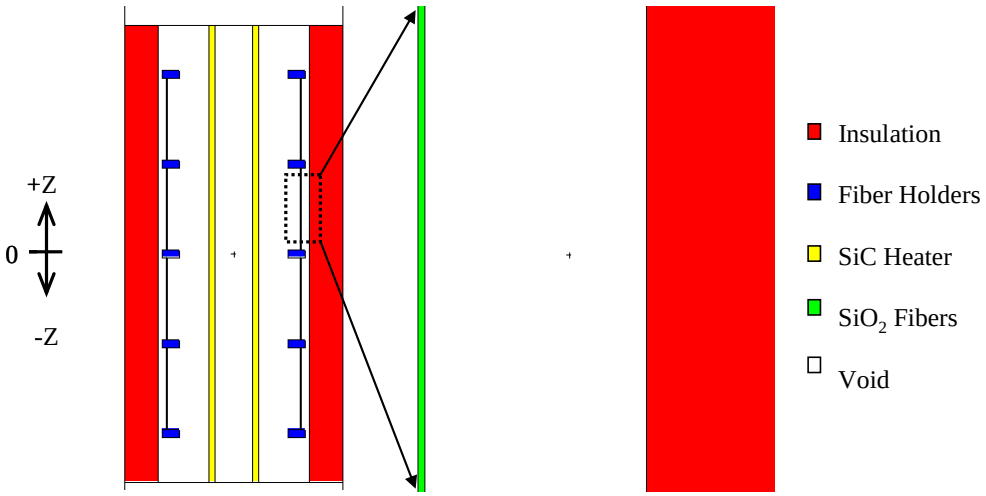

Figure 50: Revised MCNP model in the XZ plane, dashed box is enlarged on right

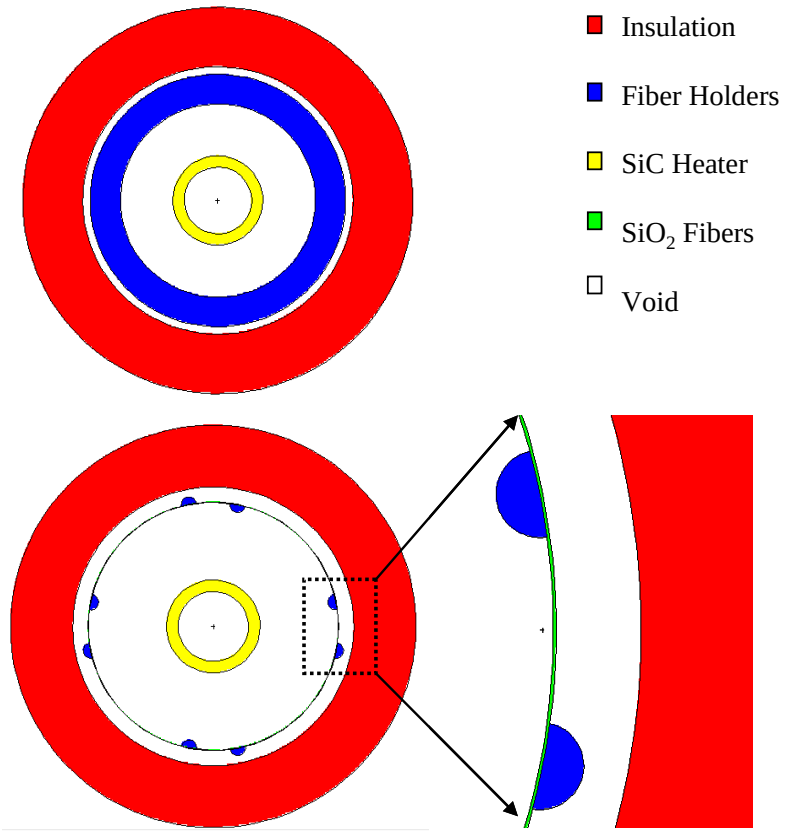

Figure 51: Revised MCNP model in the XY plane at two heights (dashed box is enlarged on right)

By tracking neutrons that entered any of the fiber cells, all collisions with silicon and oxygen atoms within the fiber cells were analyzed using conservation of energy and momentum equations to determine the location, direction, and energy of each primary knock-on atom (PKA). Analysis of the distribution of PKA location and direction showed a bias in both the location and direction of the PKAs with respect to one axis. The PKAs were occurring more often closer to the reactor core than further away from the reactor core. The PKAs were also observed to be directionally biased away from the reactor core. These findings prompted us to consider rotating the furnace during the irradiation experiment to achieve more uniform damage. Rotating the furnace with the reactor operating, however, was too difficult and this option was not pursued.

The total number of silicon and oxygen PKAs were calculated at each location within the test facility. These numbers were normalized by the number of source particles that were simulated in MCNP and the reactor power to determine an approximate number of PKAs originating in the fiber per unit time at each location in the test facility. These results were also normalized by the volume of fiber that was modeled so that a proper estimate for the total number of PKAs per unit time can be calculated once a decision is made on the length of fiber to be irradiated. Table 4 shows the number of PKAs per unit time per unit length of fiber per unit power for each location in the test facility.

	MCNP Tallies		PTRAC feature in MCNP		PKA Generation Rate
Furnace Location	% Energy to Displacement	% Energy to Ionization	% Energy to Displacement	% Energy to Ionization	[PKAs/cm^3-s]
Bottom	24.99%	75.01%	28.82%	71.18%	8.37E+10
Below Core Centerline	25.07%	74.93%	29.05%	70.95%	8.57E+10
Core Centerline	24.98%	75.02%	29.51%	70.49%	8.65E+10
Above Core Centerline	25.01%	74.99%	28.24%	71.76%	7.56E+10
Top	24.97%	75.03%	30.12%	69.88%	6.64E+10

Table 4: PKA Rates at Different Heights in Furnace

SPECTER-ANL is a more robust code for determining the PKA energy spectrum. The distribution of PKA energies calculated with MCNP was compared with the results obtained using SPECTER-ANL for each axial location. Results at the core horizontal mid-plane are shown for a reactor operating power of 450 kW in Figure 52. The results obtained using SPECTER-ANL were normalized by the number of PKAs per unit time per unit length of fiber per unit power obtained using MCNP. Table 5 compares estimates for the number of displacements per atom (DPA) per unit time at a reactor power of 450 kW using SPECTER-ANL and using displacement damage tallies in MCNP at the core horizontal mid-plane. The estimates of DPA/sec calculated with MCNP and SPECTER-ANL were in good agreement.

Method	DPA/sec at 450kW
MCNP Displacement Damage Tallies	3.93E-10
SPECTER-ANL	3.48E-10

Table 5: DPA Estimate Comparison using MCNP and SPECTER-ANL

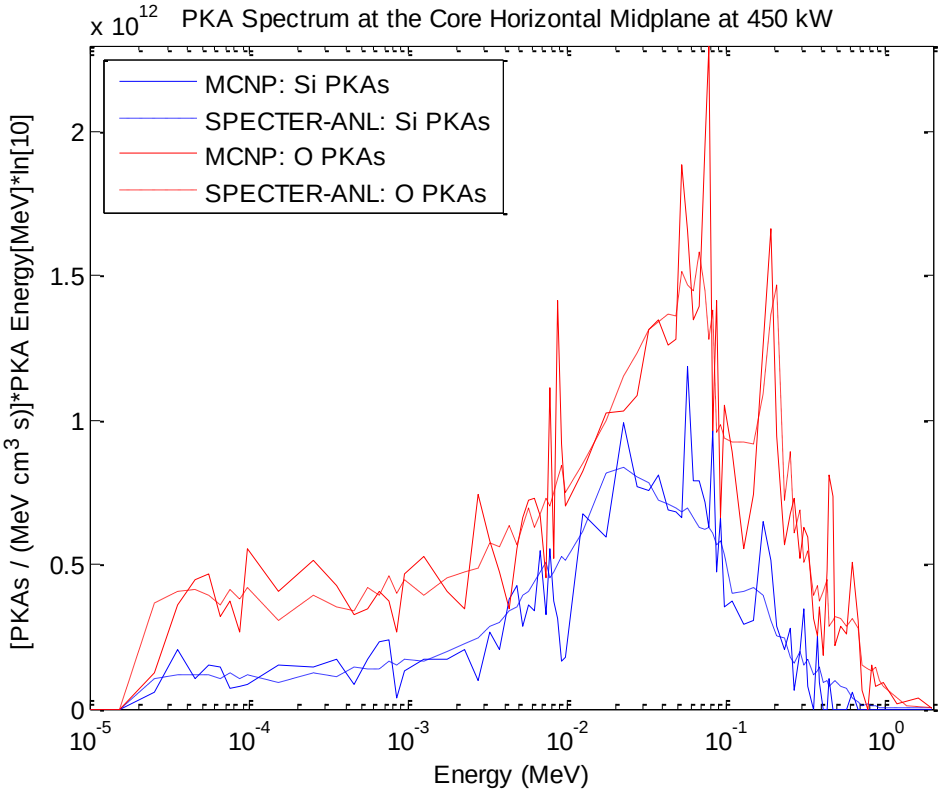

Figure 52: PKA Spectrum in the Fiber Holder at the Bottom of the Furnace at 450kW

3.5 Dosimetric Characterization of Radiation Field in Irradiation Test Rig in ULORR

We had originally planned on performing another foil activation experiment with foils inside the fiber irradiation furnace and with the furnace in position in the 7" dry tube. The purpose of this additional experiment was to confirm the neutron flux spectra inside the furnace with MCNP calculations. Performing this experiment would have caused activation of the fiber irradiation furnace which was undesirable prior to loading the optical fiber into the furnace. MCNP calculations showed that the neutron flux spectrum in the voided tube was nearly identical to the neutron flux spectrum inside the furnace, inside the dry-tube. Because of this, another foil activation analysis was not performed. In addition, the neutron flux spectrum inside the furnace was calculated with neutron cross-sections evaluated at room temperature and at 1200K and the difference was insignificant.

Chapter 4. Task C

4.1 Deliverable

Create a model of the transport of the PKAs in the fibers using the TRIM/SRIM code package. Calculate the production of defects using the TRIM/SRIM code package and PKA source term.

4.2 Modeling of PKAs using TRIM/SRIM

The PTRAC feature in MCNPX was used to determine the distribution of primary knock-on atom (PKA) energies and directions in silica. The distribution of PKA energies and directions were used to generate input files for TRIM assuming a uniform spatial distribution of the PKAs within a 110um diameter core of pure SiO_2. This was done separately for silicon PKAs and oxygen PKAs. TRIM has two limitations that affected this model. First, the target material is assumed to be at 0 Kelvin meaning there is no annealing of defects. Second, the target is 1D meaning the results have to be post-processed to determine the number of PKAs that travel beyond the boundary of the fiber radius.

4.3 Calculation of Production of Defects using TRIM/SRIM

TRIM was used to track atoms as they traveled through an infinite 3D volume of SiO_2. The number of displacements in the material per source ion (PKA) was calculated. The number of PKAs that traveled outside the fiber core was also calculated.

The estimate for DPA calculated with TRIM was about twice as large as the DPA predicted using MCNP and SPECTER-ANL. The full damage cascade calculations in TRIM use the ZBL Potential instead of the Lindhard Potential. The different methods for determining whether an atom has been displaced could explain the difference in predicted damage. There could be a directional bias or an angular coordinate bias that could have affected the results. It was also determined that very few ions escape the fiber, so the limitation of TRIM to a 1D slab geometry should not be a problem.

Based on the TRIM results, a 1MeV silicon PKA has a range of 1.27μm in SiO_2 and a 1MeV oxygen PKA has a range of 1.66μm in SiO_2. Additional results, calculated at the core centerline, are shown in Table 6.

	Displacements	Vacancies	Interstitials	Replacements	Ions Escaping Fiber
Events/atom-s at core centerline	6.134e-010	5.982e-010	6.134e-010	1.531e-011	4.510e-014

Table 6: TRIM Results Calculated at Core Centerline

Chapter 5. Task D [10]

5.1 Deliverable

Create a damage-evolution model for silica at high temperatures following previous SiC work. Use the modeled defect concentration distributions to predict the change in the optical properties of the fibers from the electronic structure.

5.2 Damage Evolution Model for Silica at High Temperatures

MD simulations were used to model the development of atomic displacement cascades in the network structure of vitreous silica when bombarded with a range of PKA energies. After sufficient time-evolution of the cascade-damage process, the atomic positions are equilibrated by scaling the velocities of the atoms to room temperature for a period of 5 picoseconds. The structure is then relaxed and analyzed for defect characterization.

5.2.1 Coordination Number

The number of neighboring atoms for each reference atom is a measure of the mis-coordination in the network. For each atom in the simulation box, a cut-off of 2.0 Å between the first and second nearest neighbor is used to account for changes due to thermal vibrations in the experimental bond-length (1.6 Å) in silica glass [69]. The virgin silica network indicates a dominant tetrahedral coordination with 99.53% of the silicon atoms having a coordination number of 4. The coordination number variation as a function of PKA energies is plotted in Figure 53.

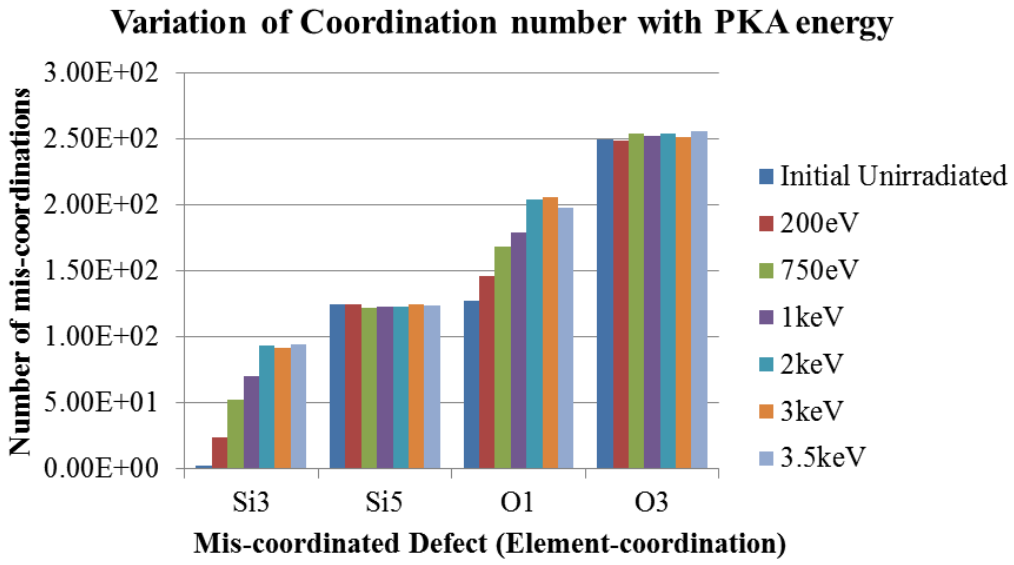

Figure 53: Variation of coordination number in amorphous silica with PKA energy

It is seen that silicon with coordination number of three which is attributed to the oxygen vacancy is the most dominant defect created upon irradiation. Since the value of coordination is calculated with a cutoff length, these under-coordinated atoms could be a true oxygen deficient center or a stretched Si-O bond. In order to prevent the over-estimation of the number oxygen deficient centers by this method, the bond-connectivity table of the silica network which provides information about the local bond environment of each atom is cross-checked to neglect the stretched Si-O bonds and account for just the oxygen deficient centers. Table 7 gives a quantitative

description of the total number of calculated Si3 defects, number of stretched Si-O bond defects and number of oxygen deficient centers with variation in PKA energy.

PKA Energy	Total number of calculated Si3 defects	Number of Stretched Si-O bond defects	Number of Oxygen Deficient Centers
200eV	34	10	2.40E+01
750eV	65	13	5.20E+01
1keV	88	18	7.00E+01
2keV	113	20	9.30E+01
3keV	112	20	9.20E+01
3.5keV	117	23	9.40E+01

Table 7: Comparison of calculated defects with variation in PKA energy

Another interesting observation from the distribution of mis-coordination is the independence of the defect concentration of silicon with coordination 5 with variation in PKA energy. The decrease in the defect concentration of silicon with coordination 5 from the initial concentration indicates that some of the defects are healed as a result of collision cascade. Table 8 shows a comparison of the percent of initial defect concentration and final defect concentration after simulating irradiation damage with a PKA energy of 3.5 keV.

Defect Type	Initial Calculated Defect Concentration %	Initial Defect Concentration % (From previous MD studies [*])	Final Defect Concentration%	Final Defect Concentration % (From previous MD studies [*])
Si3	0.007%	0.009%	0.348%	0.435%
Si5	0.463%	0.748%	0.459%	0.802%
O1	0.235%	0.570%	0.367%	0.661%
O3	0.463%	0.939%	0.474%	0.986%

Table 8: Comparison of unirradiated & irradiated defect concentration amorphous SiO_2

5.2.2 Displacement of Recoil Atoms

The displacement of atoms during the cascade damage process was monitored using a *compute* command in LAMMPS and the average and maximum displacement of atoms as a function of the PKA energies is plotted in Figure 54 and Figure 55. This provides information of the evolution of the structure during the cascade damage process and the subsequent movement of atoms during relaxation as a function of their PKA energies. From the distribution of average displacement of atoms in Figure 55, the relative saturation of atom displacements between 2keV to 3.5 keV indicates the possibility of correspondence to the saturation in the number of mis-coordinations of silicon with coordination 3 as discussed in Figure 53.

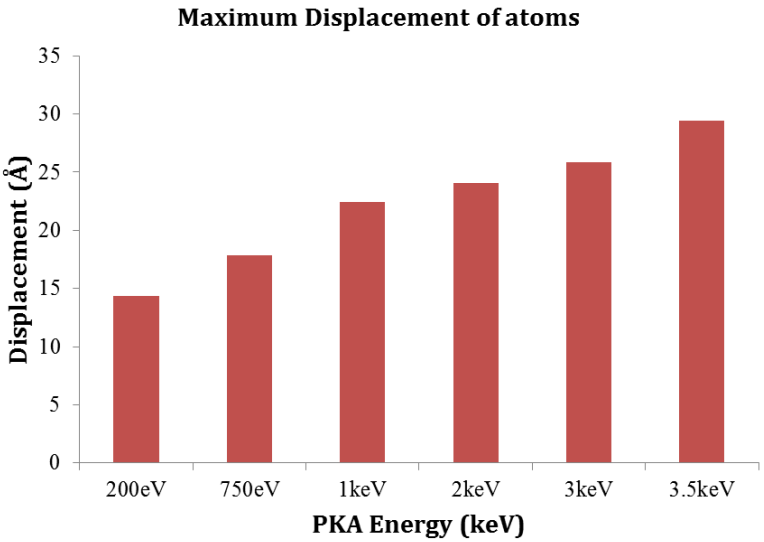

Figure 54: Maximum displacement of atoms in the silica structure as a function of PKA energies

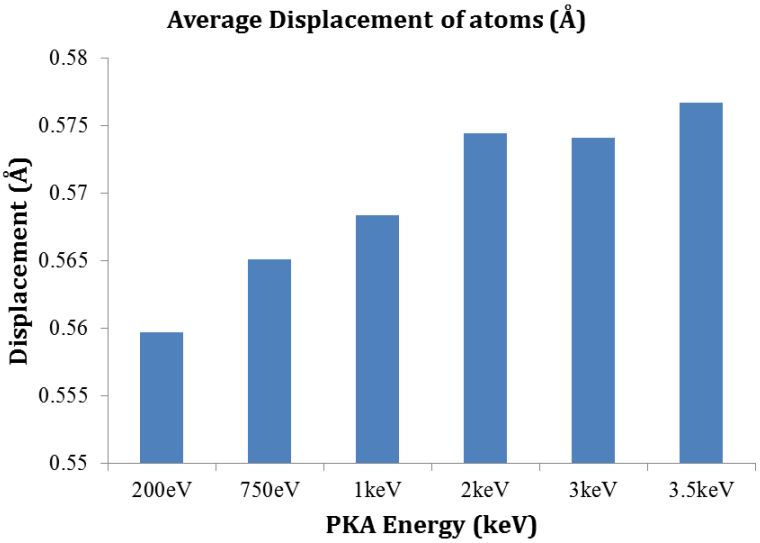

Figure 55: Average displacement of atoms in the silica structure as a function of PKA energies

5.2.3 Variation in the Structure Factor as a Function of Irradiation Damage

The structure factor, obtained as a function of the Fourier transform of the radial distribution function, was computed and compared between the irradiated structure and the pristine structure at room temperature. The structure factor, which provides information about the medium range order of amorphous materials, can be measured experimentally through x-ray or neutron diffraction. The comparison of structure factor of the irradiated structure and the relaxed structure reveals a relative decrease in the height of the peaks obtained (Figure 56).

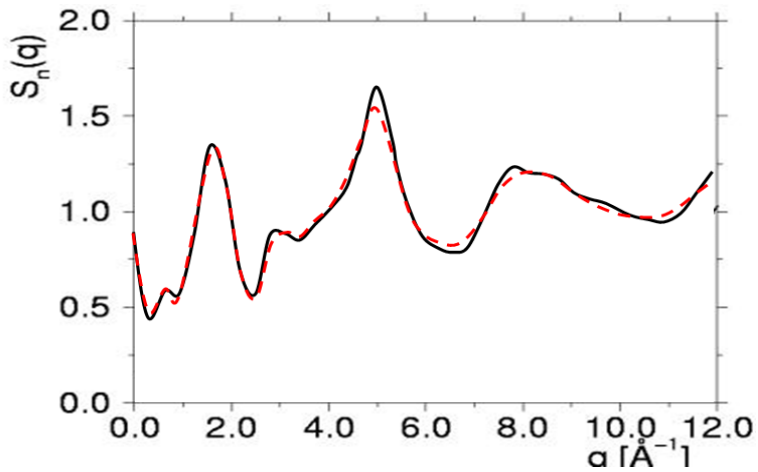

Figure 56: Comparison of structure factor for unirradiated and irradiated SiO_2 Initial amorphous structure (black solid line) and MD simulations of irradiated structure using PKA energy of 3.5keV (dashed line)

5.2.4 Ring-Order Variation

The distribution of *ring-sizes* is a useful parameter in characterizing the medium range-order of an amorphous material. Unlike most crystalline forms of silica where all rings contain six silicon atoms, vitreous silica consists of a distribution of ring-sizes. A *ring* was defined to be the shortest closed loop path that leads from a Si-atom along Si-O bonds back to itself [70]. A code was written in MATLAB which used the "*depth first search*" (DFS) algorithm [71] on the bond-connectivity table of the silica network to calculate ring-sizes ranging from 2 to 8. DFS is what is known as an 'uninformed search' which progresses by expanding the first encountered Si-O bond and goes deeper and deeper in the bond-connectivity table until the starting Si-O bond is encountered again. The nodes in the network were checked to ensure that duplicate counting of a given ring-size was avoided. Rings of order 3, 4, 5 and 6 are observed in the structure with the ring distribution centered at 6-member rings at room temperature, in conformity with existing MD studies [70] [72]. A snapshot of the vitreous silica structure at room-temperature indicating the types of rings in the structure is shown in Figure 57.

A frequency histogram was generated to examine the ring-size variation as a function of temperature and PKA energy as shown in Figure 58. The ring-order variation analysis of the structure irradiated with a PKA energy of 3.5 keV indicated an increase in the percentage of 3 and 4 member rings by 8% and 9.5% respectively and a decrease in the percentage of 6 member rings. This corroborated previous work by Mota, Caturla et al. [70] and indicated a transformation of the medium-range order in amorphous silica upon irradiation. As established in the literature, 4 and 3 member rings are very close to planar rings and have unique vibrational frequencies of 607cm^{-1} and 493 cm^{-1}, called D1 and D2 lines, which can be detected by Raman Spectroscopy [65], which thus allow experimental validation.

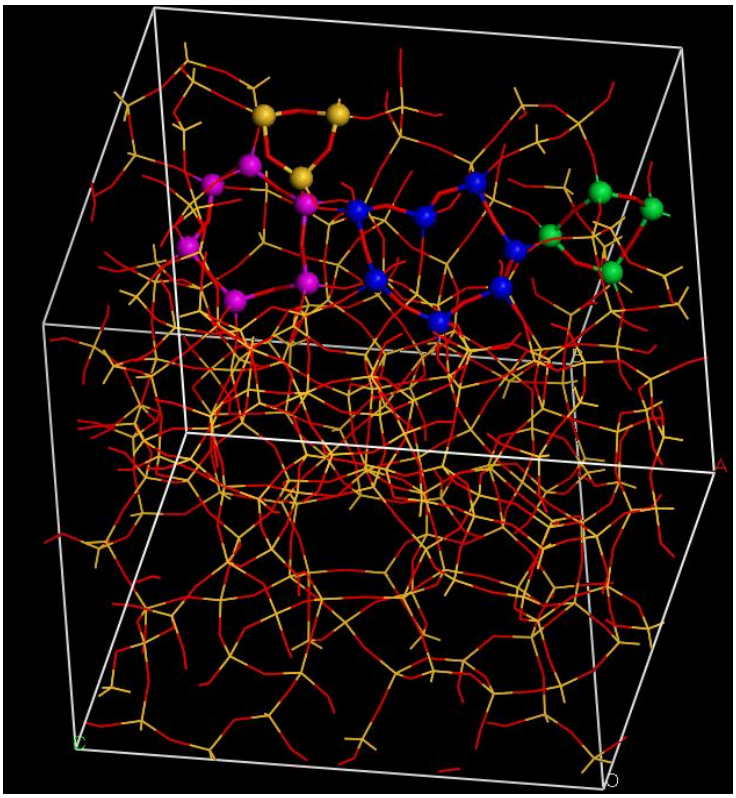

Figure 57: Snapshot from Materials Studio of amorphous silica structure at 300K
The different ring orders are illustrated: Yellow a 3-membered ring, green a 4-membered ring, pink a 6-membered ring and blue corresponds to a 7-membered ring

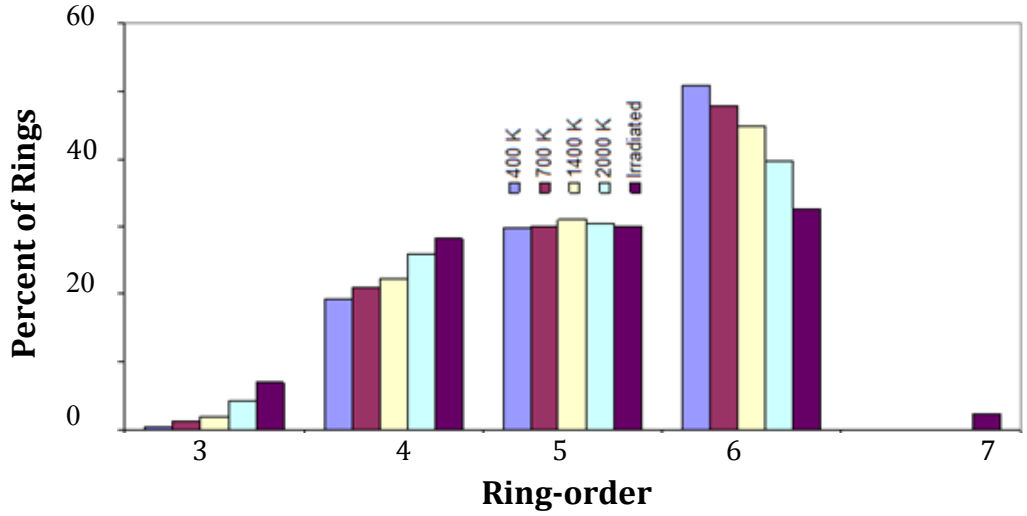

Figure 58: Variation of percentage of ring-sizes in vitreous silica with temperature and irradiation with a PKA energy of 3.5 keV

5.2.5 XRD Simulation Analysis

The relative decrease in structure factor and the increase in the percentage of small (3 and 4) member rings in the vitreous silica structure with irradiation motivated us to explore the possibility of recyrstallization (typically called devitrification in the area of glasses) in the material. For this purpose, the Crystal Maker Package [73] which has a Crystal Diffract tool capable of simulating XRD analysis is used. XRD spectra using the Crystal Diffract tool is obtained for crystalline beta-cristobalite silica, the unirradiated amorphous silica at room-temperature and the irradiated amorphous silica which is quenched down to room-temperature. The comparison of XRD spectra is shown in Figure 59. A Gaussian interpolation is used to plot the diffraction data where the symmetry and shape of the peaks give an indication of the relative devitrification of the structure. The instrumental broadening parameter is kept at the default value of 9.509°. From the XRD data of crystalline beta-cristobalite, a number of distinct peaks are observed corresponding to the planes producing reflections. The amorphous silica structure at room temperature produces a near-symmetrical peak at around 21° with a slight hump at 9.5°. The near-symmetrical peak at 21° for amorphous silica is validated by X-Ray Diffraction experiments as shown in Figure 60 for amorphous silica [68]. The irradiated structure, when analyzed, produces a second characteristic peak at 44° in addition to the peak at 21°. The second characteristic peak at 44° coincides with the second peak in the cristobalite spectrum.This indicates the possibility of a partial devitrification of the structure as a result of the cascade displacement damage. The potential energy of the perfectly crystalline and the energy of the virgin amorphous structure were compared with the energy of the irradiated structure. We observed that the potential energy of the irradiated structure lies between the energy range of the crystalline and amorphous material with the energy difference to the initial amorphous structure corresponding to 14% of the energy difference between fully amorphous and crystalline structure, indicating the possibility of a partial devitrification by that amount.

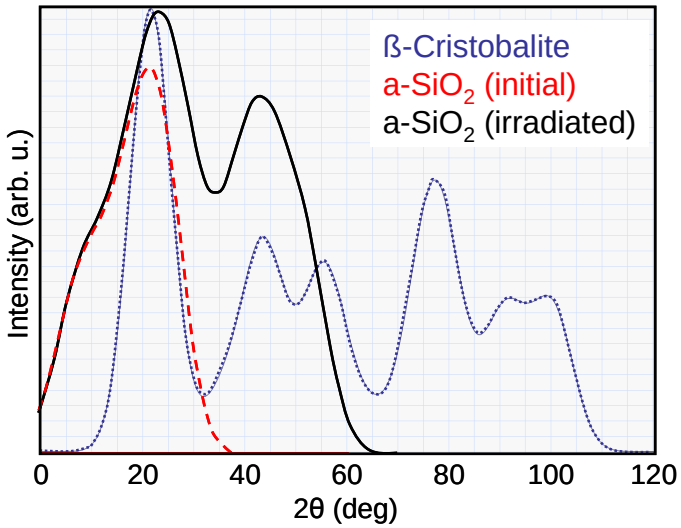

Figure 59: XRD simulation using Crystal Diffract for SiO_2
Crystalline beta-cristobalite (blue dotted line), amorphous SiO_2 before (red dashed line), and after a 3.5 keV knock-on event (black solid line).

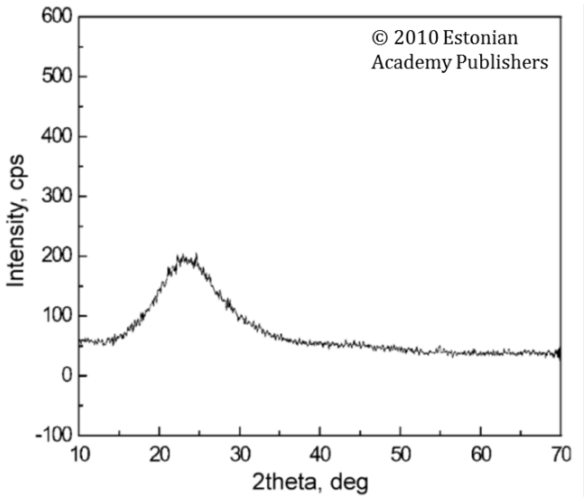

Figure 60: Experimental XRD spectrum of amorphous SiO_2 [68].
Peak near 21° matches calculated XRD spectra.
Copyright 2010, Estonian Academy Publishers [68].

5.2.6 Isolation of Defects in Irradiated Silica

Since electronic structure calculations in VASP are not computationally efficient for large simulation cells, a new method was developed to isolate the optically active defects in the MD irradiated structure to study their electronic properties. From the concentration of defects determined from the irradiated MD structure, silicon atoms with coordination number 3, which corresponds to the oxygen deficient site, are the most dominant. A box of 7.2 Å side length was defined and extracted using the *region* command in LAMMPS around each individual defective site such that the box contains a single oxygen vacancy and has 47 atoms, on average. The structural parameters to validate an amorphous structure, such as coordination number, bond-angles, bond-lengths and radial distribution functions were used to characterize the extracted cell. In order to prepare a simulation cell that can be used for electronic structure calculations, a perfect 48 atom cell of beta-cristobalite is taken as a starting structure and an oxygen atom is removed to represent the defective oxygen deficient site. Beginning with the crystalline 47 atom beta cristobalite structure with an oxygen vacancy site, ab-initio MD simulations were performed with an *NVE* thermostat to create an amorphous cell of SiO_2. The temperature was varied between 300K to 1000K and the continuously evolving structure was monitored to match structural parameters such as RDF, ring-order sizes, structure factor, bond-lengths and bond angles with the isolated structure from MD within a tolerance of 0.1%. This provides a better representation of the defective configurations obtained from MD compared to previous methods and thus provides a method to effectively translate the structure from MD to electronic structure calculations.

Recent work by Girard et al. [74] investigated the properties of the oxygen deficient centers and their generation mechanisms through ab-initio simulations. In their work, they removed an oxygen atom at the 72 possible sites in a 108 atom SiO_2 cell and studied the distribution of Si-Si bond lengths and formation energies for these configurations. The distribution of Si-Si bond lengths were then fitted with a Gaussian distribution function leading to a mean value of 2.38Å. The formation energies of all the defect configurations were plotted as a function of their bond-lengths and site location providing information on the sites where the generation of Si-ODCs preferentially occurs. These literature results were used to calculate and investigate the electronic and optical properties of the defective configurations isolated in the MD irradiated structure.

5.3 First-Principles Electronic Structure Calculations of Defects in Silica

Most macroscopic properties of materials depend directly on microscopic phenomena that often require the use of the laws of quantum mechanics to accurately describe the dynamics of atoms. First-principles calculations, also known as ab-initio methods, use fundamental quantum physics by solving the Schrödinger equation to obtain the energetics and electronic properties of atoms without the use of any empirical or semi-empirical parameters fitted to experimental data. Unlike MD simulations which are characterized by calculations using hundreds to several millions of atoms, quantum mechanical first principles calculations require the use of small simulation cells with a few tens of atoms owing to the computer-intensive, complex set of calculations they are required to perform. In real materials, the electrons determine the chemical bonding of atoms, whose dynamics are governed by the laws of quantum mechanics. The quantum mechanical approach thus leads to an accurate depiction of ground state energies, electronic and optical properties, chemical reactions and structural defects. With increasing advances in computational efficiency and capacity, there has been a great improvement in the use of quantum physics models in understanding the properties of materials. A detailed review of ab-initio studies of solids and surfaces ranging from ionic crystals and semiconductors to catalysts is described in the paper by Joachim Sauer [75].

5.3.1 Previous Electronic Structure Calculations of Point Defects in SiO_2

While several experimental [76] [77] and theoretical approaches using size-limited cluster based [16] methods have been used to characterize the optical properties of defects in silica, these properties have been determined in large periodic supercells using ab-initio molecular dynamics and DFT methods only in the last decade [78]. Prior to this, most of the interpretation of optical spectra of defects in crystalline and silica glass originated from the *tight-binding* approach inroduced by O'Reilly and Robertson [79] to calculate the electronic structure of the defects in SiO_2. An overview of the theoretical studies of intrinsic defects in amorphous silica has been presented in the paper by Edwards [80].

With extensive experimental evidence in the recent past to suggest that Oxygen Deficient Centers and Si-E' centers are the two primary defects that act as precursor sites for the generation of point defects upon SiO_2 irradiation [81] [82] [83] [84], there have been several ab-initio studies to simulate the electronic and optical properties of these defect centers and study the mechanisms for their generation or transformation upon irradiation [85]. Both neutral native point-defects [86] and charged defects in silica [85] [87] have been studied using DFT primarily with the LDA and GGA methods.

5.3.2 Simulation of Electronic Structure Properties of SiO_2 using VASP

As described previously, DFT with traditional local functionals are generally known to underestimate the band gaps of bulk semiconductors and insulators. In this project, the HSE hybrid functional, which gives a more accurate result of the band gap by including just the dominating short-range parts of the exact nonlocal Hartree-Fock-type exchange will be used to study the electronic and optical properties of neutral and charged defects identified from the MD calculations.

In this project, the Vienna Ab-initio simulation package (VASP 5.2) [88] is used to perform the DFT calculations. The ability of VASP 5.2 to perform HSE calculations and calculate dielectric and optical properties, in addition to its good performance on the parallel Glenn Cluster at the Ohio Supercomputer [89], made it an attractive option over other quantum-mechanical codes. First-principles calculations using DFT in the LDA approach has been previously performed in VASP to study oxygen deficient centers in silica [87]. In this study, the HSE method using an optimized atomic exchange parameter is used to calculate the band-structure, density of states and absorption properties of perfect and defective silica configurations. VASP can determine quantities such as

geometric structure, energies, band-structures, charge-density and the dielectric constant. Details of the equations correlating the frequency dependent dielectric matrix calculated by VASP to the absorption coefficient using the Kramers-Kronig relation is described elsewhere [90].

5.3.3 Band-Structure and Density of States of Perfect- SiO_2

A perfect 48-atom beta-cristobalite cell is used as the starting point for the electronic structure calculations. Calculations were carried out using 24, 48 and 72 atom supercells to ensure that the results obtained are adequately reproduced. A 4x4x4 k-point mesh was used for the calculations after checking for k-mesh convergence on total energies for different mesh sizes. The structure was first relaxed using the PBE functional and the density of states were calculated using the HSE method with a value of the fractional exchange in the atomic-exchange parameter as 0.35. The density of states of a 48-atom cell of crystalline β-cristobalite silica is shown in Figure 61. The band-structure of a 48-atom cell of crystalline β-cristobalite silica was calculated using the HSE method and is shown in Figure 62. The letters on the band-structure refer to a standard symmetry notation and in each horizontal segment of the band-structure, variation of energy along the direction in the Brillouin zone is displayed. In order to compute the band-structure, a path for the band structure, L-G-X in this case and the number of bands to be calculated is assigned in VASP.

The band-gap calculated using the HSE method with an optimized fractional exchange in the atomic-exchange parameter as shown in Figure 61 has a value of 8.01 eV. This matches very well with experimental results which estimate the band-gap to be between 8-9 eV [91]. Thus by using the HSE method, the traditional DFT band-gap problem [87] is overcome and an accurate value of band-gap is obtained.

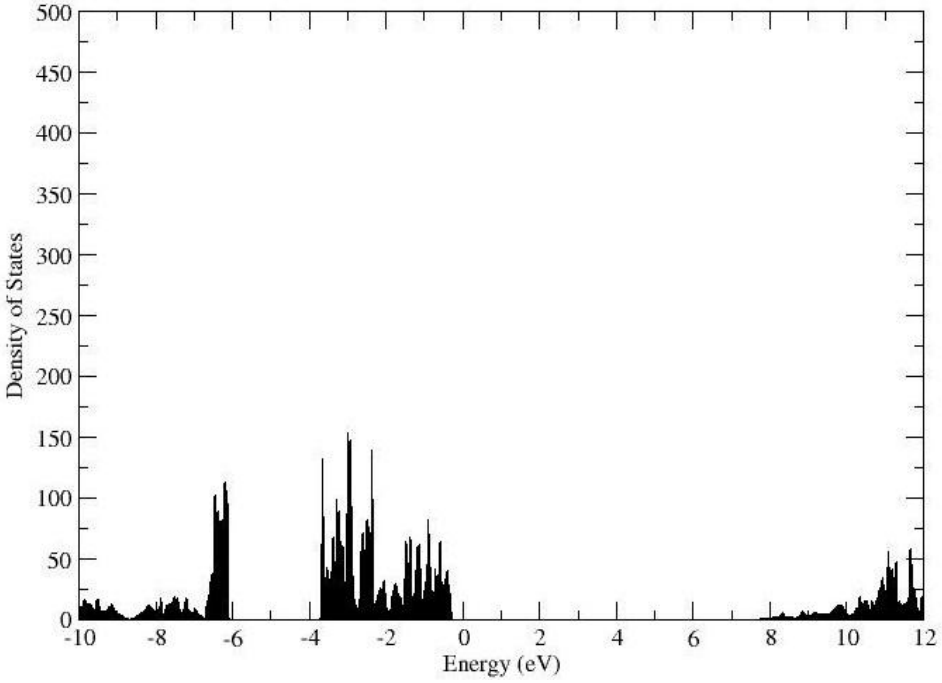

Figure 61: Density of States of 48-atom cell perfect β-cristobalite silica

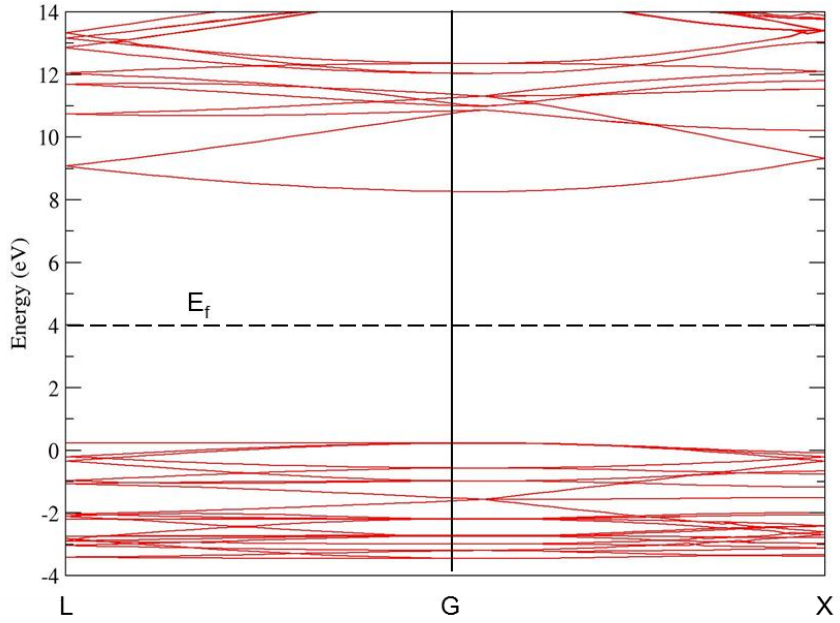

Figure 62: Band structure of 48-atom cell perfect β-cristobalite SiO2

5.3.4 Calculation of Absorption Coefficient of Perfect SiO_2

VASP calculates the frequency dependent dielectric matrix [90] after the electronic ground state has been determined. It is desirable to increase the number of frequency grid points and a value of 5000 is used. In order to obtain reasonable results, an appreciable number of empty conduction band states are required. For this purpose the number of bands is roughly doubled in the input file and a value of 112 is used. The dielectric properties were calculated and were used to calculate the absorption coefficient (cm^{-1}) as a function of energy (eV) which is plotted in Figure 63.

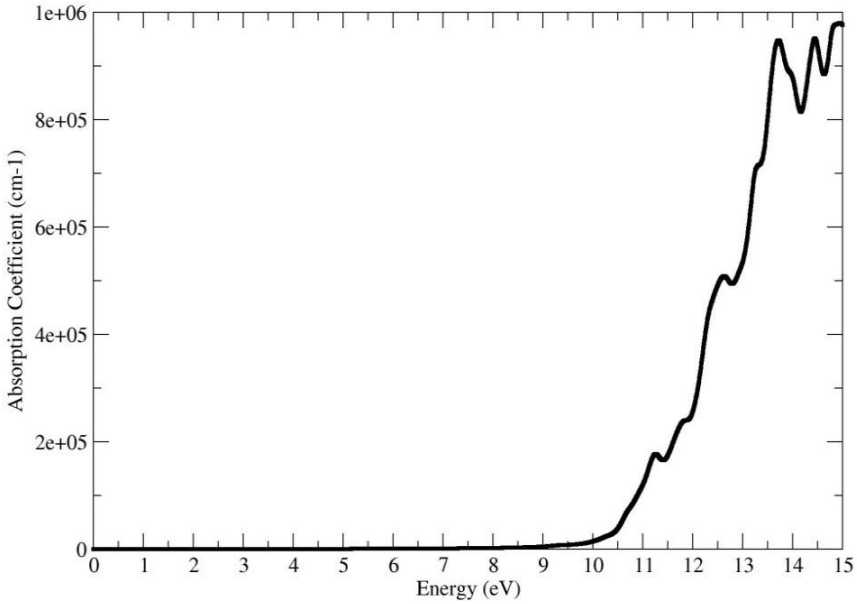

Figure 63: Plot of absorption coefficient (cm-1) vs Energy (eV) of perfect SiO_2

For crystalline, fully 4-2 connected β-cristobalite SiO_2, it is seen from Figure 63 that there are no prominent peaks in the visible region (1.65-3.1eV). In order to investigate the absorption spectrum upon irradiation, the defective configurations isolated from the MD structure were studied for their electronic structure and dielectric properties.

5.3.5 Absorption Coefficients of Defective ODC Configurations

In order to investigate the influence of the local environment on the properties of the oxygen vacancies, the defect configurations isolated from the irradiated MD structure are used. By isolating defects from the MD irradiated cell and matching their structural parameters with an evolving structure of β-cristobalite, we obtain an accurate representation of the local environment of the defect sites compared to the existing method by Girard et al. [85] where all possible ODC sites in a supercell were characterized for their structural properties. The defective sites were characterized for their Si-O bond length, representing the distance between the two atoms constituting the oxygen vacancy and had a mean value of 2.413 Å. This matches well with the value of 2.38 Å arrived at by Girard [85]. Figure 64 shows the absorption spectrum of the defective configuration closest to the mean value of 2.413 Å and a comparison to the spectrum of perfect SiO_2.

A prominent peak centered at 6.5 eV (191nm) is observed in the case of the defective SiO_2 configuration with the Oxygen Deficient Center. This matches well with previous experimental literature [92] [74], which report an absorption peak in neutron irradiated silica between 5.8 eV to 7.6 eV. However, since this does not fall in the visible region, we decided to consider these defective sites to be pre-cursors to charged defects and calculated electronic and optical properties of charged defect configurations.

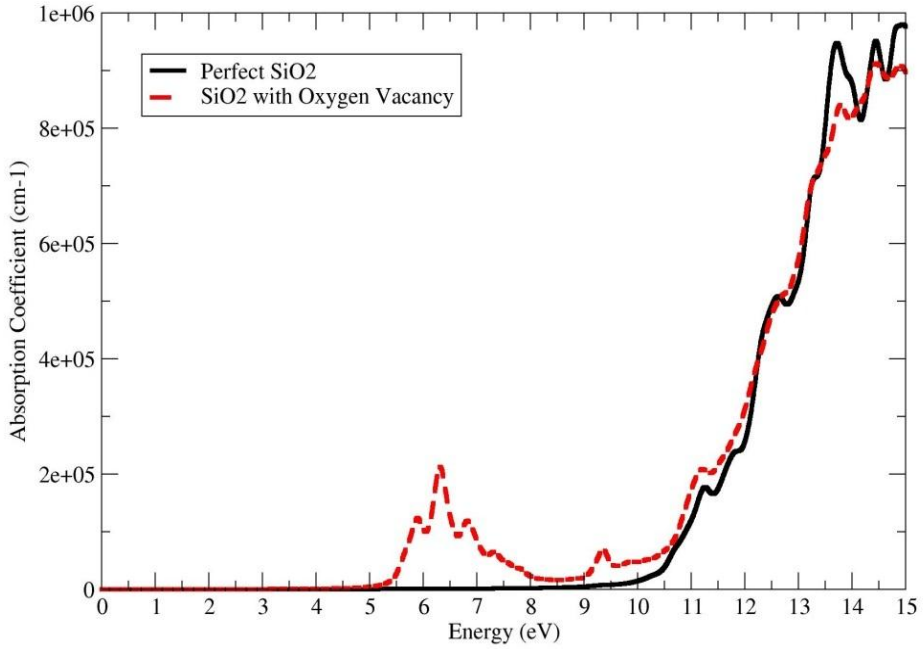

Figure 64: Comparison of absorption coefficient of SiO_2 with ODC (red-line) with perfect SiO_2

5.3.6 Calculations of Charged Defect Configurations

According to formation energy calculations of Oxygen vacancy defects by Roma et al. using DFT-LDA calculations with plane-waves and pseudopotentials [93], V_O^+ at the Fermi energy (~2.3 eV) is about 2.3 eV higher than V_O^0. According to the Roma paper, the energy to create a hole in the

"perfect" valence band is about 2.3 eV, too. Thus, it is energetically about the same to create a neutral oxygen vacancy plus a hole, or a positively charged vacancy (V_o^+ and V_o^{2+}) (Figure 65). Formation energy calculations for different charged defect configurations of oxygen vacancy in SiO_2 were calculated using the constitutional defect method described in the paper by Mishra et al. [94]. These calculations corroborated this fact (Figure 66) and we were motivated to calculate the absorption properties of the charged defect configurations.

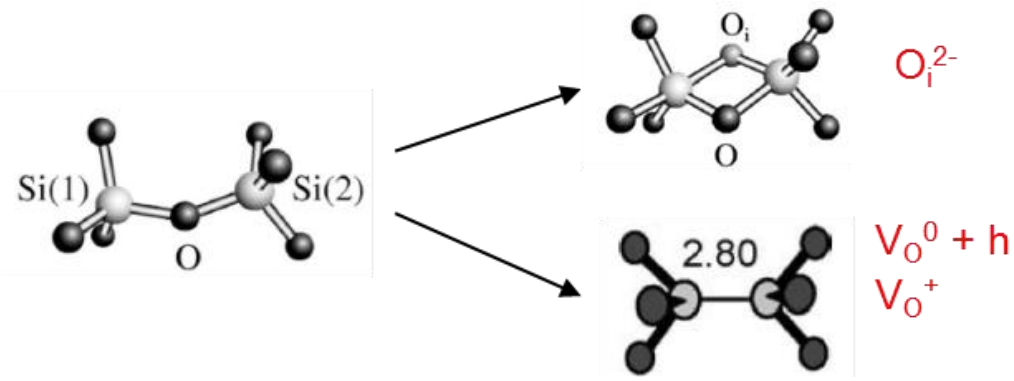

Figure 65: Energetically favorable mechanism of defect production

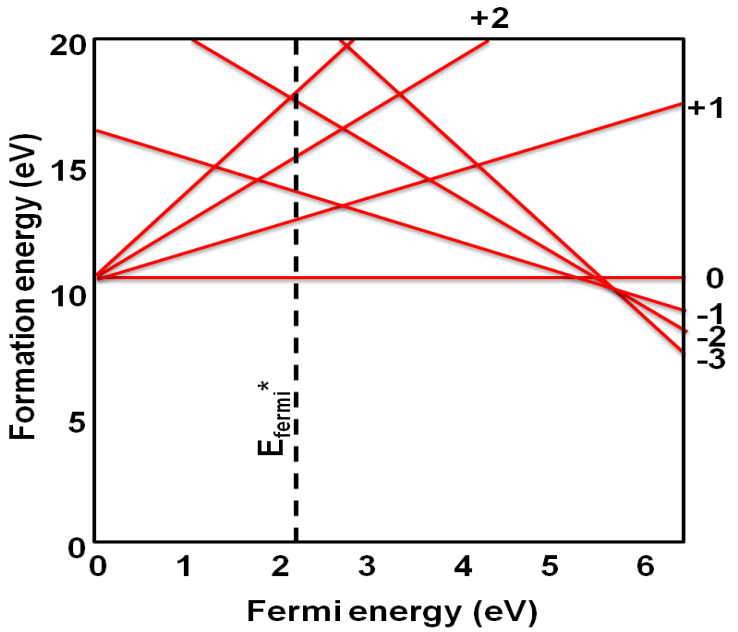

Figure 66: Formation energy calculations of charged defect configurations of O vacancies in SiO_2

The calculation of absorption coefficients for the +1 and +2 vacancy configurations is shown in Figure 67 and a prominent peak is observed for the +1 and +2 vacancy configurations at around 1.2 eV in the visible region. In order to investigate the possibility of Frenkel-pair production as a result of radiation damage, the possibility of various configurations of interstitials contributing to absorption losses will be discussed subsequently.

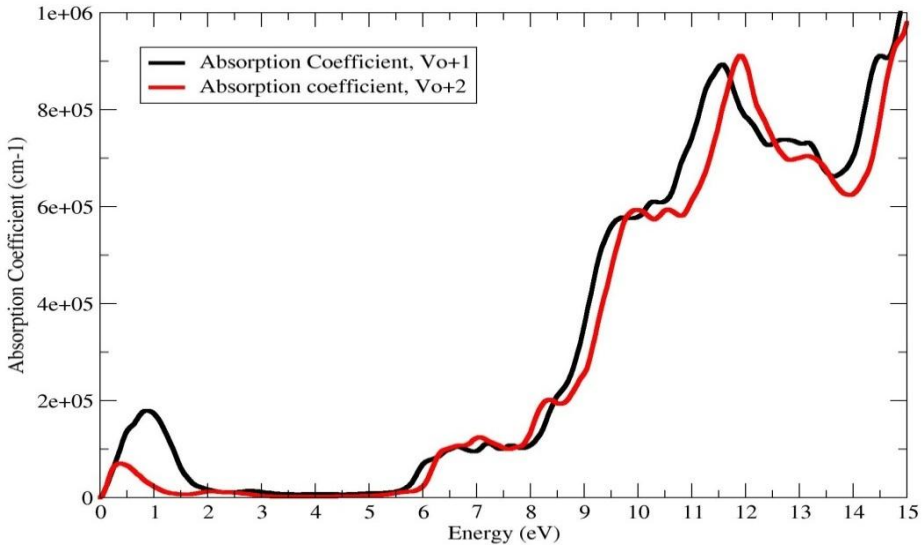

Figure 67: Absorption coefficients of +1 and +2 charged Oxygen Vacancy configurations

5.3.7 Optical Properties of Oxygen Interstitial Configurations in Silica

Considering the atomic structure of SiO_2, which is a continuation of corner-sharing SiO_4 tetrahedra with twofold coordinated oxygen atoms in the Si-O-Si bridge form, 3 possible interstitial configurations have been studied for their electronic structure in recent literature [93] [86] [95]. These include the Double-bridge, 3-fold and peroxy interstitial configurations which are illustrated in Figure 68.

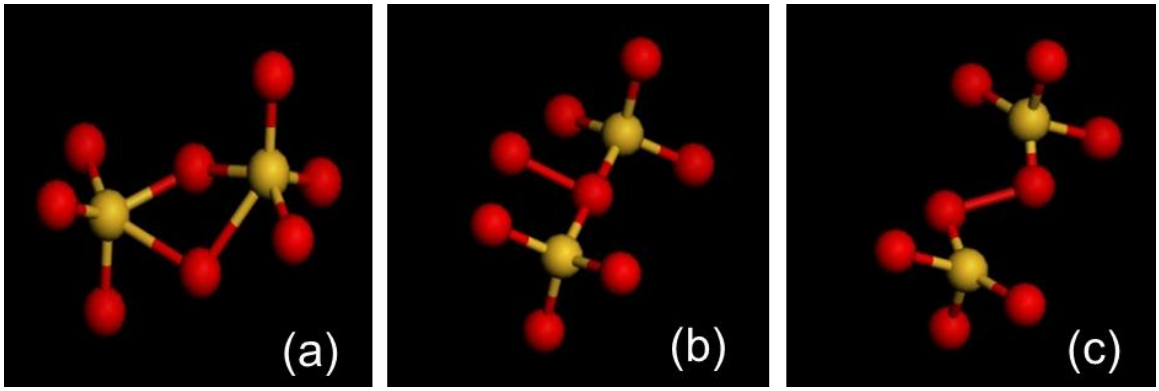

Figure 68: Oxygen Interstitial configurations in silica
(a) Double-bridge (b) 3-fold (c) Peroxy interstitial configurations

Formation Energy Calculations

In order to investigate the stability of these configurations, the formation energies of the interstitial configurations were calculated using the constitutional defect method [94]. The neutral interstitial configurations had formation energies of 1.31, 1.21 and 1.29 eV for the 3-fold, double-bridge and peroxy interstitial configurations, which match closely with literature values by Samos, Roma et al [86] [87]. The atomic structure of interstitial oxygen in SiO_2 strongly depends on its charge state. According to literature by Jin and Chang [96], for negatively charged states, the double-bridge structure with two Si-O-Si bonds is energetically more favorable than the peroxy

linkage and threefold structure. Formation energy calculations corroborated this fact and the double-bridge configuration was found to be the most stable configuration, with q = +2 being the most stable charge state between 0 and 0.4eV, q = 0 between 0.4 and 5eV and q = –2 between 5 and 5.2eV as shown in Figure 69.

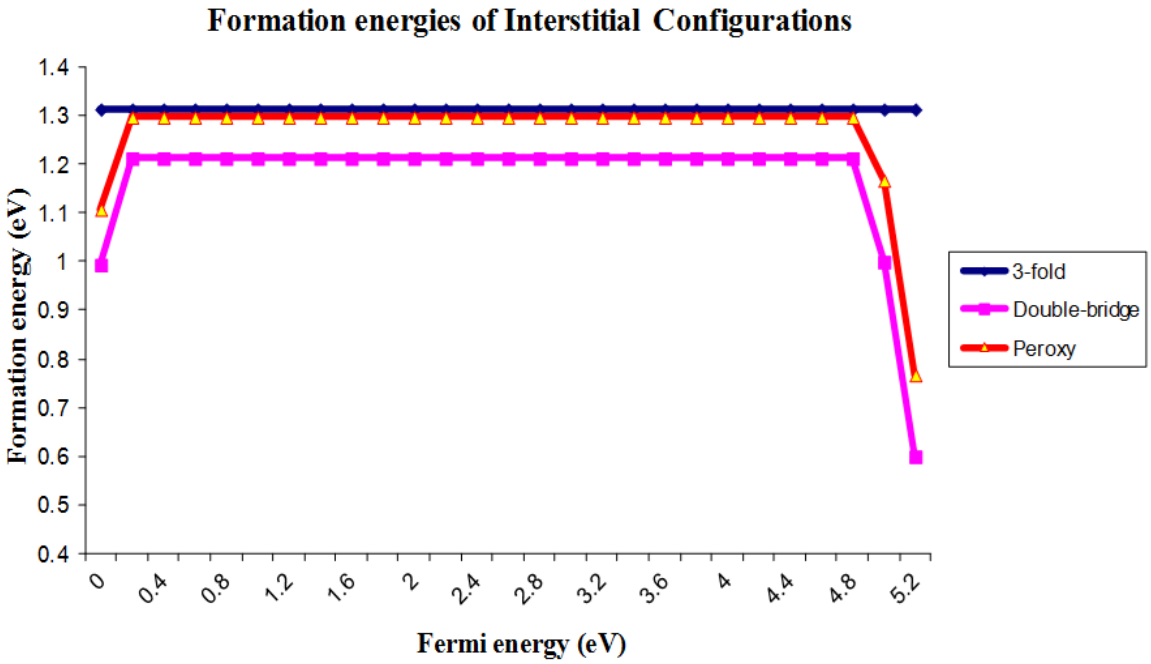

Figure 69: Formation energy calculations of interstitial configurations in SiO_2

Density of States

The density of states (DOS) of the double-bridged interstitial configuration was calculated for the neutral, positively charged, and negatively charged configurations as shown in Figure 70, Figure 71, and Figure 72, respectively. The location of the Fermi-level, as calculated by VASP, is indicated by the red-line in these figures.

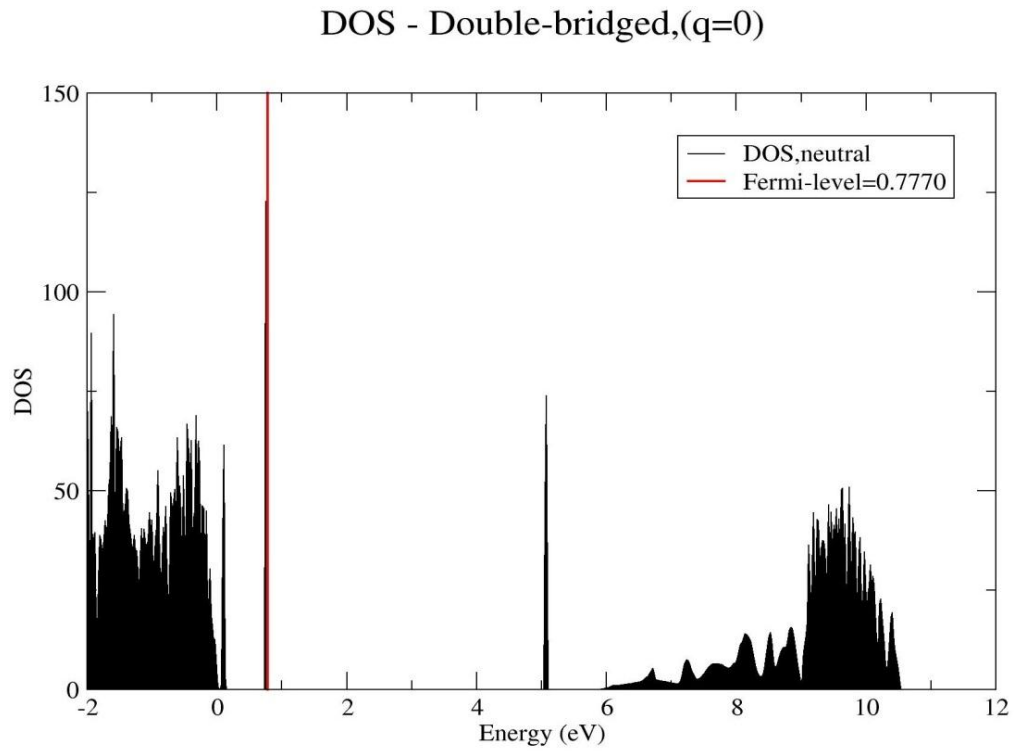

Figure 70: DOS of Double-bridged configuration with neutral charge, q=0

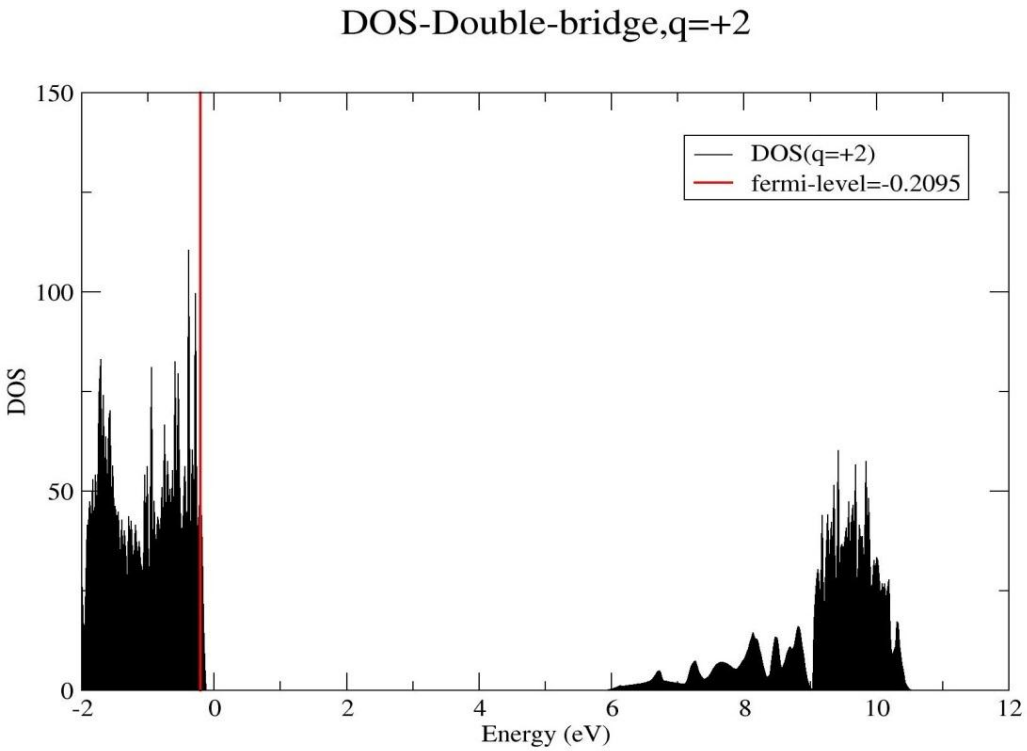

Figure 71: DOS of Double-bridged configuration with charge, q=+2

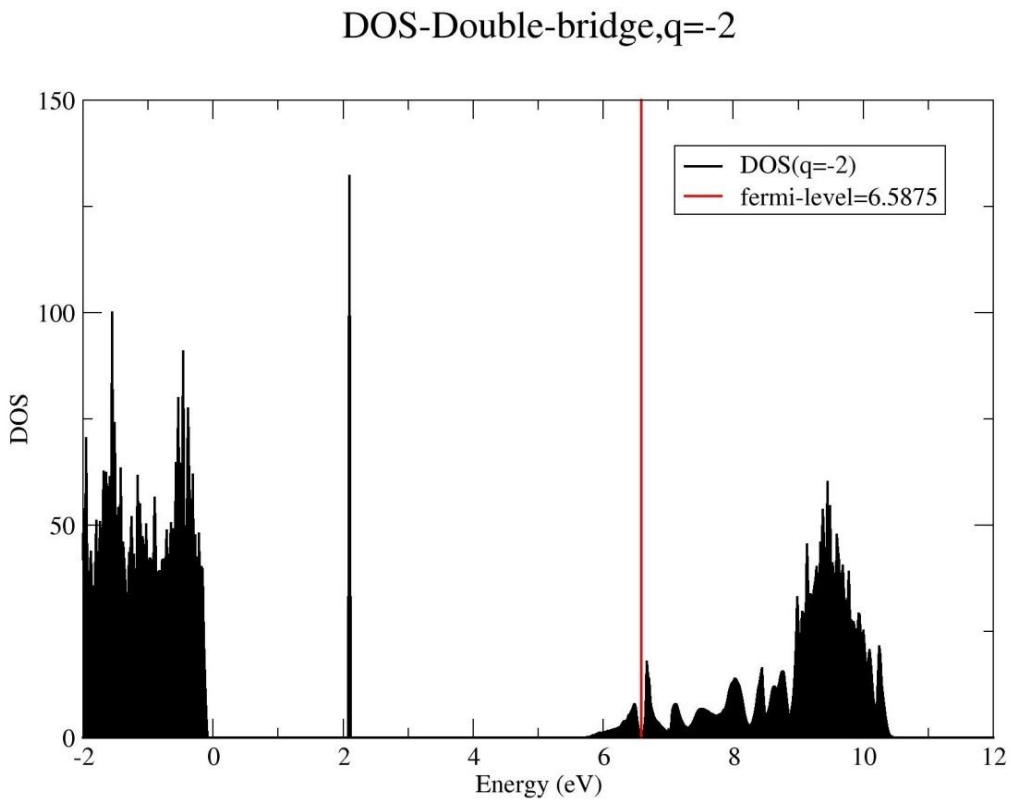

Figure 72: DOS of Double-bridged configuration with charge, q=-2

Absorption Coefficients

Absorption coefficients calculated for neutral configurations of the three interstitials considered revealed no prominent peaks in the infra-red (0.0012-6.5eV) or visible range (1.65-3.1eV) as shown in Figure 73. Since the double-bridged interstitial configuration is the most stable defect of the three interstitial configurations, absorption coefficients were calculated for the charged configurations of the double-bridged interstitials, as shown in Figure 74. A prominent peak at ~0.7eV in the visible range is observed for the double negatively charged, double-bridge interstitial configuration. Smaller peaks are seen in the visible range for the other charged configurations. This indicates that the presence of the Frenkel pair, the positively charged oxygen vacancy (V_O^+) and the double negatively charged oxygen interstitial (O_i^{2-}), contributes to absorption losses in the visible spectrum.

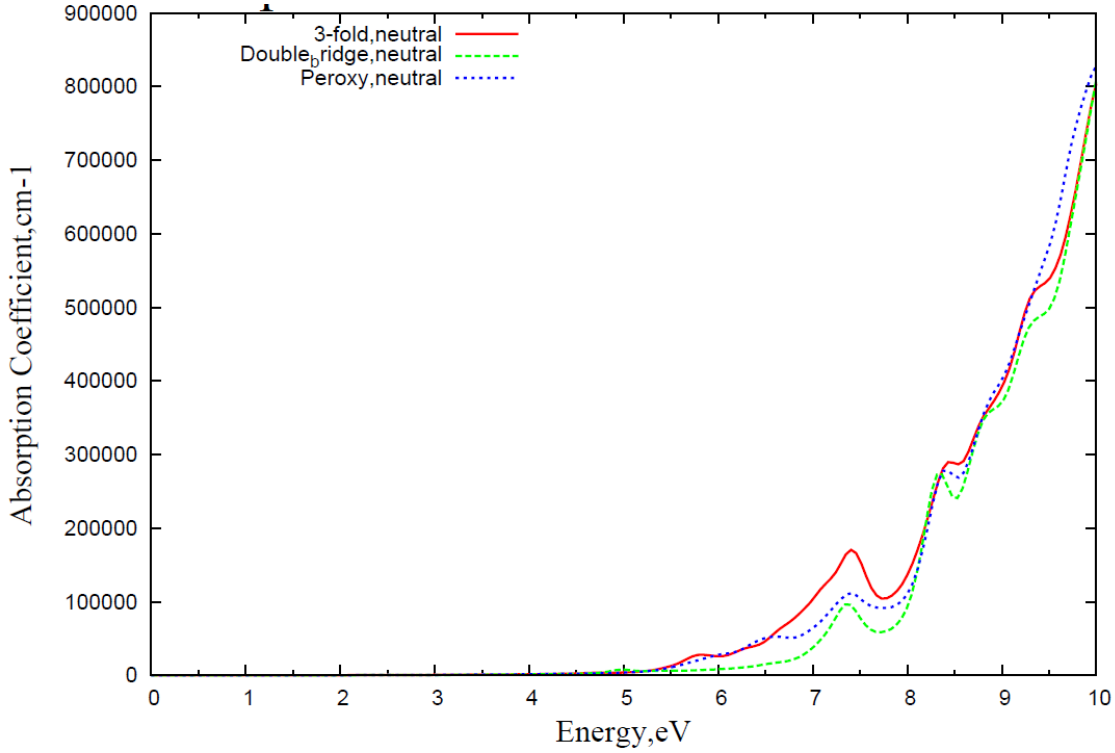

Figure 73: Absorption coefficients of neutral Oxygen interstitial configurations in SiO_2

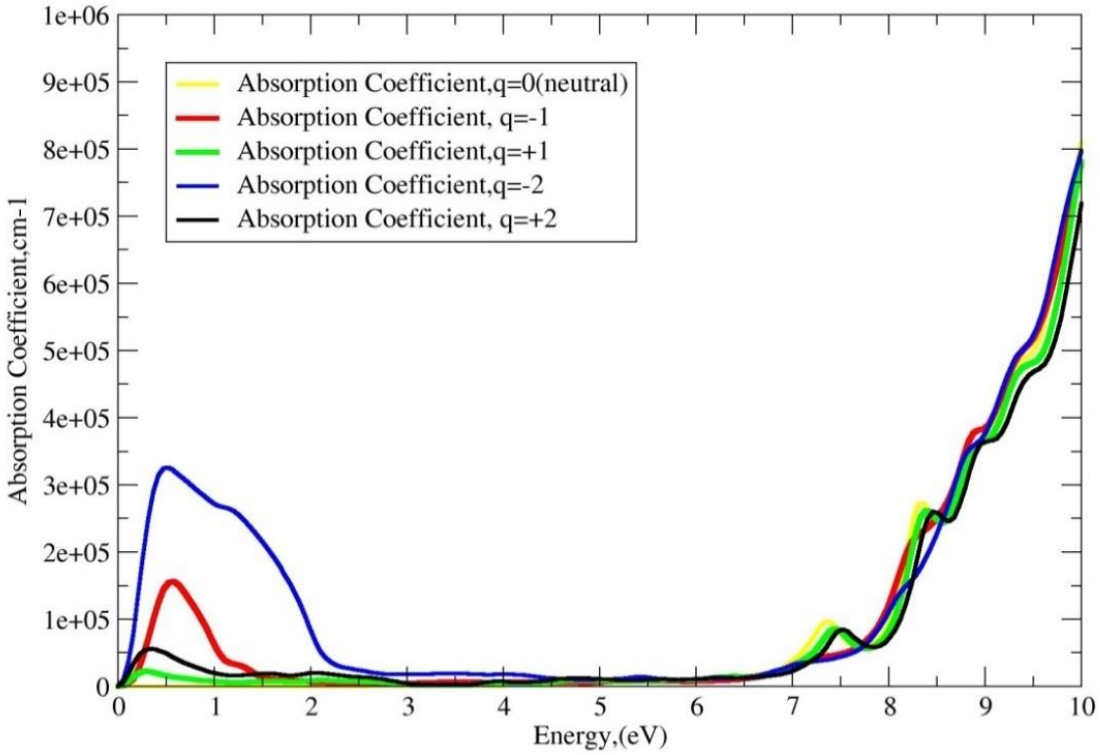

Figure 74: Absorption coefficients of charged, double-bridged O interstitials in SiO_2

Chapter 6. Task E [2] [97]

6.1 Deliverable

Identification of fiber types and wavelengths to test and purchase of fibers. Purchase of broadband fiber transmission light source.

6.2 Identification of Wavelengths to Test

Much of the optical fiber and associated technology is focused on silica fibers optimized for one of three common telecommunications wavelengths, 850nm, 1300nm and 1550nm. The composition and geometry of these fibers have been optimized to minimize intrinsic attenuation and dispersion around specific wavelength ranges. To maximize the relevance of the data collected during these experiments, a broad spectrum of wavelengths was tested that included all three of the commercially important wavelengths. Two spectrometers were purchased which were sensitive over a spectral range from 200-1080nm and 900-2300nm. Additional information about these spectrometers can be found in Section 8.2.1.

6.3 Identification of Fiber Types

From a literature review and also based on recommendations from Luna Innovations, pure silica core, fluorine doped silica clad fibers were considered to be the most radiation resistant. Pure silica core, F-doped silica clad fibers can have different intrinsic material attenuation depending on the OH content of the fiber and other material parameters. Low-OH optical fibers are usable between 380-2400nm and high-OH fibers are usable between 180-1150nm [13]. The effect of OH concentration on the material attenuation of the fiber is described in Section 1.8.2.

In addition to material attenuation, the diameter of the core of an optical fiber can be matched to a specific wavelength range to reduce the dispersion for high bandwidth data transmission. Single-mode optical fibers have small core diameters so that only one mode of 1300nm or 1550nm will transmit through the fiber. Single-mode optical fiber can transmit other wavelengths, but coupling non-laser light sources to single-mode fibers is difficult. Multi-mode optical fibers can be made with the same material composition, but with larger core diameters. The larger core diameter allows many modes to be transmitted and makes coupling of light sources to the fiber very easy.

Because we wanted to measure the broadband attenuation through silica optical fibers as a function of radiation and temperature, we used multi-mode silica optical fibers to simplify coupling to a broadband light source. The attenuation results are applicable to single-mode optical fibers as well as fused silica in general. In this project, the broadband attenuation was measured through three commercially available, inexpensive multi-mode silica optical fibers including one high-OH fiber and two low-OH fibers. Specifications for the three fiber types are shown in Table 9. Both of the Polymicro fibers were fluorine doped clad, pure silica core fibers. The CeramOptec fiber had a fluorine doped silica clad and a germanium doped silica core.

Each of the multi-mode optical fibers had a polyimide coating to provide mechanical strain relief and also protect the fiber from the environment. This low-temperature polymer coating determines the manufacturer recommended maximum use temperature of the optical fiber, but the optical fibers can survive beyond this recommended maximum temperature with the proper precautions. The maximum use temperature for polyimide coated fibers is usually around 300°C to 400°C, and the coating starts to thermally decompose above 400°C. The results of this decomposition are discussed later in this report.

Manufacturer	OH Concentration	Core Dopant	Clad Dopant	Coating Material	Core Diameter (um)	Clad Diameter (um)	Part Number	Manufacturer Specified Range (nm)
Polymicro	low	none	fluorine	polyimide	100	120	FIP100120140	380 – 2400
Polymicro	high	none	fluorine	polyimide	100	120	FVP100120140	180 – 1150
CeramOptec	very low	germanium	fluorine	polyimide	100	110	WF100110125P37	350 – 2200

Table 9: Multi-Mode Optical Fibers Investigated

The Optical Backscatter Reflectometer (OBR) 4600 is a commercially available distributed sensing instrument made by Luna Innovations. This device uses plain single-mode optical fibers to sense changes in strain at distributed locations in the connected optical fiber. The strain can be related back to other measurement quantities including temperature change, pressure change, change in strain, etc. The OBR uses single-mode optical fiber and, at the recommendation of Luna Innovations, SMF-28e+ from Corning Inc. was purchased for this testing in this project. SMF-28e+ has a low-OH germanium doped silica core with pure silica clad.

6.4 Purchase of Broadband Fiber Transmission Light Source

A fiber-coupled tungsten halogen white light source, StellarNet model SL1, was purchased. This device is connected to the other optical equipment as shown schematically in Figure 94 and with actual components in Figure 95. This light source connects fibers coupled with SMA905 connectors and the tungsten halogen incandescent bulb has a 2800K color temperature.

Figure 75: StellarNet Model SL1 Broadband Tungsten Light Source
(picture from: http://www.stellarnet-inc.com/public/download/SL1-Halogen-light.pdf)

Chapter 7. Task F [2]

7.1 Deliverable

Construction of test rigs for fiber in-situ testing at very high temperatures in and out of core.

7.2 Introduction

This project required development of some unique experimental capabilities including several furnaces and a broadband optical transmission measurement system. Three different high-temperature furnaces were constructed. These furnaces were used to heat optical fibers in different facilities and to different temperatures. The most specialized of these was a low-activation furnace for irradiating spools of optical fibers to 1000°C next to the OSU research reactor core. The numerous constraints of operating near a nuclear reactor complicated the design and precluded the use of off-the-shelf furnaces. Design justifications, feature descriptions, and pictures of the three furnaces are presented in this chapter.

A power supply and safety system was designed and fabricated that was ultimately used for all three furnaces. The power supply and safety system was initially designed to accommodate the atypical electrical characteristics of a silicon carbide (SiC) heating element and to provide sufficient active and passive safety mechanisms for operation near a nuclear reactor. The constraints of this experiment complicated the use of a single off-the-shelf product and a custom power supply and safety system was designed using a combination of commercially available and custom components. Design justifications, a description of features, modes of operation, and pictures of the power supply and control system are provided.

A system was developed to automate the measurement of broadband optical transmission through multiple multi-mode optical fibers. The system was designed to optimize wavelength range, scan time, number of optical channels, and cost. There was not an individual off-the-shelf product that satisfied the requirements and a combination of off-the-shelf components was purchased. These components came from several different companies, which complicated communication between the devices and made data acquisition impractical using manufacturer supplied software. A custom application, complete with a graphical user interface (GUI), was written in LabVIEW to automate the optical data acquisition. A description of the data acquisition application and an explanation of the user interface is provided in [2].

7.3 High-Temperature Furnaces

The purpose of this project was to experimentally determine, in-situ, the performance of silica optical fibers in a high temperature radiation environment. The reactor irradiation furnace was designed to meet the geometric, radiological and safety constraints of operating to 1000°C in a 7” dry-tube next to the OSU reactor core. The exterior of the reactor irradiation furnace is shown in the middle in Figure 76. The gamma irradiation furnace was designed to meet the geometric and safety constraints of operating in the Co-60 irradiator available at the OSU reactor lab. The gamma irradiation furnace can operate to 600°C and is shown on the right in Figure 76. The $MoSi_2$ tube furnace was designed to operate at 1600°C and was fabricated to fit inside a 7” dry-tube, although is not suitable for reactor use in its current state. The $MoSi_2$ tube furnace is shown on the left in Figure 76.

Figure 76: $MoSi_2$ Furnace (L), Reactor Furnace (C), Gamma Furnace (R)

7.3.1 Reactor Irradiation Furnace

The reactor irradiation furnace, shown in the middle in Figure 76, was designed meet all of the necessary experimental and safety constraints, and be affordable [98] [99]. Components of the reactor irradiation furnace are labeled in Figure 77 and several of the components will be described in following sections. Experimentally, this furnace was designed to reach an internal temperature of 1000°C while accommodating several long lengths of coiled optical fiber. The radial geometry of the furnace was constrained by the dry-tubes available at the OSU reactor lab and an ASTM standard relevant to this experiment. The largest dry-tube available had a 6.75inch inner diameter (ID) and purchasing a larger diameter dry-tube was impractical. An ASTM standard procedure for measuring radiation-induced attenuation in optical fibers indicated a minimum fiber wrap diameter of 10cm (~4in) and reducing this diameter would negatively affect the experimental results [100]. These two dimensions significantly define the radial geometry of the heated region of the furnace.

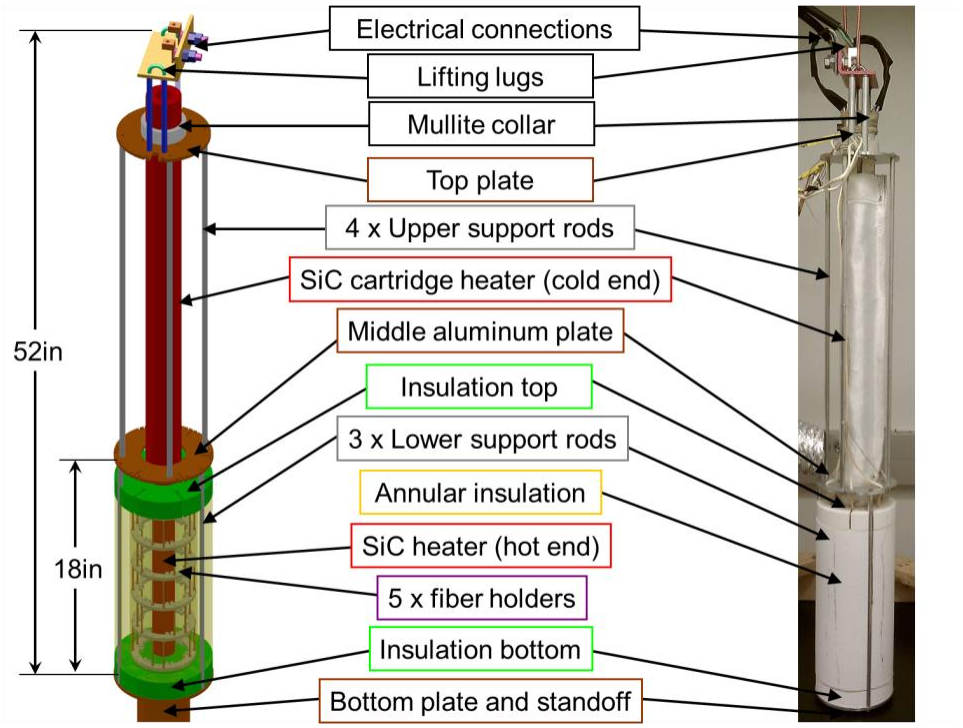

Figure 77: Components of Reactor Irradiation Furnace

The vertical geometry of the furnace was less constrained and was adjusted to accommodate other constraints. A heated length of 12 inches was, somewhat arbitrarily, chosen. The vertical mid-plane of the heated region was aligned with the peak neutron flux by adjusting the height of the standoff at the bottom of the furnace. The axial location of the peak flux was determined with a foil activation experiment. A commercially available SiC cartridge heater was used to reduce the neutron activation hazard, compared to using a typical metal sheathed heating element. The length of the cold-region of this cartridge heater was extended so that electrical connections to the heater could be made in a lower flux region above the core to reduce activation of electrical connection components and the copper wire.

All of the materials in the furnace were chosen to minimize the radiological hazard caused by neutron activation. Generally, neutron activation can be reduced by using isotopes with small neutron capture cross-sections, minimizing the mass, and minimizing the thermal neutron fluence. Minimizing neutron activation is difficult because few engineering materials are made of a single isotope and the purpose of this experiment is to maximize the neutron fluence to the optical fibers. Instead, the radiological hazard was minimized by using materials that quickly decay and designing the furnace so that it could be serviced quickly. In addition, some of the materials in the furnace needed to have good high temperature performance. Finally, the materials chosen for this furnace had to be affordable especially considering the useful life of the furnace may only include a few experiments over a few years. Cross-referencing good high temperature materials with low-activation materials and considering the material and fabrication costs was an interesting optimization problem.

Finally, it was imperative that the operation of this experiment could not endanger the OSU research reactor or the reactor lab facility. To protect the reactor, the furnace was not allowed to boil water on the outside of the aluminum dry-tube. Thermal insulation prevented this condition and this constraint was additionally enforced by passive and active features in the power supply

and control system. The experiment was designed to not release mobile radionuclides or generate an unmanageable quantity of radioactive waste by careful selection of materials and testing those materials with neutron activation analysis.

Silicon Carbide Cartridge Heater

An inexpensive, commercially available reaction bonded SiC cartridge heater capable of operating to 1650°C, in air, was used in this furnace. The cartridge heater was purchased from I Squared R Element Company and the product number was: SEU 45x12x1.50 [101]. The heater has a 12 inch hot section and a 33 inch cold section, as shown in Figure 77 and Figure 78. The long cold end allows the electrical connections to be located two feet above the reactor core where the neutron flux is lower. Braided aluminum conductors are mechanically attached to flame sprayed aluminum contacts deposited on the SiC cartridge heater, above the mullite collar. These features are shown in Figure 78.

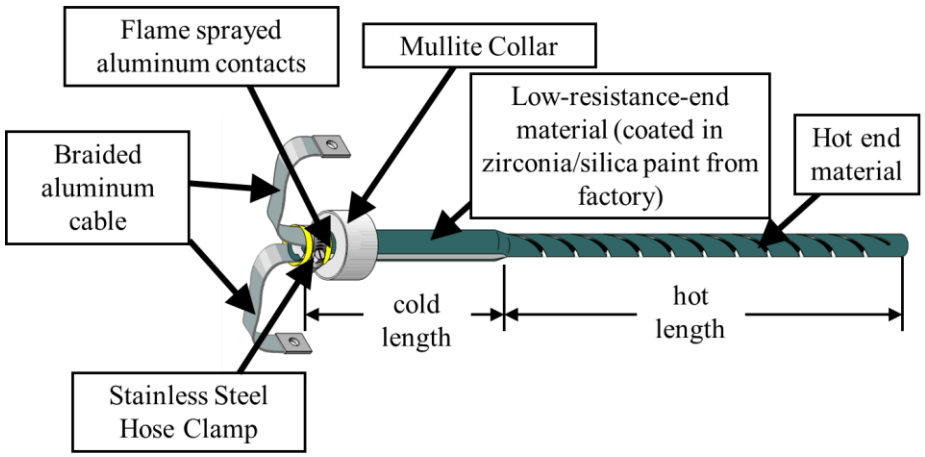

Figure 78: Features of a SiC Cartridge Heater [101]

This heating element requires a low voltage, high current power supply. Because SiC is a semiconductor, this heater has a negative thermal coefficient of resistance up to ~500°C. This property makes SiC heaters more difficult to control than typical metal element heaters. In addition, the resistance of this material is reported to increase over the life of the heater as a function of operating temperature, environment, and power control method. The lifetime of SiC heating elements is increased by using a power controller with a very short time base, such as pulse modulated DC or phase angle controlled AC power.

Silicon and carbon are good materials from a radiological hazard perspective, but the material used to produce the furnace was not very pure. Neutron activation analysis was performed on sample material provided by the company. The results of the neutron activation analysis are summarized in a later section.

Fiber Holders

During the design phase of the reactor irradiation furnace, it was specified that the furnace should accommodate long lengths of several types of optical fibers. At that time, the number of fiber types to be tested was not known and "long length" was taken to mean 50 meters of fiber, based on ASTM E1614-94 [100]. In order to accommodate more than a few inches of fiber in the heated region, the fiber had to be coiled inside the furnace. Coiling optical fiber is difficult because, unlike metal wire, glass fibers do not plastically deform when bent and the coiled fibers must be

constrained to prevent uncoiling. In addition, the fiber holders were going to be exposed to high temperature and neutron radiation. Servicing the furnace between experiments required intimate contact with the fiber holders, so the holder material had to have low residual activation.

Titanium, silicon carbide, quartz, alumina and other materials were considered for these high-temperature, low-activation, somewhat structural components. Commercially pure titanium is readily available, machinable and has a melting temperature above 1600°C, but it can ignite around 1200°C in air. 1200°C was considered too close to the planned maximum operating temperature of 1000°C. Sintered SiC has a maximum use temperature, in air, of 1900°C, and was available with material purities that would not present a neutron activation hazard. Unfortunately, the fabrication of SiC parts with tight tolerances was prohibitively expensive and quotes from two manufacturers had to be declined. Quartz was chosen because its melting temperature is above 1600°C, it is available in very pure forms (GE124 & GE214 [102]) that do not present a neutron activation hazard, it does not present a fire hazard, and because it is less expensive to fabricate than SiC or alumina. Quartz is not as strong as SiC or alumina and extra quartz parts were ordered in the event that parts were accidentally broken.

Several geometries were considered for the fiber holders, but only the final design is described here. Figure 79 shows a CAD model of the final design and an assembled quartz fiber holder loaded with optical fiber. Eight posts, shown in red in the CAD model, constrain the fiber on the outside and inside of the fiber coil. The eight posts fit loosely into eight holes in the quartz rings, shown in gray in the CAD model. The design of the posts and the spacing of the holes in the rings constrain the coiled fiber to a wrap diameter of 10cm, which is the minimum diameter recommended in ASTM E1614-94 [100]. The posts and rings were designed to accommodate fabrication tolerances, thermal expansion, manufacturing cost, and to take advantage of the positive and negative forming processes possible for quartz fabrication. The posts, for example, were fabricated using a positive process by Tim Henthorne, a talented scientific glassblower at OSU [103]. The cost per post fabricated with a positive process was around $13 compared to $180 per post fabricated with a negative process. The rings were laser cut by GM Associates, Inc. for $253 per part, compared to $490 per part from another company using a traditional milling process. The assembly shown in Figure 79 fabricated with quartz parts was $610. Based on quotes from Saint-Gobain and CoorsTek, an assembly with similar geometry but fabricated with SiC parts would cost around $2100.

Figure 79: Fiber Holder CAD (L), Quartz Assembly with Fiber(C) & with 5 TCs(R)

A detailed image of a quartz ring is shown in Figure 80. The center of these parts needed to be hollow to allow the SiC cartridge heater to be inserted as shown in Figure 77. Six equally spaced cleats were included on the inner diameter of each ring so that thermocouples could be located and

fastened at repeatable locations. In practice, the sheathed thermocouple wires fit tightly in the cleat and Nextel string was used to tie the thermocouple wire into the cleats, as shown on the right in Figure 79. Single mode fibers were included in the experiment by a similar attachment method. An assembly of five of the fiber holders fit into the reactor irradiation furnace, as shown in Figure 81, to allow multiple fiber types to be tested simultaneously.

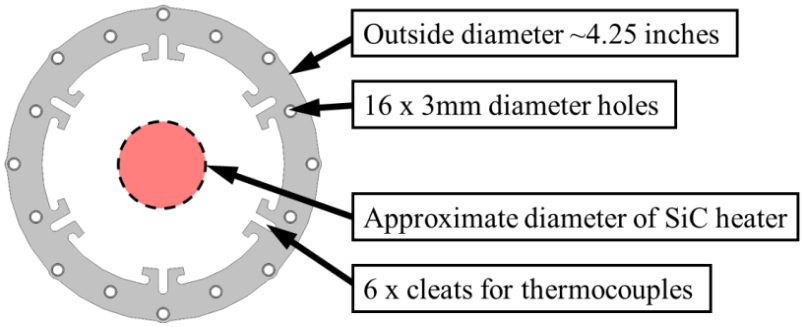

Figure 80: Quartz Fiber Holder Ring

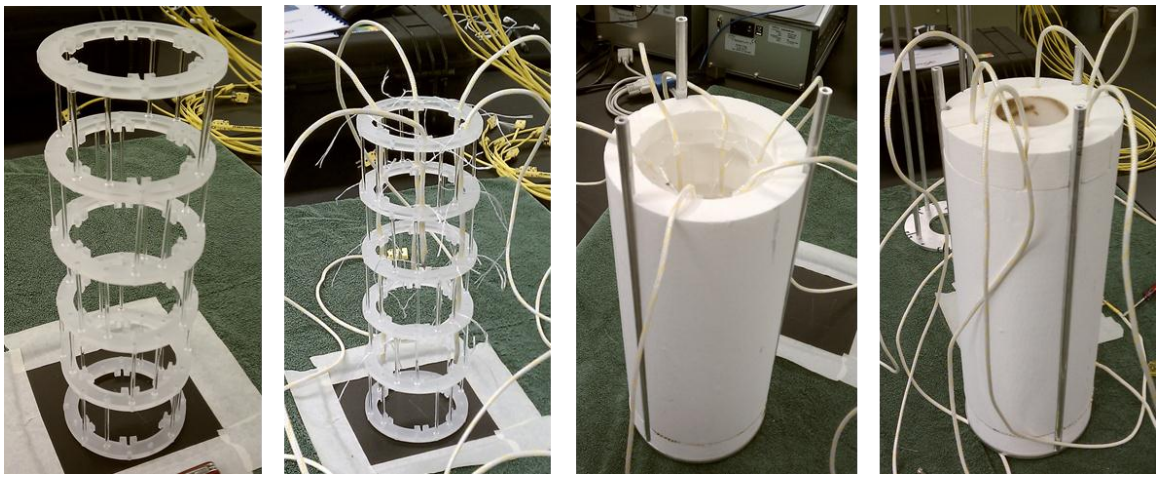

Figure 81: Assembly of Quartz Fiber Holders into Reactor Irradiation Furnace

Rigid Insulation

Low density alumina/silica materials were used for the rigid insulation on the reactor irradiation furnace. The insulation bottom and the annular insulation components, as labeled in Figure 77, were made from ZAL-15 from Zircar Ceramics, Inc [104]. The thermal conductivity of this material is low but it is brittle and has poor abrasion resistance. The manufacturer applied a surface treatment, ST6C, to these two components to improve the abrasion resistance and mechanical strength. Because of the six slots and the hole cut into the top insulation component, it was made with a higher density alumina/silica material called SALI. SALI has better mechanical strength but worse thermal conductivity compared to ZAL-15. Neutron activation analysis was performed on the ZAL-15 material with the surface treatment and the radiological hazard presented by these components is small. Results from the neutron activation analysis are included in a future section.

Nextel Insulation

Nextel 312 is a high temperature flexible fabric composed of 24.5% silica, 62.5% alumina and 13% boria, and is rated for continuous operation up to 1100°C [105]. Nextel is a proprietary 3M product that is similar to silica fabric, though the composition of Nextel appears to be better documented compared to other commonly available silica fabrics. This material does not fray as easily as silica fabric and is not a significant activation hazard. Nextel tubing was used as sheathing material for the K-type thermocouples purchased from Omega for use inside the furnace. Nextel fibers were used to tie the thermocouples into cleats on the inner diameter of the fiber holders. A Nextel sheath was designed to fit over the cold end of the SiC heater to reduce the convective losses through the center of the hollow SiC heater. This sleeve is shown covering the cold end of the heater in Figure 77. A Nextel plug was made to fill the central void of the SiC heater in the hot end. A gasket was also made to fit between the rigid annular insulation and the rigid bottom insulation. The custom Nextel insulation components were purchased from Thermostatic Industries, Inc. [106].

Aluminum Structural Materials and Fasteners

Aluminum alloys were used for the low temperature structural components in the reactor irradiation furnace, as shown in Figure 77. The melting temperature of aluminum is around 660°C, so aluminum was only used for low temperature structural components as shown in Figure 77. Pure aluminum activates but decays with a short half-life. Because pure aluminum is not available as a common engineering material, a combination of Al-6063, Al-3003, and Al-6061 were used. The support rods and the standoff were made with Al-6063. Al-3003 was used to make the top, middle and bottom plates. Al-6063 and Al-3003 have less chromium and zinc than Al-6061, which reduces the activation hazard at the expense of the mechanical properties of the material. Four Al-6061 sleeves were used near the top of the furnace as shown in Figure 82. All of the fasteners are made of aluminum alloys but the alloys were not specifically identified by the manufacturers.

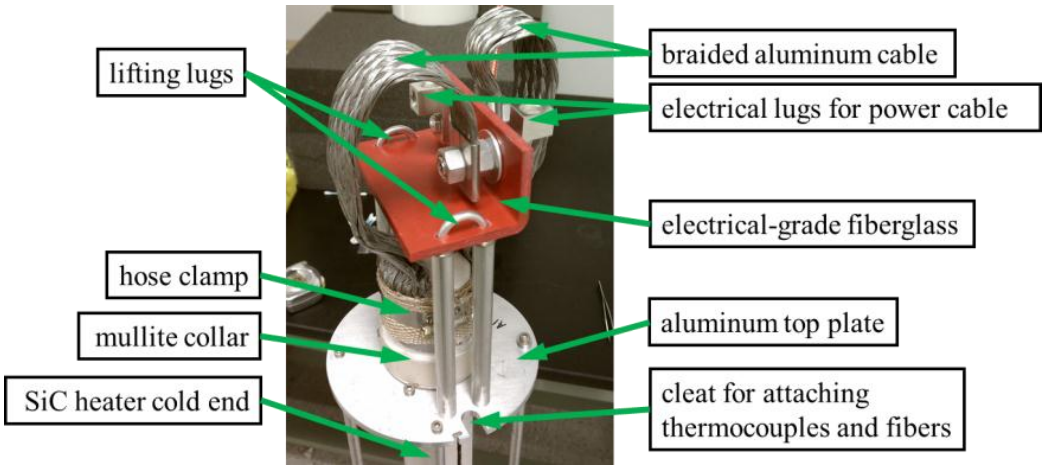

Figure 82: Electrical Connections and Lifting Lugs on SiC Furnace

Electrical Connections and Lifting Lugs

Electrical connections and lifting lugs were made at the top of the reactor irradiation furnace, as shown in Figure 82. Except for the fiberglass, the associated components were aluminum although the specific alloy was not always known. The long cold-end of the SiC heater allowed these components to be located more than two feet above the top of the reactor core where the thermal neutron flux is less than 3% of the peak in that facility. The braided aluminum cable

was included with the SiC heater and the cable was electrically insulated to prevent electrical connection with the aluminum dry-tube. Three 12-gauge stranded copper wires are bolted to each electrical lug and deliver electrical power to the furnace.

7.3.2 Gamma Irradiation Furnace

The high temperature furnace fabricated for reactor irradiations was designed to fit inside a dry tube an ID of 6.75 inches. Unfortunately the Co-60 irradiator at the OSU nuclear reactor lab is currently fitted with a dry tube with a 6 inch ID. To facilitate high temperature testing inside the Co-60 irradiator, another furnace was designed and fabricated specifically for this work. The design requirements were not as strenuous for this furnace because neutron activation does not occur in this facility. The quartz fiber holders and the power supply designed for the reactor irradiation furnace were reused with this furnace. Two views of this furnace are shown in Figure 83. A stainless steel sheathed electric resistance cartridge heater (Hotwatt HS75-8) was used with a maximum power of 2kW. Because of the reduced insulation thickness, 600°C was the maximum operating temperature for this furnace. This temperature limit was dictated by the low melting temperature of aluminum.

Figure 83: Co-60 Gamma Irradiation Furnace

7.3.3 Molybdenum di-Silicide Tube Furnace

A tube furnace with a maximum continuous use temperature of 1600°C was designed and constructed. The heater core was a 2200 watt Inline UltraCoil Robust Radiator purchased from Micropyretics Heaters International, Inc. [107]. The heating element is made out of molybdenum di-silicide ($MoSi_2$) and MoSi2 heating elements are commercially available in many geometries from several sources. The heating element required a low-voltage, high-current power supply and the power supply fabricated for the SiC reactor irradiation furnace was reused for this furnace. The room temperature resistance of this heating element is too low to use the 48V transformer configuration. Instead, the 24V setting must be used to heat the furnace to 1000°C, after which the 48V setting is used to achieve higher temperatures.

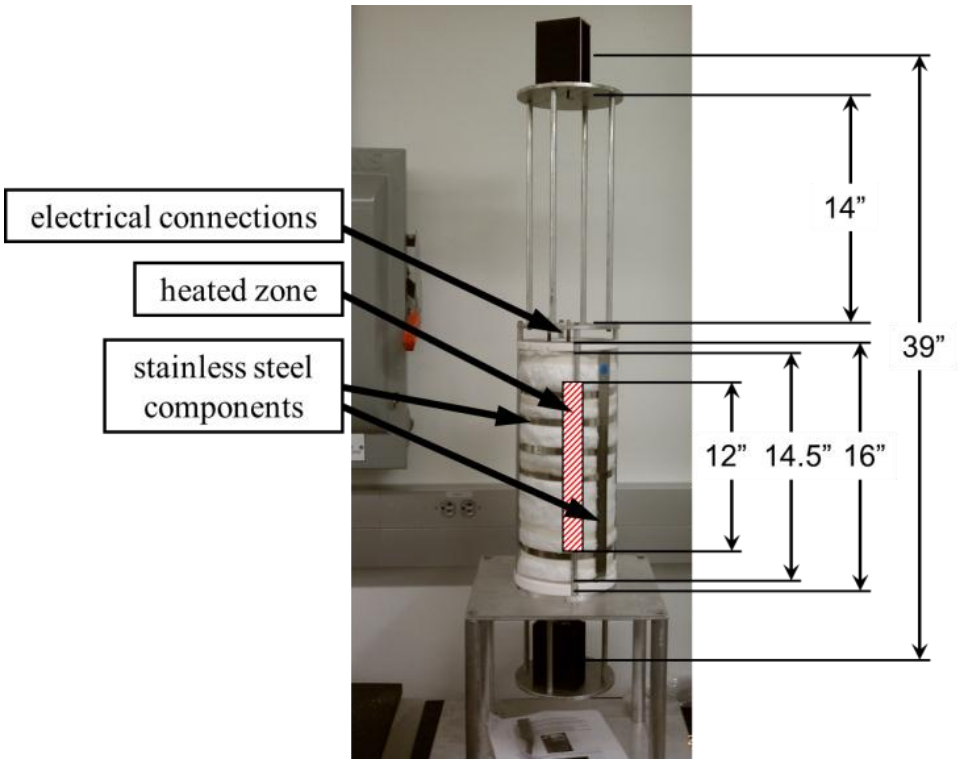

Figure 84: Molybdenum di-Silicide Furnace

The heater core was assembled with a frame that allows the furnace to be used as a vertical tube furnace in the lab, as shown in Figure 76 and Figure 84. The larger square components can be removed leaving a cylindrical frame that should fit into the 7 inch dry-tubes at the OSU reactor lab. Several obvious modifications need to be made to this furnace to make it suitable for reactor irradiation. First, the heater core has several stainless steel support pieces that would need to be replaced with a moderate-temperature, low-activation material such as commercially pure titanium. The thermocouple is currently fitted into a hole at the vertical mid-plane of the heater and perpendicular to the vertical axis. The thermocouple would need to be inserted vertically to avoid interference with the dry tube. Less obvious modifications may also need to be made and would depend on the potential activation of other materials used in the $MoSi_2$ heater core. Finally, thermal testing of the furnace in a mock-dry tube would be necessary to determine the maximum achievable temperature during a reactor experiment.

7.4 Neutron Activation Analysis

Neutron activation of the reactor irradiation furnace would cause logistical challenges in reusing the furnace. In addition to other constraints, furnace materials were selected with short half-lives and/or low-activation cross-sections. During the design of this furnace it was not known how many reactor irradiations would be needed and the furnace was designed to be serviced after a 30-day decay following an 8-hour irradiation at full power. Additionally, this design philosophy reduced the amount of radiation waste produced.

Engineering materials are rarely elementally pure, either intentionally or unintentionally. Elemental aluminum, for example, is well suited for use in reactor experiments. Al-27 is the only naturally occurring aluminum isotope and Al-27 has a relatively small thermal neutron capture cross-section. When Al-27 does capture a neutron, it becomes Al-28 which has a half-life of 2.2

minutes and decays into a stable isotope, Si-28. Unfortunately, aluminum that is available as an engineering material is always alloyed with other elements, which are essentially intentional impurities. Most engineering materials, including aluminum, also include unintentional impurities that may or may not be known to the manufacturer. The intentional and unintentional impurities must be considered in the neutron activation analysis of any material.

Radioactive components can be handled safely and elimination of all neutron activation is both unnecessary and impractical. During servicing, some of the furnace components were quickly removed and placed behind shielding. When the dose to the user could be minimized by reducing the interaction time with a component, minimizing the activation of those components was less of a constraint. Components that did not require much interaction during servicing included the SiC heater, the rigid insulation, and the aluminum frame. The fiber holders required extended intimate contact during furnace servicing. The thermocouples were not reused between experiments, but removing them from the furnace required minutes of user interaction time.

Neutron activation analysis was completed on the SiC heater material, the rigid insulation material, the Nextel flexible insulation, the optical fiber, and Hexoloy SiC. The composition of these components was not well characterized or publicly disclosed by the manufacturer. The composition of the aluminum alloys and the quartz fiber holders were well characterized by the manufacturer and the neutron activation of these components were calculated instead and not experimentally determined. Details of the activation analysis can be found in [2].

7.5 Power Supply and Safety System

A combined power supply and safety system was developed to provide electrical power to the reactor irradiation furnace. The safety requirements associated with operation near a nuclear reactor precluded the direct use of a COTS power supply. In addition to providing electrical power, this system includes several active and passive safety features to protect the experimental facility. The power supply components were chosen to accommodate the atypical electrical characteristics of the SiC heating element used in the irradiation furnace. The safety limit monitor is a COTS component that monitors internal and external furnace temperatures as well as the electrical power going to the transformer. There is a health monitoring circuit inside the safety limit monitor that checks for correct operation of the device. The functionality of the safety and control systems were separated and the safety system overrides the control system. A block diagram of the power supply and safety system is shown in Figure 85 and the front panel is shown in Figure 86. The power supply components and the safety system components are described in detail in following sections.

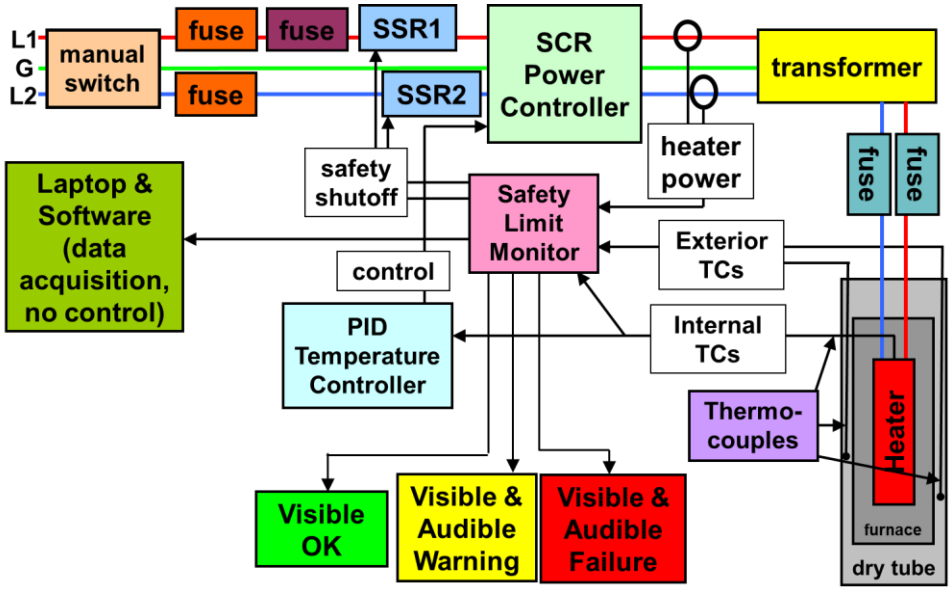

Figure 85: Block Diagram of the Power Supply & Safety System

Figure 86: Front Panel of the Power Supply & Safety System

7.5.1 Power Supply

The power supply and safety system was designed as an integrated unit, but the power components are described in this section. An overview of the power supply is shown by the block diagram in Figure 85. A 120VAC line supplies power to individual components inside the power supply, but cannot supply any power to the furnace. Two lines of three-phase 208VAC were used as the primary electrical power, indicated as L1 and L2 in Figure 85. The primary voltage passed through fuses and solid state relays (SSRs) into the silicon controlled rectifier (SCR) phase angle controlled power controller. The output of the SCR power controller feeds a 5KVA step-down transformer that reduces the voltage to, nominally, 24 or 48VAC depending on how the transformer secondary is wired. The transformer secondary voltage passes through two additional fuses and is

then connected to the SiC or $MoSi_2$ furnace with appropriate gauge wire. The transformer is not used with the gamma irradiation furnace.

A DIN-A-MITE C, Watlow model DC10-20L5-000, was the SCR power controller used and is shown in Figure 87 [108]. This device controls the output voltage by manipulating the turn-on phase angle for each half-cycle of the 60Hz AC sine wave. This enabled the electrical power to the load to be varied every $1/120^{th}$ of a second. The phase angle is controlled from 0 to 100% by varying a control voltage from 0-10VDC. The low voltage DC control signal can be provided automatically by a PID controller or manually using a potentiometer input. The selection of automatic or manual power control is made using a switch on the front panel of the power supply, as shown in Figure 86. This device is rated for a maximum current of 55 amps. The short time base was important for the efficient operation of the transformer and also to improve the longevity of the SiC and $MoSi_2$ heating elements. This particular model also included a built-in current limit feature and a soft-start feature that slowly increases electrical power to the load.

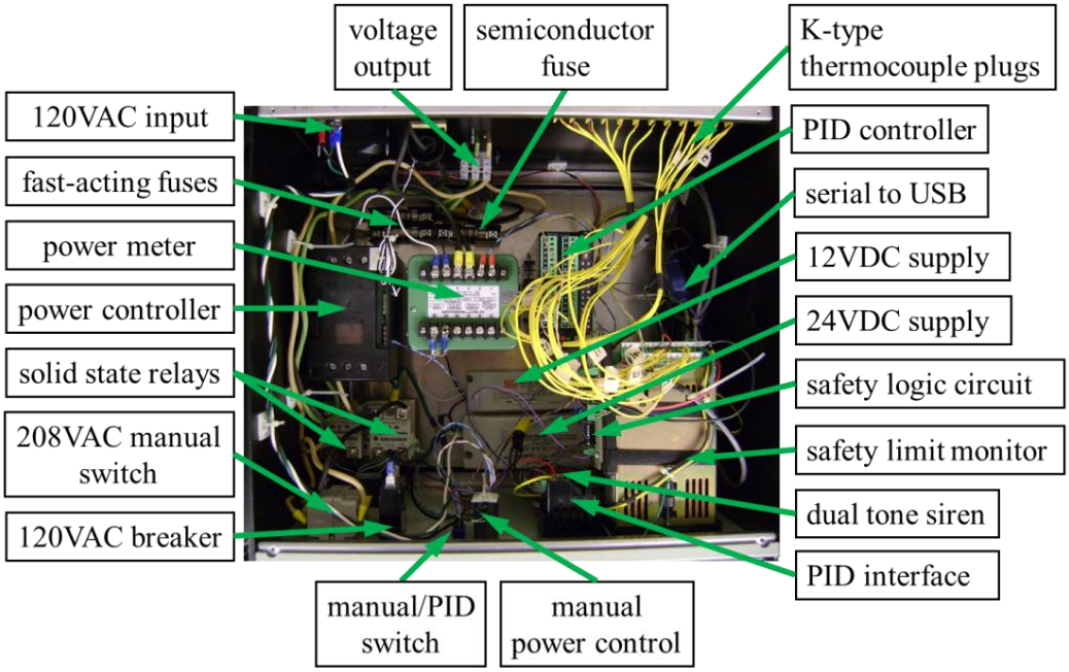

Figure 87: Top View of Assembled Power Supply & Safety System

A PID controller, Watlow model RMC3P5F1P5FAAAA, was included in the power supply for automatic temperature control. This PID controller accepts up to four inputs and generates a linear DC signal to control the power controller. The four inputs can be averaged or weighted in the control scheme and can be setup to ignore thermocouple breaks during an experiment. This PID controller is capable of auto-tuning the P, I, and D values for a particular furnace. The temperature set-point can be set with software by connecting to the USB port on the front of the power supply, or by manual entry using the PID interface module, also on the front panel. The power controller and the PID controller are both shown in a top-down view of the completed power supply, shown in Figure 87.

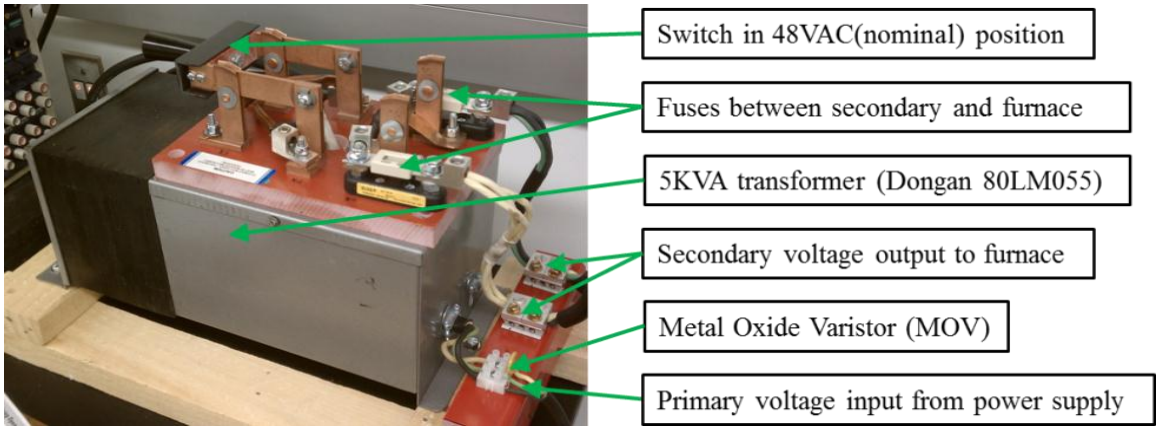

Figure 88: 5kVA Dongan Transformer with 24/48VAC Switch

A 5KVA transformer, Dongan model 80LM055, was used to step down the voltage output of the power controller to a voltage appropriate for the SiC and $MoSi_2$ heating elements. There primary and secondary wiring was configured so that a 240VAC input would provide a 24 or 48VAC output depending on the secondary wiring. A large knife switch was attached to the transformer so the secondary voltage could be easily switched, as shown in Figure 88. The secondary voltage should never be changed while the transformer is energized. For resistive loads on the secondary, the maximum primary current at 208VAC is 24 amps.

The soft-start feature built into the power controller prevents a large initial in-rush current into the transformer to prevent damage to components and unnecessary fuse failures. When the safety system abruptly turns off furnace power, there is an equivalent out-rush current from the transformer. The voltage spike associated with the out-rush current consistently failed the semiconductor fuse and could cause damage to other components. A metal oxide varistor (MOV), Tyco model ROV20H391K-S, was placed across the primary input to the transformer, as shown in Figure 88, to suppress the voltage spikes. A circuit diagram for this addition is shown in Figure 89. Up to a maximum voltage of 250VAC, the MOV does not conduct and looks like an open circuit. When the power supply is abruptly turned off, the transformer primary voltage increases above the maximum allowable voltage causing breakdown and conduction across the MOV. The primary lines of the transformer are shorted together and the excess energy is dissipated without causing harm to other components in the power supply. The MOV can sustain a finite number of surges, however, and may eventually need to be replaced.

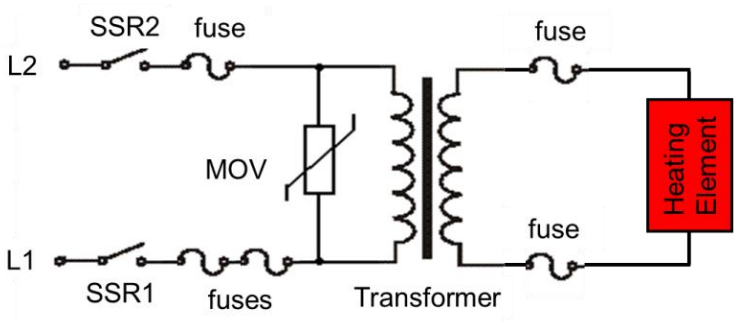

Figure 89: Metal Oxide Varistor for Surge Suppression

7.5.2 Safety System

The safety system was designed to maintain the safety of the experimental facilities including the reactor, the attached load, the power supply components, and the user. The system was designed to fail-safe on a component by component basis but to also maximize the probability of a successful experiment. To accomplish this, a combination of active and passive components was included in the safety system.

As shown in Figure 85, five fuses were included. Three fuses are internal to the power supply shown in Figure 87 and the other two are attached to the transformer, as shown in Figure 88. The two orange fuses in the block diagram are fast-acting fuses, KTK Limitron, that provide over-current protection. Based on the other components in the system, fuses rated for 20A or less should be used. Even though the KTK fuses are fast-acting, they are not fast enough to protect the SCR power controller or SSRs from damage in the event of a short circuit. A very-fast-acting semiconductor fuse, Littlefuse model LA60Q202, was used to protect equipment and facilities in the event of a short circuit. This fuse is shown as the purple block on L1 in Figure 85 and is designed to open in milliseconds in the event of a short circuit. The semiconductor fuse, however, does not provide conventional over-current protection. Two additional fuses were included between the transformer secondary and the electrical connections on the furnace.

The safety system can actively monitor up to twelve thermocouple inputs and the electrical power going to the transformer primary. The CAS200, Watlow model EZKB-LAAA-AAA, was used to monitor these inputs and control the state of the two SSRs as well as the audible and visual feedback. Each SSR, shown as blue blocks on L1 and L2 in Figure 85, has a current rating of 25A and is used to switch the high voltage AC primary lines with a low voltage DC control signal. Both SSRs are controlled by the CAS200, but in different ways. SSR2 is turned on during normal conditions and high deviation alarms but is turned off for high process alarms. A watchdog circuit inside the CAS200 monitors the operation of the CAS200 microprocessor. The watchdog circuit turns on SSR1 during normal operation, but turns off SSR1 if the microprocessor stops working. Turning off either of the two SSRs immediately turns off electrical power to the load.

The CAS200 safety limit monitor is an archaic piece of equipment that is typically used in industry. Being archaic and used in industry gives the device credibility for reliable operation, but also makes interfacing with the device difficult. Proprietary Watlow software was used to setup channel input types, define nominal process set-points, acceptable process deviations, and high process alarm conditions. For each thermocouple, for example, the user defines a nominal set-point based on the expected temperature at that location for the particular experiment. The user also defines a high deviation value to accommodate any over shoot. For temperatures up to the set-point plus the deviation, there is no alarm. If the temperature goes beyond the set-point plus the deviation, an intermittent siren and the yellow LED are activated to indicate a high deviation alarm. The furnace is still powered during a high deviation alarm and it is important for the user to set conservative limits for the deviation value. If the temperature goes beyond the user-defined high process value, a single-tone siren and the red LED are activated. In the event of a high process alarm, SSR2 is turned off which turns off power to the furnace. Examples of these conditions are shown graphically in Figure 90. Thermocouple breaks are also identified by the CAS200 and are handled like a high deviation alarm.

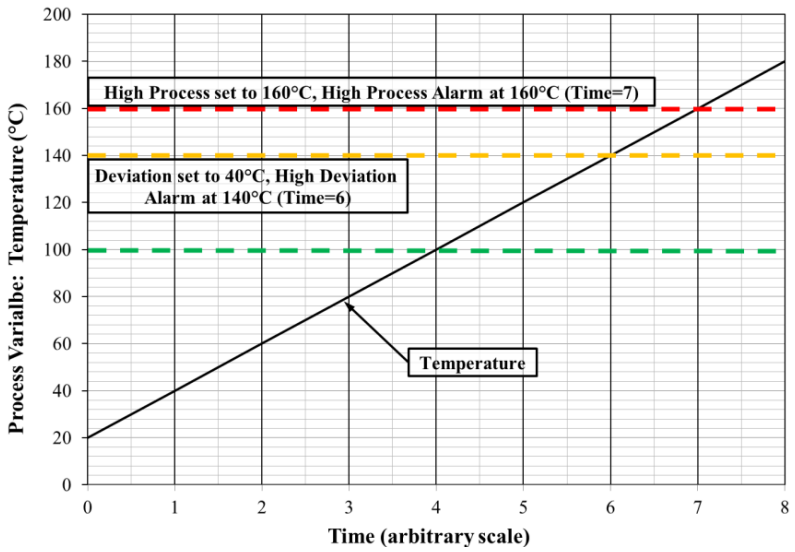

Figure 90: Example of Alarming Conditions for the CAS200

The CAS200 digital outputs are open collectors and sink current in the on-state and provide a high impedance input in the off-state. The state of digital output 1, 2 and the Global Alarm on the CAS200 were defined to sink current for alarm conditions associated with each output. Because of the limitations of the CAS200, a supplemental logic circuit was fabricated to interface the digital outputs of the CAS200 with the dual-tone siren, the three LEDs, and SSR2. A diagram of the circuit is shown in Figure 91 and the constructed circuit with labeled components and pin-outs is shown in Figure 92. A truth table describing the behavior of this circuit is shown in Figure 93. The circuit has been tested and operates as designed. The operation of the active safety components have been tested intentionally and unintentionally and behave as designed. The passive safety system components have been unintentionally tested on several occasions and also perform as expected. A more detailed analysis of the safety system can be found in [2].

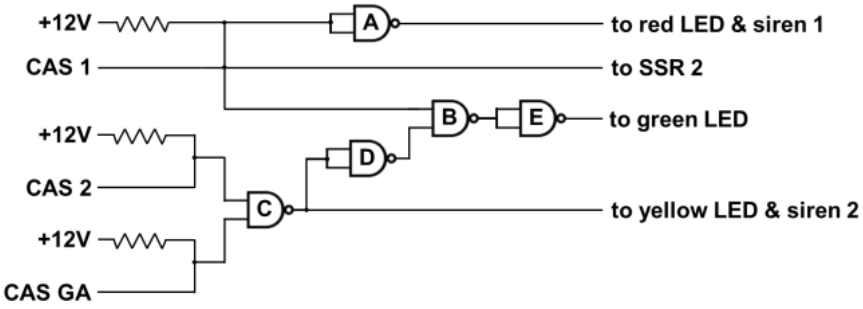

Figure 91: Diagram of Supplemental Safety Logic Circuit

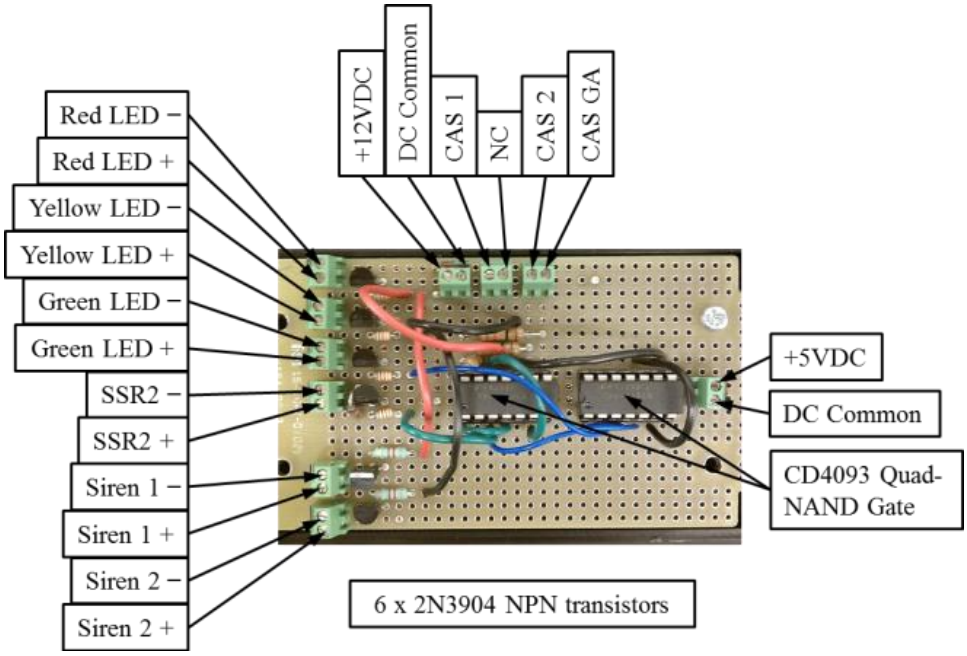

Figure 92: Supplemental Safety Logic Circuit with Labels

Alarm Case				CAS Output States			Logic Gate States					Feedback States			
No Alarm	High Deviation	High Process	TC Break	CAS Output 1	CAS Output 2	GA Output	A	B	C	D	E	SSR 2	Green LED	Yellow LED & Siren 2	Red LED & Siren 1
X				1	1	1	0	0	0	1	1	on	on	off	off
	X			1	0	1	0	1	1	0	0	on	off	on	off
		X		0	1	1	1	1	0	1	0	off	off	off	on
			X	1	1	0	0	1	1	0	0	on	off	on	off
	X	X		0	0	1	1	1	1	0	0	off	off	on	on
	X		X	1	0	0	0	1	1	0	0	on	off	on	off
		X	X	0	1	0	1	1	1	0	0	off	off	on	on
	X	X	X	0	0	0	1	1	1	0	0	off	off	on	on

Figure 93: Truth Table for Supplementary Safety Circuit

Chapter 8. Task H [2] [97]

8.1 Deliverable

Setup of fiber transmission testing facility for fiber in-situ and perform experiments at low and high temperatures, using Ocean Optics spectrophotometer. Test fiber using Luna Innovations' Optical Backscatter Reflectometer (OBR) at low and high temperatures.

8.2 Broadband Optical Transmission Measurement System [2]

An automated system was developed to measure the broadband optical transmission through multiple optical fibers. Two fiber-coupled optical spectrometers were purchased from StellarNet Inc. The NIR spectrometer is sensitive from 900-2300nm and the UV-vis spectrometer is sensitive from 200-1080nm. Two fiber-coupled multimode optical multiplexers were purchased from Avantes Inc. to enable interrogation of multiple fibers during one experiment. A fiber-coupled tungsten light source, also from StellarNet, was purchased to provide a broadband photon source. Finally, a fiber-coupled optical power meter has been purchased from Newport Corporation. This optical equipment has been connected as shown in the block diagram in Figure 94 and the picture shown in Figure 95.

Except for the light source, each device included proprietary software from the manufacturer. These pre-compiled applications did not interface with each other and using multiple applications to manually collect data was difficult, time consuming, and prone to error. An application was written in LabVIEW which connects all of the optical measurement equipment and allows data to be collected automatically. This application, combined with remote desktop and an internet connection, allows a user to remotely monitor and control the collection of optical data during an experiment.

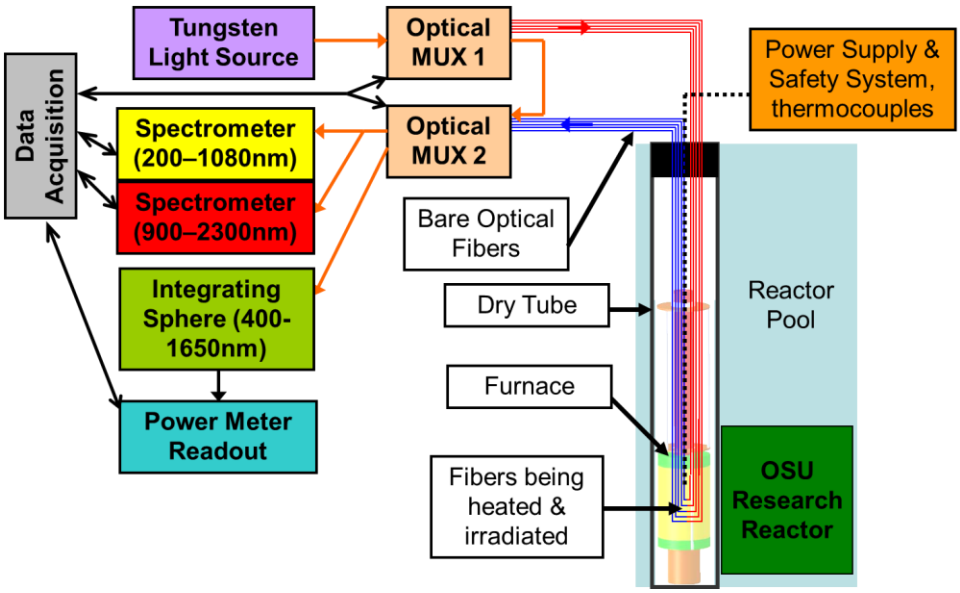

Figure 94: Block Diagram of Experimental Setup

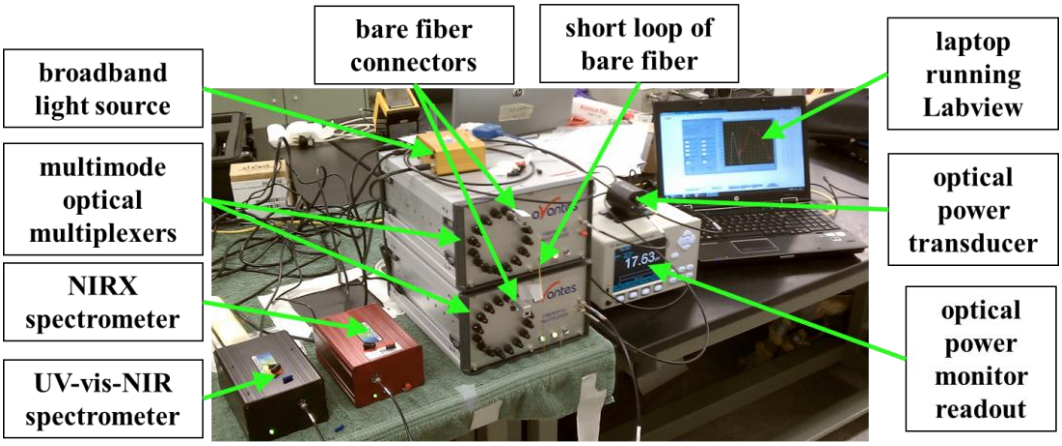

Figure 95: Broadband Optical Measurement Equipment

8.2.1 Spectrometers

An extended-range near-infrared (NIRX) spectrometer, StellarNet model RW-NIRX-SR-1024, and an ultraviolet-visible-near infrared (UV-vis-NIR) spectrometer, StellarNet model BLK-C-SR, were purchased. Both spectrometers use a fixed diffraction grating and other optics to separate and distribute the incoming broadband spectrum onto a linear CCD. The UV-vis-NIR spectrometer has a 50µm slit and uses a 2048 pixel linear CCD (Sony ILX511) that is sensitive from 200-1080nm [109]. The NIRX spectrometer has a 25µm slit and uses a 1024 pixel linear Indium-Gallium-Arsenide (InGaAs) CCD that is sensitive from 900-2300nm [110]. The relative spectral sensitivities of these CCDs are shown in Figure 96. The Sony CCD operates at room temperature and has a minimum resolution of 2nm. The InGaAs CCD includes a thermoelectric cooler and has a minimum resolution of 8nm. Both spectrometers are fiber-coupled with an SMA905 optical fiber input and connect to a computer with USB.

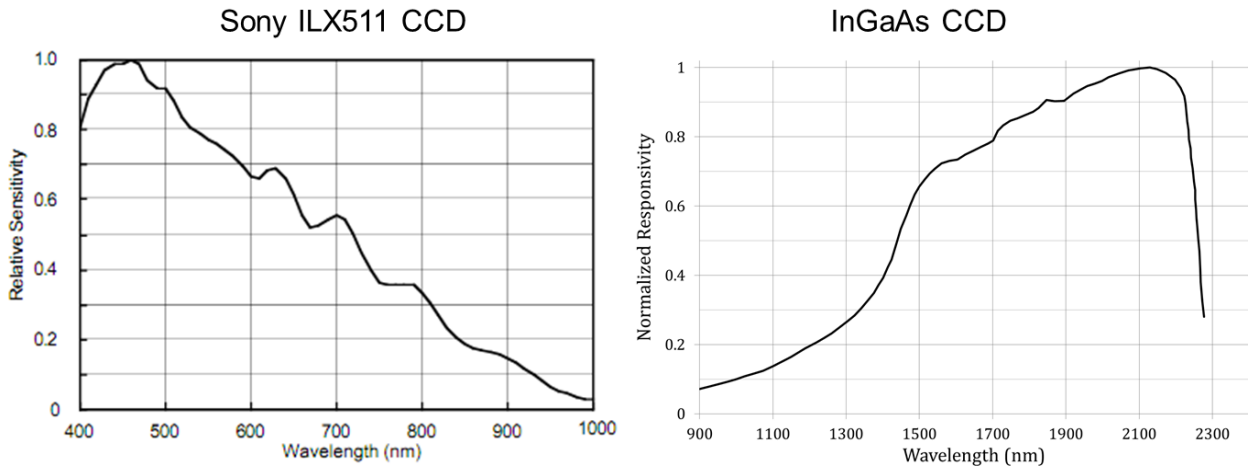

Figure 96: CCD Sensitivity in UV-vis-NIR [109](L) & NIRX (R) Spectrometers

Neither of the CCDs used in these spectrometers can differentiate between wavelengths, they can only identify light intensity. The diffraction grating in each spectrometer separates the spectrum spatially across the pixels on the CCD. There is a 16-bit analog to digital converter that samples the voltage on each pixel during each scan. Charge is developed on each pixel as a result of

photons striking the pixel. The quantity of charge developed is a function of the number of photons striking the pixel and the sensitivity of the particular CCD to that particular wavelength, as shown in Figure 96. The resulting data stream for a 2048 pixel CCD is a 2048-element integer array with values ranging from 0 to 65535.

At the manufacturer, light sources with characteristic wavelength emission were used to calibrate wavelengths to CCD pixels. This calibration is stored in memory on each spectrometer but the post processing of the raw CCD data with the calibration curve is done on the computer connected to the spectrometer. The data from the spectrometers does not correct for the wavelength dependent sensitivity of the respective CCDs shown in Figure 96.

Because the spectrometers used a fixed diffraction grating with a CCD, there were no moving parts and spectral intensity data could be acquired quickly. Integration time, sample averaging, and other parameters were configured using provided software or with the custom data collection application. The sensitivity of both of these spectrometers was affected by the ambient temperature. To minimize the effect of fluctuations in ambient temperature, both spectrometers and the power monitor were kept inside a refrigerator.

8.2.2 Multiplexers

Two fiber-coupled multimode optical multiplexers, Avantes model FOM-IR400-2x8, were purchased. One of the multiplexers was used to switch the light source between the fibers being tested. The second multiplexer was used to switch the output of each fiber to either of the spectrometers or to the power meter. The optical connections are shown schematically in Figure 94 and the actual devices are shown in Figure 95. All of the fiber coupled optical equipment used SMA905 connectors.

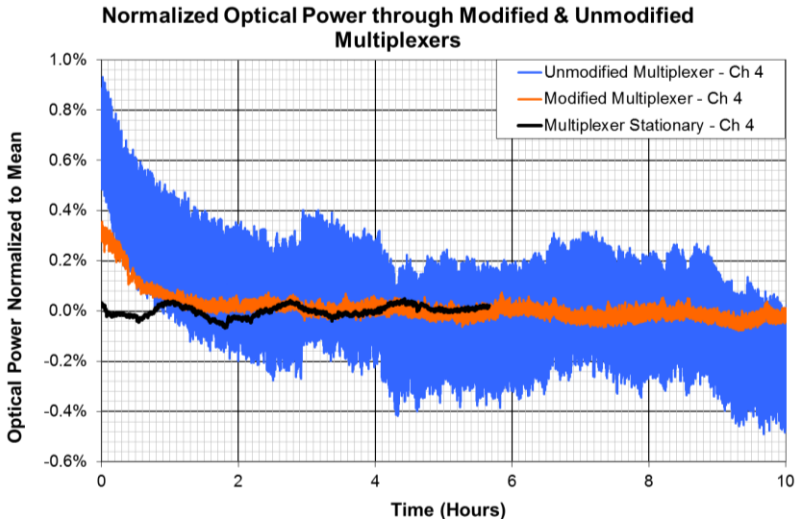

Figure 97: Hysteresis Reduction in Modified vs Unmodified Multiplexers

Inside the multiplexers, the optical multiplexing was accomplished mechanically by the rotation of an internal optical fiber that completed an optical path between two externally connected fibers. During this project one of the two multiplexers failed because the internal optical spindle stopped aligning the internal optical fibers reliably. The unreliable fiber alignment caused substantial errors in the optical transmission data. The stepper motor was not accurately positioning the optical spindle because a faulty stepper driver was causing the motor to overheat. Unfortunately, Avantes is located in the Netherlands and shipping the device back for repair was

likely to take several weeks. In an attempt to reduce the downtime caused by the faulty equipment, the multiplexer was reverse engineered and repaired at OSU. The original integrated stepper controller, driver and communication module was replaced with a COTS stepper driver and an Arduino microcontroller. Software was written for the microcontroller to mimic the original serial communication protocol over USB so that the original Windows drivers would not need to be modified. This repair was successful and several features were added to the multiplexer that were not included in the original Avantes product. In addition, the hysteresis associated with switching to a channel was reduced by a factor of 10, as shown in Figure 97.

8.2.3 Power Meter

A fiber-coupled optical power meter, Newport model 918D-IS-1, sensitive from 410-1650nm was purchased. The optical power transducer and the readout are both shown in Figure 95. An SMA905 connector was not included with this device and a custom connector was fabricated. The power meter does not differentiate photons by wavelength and all of the light entering the power meter is incident onto the photodiode and contributes to one output current. The spectral sensitivity of the photodiode is shown in Figure 98. The photodiode current output was calibrated at Newport for specific power and wavelength monochromatic sources. Using the power meter with broadband light is possible, but the power output value displayed by the power meter will not be correct. In addition, because of the spectral sensitivity of the photodiode, different broadband spectra could result in the same power output value.

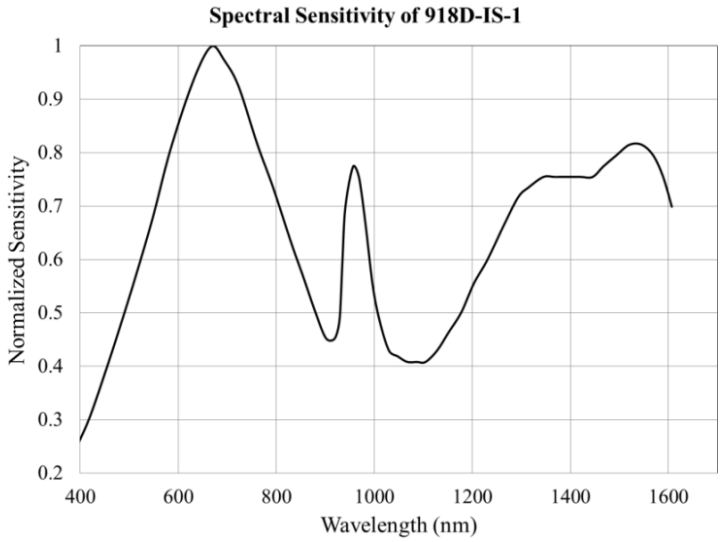

Figure 98: Spectral Sensitivity of Power Meter [111]

8.2.4 Light Source

A fiber-coupled tungsten halogen white light source, StellarNet model SL1, was purchased. This device is shown schematically in Figure 94 and the actual device is shown in Figure 95. This light source connects fibers coupled with SMA905 connectors and the tungsten halogen incandescent bulb has a 2800K color temperature. The black body emission from an object at 2800K is shown in Figure 99 but this is not the actual spectral emission curve for the light source. The spectral emission of the source is affected by the spectral attenuation of the quartz glass surrounding the incandescent bulb. The actual spectral emission curve of the light source is difficult to quantify absolutely, but doing this is also unnecessary.

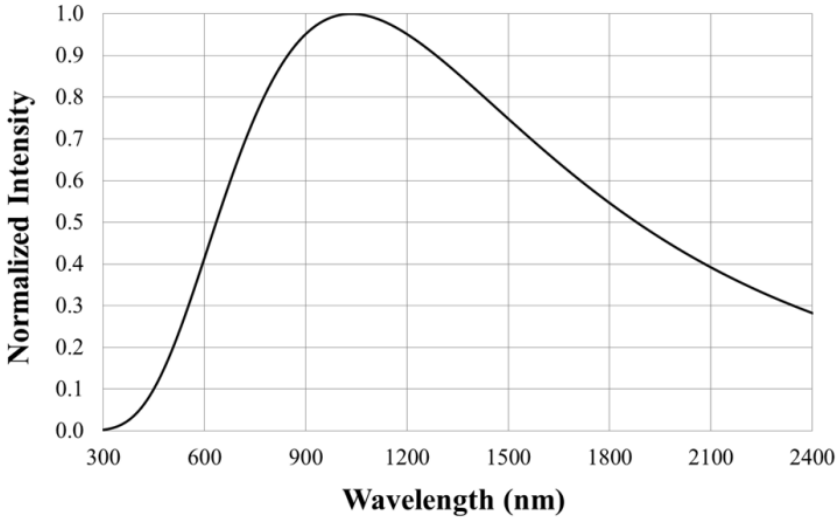

Figure 99: Normalized Emission from a 2800K Black Body Emitter

8.3 Software Used for Setup & Data Collection [2]

Several pieces of custom and manufacturer-supplied software were used in this experiment. WatView and EZ-Zone Configurator, both from Watlow, were used to interface with the safety limit monitor and the PID controller, respectively. WatView allowed the CAS200 to be configured with a computer over a serial connection. WatView also enabled the CAS200 to be used to log temperature and power data over the serial connection. WatView is not Windows 7 compatible, but by installing the necessary Visual Basic runtime libraries, the software will function with some occasional bugs. EZ-Zone Configurator was used to setup the PID controller and the remote user interface. WatView is an end-of-life product and no additional updates will be provided by Watlow. EZ-Zone Configurator is an active product and updates are occasionally provided on Watlow's website.

The multiplexers, spectrometers, and the power meter each came with manufacturer supplied control applications. These pre-compiled applications did not interface with each other and were insufficient for reliable or automated data collection. A custom application was written in LabVIEW, complete with a graphical user interface, which connects all of the optical measurement equipment and allows data to be collected automatically. The software architecture is based on a standard state machine with a single event handler. A simplified block diagram of the application execution is shown in Figure 100. Application execution is restricted by enabling or disabling user controls based on the state of program execution. Screen shots of the application GUI are shown in Figure 101, Figure 102, and Figure 103.

This application was developed specifically for this project and data collected using the application was compared against data collected using manufacturer supplied software. This application still relies on manufacturer supplied driver files. The spectrometer drivers provided by StellarNet are not currently 64-bit compatible and must be used with a 32-bit Windows operating system. Updated drivers and BIOS updates may become available from StellarNet or Newport.

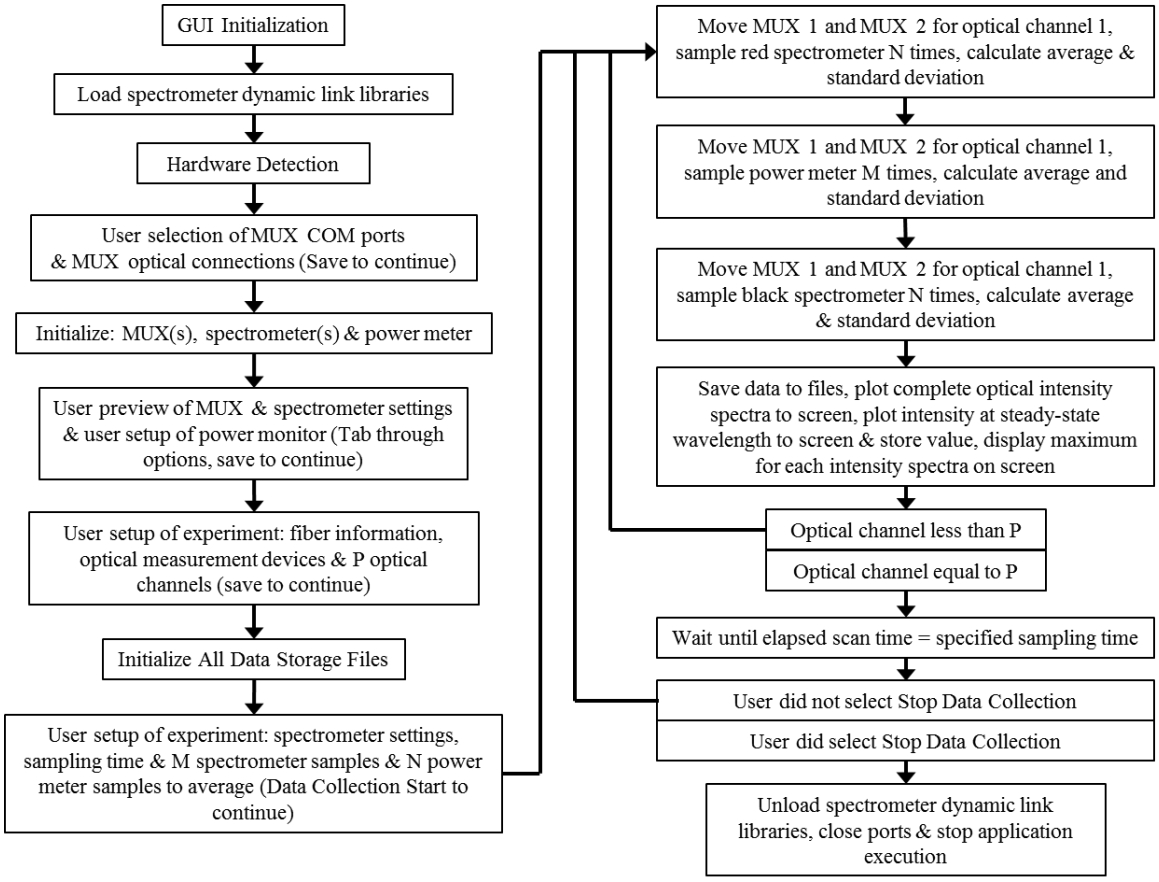

Figure 100: Block Diagram of Optical Data Acquisition Program Execution

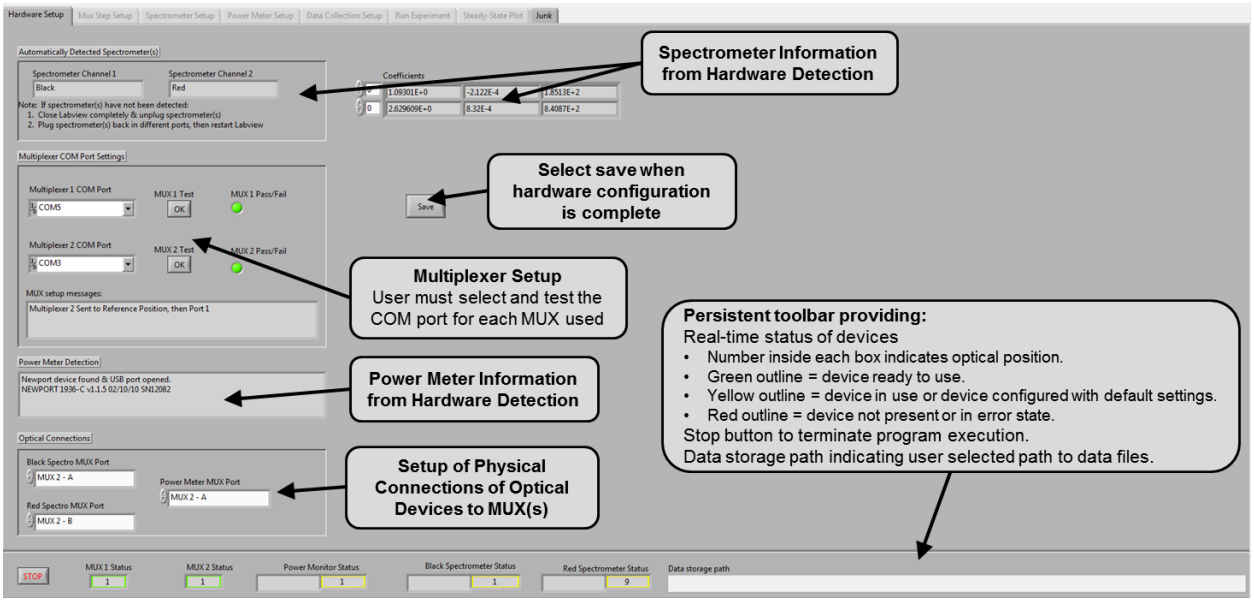

Figure 101: Hardware Setup Tab in Optical Data Acquisition Application

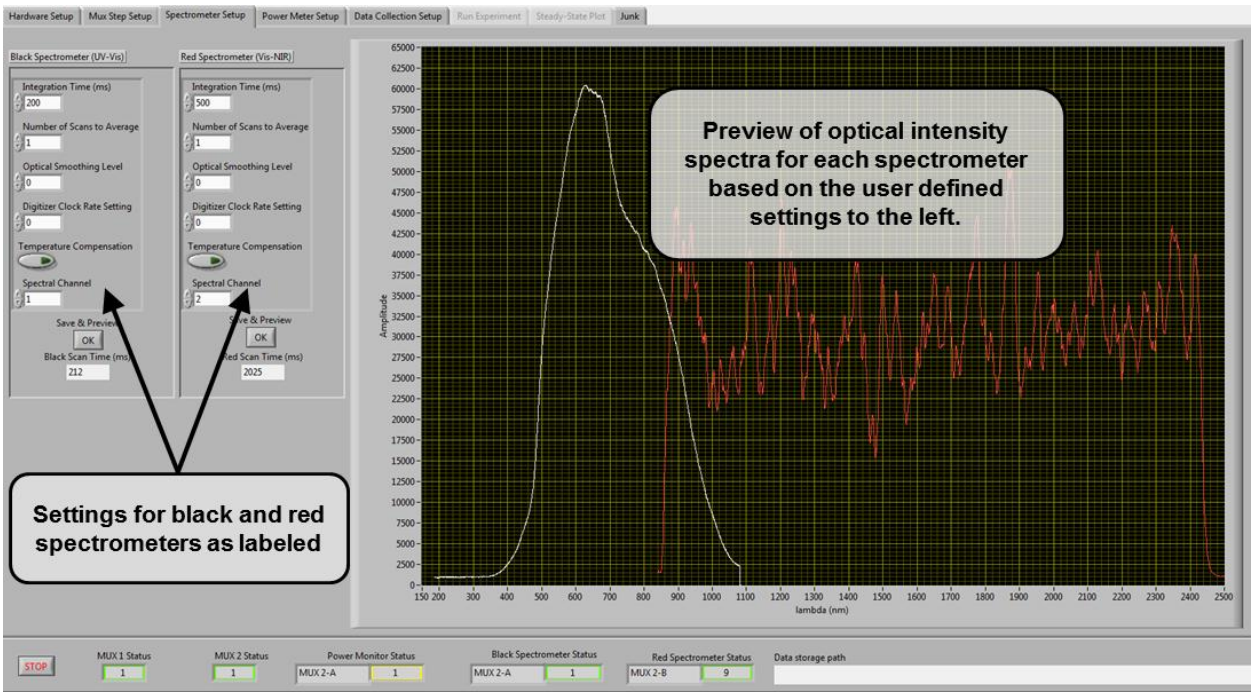

Figure 102: Spectrometer Setup & Preview in Data Acquisition Application

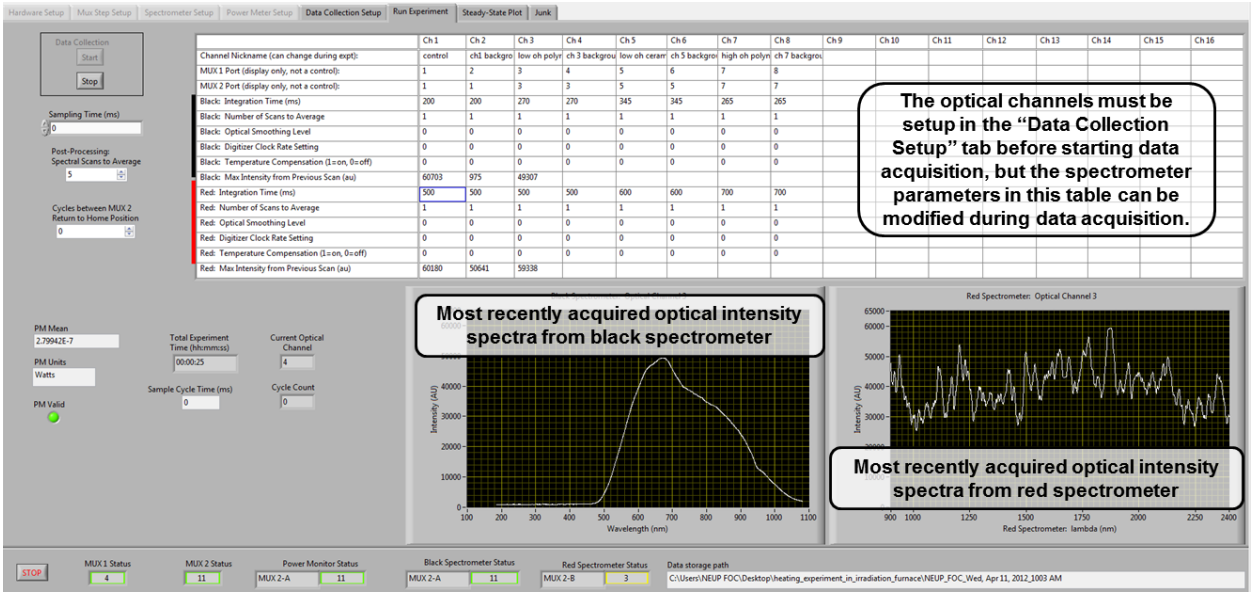

Figure 103: Run Experiment Tab in in Optical Data Acquisition Application

8.4 Optical Fiber Spooling Mechanism [2]

Long lengths of bare optical fiber are difficult to handle and, unlike metal wire, optical fiber does not plastically deform when bent. In this experiment, many meters of delicate optical fiber needed to be spooled onto fragile fiber holders, as shown in the middle of Figure 79. In addition to spooling the fiber, the quantity of fiber spooled onto the fiber holder needed to be precisely measured. It was also important to avoid adding any torsional stress to the fiber or getting the fiber

dirty in the spooling process. Because the long fiber lengths were tedious and difficult to manage by hand, a device was fabricated to mechanize the loading and measuring of optical fiber.

Several iterations of fiber spooling mechanisms were designed and fabricated and the final mechanism is shown in Figure 104. Three spools are used to hold fiber after it is transferred off of the bulk spool. The diameters of the spools are known and the length of the spooled fiber is determined by counting rotations of each spool. The two black spools in Figure 104 hold fiber that is used to lead-in and lead-out of a furnace at the bottom of a dry-tube. The center white spool holds fiber that will eventually be loaded onto a quartz fiber holder and placed in a furnace. For an experiment in the Co-60 irradiator, for example, 9.8 meters of fiber are spooled onto each of the spools which is about 32 rotations per spool.

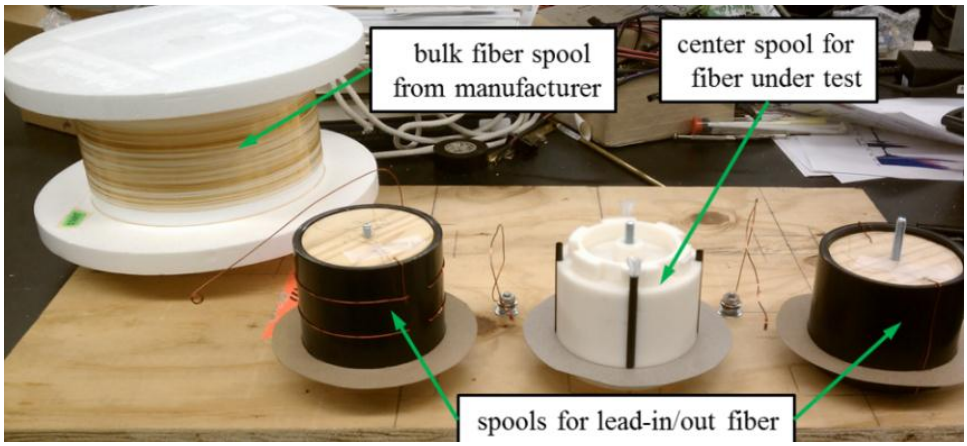

Figure 104: Fiber Spooling Mechanism

8.5 Setup of Thermal-Only Multimode Experiments without Radiation

The goal of this project was to determine the performance of silica optical fibers in a high temperature reactor radiation environment. Optical performance was quantified by measuring broadband optical transmission through the fibers as the fibers were subjected to different temperatures and radiation environments. Several experiments were conducted to expose the optical fibers to various combinations of thermal and radiation environments with the goal of separating the degradation effects. A list of the experiments completed for the high temperature only, multimode fiber attenuation part of this project is shown in Table 10.

	Date Started	Duration (hours)	Location	Maximum Temperature (°C)	Radiation Environment
First high temperature experiment	1/27/2011	5	W470 Scott Lab	1000	no radiation
Second high temperature experiment	6/21/2011	15	W470 Scott Lab	1000	no radiation
Third high temperature experiment	10/16/2011	622	W470 Scott Lab	1000	no radiation
Fourth high temperature experiment	3/26/2012	532	W470 Scott Lab	1000	no radiation

Table 10: High Temperature Fiber Experiments (no radiation)

Initial high temperature experiments were conducted without radiation so that the effects of high temperature could be determined and to gain operation experience. The first two high temperature experiments identified necessary improvements in experimental procedures, equipment, and software that were implemented in following experiments. Because the optical fibers did not break, these experiments also provided confidence that the fibers would survive mechanically at high temperature. Details of the experimental setup for the second, third and fourth high temperature experiments are presented in this chapter and quantitative results for the third and fourth experiments are presented in a following chapter. Quantitative results are not presented for the first two high temperature experiments.

Four experiments were conducted in furnaces at Scott Laboratory. The first three experiments used a commercial box furnace and the fourth experiment used the reactor irradiation furnace. During the first experiment, 26 meters of low-OH silica fiber (Polymicro FIP200220240) were spooled on a quartz fiber holder and were heated to 1000°C. Data acquisition was attempted using the individual manufacturer supplied applications for each piece of optical instrumentation. During this experiment it was determined that data could not be collected effectively using the manufacturer supplied software and that new data acquisition software needed to be written. This experiment did not provide any useful quantitative data, but it did show that optical fibers spooled on the custom quartz fiber holders would survive mechanically after removal of the polyimide coating.

8.5.1 Second High Temperature Experiment without Radiation

The second experiment included 8.4 meters of low-OH silica fiber (Polymicro FIP200220240), spooled on a quartz fiber holder and heated to 1000°C with the temperature profile shown in Figure 105. An additional length of fiber was used to lead into and lead out of the furnace. The optical equipment was setup as shown in Figure 106. Only one optical fiber was tested and it was directly connected to the broadband light source. Data acquisition and control of the optical instrumentation was accomplished using an early version of custom software written in LabVIEW. Optical transmission measurements were recorded throughout the experiment.

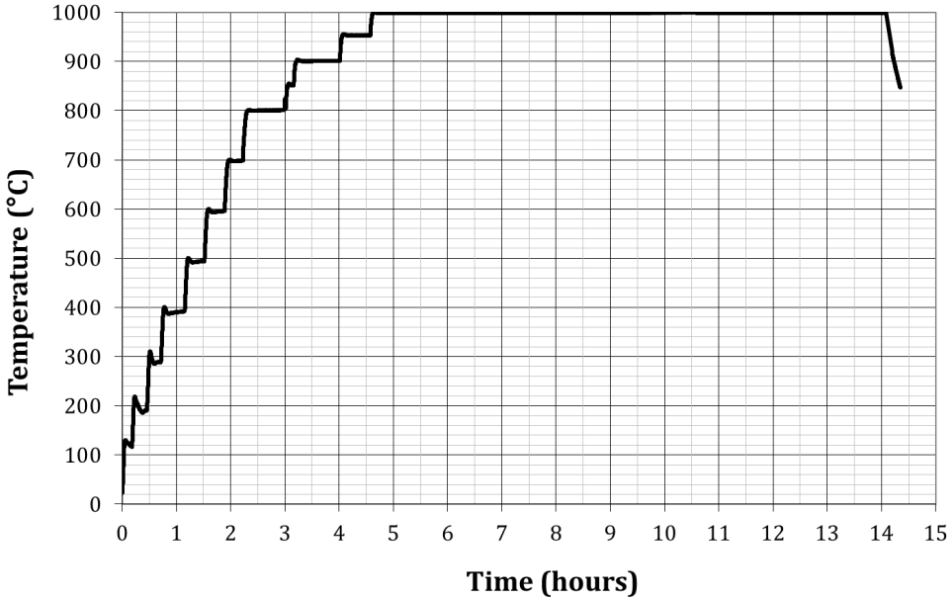

Figure 105: Temperature Profile for Second Thermal-Only Experiment

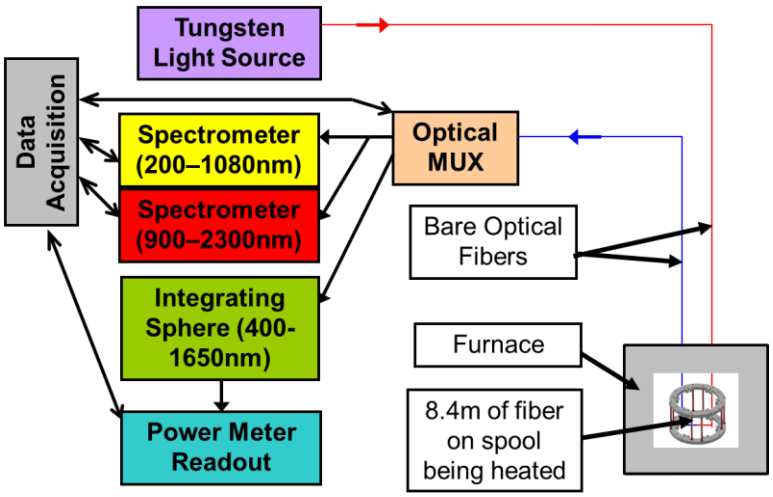

Figure 106: Equipment Setup for Second Thermal-Only Experiment

In addition to quantitative results, this experiment led to several changes in the experimental setup and data acquisition software. During this experiment, several optical transmission measurements were averaged in hardware and only the averaged spectrum was recorded during each optical scan. Unfortunately the spectrometers do not calculate the standard deviation of the averaged measurements which made it impossible to calculate uncertainty in this data. The data acquisition software was revised to acquire and average several measurements in software which allowed standard deviations of the transmission intensities to be calculated. In this experiment, the transmission spectrum was acquired, displayed and saved every 10 seconds throughout the experiment but a time history of the transmission was not displayed to the user. Without a transmission intensity history, it was not possible to determine when the induced attenuation had reached steady state and when to change the experimental conditions. The data acquisition software was revised to include a time history of the intensity values for each optical channel at one user-selected wavelength.

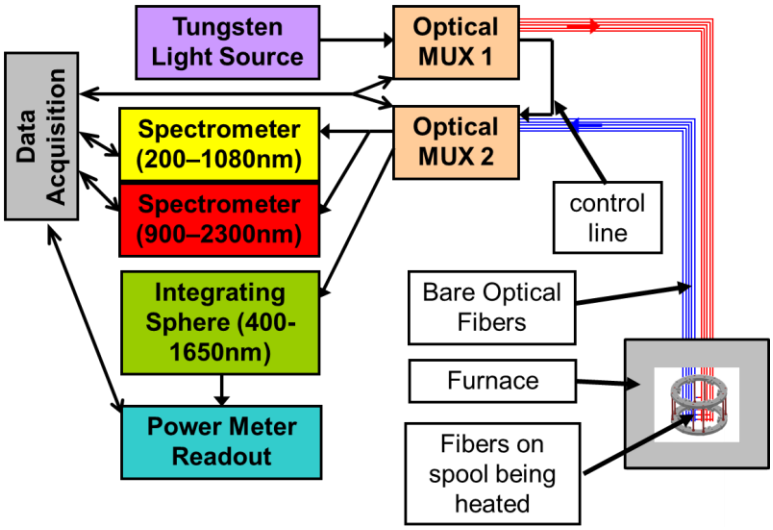

Figure 107: Equipment Setup for Third Thermal-Only Experiment

During this experiment the light source was directly connected to the fiber being tested, as shown in Figure 106. This arrangement inconveniently required the light source to be manually turned off for measurements of the background noise to be recorded. Also, the arrangement shown in Figure 106 prevented the use of a control line to monitor changes in light source intensity. In the setup for all following experiments, the light source was also multiplexed as shown in Figure 107. This arrangement enabled a control line fiber to be added and also allowed a background measurement to be automatically taken for each channel immediately following the active measurement without requiring the light source to be switched on and off.

8.5.2 Third High Temperature Experiment without Radiation

The third thermal-only experiment included two 7.39±0.3 meter lengths of optical fiber, spooled on a quartz fiber holder and heated with the temperature profile shown in Figure 108. The fibers being tested were a low-OH silica fiber (Polymicro FIP100120140) and a high-OH silica fiber (Polymicro FVP100120140). Both of these optical fibers had a pure silica core with fluorine doped silica cladding and, to reduce bend losses, were smaller in diameter than the fiber tested previously. The optical equipment for this experiment was setup as shown in Figure 107. During this experiment, the optical transmission at 1300nm was monitored to determine when the attenuation reached steady state at a particular temperature.

As shown in Figure 108, the temperature was initially increased to 500°C to thermally remove the polyimide coating on the optical fibers and was then returned to room temperature. The fiber was maintained at each subsequent temperature until the transmission at 1300nm appeared to be at steady state for both fibers. Before increasing the temperature, the fiber was cooled to room temperature so that the permanent and transient thermal effects could be observed. Quantitative data from this experiment is presented in the results chapter.

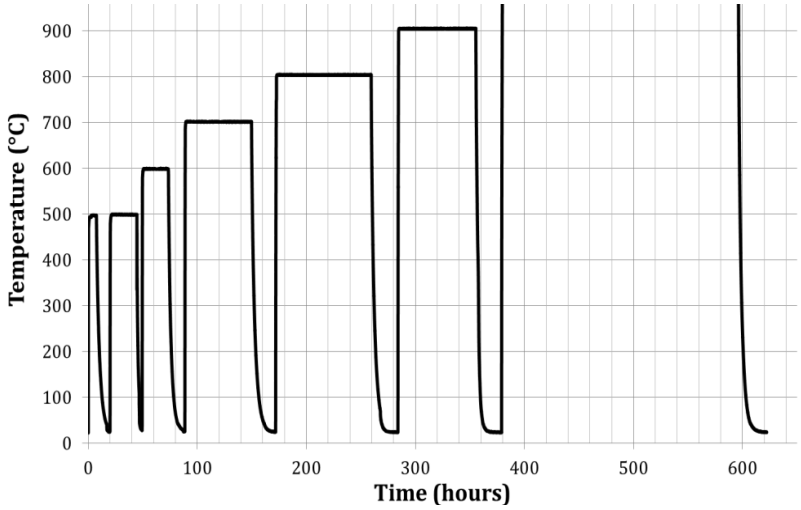

Figure 108: Temperature Profile for Third Thermal-Only Experiment

8.5.3 Fourth High Temperature Experiment without Radiation

The fourth thermal-only experiment included three 9.85±0.3 meter lengths of silica optical fiber, spooled and heated with the temperature profile shown in Figure 109. The fibers being tested were two low-OH silica fibers (Polymicro FIP100120140 & CeramOptec WF100110125P37) and a high-OH silica fiber (Polymicro FVP100120140). The Polymicro fibers both have a pure silica core and fluorine doped silica clad. The CeramOptec fiber has a germanium doped silica core and

fluorine doped silica clad. During this experiment, the optical transmission at 800nm was monitored to determine when the fiber had reached a steady state condition at a particular temperature.

The optical equipment for this experiment was setup as shown in Figure 107 but the reactor irradiation furnace and its accompanying power supply were used instead of the commercial box furnace. At the beginning of this experiment the PID controller in the power supply had not been configured and the furnace temperature was set by manually adjusting the duty cycle of the power controller. Unfortunately the 208VAC line voltage in Scott Laboratory varied resulting in the poor temperature control shown in Figure 109. Around 302 hours into the experiment, the PID controller was configured to automatically control the furnace power to account for variations in line voltage. This improved the temperature control but the variable convective losses in the room still caused undesirable temperature fluctuations. After this experiment was completed the PID controller was reconfigured to automatically control the furnace temperature. Quantitative data from this experiment is presented in the results chapter.

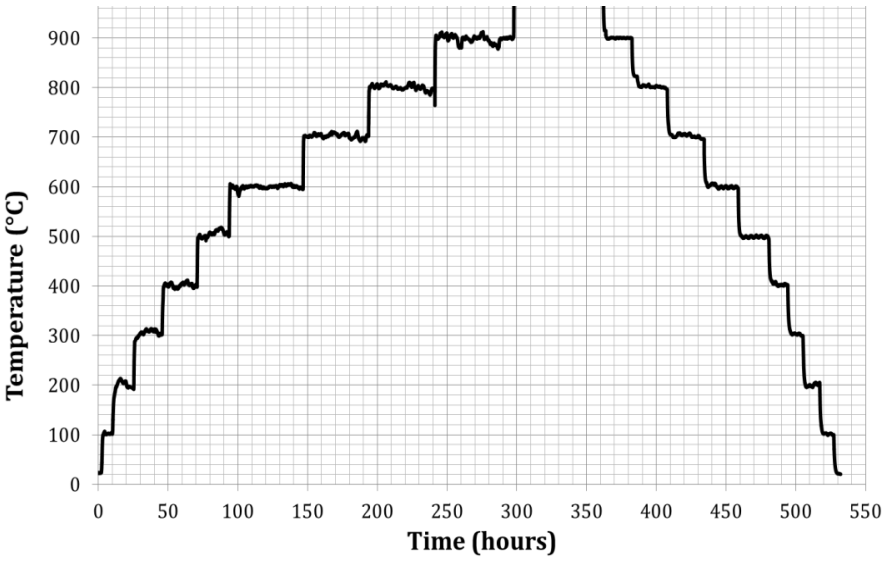

Figure 109: Temperature Profile for Fourth Thermal-Only Experiment

8.6 Results from Thermal-Only Multimode Experiments without Radiation

Heated experiments without radiation were completed to determine the effect of high temperature on the optical transmission of the tested fibers [15]. Results from the 3rd and 4th heated experiments are presented and discussed in this section. For the 4th heated experiment, broadband results are shown for each fiber at several temperatures and the attenuation increase with time is shown for several low-attenuation wavelengths. For reference, the temperature profile of the 4th heated experiment is shown on each time dependent plot. The attenuation increase at 850nm, 1300nm and 1550nm is plotted for the low-OH fibers because these wavelengths are used in commercially available optical instrumentation. 1300nm and 1550nm are not plotted for the high-OH fiber because the large intrinsic attenuation in the high-OH fiber makes those wavelengths unusable. Results from the 3rd heated experiment are shown to highlight the effect of operation at 900°C and 1000°C.

8.6.1 Results from Heated Experiments up to 900°C

Figure 110 shows the broadband attenuation increase in the low-OH Polymicro fiber at the four temperatures and times indicated. The as-manufactured concentration of NBOHCs in this fiber indicates that it was produced with an oxygen excess. Hydrogen diffusing into the fiber from the decomposing polyimide coating bonds with pre-existing NBOHCs, increasing the Si-OH concentration. Prominent absorption peaks caused by vibrational modes of Si-OH and Si-O-Si are observed in Figure 110 around 950nm, 1250nm, and 1400nm. The tails of these broad inhomogeneous peaks increase the attenuation at 1300nm and 1550nm. The tails of the fundamental Si-OH peak and a combination mode of Si-OH and Si-O-Si cause the attenuation increase starting at 1800nm. Higher order vibrational modes do not have prominent peaks but still cause increased attenuation at wavelengths tabulated in Table 2.

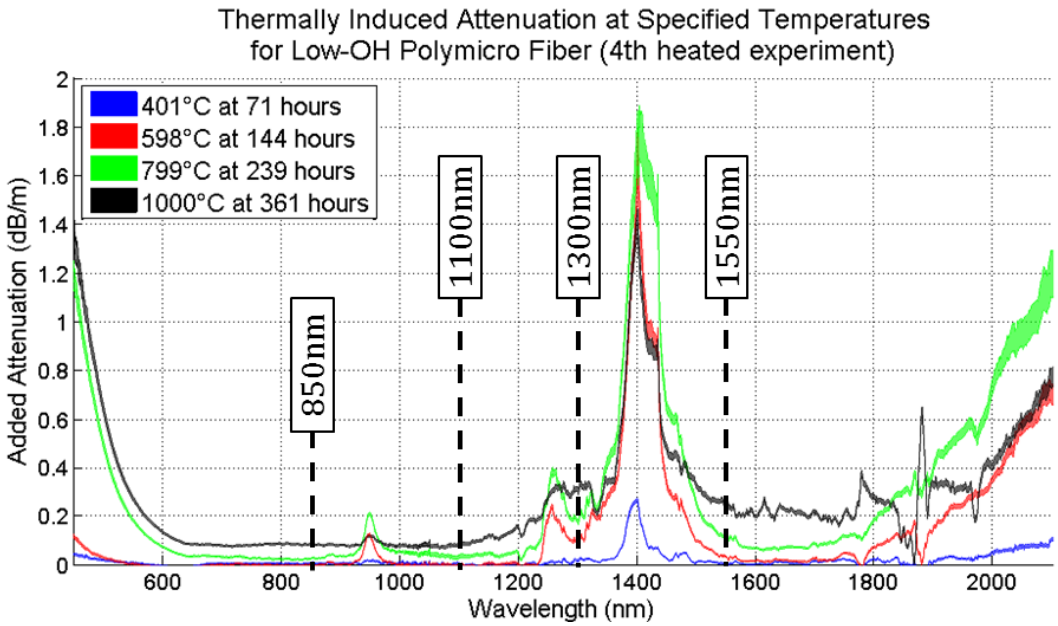

Figure 110: Broadband Thermal Attenuation in Low-OH Polymicro Fiber (line width indicates ±1σ, pure silica core, F-doped silica clad, FIP100120140, 4th heated experiment)

The absorption increase below 600nm in Figure 110 is a tail from a structural defect, or a combination of structural defects, that cannot be explicitly identified with the data acquired in this work. It is likely that the defects being formed are typical oxygen excess defects. Even though the structural defect, or defects, causing the attenuation below 600nm cannot be explicitly identified, the sharp increase in attenuation between 600°C-800°C indicates the onset of increased oxygen mobility.

The Si-OH concentration increase below 600°C is caused by the large initial concentration of NBOHC defects in the as-manufactured fiber bonding with hydrogen. Hydrogen readily bonds with NBOHCs to form Si-OH and the Si-OH concentration increases as the hydrogen migrates from the clad into the core. The Si-OH concentration continues to increase up to 800°C, and above 900°C the concentration starts to decrease as shown by the reduced height of the Si-OH absorption peaks at 1000°C in Figure 110.

Figure 111 shows the time evolution of the attenuation increase at 850nm, 1100nm, 1300nm and 1550nm in the low-OH Polymicro fiber. These wavelengths are also highlighted in Figure 110. Up to 300°C, the attenuation increase at these wavelengths is negligible and at 400°C

the attenuation increases at 1300nm and 1550nm. These temperatures correspond well with the manufacturer recommended maximum use temperature of 300°C with intermittent use to 400°C [112]. In Figure 111, at 500°C and around 75 hours, there is a temporary spike in attenuation attributed to decomposition of the polyimide coating. It is likely that the breakdown of the coating creates a non-uniform stress state along the fiber resulting in microbends and associated losses [6]. After the polyimide has completely decomposed the bare glass fiber can return to a minimal stress state without the microbend losses.

As shown in Figure 111, the attenuation at the four plotted wavelengths continues to increase between 400°C and 800°C. In both the 3rd and 4th heated experiments, the attenuation at 1300nm and 1550nm start to decrease at 900°C. Morimoto et al reported a maximum hydrogen release from fused silica around 900°C [51] and the decreased attenuation at 1300nm and 1550nm is caused by the decrease in Si-OH concentration.

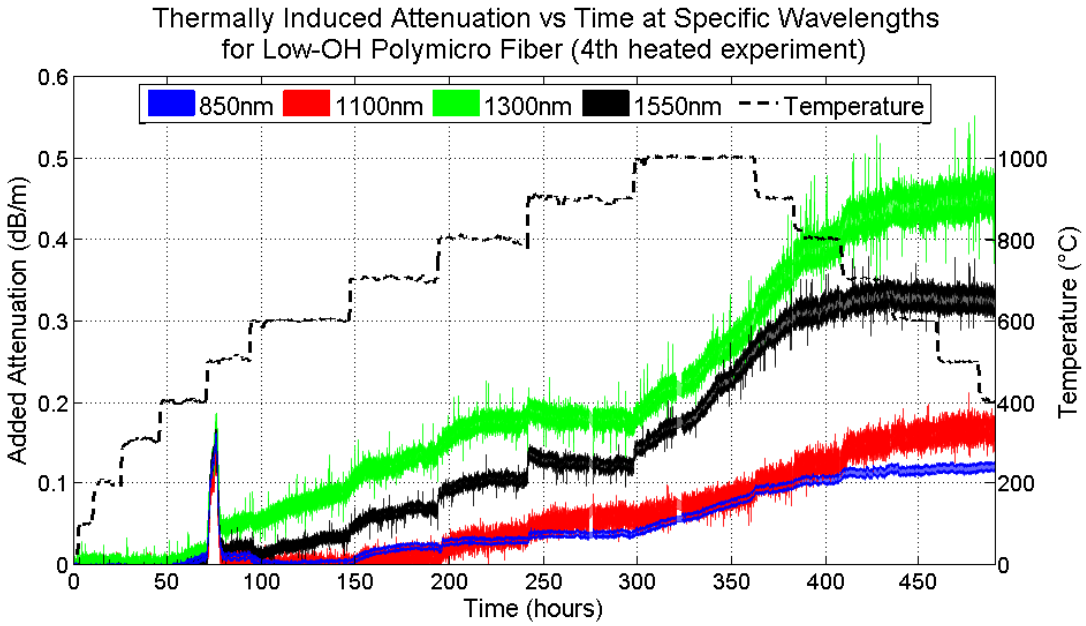

Figure 111: Time Dependent Thermal Attenuation in Low-OH Polymicro Fiber (line width indicates ±1σ, pure silica core, F-doped silica clad, FIP100120140, 4th heated experiment)

The fibers were kept at 900°C for 70 and 50 hours in the 3rd and 4th heated experiments, respectively. Figure 112 shows the broadband attenuation increase in the low-OH Polymicro fiber at the beginning, middle and end of the 70 hour 900°C exposure and also at the end of the 220 hour 1000°C exposure. At 900°C in the 3rd heated experiment, the added attenuation in low-OH Polymicro fiber reaches steady state for several wavelength ranges including 850nm, 1100nm, 1300nm and 1500nm. This indicates that optical instrumentation utilizing low-OH silica fibers could be used at 900°C continuously.

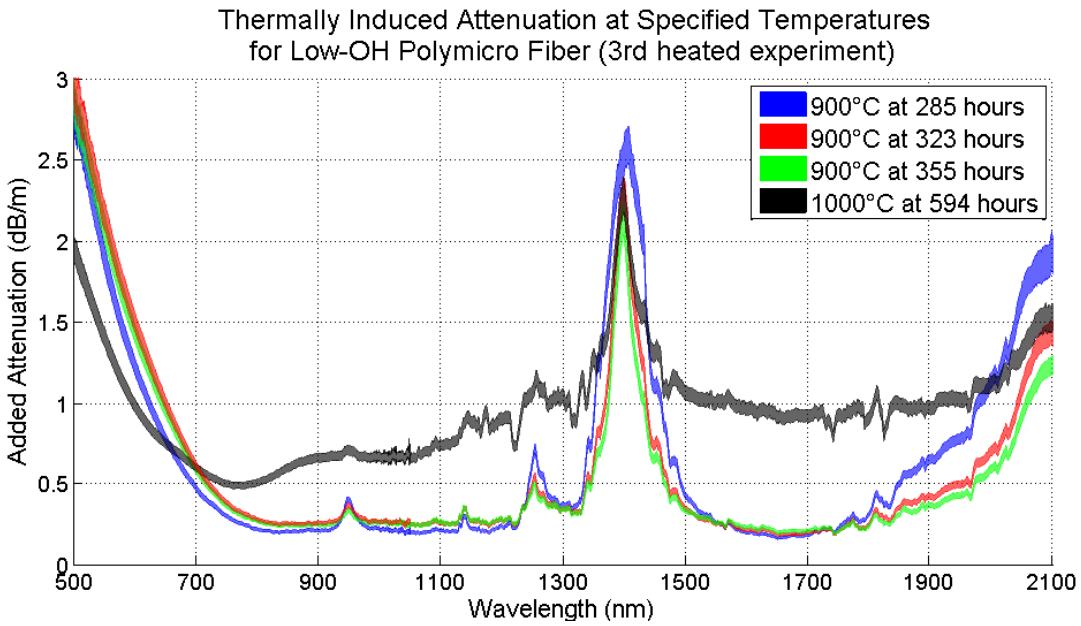

Figure 112: Broadband Thermal Attenuation at 900°C in Low-OH Polymicro Fiber (line width indicates ±1σ, pure silica core, F-doped silica clad, FIP100120140, 3rd heated experiment)

The finite hydrogen impurity concentration should result in the Si-OH concentration reaching steady state at temperatures below 900°C. If the Si-OH concentration reaches steady state, the attenuation increase at wavelengths affected by the Si-OH concentration (1100nm, 1300nm & 1550nm) should also reach steady state. As shown in Figure 111, the attenuation increase at 1300nm and 1550nm at 800°C between 225-250 hours appears to be reaching steady state. This would allow optical instrumentation using low-OH silica fibers to be used continuously up to and including 900°C. At 1000°C, the attenuation steadily increases at all four wavelengths plotted in Figure 111. The broadband attenuation increase at 1000°C does not reach steady state and is discussed later in this chapter.

Figure 113 shows the broadband attenuation increase in the low-OH CeramOptec fiber from the 4th heated experiment. Unlike the low-OH Polymicro fiber, the as-manufactured CeramOptec fiber had negligible intrinsic NBOHC defects and was probably manufactured with less oxygen than the low-OH Polymicro fiber and possibly an oxygen deficit. Because of the low initial concentration of NOBHCs, the Si-OH absorption does not increase substantially until the oxygen mobility increases between 600°C and 800°C. As shown in Figure 113, the attenuation increase at 400nm is small but the obvious tail indicates an increase in structural defect concentration affecting wavelengths below 400nm.

Figure 114 shows the time evolution of the attenuation increase at 850nm, 1100nm, 1300nm and 1550nm in the low-OH CeramOptec fiber. The temporary spike in attenuation around 75 hours is attributed to the thermal decomposition of the polymer coating. Because of the Si-OH concentration, the attenuation at 1300nm and 1550nm increases sharply at 800°C and decreases sharply at 900°C. Over the 50 hours at 1000°C, the attenuation at 1100nm and 850nm increases while the attenuation at 1300nm and 1550nm stays the same or decreases. This behavior is difficult to explain and additional testing at 1000°C may be needed. The possibility that optical instrumentation using 1300nm or 1550nm could operate continuously at 1000°C in this type of silica optical fiber is interesting.

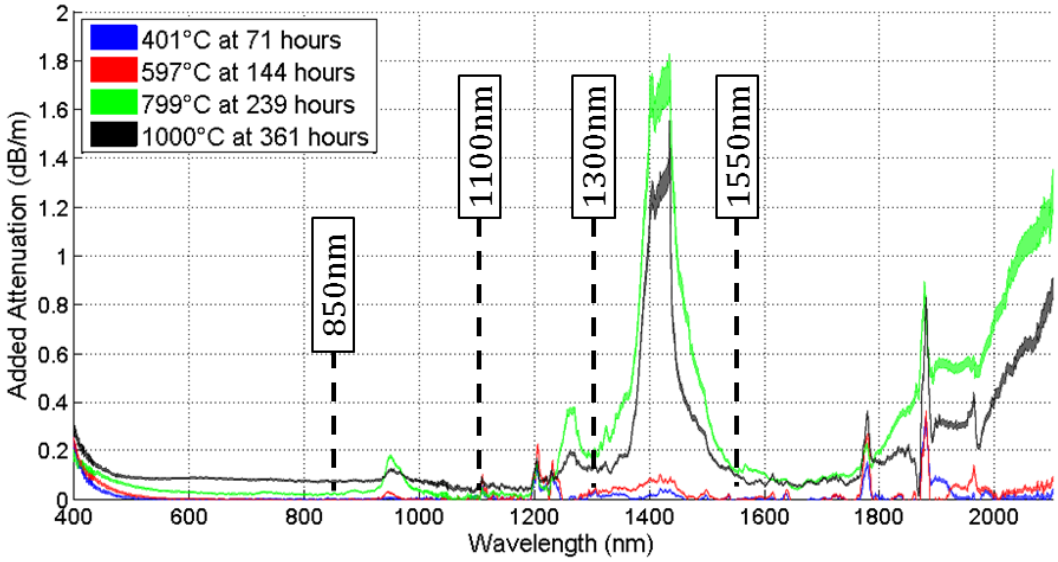

Figure 113: Broadband Thermal Attenuation in Low-OH CeramOptec Fiber (line width indicates ±1σ, Ge-doped silica core, F-doped silica clad, WF100110125P37, 4th heated experiment)

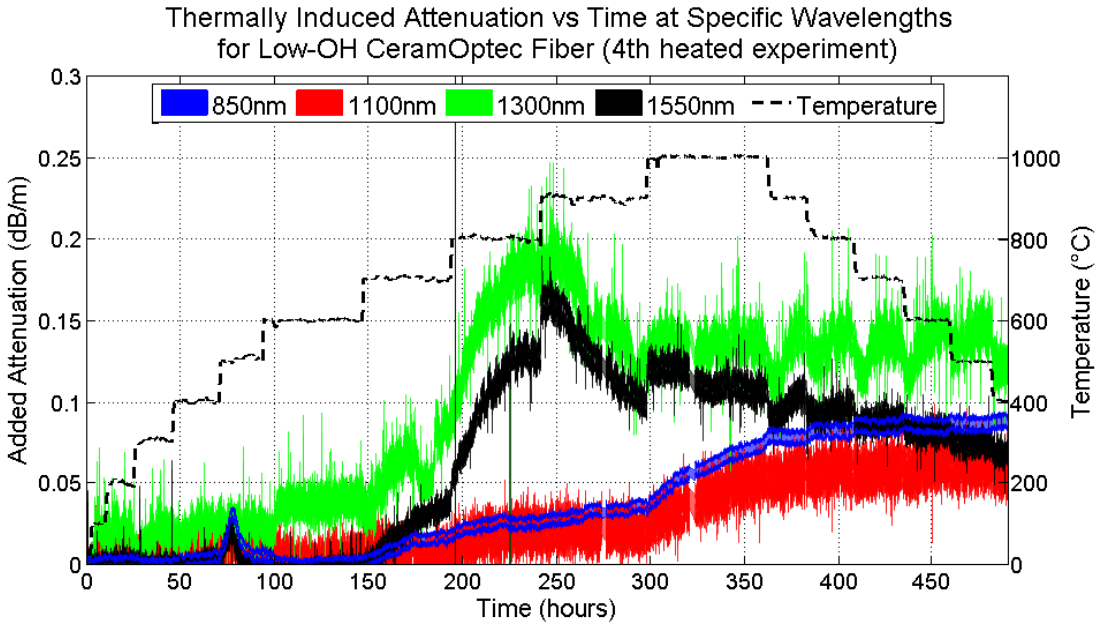

Figure 114: Time Dependent Thermal Attenuation in Low-OH CeramOptec Fiber (line width indicates ±1σ, Ge-doped silica core, F-doped silica clad, WF100110125P37, 4th heated experiment)

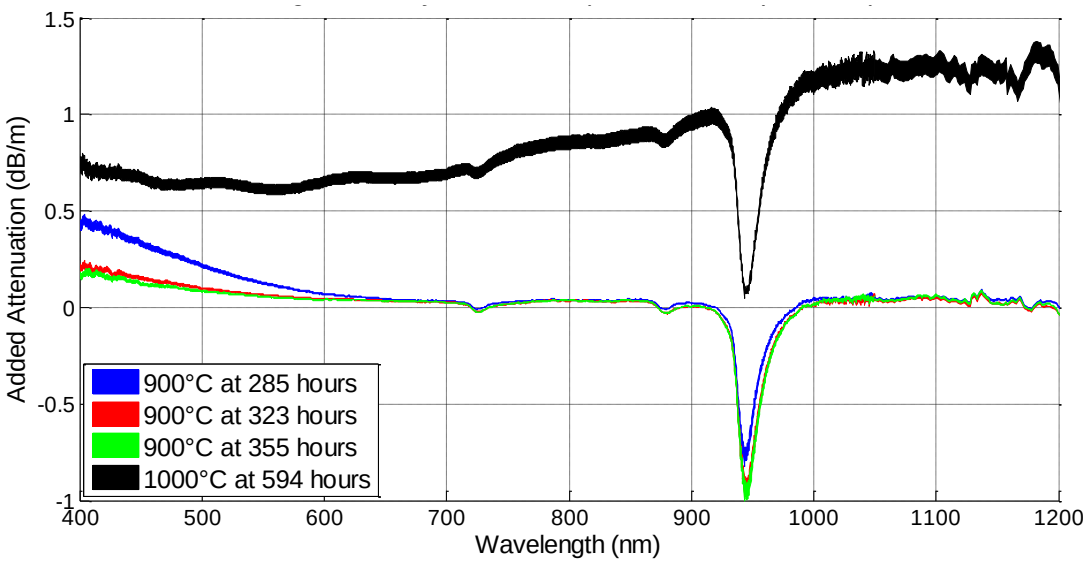

Figure 115: Broadband Thermal Attenuation in High-OH Polymicro Fiber (line width indicates ±1σ, pure silica core, F-doped silica clad, FVP100120140, 3rd heated experiment)

Figure 115 shows the broadband attenuation in the high-OH Polymicro fiber at the beginning, middle and end of the 900°C exposure, and at the end of the 1000°C exposure. The intentionally high hydrogen content in the as-manufactured fiber causes a high Si-OH concentration that makes this fiber unusable above 1150nm. The large hydrogen concentration reduces the intrinsic absorption caused by NBOHC defects in the low-OH Polymicro fiber making the high-OH fiber usable at lower wavelengths compared to the low-OH Polymicro fiber. The Si-OH concentration decreases as hydrogen diffuses out of the high-OH fiber resulting in the improved transmission at Si-OH absorption peaks, as shown in Figure 115.

8.6.2 Results from Heated Experiments at 1000°C

Figure 116 and Figure 117 show the broadband attenuation increase in the low-OH and high-OH Polymicro fibers from the 3rd heated experiment. The fibers were exposed to 1000°C for 214 hours after being exposed to 900°C for 70 hours. In general, the attenuation continued to increase over the entire spectrum for both Polymicro fibers and the attenuation does not appear to be approaching steady state. Similar broadband attenuation increase was starting to occur in the low-OH Polymicro fiber in the 4th heated experiment.

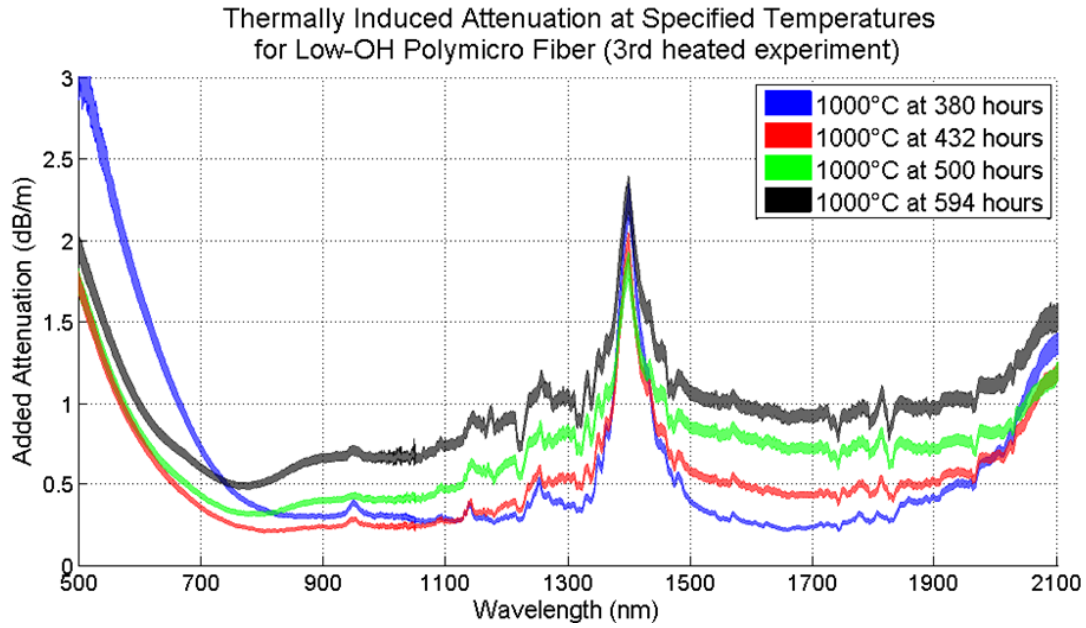

Figure 116: Broadband Thermal Attenuation at 1000°C in Low-OH Polymicro Fiber (line width indicates ±1σ, pure silica core, F-doped silica clad, FIP100120140, 3rd heated experiment)

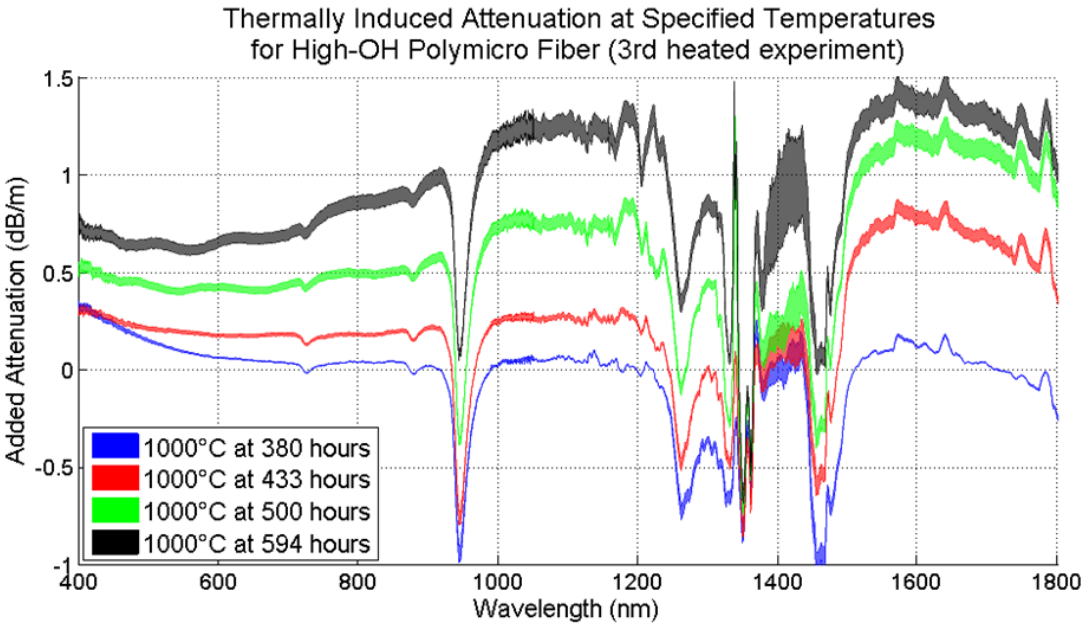

Figure 117: Broadband Thermal Attenuation at 1000°C in High-OH Polymicro Fiber (line width indicates ±1σ, pure silica core, F-doped silica clad, FVP100120140, 3rd heated experiment)

Unfortunately, direct experimental evidence of the cause of the broadband attenuation increase in the two Polymicro fibers could not be identified. Based on diffusion calculations of the fluorine and germanium dopants, it seems unlikely that significant dopant migration is occurring. In spite of the diffusion calculations, experimental evidence from Gibson indicates substantial fluorine

migration out of the clad of a silica optical fiber below 1000°C at a rate much faster than the diffusion coefficient predicts [55]. The fluorine migration effectively results in a reduced cladding thickness making the waveguide leakier. Experimental evidence by another researcher [27] [44] indicates the crystallization rate of silica starts to increase around 1000°C. Both crystallization of the fiber and a reduced cladding thickness could cause the broadband optical attenuation increase observed experimentally.

The low-OH CeramOptec fiber was not exhibiting a broadband attenuation increase over all wavelengths by the end of 60 hours at 1000°C in the 4th experiment (Figure 114). It is possible that additional high temperature exposure would have resulted in a similar broadband attenuation increase. If fluorine diffusion is responsible for the steady attenuation increase at 1000°C in the Polymicro fibers, it is possible that the combination of germanium and fluorine dopants in the CeramOptec fiber will extend the usable temperature of the CeramOptec fiber. Additional work is needed to understand the behavior of the three fibers at 1000°C, but from an applications perspective it is probably better to consider 900°C as the maximum continuous use temperature for silica optical fibers.

The Polymicro silica optical fibers cannot be used indefinitely at 1000°C. The rate of attenuation increase, however, was very slow. At 1550nm in the low-OH Polymicro fiber, the attenuation increased at a rate less than 0.004dB/m/hour and the attenuation limit of 1.1dB/m in the example application was only reached at the end of the 1000°C testing in the 3rd heated experiment. This indicates that optical instrumentation using silica fibers could withstand intermittent use at 1000°C.

8.7 High Temperature OBR Experiments without Radiation [97]

A thermal-only experiment was conducted with the OBR and a length of Corning SMF-28e+ optical fiber. A one meter length of Corning SMF-28e+ single-mode optical fiber was heated from room temperature to 1000°C according to the temperature profile shown in Figure 118 [97]. The amplitude of the optical power reflected back to the OBR was spatially resolved by the OBR. The fiber Amplitude (dB) was averaged for the central section of the heated region from 13.4 to 13.6 meters. Figure 118 shows the evolution of the average fiber Amplitude (dB) for the aforementioned spatial region along with the temperature-time profile.

Relative to the initial average fiber Amplitude (dB) of -130.25 dB at the beginning of the experiment, the maximum loss was just less than one decibel and occurred once the temperature was returned to room temperature around 72 hours into the entire experiment. The return to room temperature followed an 18 hours period at 900°C. The minimum average fiber Amplitude (dB) of -131.1 dB is much greater than the noise floor of -143 dB. Therefore, light continues to reach the heated region and a signal is measured from the heated region.

The data Bryan collected in this experiment was later reprocessed into a meaningful engineering quantity, specifically the temperature measured at a specific point in the optical fiber. The reprocessing was accomplished with proprietary software purchased from Luna Innovations. The temperature measured by the OBR using the Rayleigh backscatter from the plain Corning SMF-28e+ optical fiber is shown in Figure 119. This data shows that even though the attenuation in the optical fiber had not increased significantly, the intrinsic Rayleigh signature of the optical fiber is affected by exposure to 800°C. Between 200°C and 600°C, the linear factory-default strain-to-temperature calibration coefficients caused a discrepancy between the temperature measured by the OBR and the thermocouple. Higher order calibration coefficients were generated for the Corning SMF-28e+ to reduce this error. Based on additional thermal-only OBR experiments completed at OSU, above 700°C the OBR temperature data taken with the Corning SMF-28e+ fiber cannot be reprocessed into temperature measurements with the current reprocessing method.

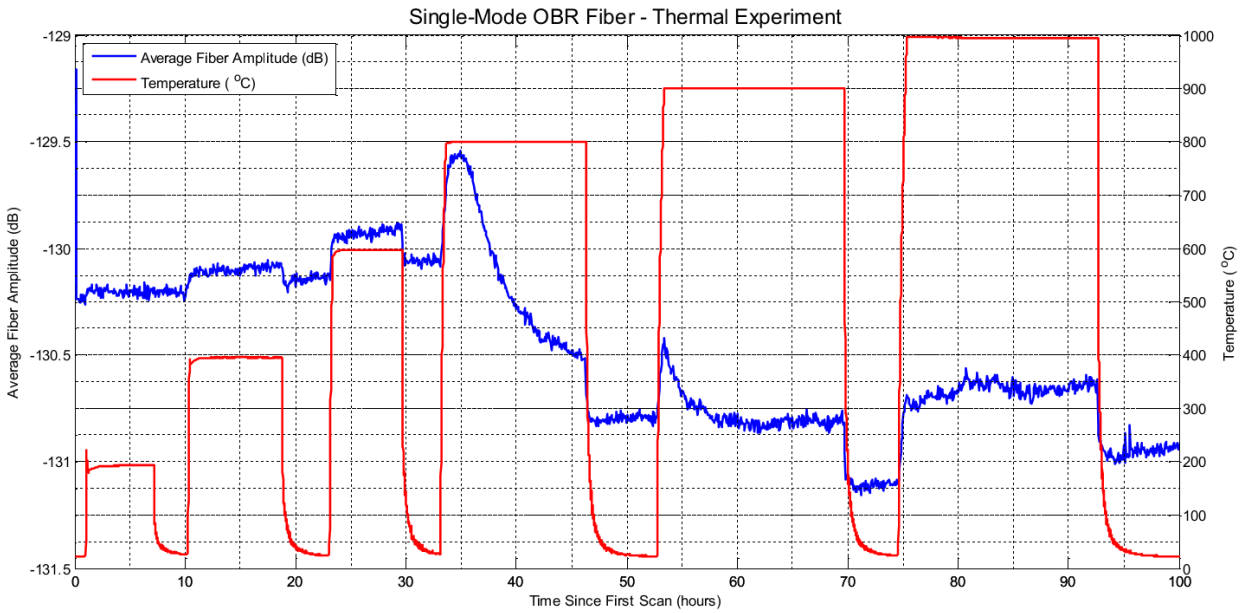

Figure 118: Average optical power returned from single-mode OBR fiber [97]

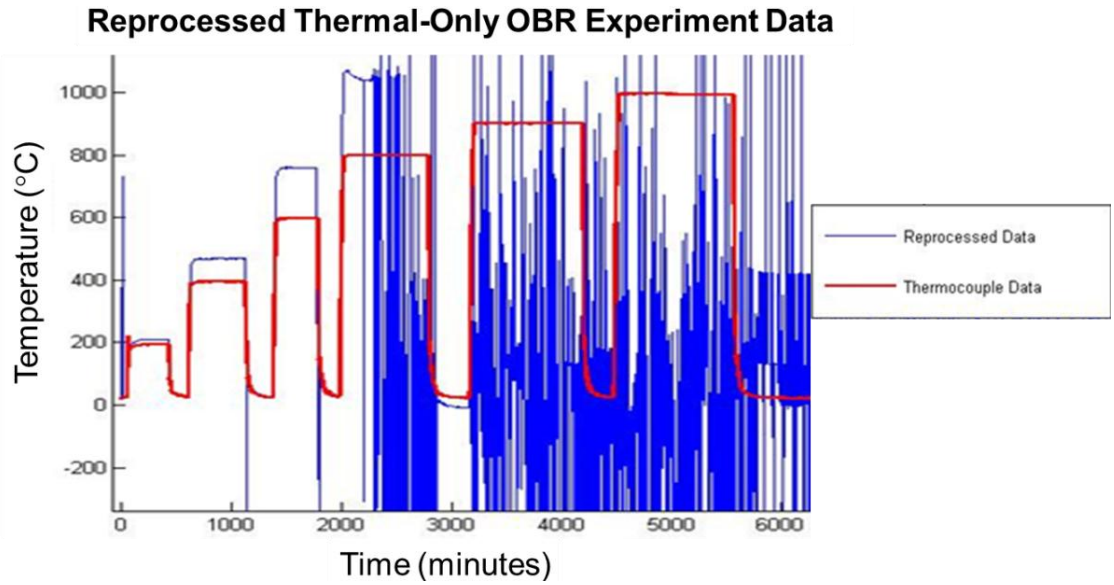

Figure 119: Reprocessed OBR Thermal-Only Experiment Data

Additional thermal-only experiments were completed with the OBR using the intrinsic Rayleigh scatter of the Corning SMF-28e+ singlemode fiber for distributed temperature sensing. These experiments were completed after Bryan's graduation and are not in his thesis. The purpose of one of these experiments was to more closely determine the upper temperature limit of the distributed sensing using Rayleigh backscatter and to determine the necessity of removing all of the polymer coatings from the optical fiber prior to heating. In previous OBR experiments, all of the protective polymer coatings were mechanically stripped from the singlemode fiber. This process left the optical fiber fragile and made loading the fiber into furnaces difficult. If it were not detrimental to skip removing the polymer coatings, future experiments would be simplified.

Figure 120 shows some additional experimental results from the OBR testing. Two short lengths of Corning SMF-28e+ were heated in a box furnace with the temperature profile shown in Figure 120. Between 300°C and 600°C, the temperature measured by the OBR is higher than the reported temperature from the thermocouple. It is likely that calibration coefficients relating strain to temperature for this optical fiber could be improved to remove this offset. At 700°C, however, it appears that the intrinsic defects used by the OBR to measure strain are starting to degrade and at 750°C it is clear that the OBR is no longer measuring the correct temperature. After the intrinsic defect distribution in the optical fiber changes from the initial reference distribution, the OBR cannot correctly calculate the change in strain in the optical fiber.

An attempt was made to redefine the reference distribution to a room temperature scan following a several hours at 800°C. It was hoped that the re-defined reference distribution of intrinsic defects would allow the OBR to correctly calculate temperatures from data collected at the subsequent 900°C heating, but unfortunately this was not the case.

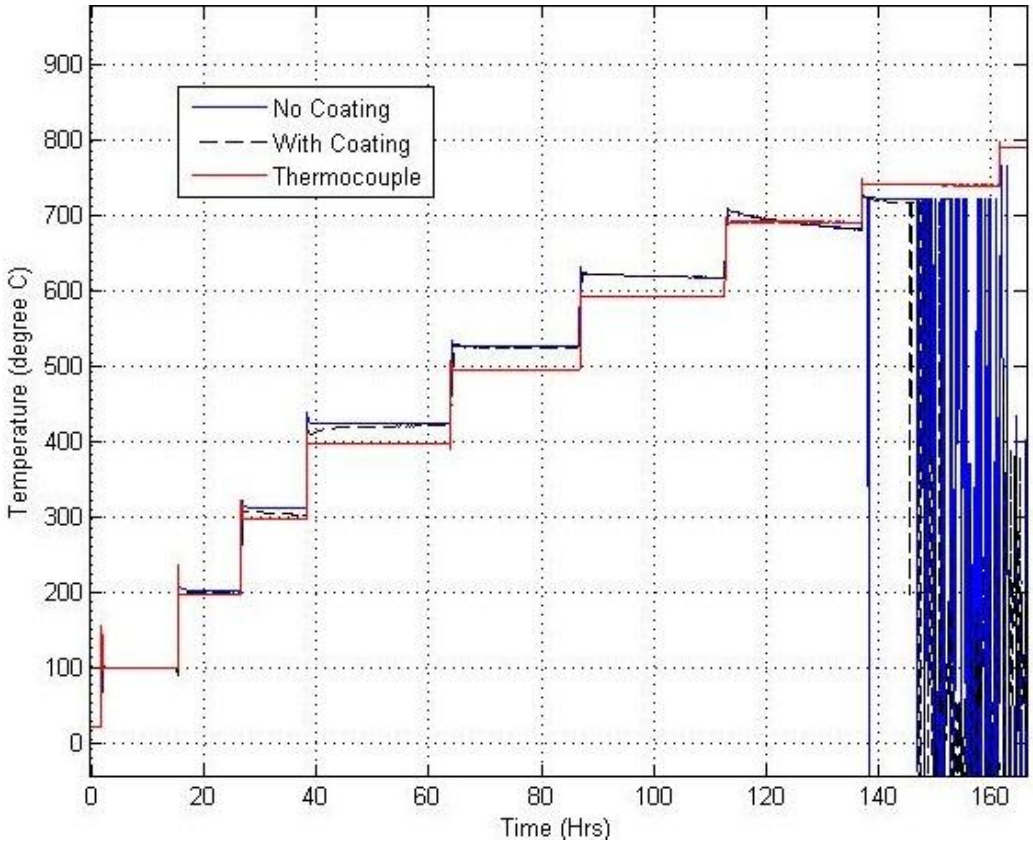

Figure 120: Additional Thermal-Only OBR Results

8.8 Summary of Heated Experiments

Three multimode and one singlemode silica optical fibers were tested in air to 1000°C and survived optically and mechanically. Based on the results of these experiments, silica optical fibers can be used continuously to 900°C. At 1000°C, the broadband attenuation increase in the Polymicro fibers allows intermittent use at 1000°C but precludes continuous use at this temperature. The cause of the increased attenuation at 1000°C has not been explicitly determined but is probably caused by crystallization of the silica, dopant diffusion or a combination of these two effects.

Additional work to determine the cause of the broadband attenuation increase at 1000°C is proposed for future work.

The increased attenuation in the visible and IR range was primarily caused by vibrational absorption from increased Si-OH concentration. Based on research published by Rose and Bruno, thermal decomposition of the polymer coating was the primary source of hydrogen into the silica fiber and humidity from the air had little effect [44]. Removing the polymer coating chemically instead of thermally would eliminate the source of hydrogen partly responsible for the increased Si-OH attenuation. After the polymer coating has been removed, however, the fibers are fragile and are a challenging to handle. Additional testing of silica optical fibers coated with metal instead of polyimide is proposed for future work.

While silica optical fibers survive optically and mechanically at high temperatures, the intrinsic or extrinsic optical features used as the sensing mechanism must also survive. The OBR can measure strain in a silica fiber by comparing the spatial distribution of intrinsic defects in a strained state to the distribution of intrinsic defects in an initial reference state. Using the thermal expansion coefficient of the optical fiber, the strain can be related back to temperature. In the thermal only OBR experiments, the intrinsic features of the Corning SMF-28e+ started changing around 700°C and invalidated the initial reference calibration data. Attempts to recalibrate the heat-affected optical fiber were not successful.

Chapter 9. Task I [2] [97]

9.1 Deliverable

Setup fiber transmission test facility and rig for in-situ testing of fibers in OSU Research Reactor. Test fiber using Luna Innovations' Optical Backscatter Reflectometer (OBR) at low temperatures. Process data and compare with results of modeling. Test fiber at high temperatures in OSURR.

9.2 Introduction [2]

The purpose of this work was to experimentally investigate the change in attenuation in silica optical fibers in a high temperature reactor radiation environment. The goal of this work is to determine the feasibility of extending commercially available optical instrumentation to this harsh environment. A generic schematic of an optical measurement system using intrinsic fiber Bragg grating (FBG) temperature sensors is shown in Figure 121. Photons emitted by the transmitter travel in the silica fiber toward the FBGs. Each FBG is etched into the silica fiber with a specific grating spacing to reflect photons within a specific wavelength range back to the receiver in the optical sensor interrogator. Temperature variation at each FBG slightly changes the grating spacing and shifts the reflected wavelength allowing the temperature at that FBG to be determined. Using a variable wavelength laser as the transmitter enables multiple discrete FBGs in a single silica fiber to be interrogated. The schematic in Figure 121 indicates intrinsic FBG temperature sensors, but FBG sensors can be designed to measure other quantities. In addition, FBG sensors were convenient for this example but optical sensor types other than FBGs are commercially available.

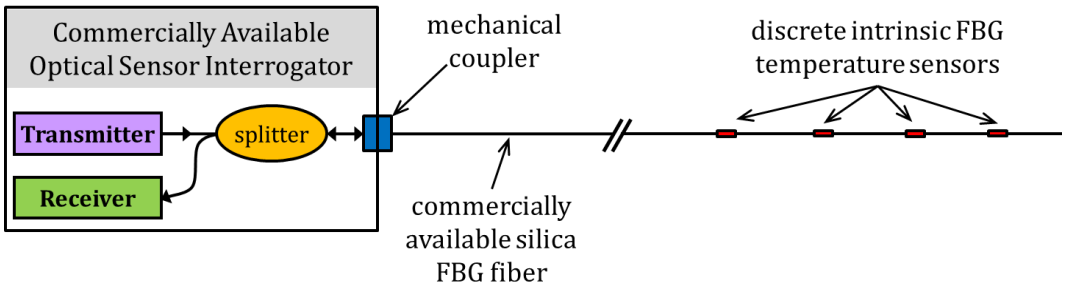

Figure 121: Optical Instrumentation for Distributed Measurements with FBGs

The temperature measurements made with the described system are dependent on measured wavelength shifts and are not dependent on the intensity of the transmitted signal. However, the returning signal reflected back from each FBG must be above the minimum sensitivity of the receiver. Photons emitted by the transmitter can be lost from the system at mechanical connections, fiber splices and by attenuation in the silica fiber. In addition, each FBG does not reflect all of the optical power in its specific wavelength range. The number of mechanical couplings, the transmitter power, the receiver sensitivity, the FBG reflectivity, and the total attenuation in the silica fiber must be considered when designing an optical measurement system.

In the context of this project, the FBG sensors would be measuring quantities in a high temperature radiation environment. Exposure to high temperature and nuclear radiation increases the attenuation in the silica optical fiber and ultimately decreases the signal measured by the receiver in Figure 121. Knowing the effect of high temperature and nuclear radiation on the optical transmission of silica optical fibers is an important step in determining whether commercially available optical instrumentation can be used in high temperature reactor environments. The survivability of the FBG sensors is not considered in this project.

With this goal in mind, many of the results presented show the time evolution of the thermal and radiation induced attenuation at the three commonly used instrumentation wavelengths: 850nm, 1300nm and 1550nm. The added attenuation around 1300nm and 1550nm was, for the most part, low and coincidentally boring. Despite being boring, the experimental determination that silica fibers can survive optically and mechanically at high temperatures in a reactor radiation environment is important for the extension of optical instrumentation into harsh radiation environments.

Experimental results are also presented showing thermal and radiation induced attenuation between 400nm and 2200nm at selected times. In addition to the three commonly used wavelengths, these broadband plots identify other low-attenuation wavelength ranges that could be useful for future instrumentation development. The broadband plots also show wavelength ranges where the added attenuation was large. While it is unlikely that optical instrumentation would be designed around wavelengths experiencing substantial attenuation, the information is useful for explaining the degradation mechanisms occurring in the silica fibers.

Quantifying the change in concentration of defects and impurities from the change in optical attenuation alone is difficult for several reasons. First, most of the radiation induced defect attenuation peaks are centered at wavelengths in the UV region and could not be resolved with the optical measurement system used in this project. Second, the identifiable vibrational absorption peaks in the visible-IR region are inhomogeneously broad and many overlap partially or completely, complicating quantification. Instead, qualitative explanations are provided for the increase in attenuation based on the background material presented in previous chapters.

An application specific example is presented in this chapter using specifications from commercially available optical equipment [8] [113] to illustrate the effect of the attenuation increase on an actual system. In addition to illustrating the utility of the data developed in this project, the example will be used as a metric for the attenuation data presented. The features and specifications of the equipment used in this example are available in products from other manufacturers [114] [7].

Pertinent experimental conditions are included with the presented results. Additional details for the experimental setup, thermal profile, and radiation environment for each experiment are described in [2]. Optical transmission was measured during the experiment and optical attenuation was calculated later during post-processing. Data processing methods are described briefly in this chapter with a thorough explanation presented in [2]. Sources of experimental error are also described at the end of this chapter.

A large amount of unique data was developed as a result of these experiments. Presenting portions of the data in static plots is necessary for printed documents [115] [15], but doing so poorly represents the scope of the work completed. While processing and analyzing the results from these experiments, time-lapse videos showing the time evolution of the attenuation spectra were rendered and are posted publicly on the internet [1].

9.2.1 Data Processing Methods for Multimode Attenuation Data

Optical connections between fibers and equipment were made as shown in Figure 122. Photons emitted by the light source could be lost from the system at mechanical connections (MCs), in either patch cable, or in either multiplexer. The light source intensity could drift over time and, at high temperatures, the furnace acts as a secondary light source. The interfering effects must be separated to calculate the evolution of the optical attenuation through each fiber as a result of exposure to high temperature and radiation. The equations, assumptions and data acquisition methods used to separate the interfering effects and calculate corrected active intensities were summarized in Section 1.5 and are presented in detail in [2].

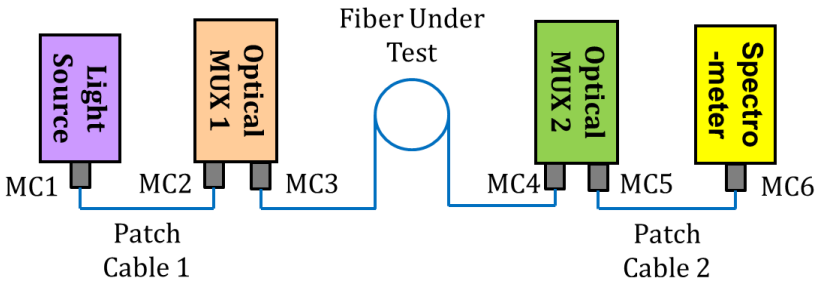

Figure 122: Block Diagram of Optical Connections

MATLAB was used extensively to process, analyze, and plot the data acquired in these experiments. Results generated with these codes were compared against calculations in Microsoft Excel using subsets of the same data for validation. In addition, results generated with the author's codes were compared against results generated by codes independently written by another group member. The MATLAB codes written for this project have not been included with this document but can be made available by contacting the author.

Attenuation Calculation

The change in attenuation can be calculated using the ratio of the corrected active intensity to the initial corrected active intensity, as shown in Equation 4. Because of the corrections made to the intensities used in Equation 4, the calculated change in attenuation is only caused by changes to the fiber under test. Figure 123 graphically depicts the conversion between transmission and attenuation in dB.

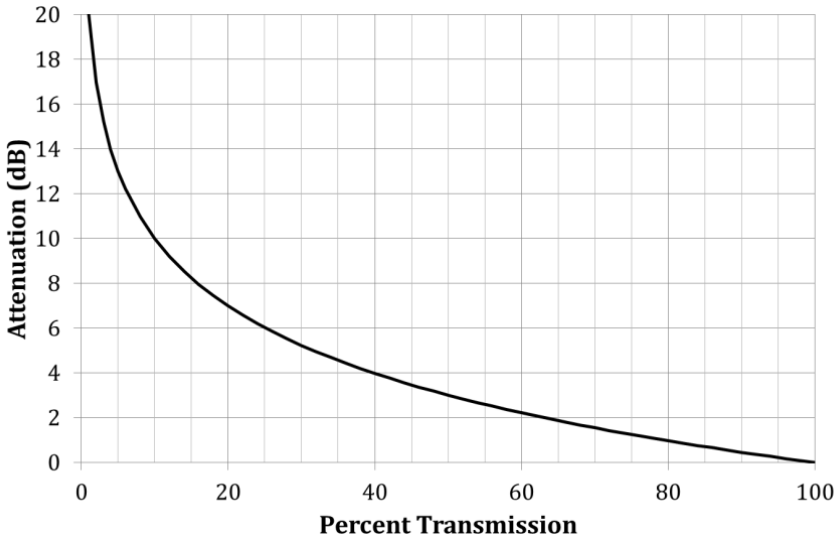

Figure 123: Conversion between Percent Transmission and Attenuation in dB

Uncertainty Calculation

During data acquisition, each recorded intensity measurement was actually the average of five consecutively averaged measurements. In addition to recording the average, the standard deviation of the five measurements was also recorded. These measurements enabled uncertainties to be calculated for the optical measurements. The uncertainty contribution was high for measurements made at wavelengths where the fiber was strongly attenuating, the light source did

not provide many photons, or the sensitivity of the spectrometer at the particular wavelength was poor.

In addition to the uncertainty contributed by the optical measurements, there is an uncertainty contribution based on the length of fiber under test. The length of fiber under test is estimated to have a length of plus or minus one wrap diameter on the fiber spool (±0.3 m). Uncertainty contributions from the optical fiber leading into and out of the experimental facilities were not considered. The equations used to calculate the optical uncertainty are presented in [2].

The large number of data points per plot makes including error bars on each data point messy and confusing. In the plots presented in this chapter, the line width of each dataset represents ±1 standard deviation. Thin lines indicate small uncertainty and thick lines indicate larger uncertainty.

9.2.2 Example Optical Instrumentation Application

A simple schematic of a distributed temperature measurement system using optical instrumentation was shown in Figure 121. In this example, the optical sensor interrogator is the PXIe-4844 from National Instruments [8] and the temperature sensing FBG fiber is the os1200 from Micron Optics [113]. The transmitter in the PXIe-4844 is a tunable laser with a frequency range of 1510nm to 1590nm and an output power range of 0.06mW to 0.25mW. The laser power can be varied to overcome attenuation and also prevent saturation of the receiver, but in this example the maximum laser power is assumed. The minimum power for a returning signal is 25nW which equates to a 40dB loss. The loss at the mechanical connector is assumed to be 0.75dB and affects both the outbound and returning signal. The reflectivity of the FBGs is specified to be greater than 70%. The intrinsic attenuation at 1550nm is 0.015dB/m and 0.005dB/m in the as-manufactured low-OH Polymicro fiber [12] and the low-OH CeramOptec [116] fiber, respectively.

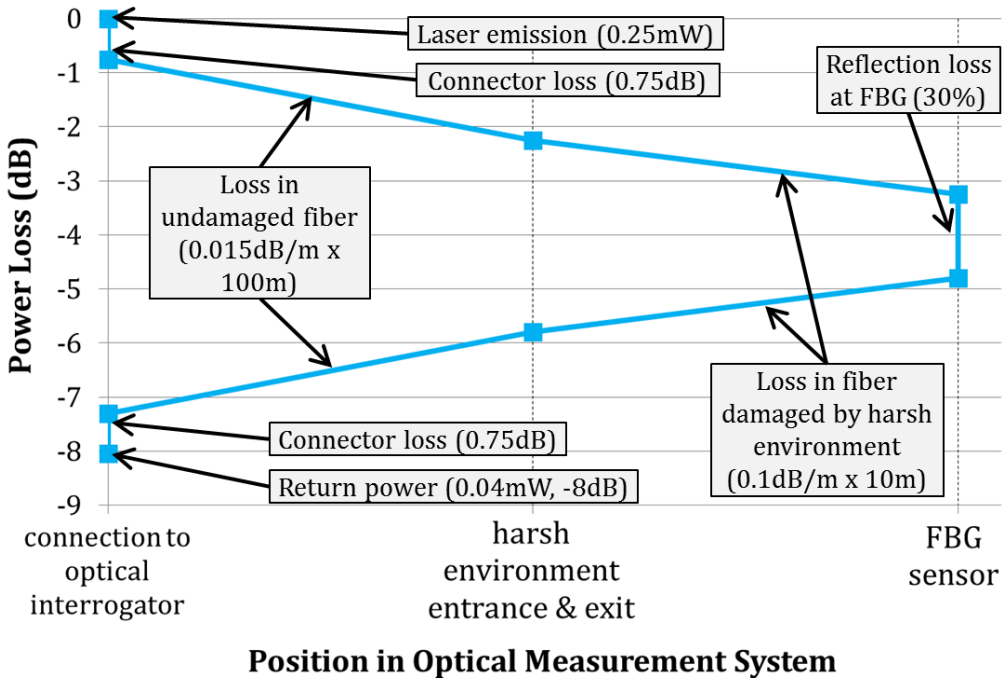

Figure 124: Loss Analysis for Example Optical Measurement System

Based on the described equipment and assuming a 100 meter length of undamaged low-OH Polymicro fiber and a 10 meter length of fiber exposed to a harsh environment resulting in a uniform attenuation of 0.1dB/m, the losses in the optical system can be determined as shown in Figure 124. The calculated return power is 0.04mW which results in an 8.05dB loss. An additional 32dB of losses can be tolerated before the sensitivity limit of the receiver in the PXIe-4844 is reached. The system loss before the 10 meters of fiber are damaged is about 6.5dB leaving a loss margin of 33.5dB. Replacing the low-OH Polymicro fiber with CeramOptec fiber reduces the initial system loss to 4.2dB leaving a loss margin of 35.8dB.

Assuming connections and equipment in the mundane environment do not degrade, the loss margin can be used to determine the longevity of the silica fiber and the FBG in the harsh environment. The FBG reflectivity is arbitrarily assumed to decrease by an order of magnitude in the harsh environment. Assuming uniform attenuation over the 10 meter fiber length indicated in Figure 124, the maximum tolerable attenuation increase at 1550nm is about 1.1dB/m in the low-OH Polymicro fiber and 1.3dB/m in the low-OH CeramOptec fiber.

9.3 High Temperature Multimode Experiments with Radiation [2]

The goal of this project was to determine the performance of silica optical fibers in a high temperature reactor radiation environment. Optical performance was quantified by measuring broadband optical transmission through the fibers as the fibers were subjected to different temperatures and radiation environments. Several experiments were conducted to expose the optical fibers to various combinations of thermal and radiation environments with the goal of separating the degradation effects. A list of all of the experiments completed for the multimode fiber attenuation part of this project is shown in Table 11.

	Date Started	Duration (hours)	Location	Maximum Temperature (°C)	Radiation Environment
First high temperature experiment	1/27/2011	5	W470 Scott Lab	1000	no radiation
Second high temperature experiment	6/21/2011	15	W470 Scott Lab	1000	no radiation
Third high temperature experiment	10/16/2011	622	W470 Scott Lab	1000	no radiation
First gamma experiment	12/20/2011	46	OSU Co-60 Facility	200	~48krad/hr
Second gamma experiment	1/4/2012	127	OSU Co-60 Facility	600	~48krad/hr
Fourth high temperature experiment	3/26/2012	532	W470 Scott Lab	1000	no radiation
First reactor experiment	5/15/2012	33	OSU research reactor	1000	10% power
Second reactor experiment	5/29/2012	10	OSU research reactor	900	10%-20%-40%-20%-10%
Third reactor experiment	6/8/2012	4.5	OSU research reactor	600	90% power

Table 11: List of Multimode Optical Fiber Degradation Experiments

9.4 High Temperature Multimode Experiments in the Co-60 Irradiator [2]

Two heated experiments were conducted in the Co-60 irradiator at the OSU Nuclear Reactor Lab (OSUNRL) to determine the combined effect of high temperature and gamma irradiation on optical transmission in silica optical fiber. The fibers were positioned in the maximum dose rate region of the Co-60 facility with an exposure rate of 47.6kRad per hour (in silica). The first

experiment failed before completion because several of the fibers leading into and out of the furnace were accidentally broken. In all of the previous experiments the fibers leading into and out of the furnace were short and easily managed. In this experiment, the lead in and out fibers needed to be 10 meters long to access the Co-60 irradiator at the bottom of a 20 foot dry-tube. When reloading the furnace for the second experiment, the lead in and out fibers were fed through a sheath for mechanical protection.

Gamma irradiation causes ionization in silica resulting in broken bonds and trapped charger carriers, but little displacement damage [5]. The increased concentration of defect structures and trapped charge carriers increase the optical attenuation as described in Section 1.8. The concentration of optically active defects produced is dependent on the intrinsic concentration of incorrectly bonded defects in the silica fiber. Regardless, gamma induced attenuation creates electronic defects with absorption peaks mostly below 400nm. Because of this, gamma radiation has little effect on the attenuation at 1300nm and 1550nm. Tails from the gamma induced attenuation can affect the attenuation at 850nm.

The exception is the NBOHC defect which has a small absorption peak around 620nm in addition to a strong absorption peak around 258nm. Broken Si-OH bonds result in an NBOHC defect plus a hydrogen atom and peroxy linkages can break in two NBOHC defects. The broken bonds can recombine, but until recombination occurs, the NBOHCs contribute to the optical attenuation. The recombination rate of NBOHC defects with hydrogen is dependent on the hydrogen mobility. As the silica temperature increases, the hydrogen mobility and the recombination rate increase. NBOHCs not formed by broken Si-OH bonds can also be passivated by bonding with a hydrogen atom.

Si-Si bonds exist in large concentrations in oxygen-deficient fibers and form a charged and an uncharged E'-center when broken (Equation 12). Pre-existing uncharged E'-centers can also trap holes and become charged. Charged E'-centers create optical absorption with a peak around 215nm with tails that can affect the visible spectrum. Trapped charge carriers are less stable at higher temperatures and charge carrier recombination increases with increasing temperature [40].

9.4.1 Setup of Second Heated Gamma Experiment

The second heated gamma experiment included three 9.85±0.3 meter lengths of silica optical fiber, spooled and heated with the temperature and radiation profile shown in Figure 125. The fibers being tested were two low-OH silica fibers (Polymicro FIP100120140 & CeramOptec WF100110125P37) and a high-OH silica fiber (Polymicro FVP100120140). The gamma irradiation furnace had a maximum use temperature of 600°C and was only operated during OSUNRL business hours. The fibers were exposed to the maximum dose rate throughout the experiment for 126.5 hours and a total dose of 6.07MRad in silica [115]. The optical equipment for this experiment was setup as shown in Figure 107 but the gamma irradiation furnace was used instead of the commercial box furnace. Optical transmission measurements were collected throughout the experiment and quantitative results for the second experiment are presented next. Results for the first gamma experiment are not presented.

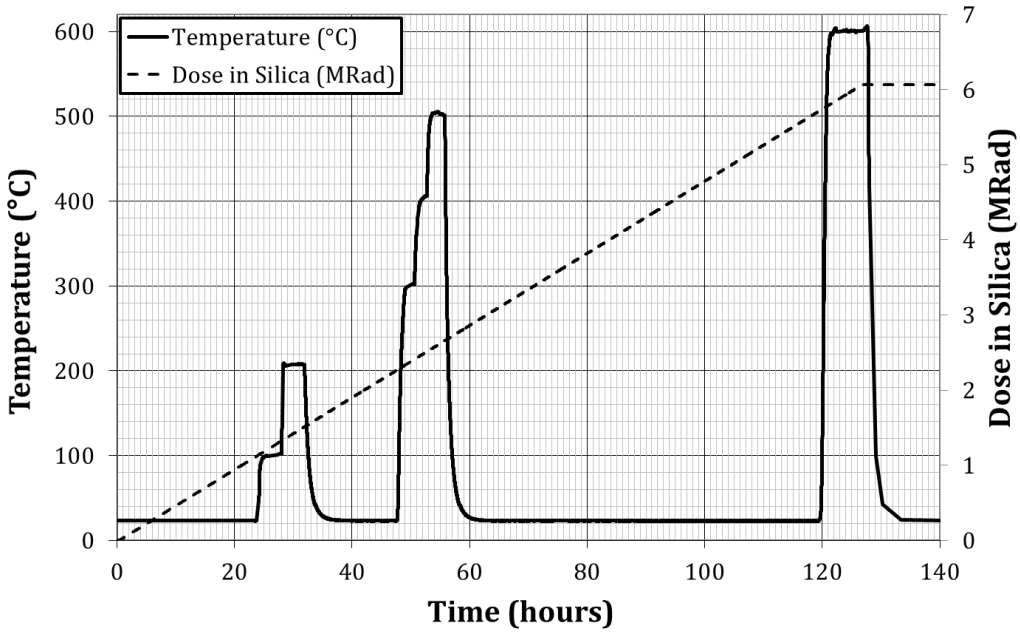

Figure 125: Temperature and Dose Profile for Heated Gamma Experiment

9.4.2 Results from the Multimode Heated Gamma Irradiation Experiment

Figure 126, Figure 127, and Figure 128 show the broadband attenuation increase in the low-OH Polymicro, low-OH CeramOptec, and high-OH Polymicro fiber, respectively. In these three figures, spectra are plotted at the end of the exposure to the respective temperature. The attenuation tail starting at 1800nm and the prominent attenuation peaks around 940nm, 1250nm and 1400nm in Figure 126 are caused by the increase in Si-OH concentration as a result of the high temperature and are not caused by gamma radiation. Because of the low intrinsic NBOHC concentration, increased Si-OH absorption is not occurring in the CeramOptec fiber as shown in Figure 127. The large intrinsic Si-OH concentration in the as-produced high-OH fiber is a constant source of NBOHCs through the radiolysis of Si-OH.

The low-OH Polymicro fiber was produced with an oxygen excess resulting in a large intrinsic concentration of NBOHC and peroxy linkages. In Figure 126, the absorption tail from the gamma induced structural defects after 23 hours at 24°C extends to 1100nm. As the temperature is increased, this tail recedes as defect recombination increases. The absorption peak around 620nm makes it obvious that NBOHC defects are contributing significantly to the radiation induced absorption. At 600°C the absorption peak at 1400nm indicates the Si-OH concentration has increased corresponding to an increased hydrogen concentration from the thermal breakdown of the polyimide coating.

The low-OH CeramOptec fiber was produced with less oxygen than the low-OH Polymicro fiber, and possibly an oxygen deficiency. The intrinsic defects in the CeramOptec fiber do not result in a significant NBOHC concentration as a result of the broken bonds caused by gamma irradiation. As shown in Figure 127, the absorption tail from the gamma induced structural defects after 23 hours at 24°C extends to 1100nm. This tail recedes as the temperature is increased, although not as completely as in the low-OH Polymicro fiber.

Is likely that the charge trapping at E'-Centers is the primary contributor to the observed attenuation tail, although this cannot be explicitly determined. As the temperature increases, de-trapping increases and the observed attenuation tail decreases. The room temperature gamma exposure is also creating a broadband attenuation increase in the CeramOptec fiber, as shown in

Figure 127. Although the source of this broadband attenuation increase is not known, this attenuation increase disappears at elevated temperatures.

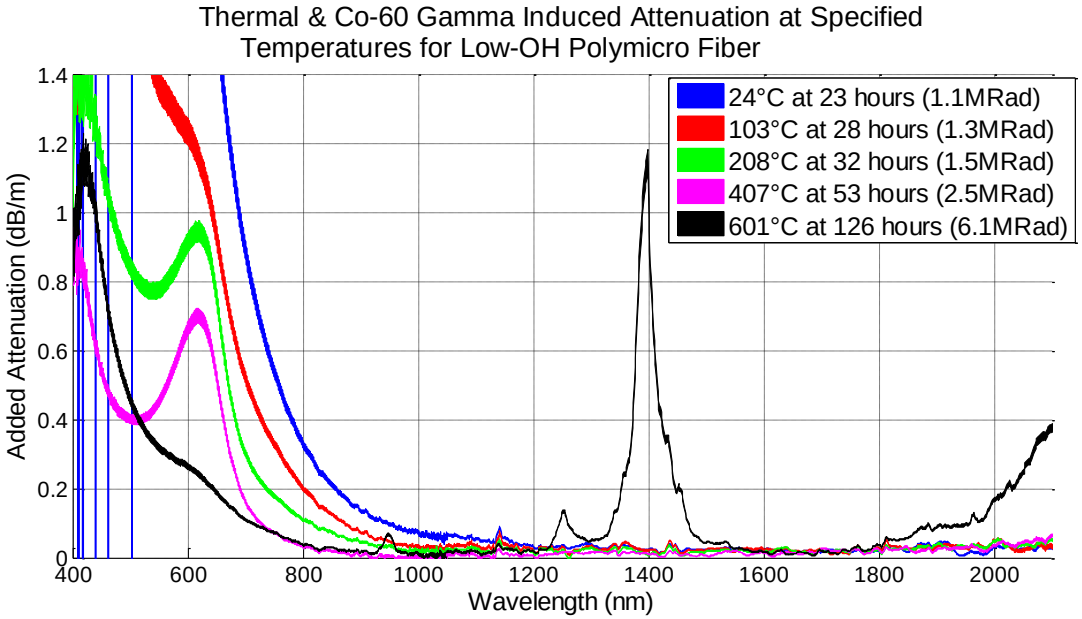

Figure 126: Broadband Thermal & Co-60 Gamma Attenuation in Low-OH Polymicro Fiber (line width indicates ±1σ, pure silica core, F-doped silica clad, FIP100120140, gamma experiment)

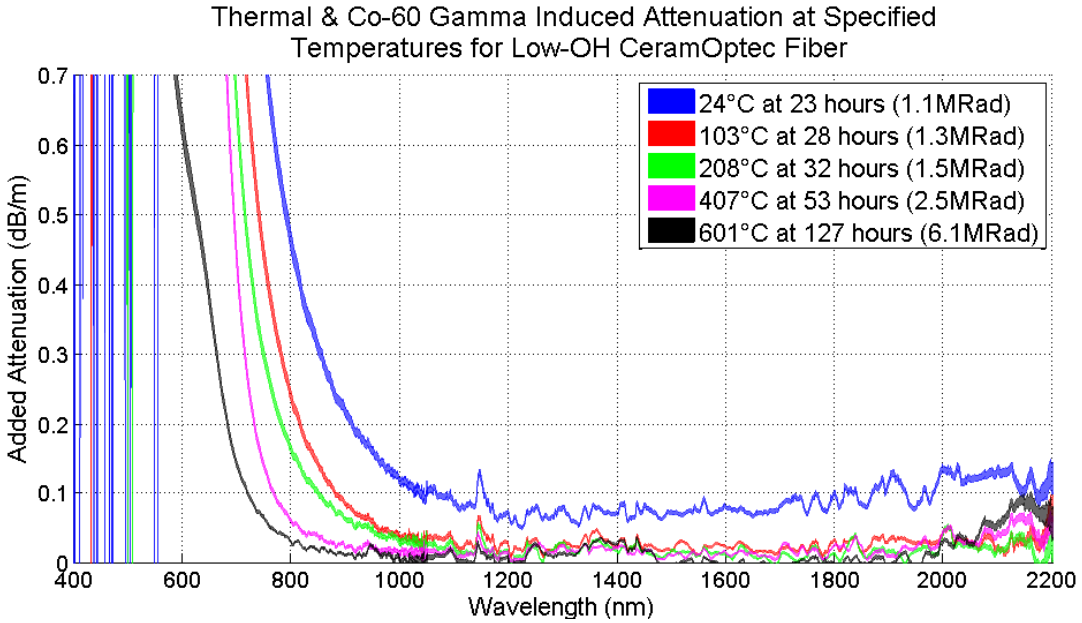

Figure 127: Thermal & Co-60 Gamma Attenuation in Low-OH CeramOptec Fiber (line width indicates ±1σ, Ge-doped silica core, F-doped silica clad, WF100110125P37, gamma experiment)

The as-manufactured high-OH Polymicro fiber has a large concentration of Si-OH and additional molecular hydrogen is probably dissolved in the silica. NBOHCs created from broken Si-OH bonds and peroxy linkages are quickly passivated by the abundant hydrogen in this fiber. The generation rate of NBOHCs depends on the gamma dose rate and the Si-OH concentration. The recombination rate of NBOHCs with hydrogen increases with temperature. As shown in Figure 128, the NBOHC peak around 620nm is easily identifiable and decreases with increasing temperature up to 400°C. The NBOHC concentration at 600°C is larger than the NBOHC concentration at 400°C. This could be a result of hydrogen diffusion out of the silica or conversion of other defects to Si-OH impurities with dose.

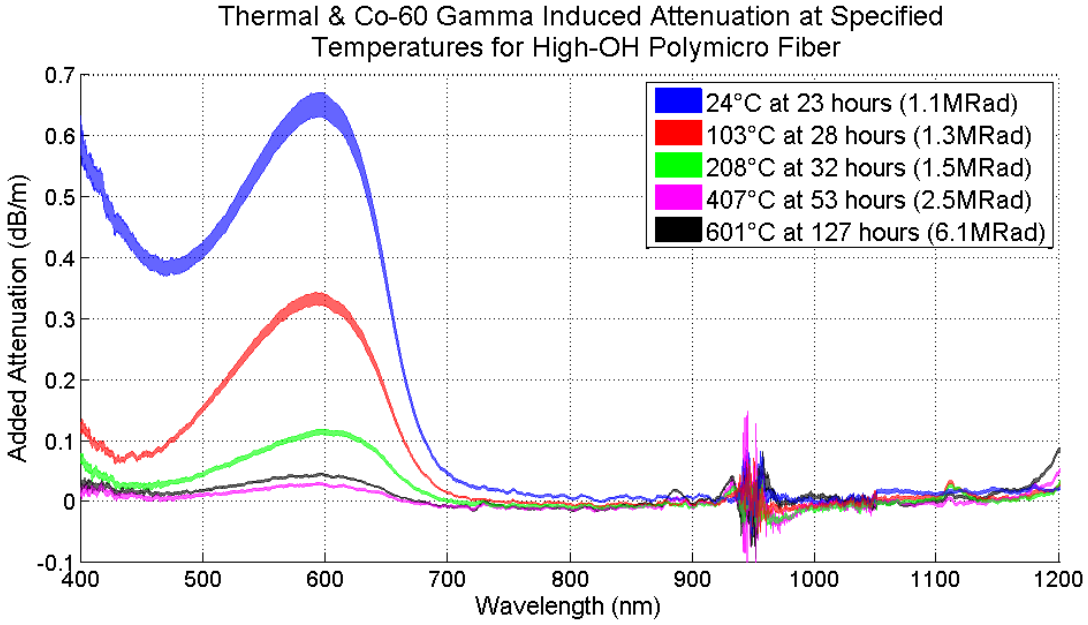

Figure 128: Broadband Thermal & Co-60 Gamma Attenuation in High-OH Fiber (line width indicates ±1σ, pure silica core, F-doped silica clad, FVP100120140, gamma experiment)

9.5 High Temperature OBR Experiment in the Co-60 Irradiator [97]

The OBR gamma irradiation experiment was performed in the Co-60 gamma irradiator at the OSUNRL separately from the multimode gamma irradiation experiments. Two Corning SMF-28e+ single-mode optical fibers were spooled around a fiber holder and loaded into the gamma irradiation furnace described in Section 7.3.2. The total length of optical fiber included in this experiment was approximately one meter. Figure 129 shows the singlemode fiber spooled on the fiber holder prior to loading into the gamma furnace. All of the protective polymer coatings were stripped from the heated section of fibers making the fibers fragile and difficult to handle. About nine inches of silica capillary tube was used to protect the bare optical fibers at the entrance into the furnace. The capillary tube, TSP320450, was purchased from Polymicro Technologies and was secured to the fiber jacket outside the furnace with shrink tubing.

The furnace, loaded with optical fiber, was lowered into the gamma irradiator at the beginning of the experiment and remained in the irradiation facility for the remainder of the experiment. The experiment was in the Co-60 irradiator continuously for 161.5 hours. The dose rate in the irradiator was 47.6kRad per hour in silica and the total gamma dose to the fibers was around 8 Mrad.

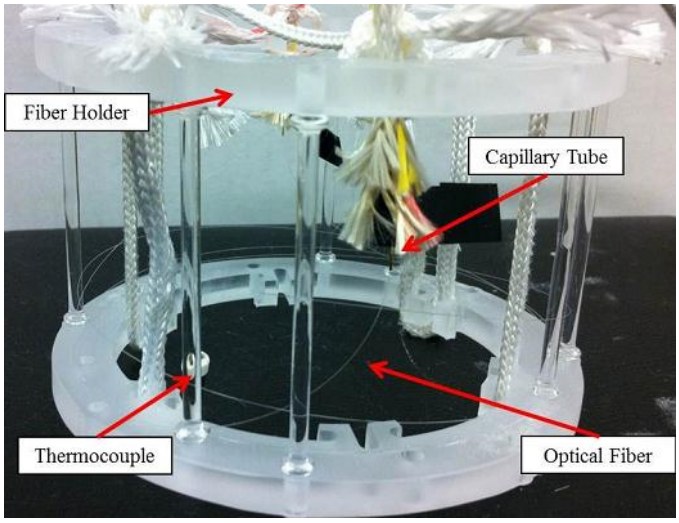

Figure 129: Singlemode fiber spooled on a fiber holder

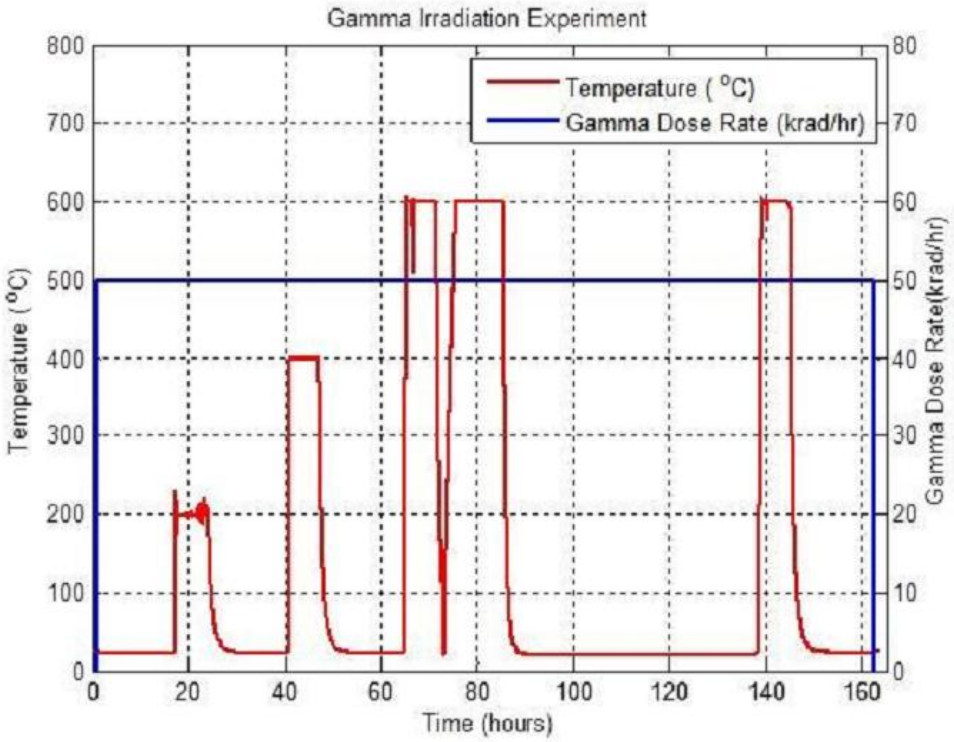

Figure 130: Dose Rate and Temperature Profile for OBR Gamma Experiment

While the experiment was in the Co-60 irradiator, the temperature of the furnace ranged between room temperature and 600°C. The original plan for the experiment was to have three temperature steps to 200°C, 400°C, and 600°C. Following each temperature step, the furnace would hold at temperature for six hours. Unfortunately, the OBR stopped acquiring data overnight prior to the first period of time at 600°C. This was not discovered until the data was being post-processed. Because of the missing data, the system was restarted and the 600°C step was repeated. Figure 130

shows the gamma dose rate and actual temperature profile as a function of experiment time for the OBR gamma irradiation experiment.

During the OBR gamma irradiation experiment, both optical fibers loaded in the gamma furnace broke around 73 hours into the experiment for an unknown reason. This was not discovered until the experiment was completed and the data was being post-processed. The data collected in the first 50 hours was analyzed. This included the 400°C temperature step and a total dose of 2.5 Mrad. The heated and irradiated region of the first optical fiber in the gamma irradiation experiment in channel 1 was from 21.5 to 22.4 meters. The heated and irradiated region of the second optical fiber in the gamma irradiation experiment in channel 2 was from 21.05 to 21.85 meters. The average fiber Amplitude (dB) from 21.25 to 21.50 meters in the heated and irradiated region of the fiber from channel 2 is shown in Figure 131. A similar plot for channel 1 is shown in [97].

The change in average fiber Amplitude (dB) for the gamma irradiation experiment was minimal with no permanent loss induced. Similar to the thermal experiment, light continued to reach the heated and irradiated region and a signal was measured from the heated and irradiated region. The OBR gamma irradiation data was not reprocessed into engineering units of strain or temperature as was the heated data without radiation (Figure 119). The OBR data taken during the reactor radiation experiments was reprocessed into useful engineering units.

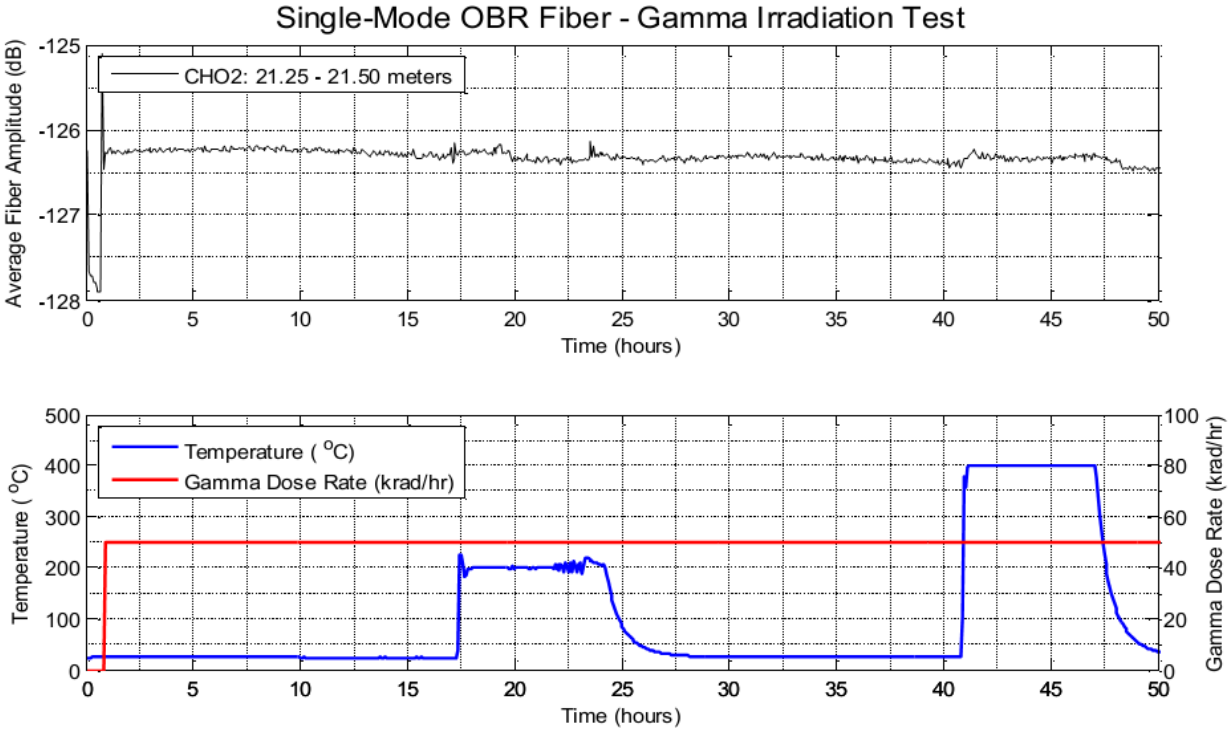

Figure 131: Average Amplitude (dB) for Channel 2 in OBR Gamma Irradiation Experiment

9.6 Summary of Gamma Experiments

Gamma irradiation of silica optical fibers creates additional attenuation by increasing the defect concentrations and trapping charge carriers at defect sites. At high temperature, trapped charges are less stable and broken Si-OH bonds recombine faster resulting in significantly reduced gamma induced attenuation. Even at room temperature, the attenuation increase is primarily below 1000nm and has little effect on transmission at 1300nm and 1500nm. In the low-OH Polymicro

fiber, the thermally induced attenuation at 1300nm and 1550nm was greater than the gamma induced attenuation at 600°C.

The gamma dose rate, total dose, and 400°C exposure had little effect on the singlemode Corning SMF-28e+ optical fiber. The singlemode optical fiber interrogated with the OBR in the Co-60 gamma environment at moderate temperatures performed well and no permanent damage or loss was seen. However, at low temperature no severe loss or degradation was expected and higher temperatures or larger dose rates may cause damage.

9.7 Experiments in a High Temperature Reactor Radiation Environment

Three experiments were conducted in a mixed gamma and neutron field provided by the 500kW pool-type OSU Research Reactor (OSURR). Other researchers have previously irradiated optical fibers in reactor environments to fluences on the order of 1E+20n/cm^2 but at temperatures much lower than those achieved in this project [117]. Achieving a comparable fluence with the OSURR is not possible within the constraints of this project. Instead, reactor experiments for this project were focused on high temperature irradiations which Cheymol et al. identified as a next step to their work [117].

High temperature experiments were completed in a mixed neutron and gamma radiation environment using the research reactor at the OSUNRL. These experiments were conducted to determine the combined effect of high temperature and reactor irradiation on the optical transmission of silica optical fiber. Three reactor experiments were completed with different combinations of neutron flux and temperature. The maximum temperature in these experiments was 1000°C and the total fast neutron fluence accumulated in all of the reactor experiments, including reactor operations for purposes other than this experiment, was 1.27E16n/cm^2.

Fast neutrons create displacement damage and increase defect concentrations regardless of the initial silica stoichiometry. A displaced atom is unlikely to recombine with atoms at its original location, but can form bonds at its stopping location. In addition to producing neutrons, the OSU research reactor is also a large gamma radiation source. At the end of each reactor irradiation the OSURR was turned off and the fast neutron source was terminated. The gamma dose from the reactor, however, only begins to decay when the reactor is shut down and the dose rate and decay rate are dependent on the recent operating history of the reactor. The gamma field is not easily measured or calculated, but the gamma dose rate to the fiber is estimated to be several orders of magnitude greater than the dose rate in the OSUNRL Co-60 facility.

The increase in attenuation measured in the reactor experiments is caused by a combination of thermal effects, ionization effects, and displacement damage. In addition, daily temperature fluctuations in the reactor bay caused variation in the sensitivity of the NIR spectrometer that could not be completely corrected. To minimize the error introduced by the sensitivity fluctuations, quantitative analyses were only performed for datasets collected over short time periods.

9.7.1 Setup of Reactor Experiments

Three 9.85±0.3 meter lengths of silica optical fiber were spooled onto a quartz fiber holder and loaded into the reactor irradiation furnace (Section 7.3.1). The total length of each fiber type was around 40 meters with 15 meters of fiber being used to lead into and out of the dry-tube and reach the optical instrumentation located at the BSF pool top. In addition, three short sections of Corning SMF-28e+ singlemode optical fiber were included for interrogation by the OBR. The bare singlemode fibers were fragile and only one of the fibers was still working at the start of the reactor experiment.

The multimode optical equipment for this experiment was setup as shown in Figure 107 but the reactor irradiation furnace and its accompanying power supply were used instead of the

commercial box furnace. The fibers being tested were two low-OH silica fibers (Polymicro FIP100120140 & CeramOptec WF100110125P37) and a high-OH silica fiber (Polymicro FVP100120140). The same optical fiber was used for all three reactor experiments.

The furnace was positioned at the bottom of a 7"OD dry tube located on the east edge of the reactor core between the rabbit tube and the startup source, as shown in Figure 132 and Figure 43. The neutron flux energy spectra at different axial positions in the furnace are shown in Figure 133 [118]. The multimode optical fibers in this experiment were loaded into the furnace at an axial position corresponding to 'below core centerline' as labeled in Figure 133. The neutron flux with energy greater than 0.1MeV at 450kW (henceforth called fast neutron flux) in this position is 3.08E11n/cm^2/sec and the variation of flux with power is assumed to be linear. The displacement damage rate for silica in this position at 450kW is 4.03E-10DPA/sec [118]. The gamma dose rate at this position was estimated based on measurements made in a 10" dry-tube previously installed in the same position as the 7" dry-tube used in this experiment [119]. The dose rate in silica was estimated to be 8MRad per hour at 450kW.

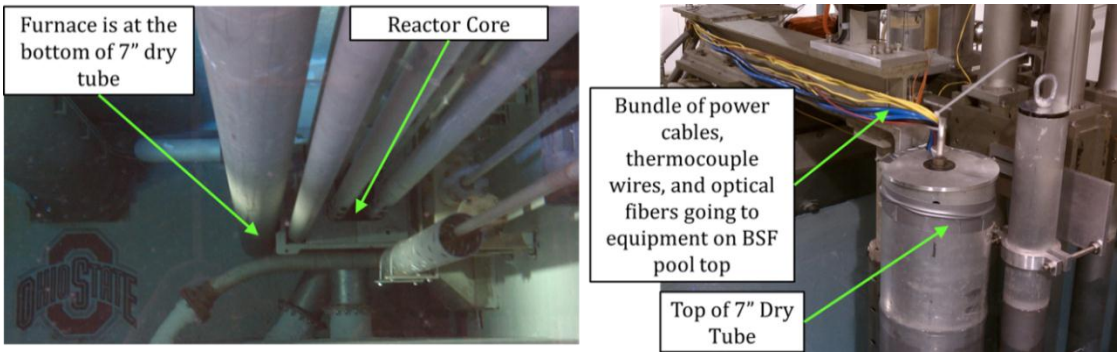

Figure 132: Reactor Irradiation Position

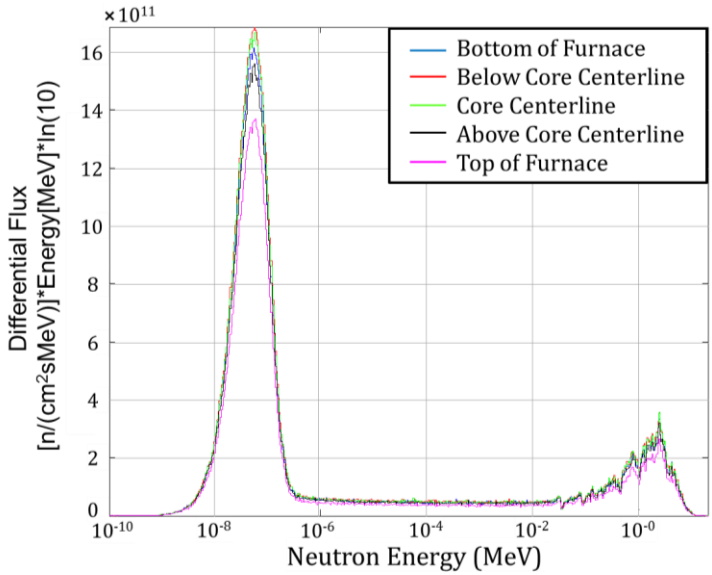

Figure 133: Neutron Energy Spectrum at Fiber Holders in Reactor Furnace [118]

The three reactor experiments were conducted consecutively over three weeks without moving the 7" dry tube and without changing the optical fiber and without moving the dry tube. During this time the OSURR was operated for other reasons and this project benefitted from the additional neutron fluence. Reactor operating data, including the reactor power, was recorded each time the reactor was operated during the three week period.

The gamma dose received during the reactor experiments was not measured but is estimated to be on the order of 100Mrad based on previous measurements in another experimental facility at the same location. The radiation induced attenuation observed in the fibers during the reactor experiments was mainly a result of the large gamma dose. The effects of displacement damage from fast neutron irradiation were not apparent because of the low fast fluence.

9.7.2 First Reactor Experiment

In the first reactor experiment, the reactor was operated at 10% power for 33 hours over six days. The furnace temperature was varied from a minimum near room temperature to a maximum of 1000°C, as shown in Figure 134. The purpose of this experiment was to determine the effect of fiber temperature on the optical attenuation at a constant neutron flux. The conservatively low reactor power was chosen for the first experiment because the effect of reactor irradiation at high temperature was unknown. By irradiating at low power the likelihood of increasing the broadband attenuation beyond the detection capability of the optical instrumentation was reduced. In the event that the fibers failed early in the experiment, operation at low power would have also reduced the decay time before the furnace could be disassembled to load new fibers.

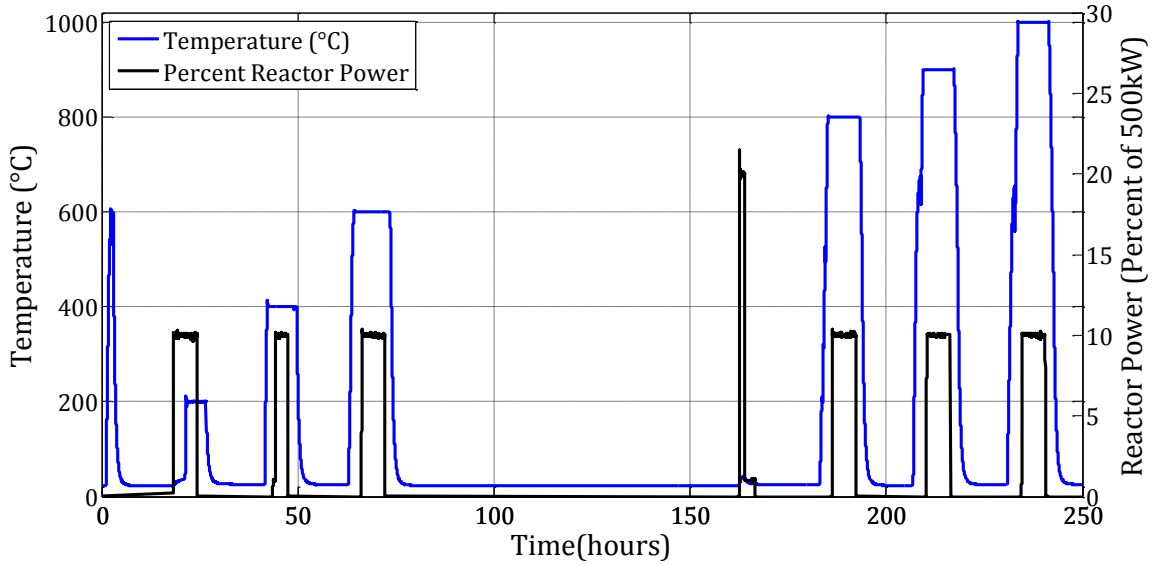

Figure 134: Temperature & Reactor Power for 1st Reactor Experiment

In previous experiments a temporary increase in attenuation occurred the first time the fibers were heated to 500°C and this attenuation was attributed to the thermal removal of the polyimide coating on the optical fibers. At the beginning of this experiment and prior to irradiations, the furnace was heated to 600°C for several hours to remove the polyimide coating. During the first irradiation the fibers were irradiated near room temperature for three hours and at 200°C for three hours. Gamma heating increased the furnace temperature from 21°C to 36°C during the room temperature irradiation. For the remaining irradiations in the first reactor experiment,

the temperature was increased to the set point temperature about an hour before reactor startup so that the fibers could anneal and reach a steady state condition prior to the irradiation.

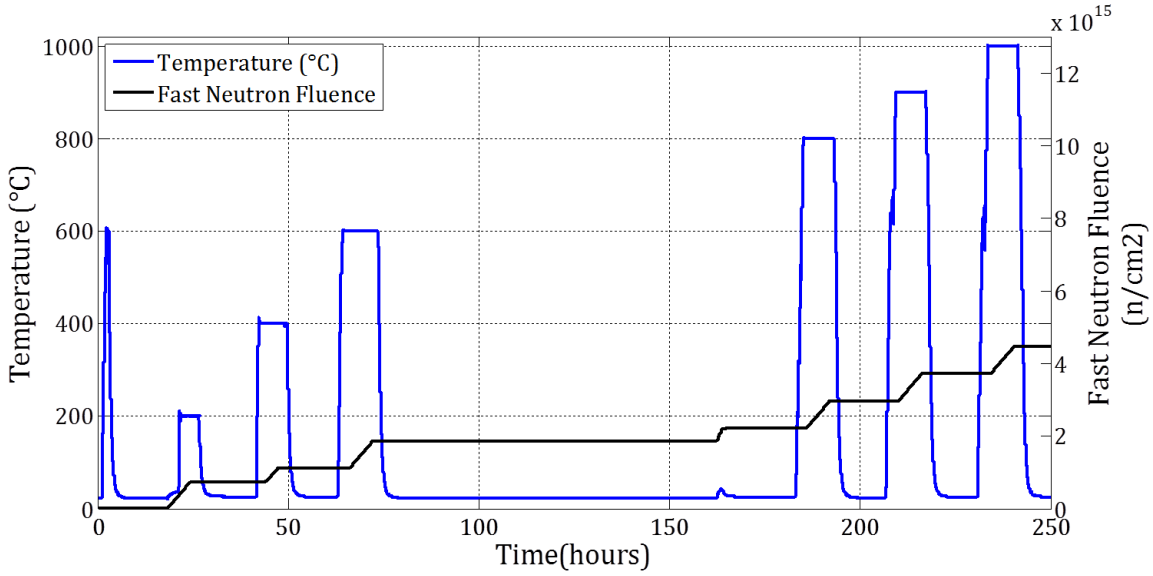

Figure 135: Temperature & Fast Neutron Fluence for 1st Reactor Experiment

Figure 135 shows the fast neutron fluence profile along with the temperature profile for the first reactor experiment. The reactor operation at 160 hours was for another researcher. The fast neutron flux at 10% power in the fiber location is 3.42E10n/cm^2/sec and the fluence accumulated in the first experiment was 4.47E15n/cm^2.

9.7.3 Second Reactor Experiment

In the second reactor experiment the fibers were irradiated for 5 hours at 600°C and at 900°C with the reactor power profile shown in Figure 136. The optical fibers were not replaced between the first and second reactor experiments. The purpose of this experiment was to measure the effect of varying the neutron flux while keeping the fiber temperature constant. The fast neutron flux in the fiber location at 10%, 20% and 40% power is 3.42E10n/cm^2/sec, 6.84E10n/cm^2/sec and 1.37E11n/cm^2/sec, respectively. Figure 137 shows the fast neutron fluence profile and the temperature profile for the second reactor experiment. The fast neutron fluence accumulated in the second experiment was 2.48E15n/cm^2.

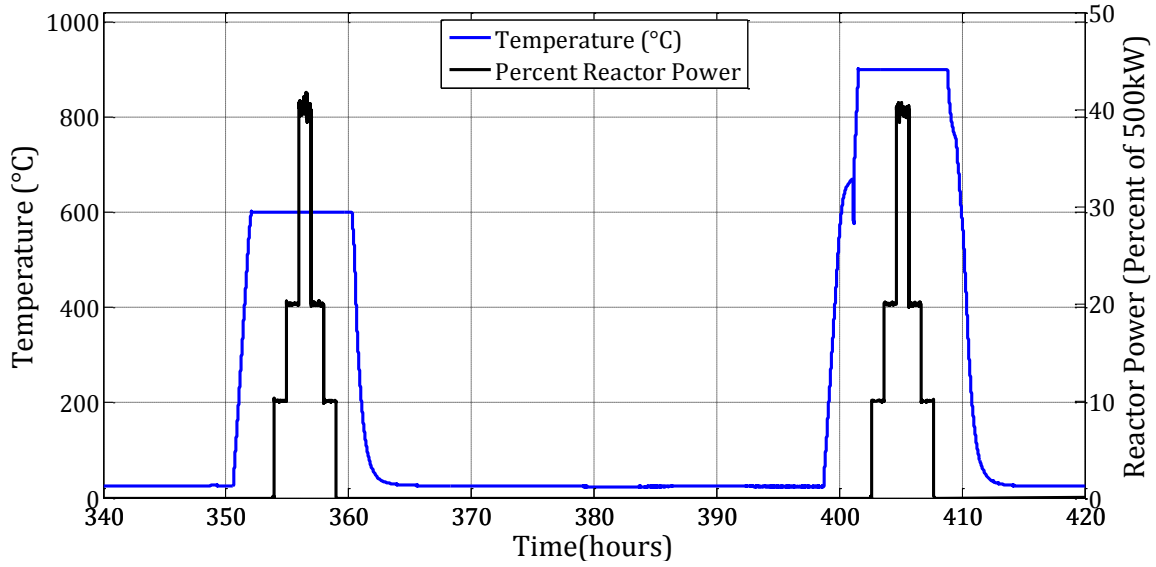

Figure 136: Temperature & Reactor Power for 2nd Reactor Experiment

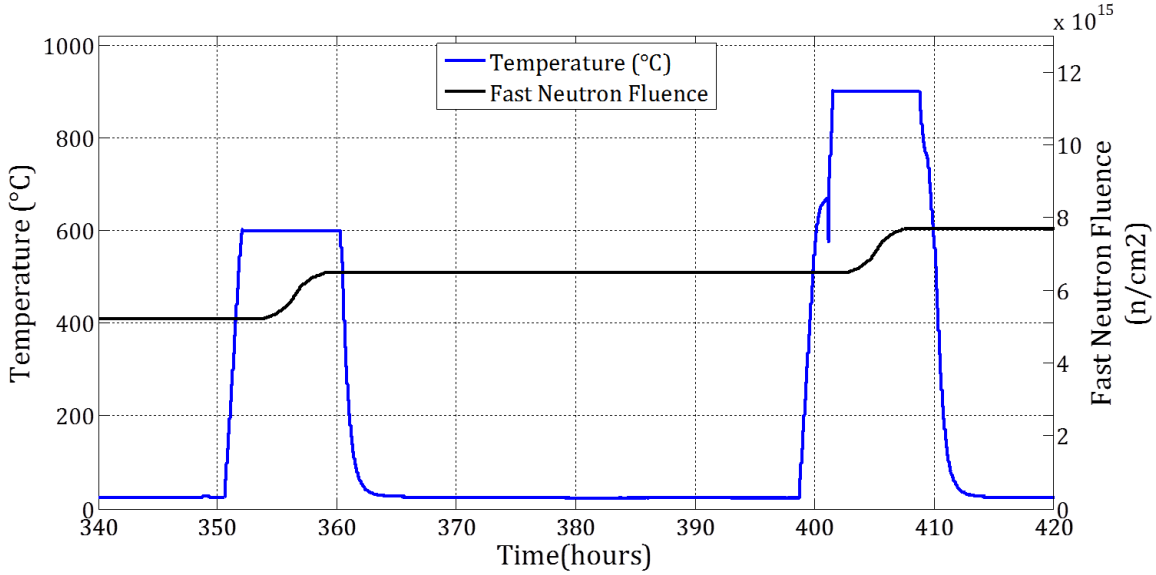

Figure 137: Temperature & Fast Neutron Fluence for 2nd Reactor Experiment

9.7.4 Third Reactor Experiment

In the third reactor experiment the fibers were irradiated at 90% reactor power near room temperature and at 600°C, as shown in Figure 138. The optical fibers were not replaced between the second and third reactor experiments. The primary purpose of this experiment was to create the most damage possible in the fibers by exposing them to the maximum flux possible in the 7" dry tube at the OSURR and not actively heating the fibers. Despite not actively heating the fibers, gamma heating increased the furnace temperature from 21°C to 113°C. The fibers were irradiated again at 600°C and 90% reactor power for comparison.

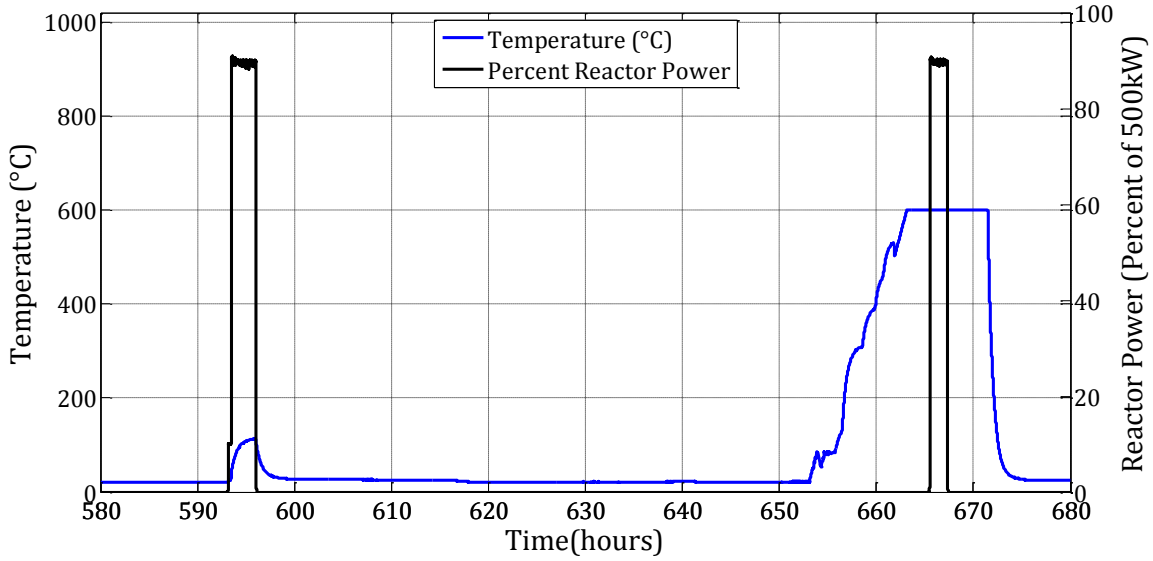

Figure 138: Temperature & Reactor Power for 3rd Reactor Experiment

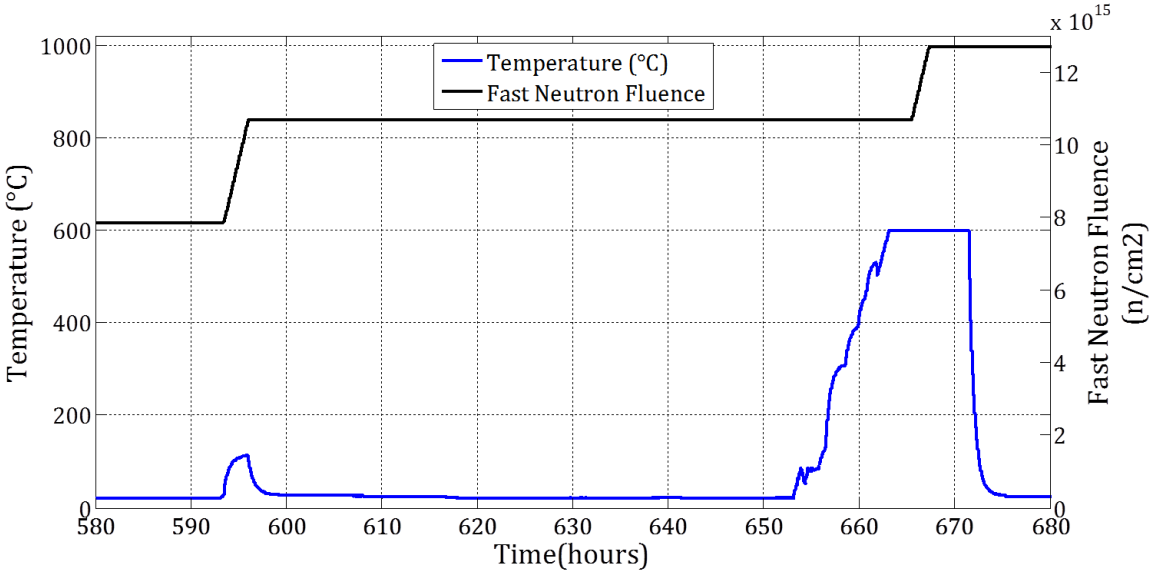

Figure 139: Temperature & Fast Neutron Fluence for 3rd Reactor Experiment

In previous heated experiments the rate of temperature increase was between 5°C and 10°C per minute because the goal was to quickly anneal the fiber prior to an irradiation. To measure the temperature dependence of the annealing, an attempt was made to increase the furnace temperature at 1°C per minute with a constant ramp before the second irradiation in this experiment. Unfortunately the PID controller was not tuned for such a slow ramp and the resulting temperature profile was not linear, as shown in Figure 138.

The fast neutron flux in the fiber location at 90% reactor power is 3.08E11n/cm^2/sec and the fast neutron fluence accumulated in the third reactor experiment was 4.89E15n/cm^2. Figure 139 shows the fast neutron fluence profile and the temperature profile for the third reactor

experiment. The total fast neutron fluence accumulated in all of the reactor experiments, including reactor operations for purposes other than this experiment, was 1.27E16n/cm^2.

9.8 Results for Multimode Fiber Irradiations in the OSU Research Reactor [2]

9.8.1 Reactor Irradiation at Room Temperature

Figure 140 and Figure 141 show the broadband attenuation increase in the low-OH Polymicro and the low-OH CeramOptec fiber, respectively, as these fibers were exposed to a fast neutron flux of 3.42E10n/cm^2/second (10% power) for three hours. The furnace was not powered to minimize thermal effects but gamma heating increased the temperature in the furnace by 13°C. The results shown in Figure 140 and Figure 141 indicate that reactor irradiation of silica fibers has negligible direct effect on the attenuation at 1550nm. Neutron and gamma irradiation increase the concentration of defects with absorption peaks primarily below 400nm. In the low-OH Polymicro fiber near room temperature, the tail from the defect absorption peaks extends to 1400nm. In the low-OH CeramOptec fiber near room temperature, the tail from the defect absorption peaks extends to 1300nm.

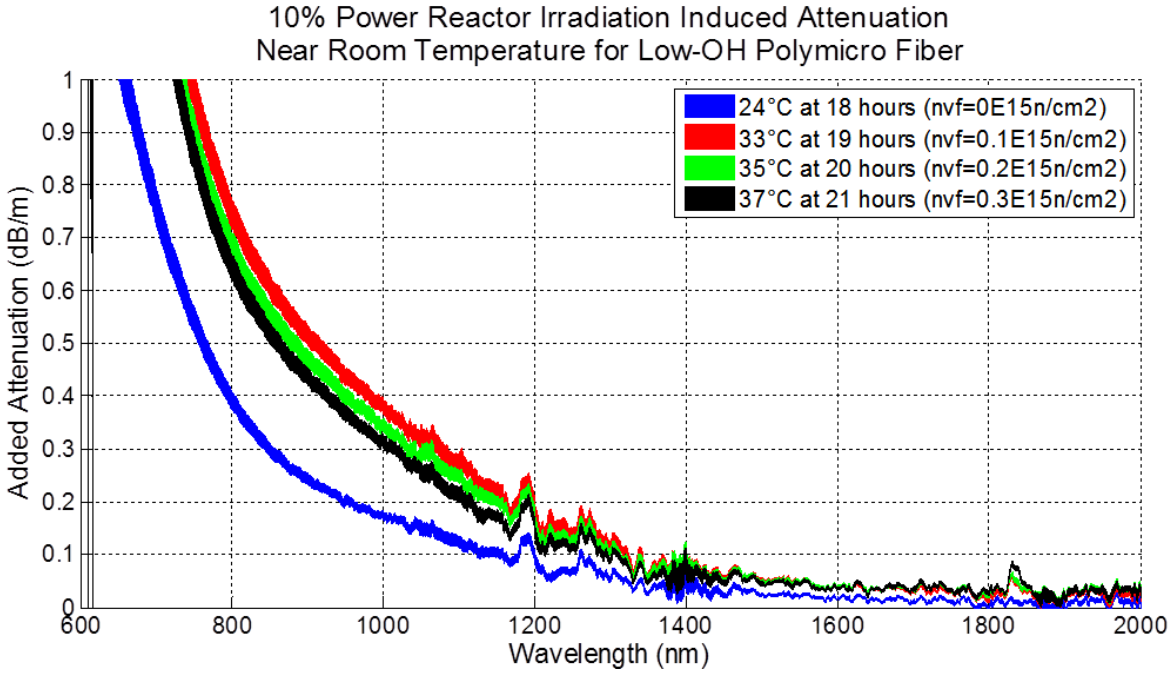

Figure 140: Broadband Reactor Radiation Induced Attenuation in Low-OH Poly-micro Fiber (line width indicates ±1σ, Ge-doped core, F-doped clad, WF100110125P37, reactor experiment)

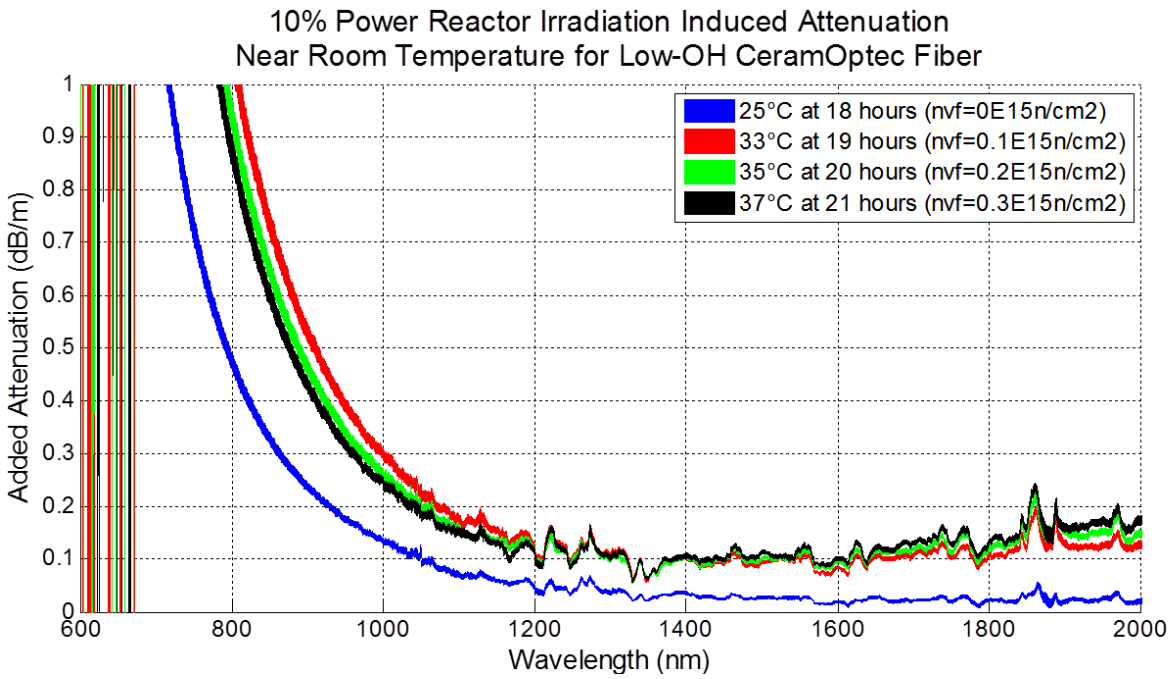

Figure 141: Broadband Reactor Radiation Induced Attenuation in Low-OH CeramOptec Fiber (line width indicates ±1σ, Ge-doped silica core, F-doped silica clad, WF100110125P37, reactor experiment)

9.8.2 Results from the Heated Reactor Irradiation Experiment

As was observed in the Co-60 irradiation results, increasing the fiber temperature increases the charge carrier and defect recombination rates, reducing the optical attenuation. Figure 142 shows the broadband attenuation in the low-OH Polymicro fiber for the first reactor experiment. In this experiment the fibers were irradiated for 33 hours over 6 days with a fast neutron flux of 3.42E10n/cm^2/sec.

The attenuation increase below 1000nm is very similar to the attenuation increase in the Co-60 irradiated low-OH Polymicro fiber (Figure 126) except that the magnitude is greater by a factor of three in the reactor experiment. The behavior of the Si-OH absorption increase is similar in shape and magnitude to the thermally induced attenuation increase in the low-OH Polymicro fiber (Figure 110). Unlike the thermal-only experiments, however, the Si-OH concentration did not start to decrease in the low-OH fibers at 900°C. The increased defect concentration is probably providing ample bonding sites for the hydrogen.

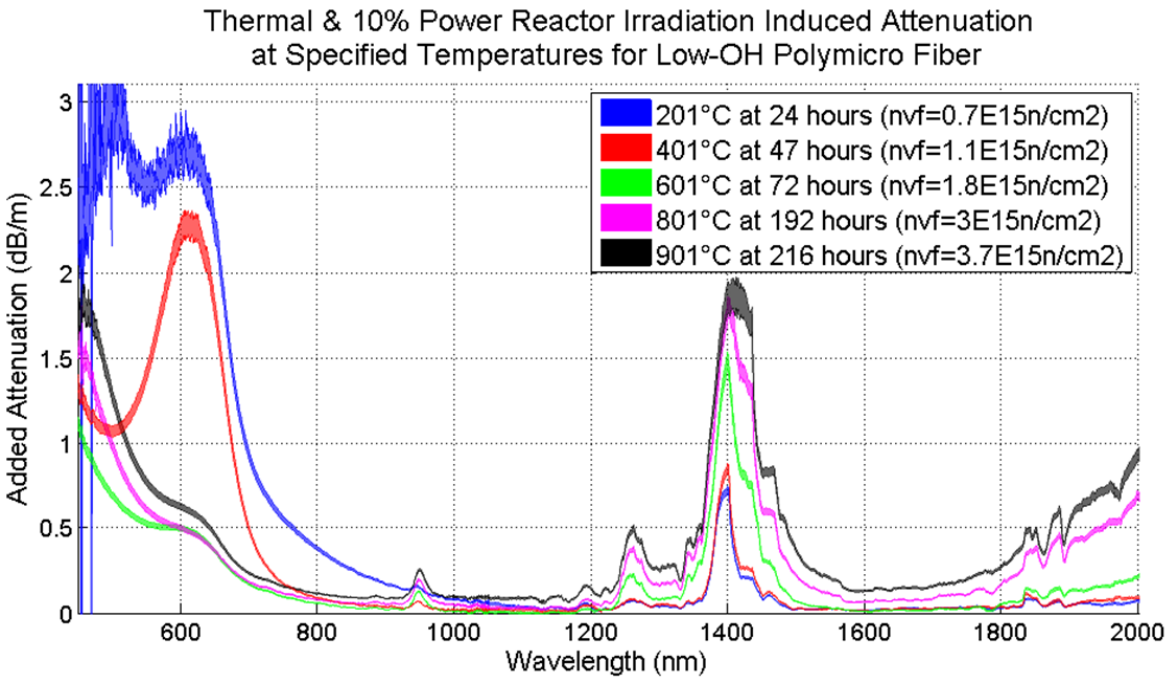

Figure 142: Broadband Thermal & 10% Power Irradiation Attenuation in Low-OH Polymicro Fiber (line width indicates ±1σ, pure silica core, F-doped silica clad, FIP100120140, reactor experiment)

Figure 143, Figure 144, and Figure 145 show a condensed time history of the reactor experiments. Room temperature data from nights, weekends, and days without experiments was removed and only nominal attenuation values were plotted to condense and simplify the figures. Attenuation from increasing Si-OH concentration was the primary attenuation mechanism at 1300nm and 1550nm in the low-OH fibers. The larger initial concentration of oxygen excess defects resulted in more NBOHCs and consequently a greater Si-OH concentration in the low-OH Polymicro fiber compared to the CeramOptec fiber.

The maximum attenuation at 1550nm in the low-OH fibers occurred as a result of the room temperature 2.5 hour irradiation at 90% power (fast neutron flux=3.08E11n/cm^2/sec). Despite the furnace being unpowered, gamma heating increased the furnace temperature to 113°C which helped reduce the radiation induced attenuation. The maximum attenuation at 1550nm for the low-OH Polymicro and CeramOptec fibers was 0.48±0.02dB/m and 0.46±0.02dB/m, respectively. These values are both below the tolerable attenuation increase based on the example optical instrumentation system described previously.

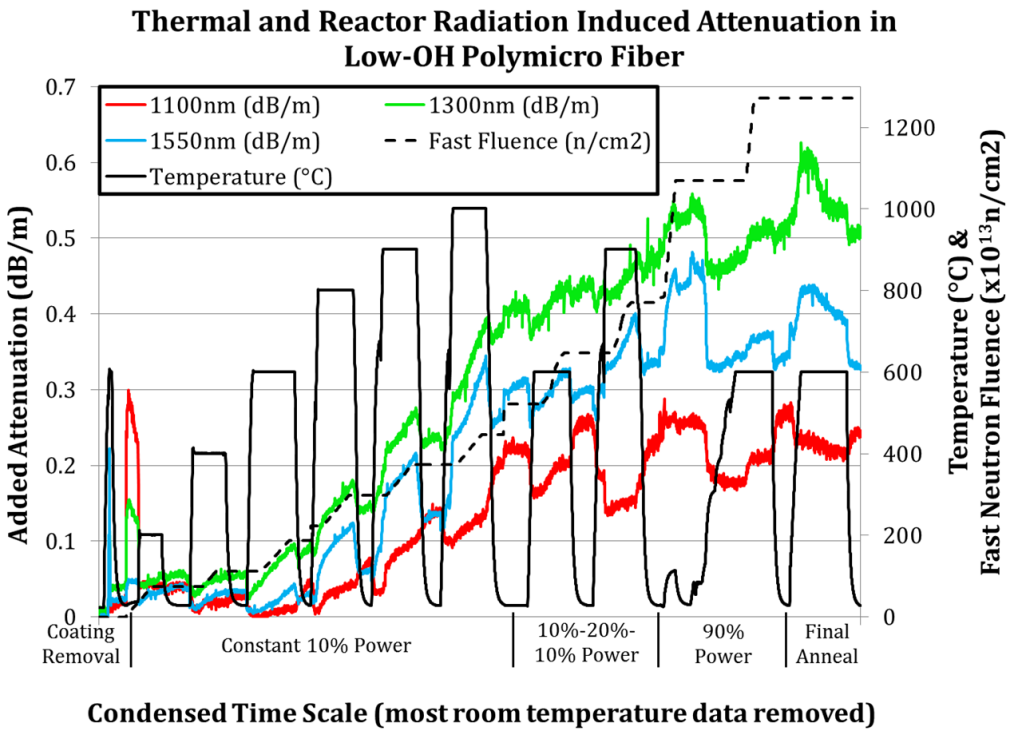

Figure 143: Thermal & Reactor Radiation Induced Attenuation in Low-OH Polymicro Fiber

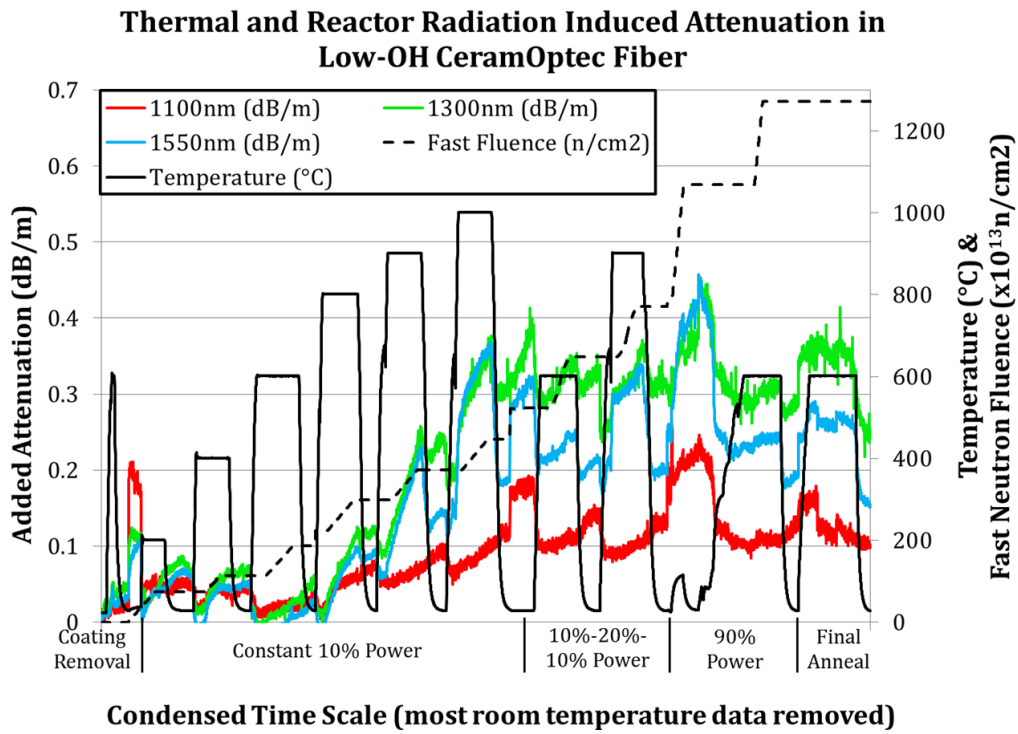

Figure 144: Thermal & Reactor Radiation Induced Attenuation in Low-OH CeramOptec Fiber

The reactor radiation and thermally induced attenuation in the high-OH Polymicro fiber is shown at 700nm, 850nm and 1050nm. The attenuation increase is remarkably low for these wavelengths because of the abundant hydrogen available to passivate defects. The intrinsic attenuation in the high-OH fiber is only 0.009dB/m at 850nm and the maximum total attenuation at this wavelength during reactor irradiation was around 0.12dB/m. The high-OH fiber is a good option for optical instrumentation using 850nm in a high temperature radiation environment.

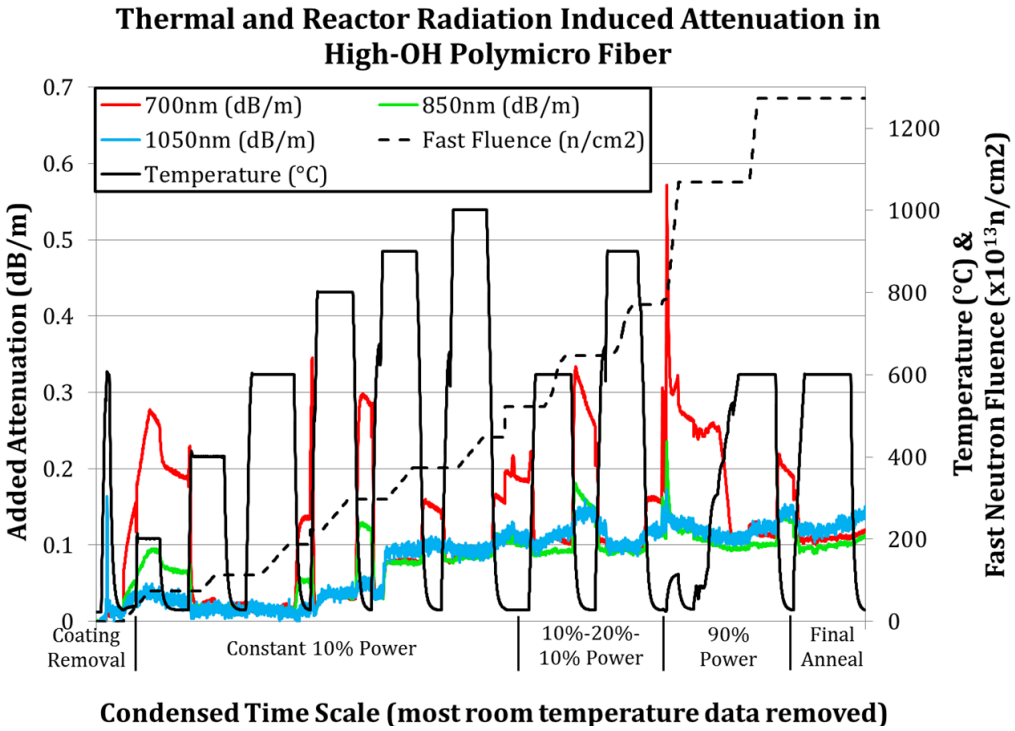

Figure 145: Thermal & Reactor Radiation Induced Attenuation in High-OH Poly-micro Fiber

9.8.3 Sources of Experimental Error in Multimode Measurements

Sources of experimental error identified in this experiment are described in this section. Some of these error sources were expected and some were discovered during experiments. Most of the error sources related to the optical measurements could be eliminated in data post-processing as long as the correct set of measurements were taken during data acquisition. In addition to the optical measurements, there are sources of error that affect quantification of the furnace temperature and dosimetry.

Temperature dependent sensitivity of the spectrometer CCDs, variation in light source intensity and repeatability of the internal multiplexer alignment affect the intensity measurements. Variations in CCD sensitivity and light source intensity could be removed in post-processing as long as active and background intensity measurements were made through the control line and the fiber under test during each scan cycle. Variation in CCD sensitivity was minimized by keeping both spectrometers inside a refrigerator. During the experiments at the reactor lab, however, the unseasonably warm spring was taxing on the refrigerator in the un-air-conditioned reactor bay. Thermal noise variation caused occasional saturation of the control line data for the NIR spectrometer. For this reason the currently available post-processed NIR data for the reactor

experiments is only qualitatively useful. It may be possible to improve this dataset with a different post-processing algorithm.

Small random variations in the internal positioning of the multiplexer components add a small random fluctuation in the transmission intensity measurements. The variation in transmitted optical power was around ±0.25% for the unmodified multiplexer and around ±0.04% for the modified multiplexer (Figure 97). The error from the multiplexers was minimized by keeping the channel switching order constant throughout each experiment.

Variation in the length of fiber being affected by the high temperature and/or radiation environment affects the attenuation calculated from the intensity data. Fiber was methodically spooled onto the fiber holders using a manual spooling mechanism (Figure 104) and it was assumed for calculations that the uncertainty in the length of fiber under test was ±1 spool diameter (±0.3m). The spooling process is obviously affected by human reliability, but the spooling mechanism allowed the number of fibers wrapped on each spool to be counted at each stage of spooling. In addition, the fiber spooling process was usually completed by two people with the second person providing assistance and supervision. The length of fiber under test was assumed to vary by ±0.3 meters and this value was used to calculate attenuation uncertainty. In the gamma and reactor experiments, however, the fiber used to lead into and out of the furnaces was also exposed to a radiation field. The intensity of the radiation field drops off quickly with distance from the radiation source which minimizes the introduced error.

Furnace temperature was measured with K-type thermocouples located in close proximity to the coils of optical fiber. Because of the radial symmetry of Co-60 and reactor irradiation furnaces, temperature measurements were only taken at one radial position in close proximity to the optical fibers. 24 gauge thermocouples and 20 gauge extension wire was used to minimize resistance losses and the thermocouple were read using standard commercial equipment.

The dose rate in the Co-60 facility and the neutron flux in the 7" reactor dry-tube were calculated using MCNP [118]. The MCNP models of these facilities were developed with the explicit geometry and materials used in each facility and validated against measurements. Bounds on the dose rate to the fibers can be determined based on uncertainty in the axial position of the fibers in each facility. The dose rate in the Co-60 facility varies axially but there is a four inch axial range in the facility where the dose rate is within 2.1% of the peak dose rate of 47.6kRad per hour in silica. Dimensional tolerances on the furnace components were such that the fibers were certainly located in this range. Based on the 2.1% variation, bounds on the gamma dose rate at the fiber location are 47.6kRad/hr to 46.6kRad/hr.

The 7"dry tube used for the reactor experiments was positioned as described in Chapter 3. The neutron flux in the 7" dry-tube was calculated with MCNP [118]. The axial flux profile was measured by reactor staff and was also calculated with MCNP. The neutron flux in the 7" dry tube varies axially but there is a five inch axial range in the dry tube where the flux is within 1.9% of the peak flux. Furnace dimensions were chosen to locate the fibers in the peak flux region. Dimensional tolerances on the furnace components were such that the fibers were certainly located in this range. Based on the 1.9% variation, bounds on the fast neutron flux at 450kW at the fiber location are 3.08E11n/cm^2/sec to 3.02E11n/cm^2/sec.

9.9 Results for OBR Experiments in the OSU Research Reactor [97]

The reactor irradiation experiment was the longest test and provided the majority of the results. For the reactor irradiation experiment, the heated and irradiated region of the optical fiber was from 23.15 to 24.05 meters. Therefore, the fiber amplitude (dB) was averaged from 23.65 to 23.75 meters. Figure 146 shows the evolution of the Average Fiber Amplitude (dB) for the averaged spatial region for the entire experiment.

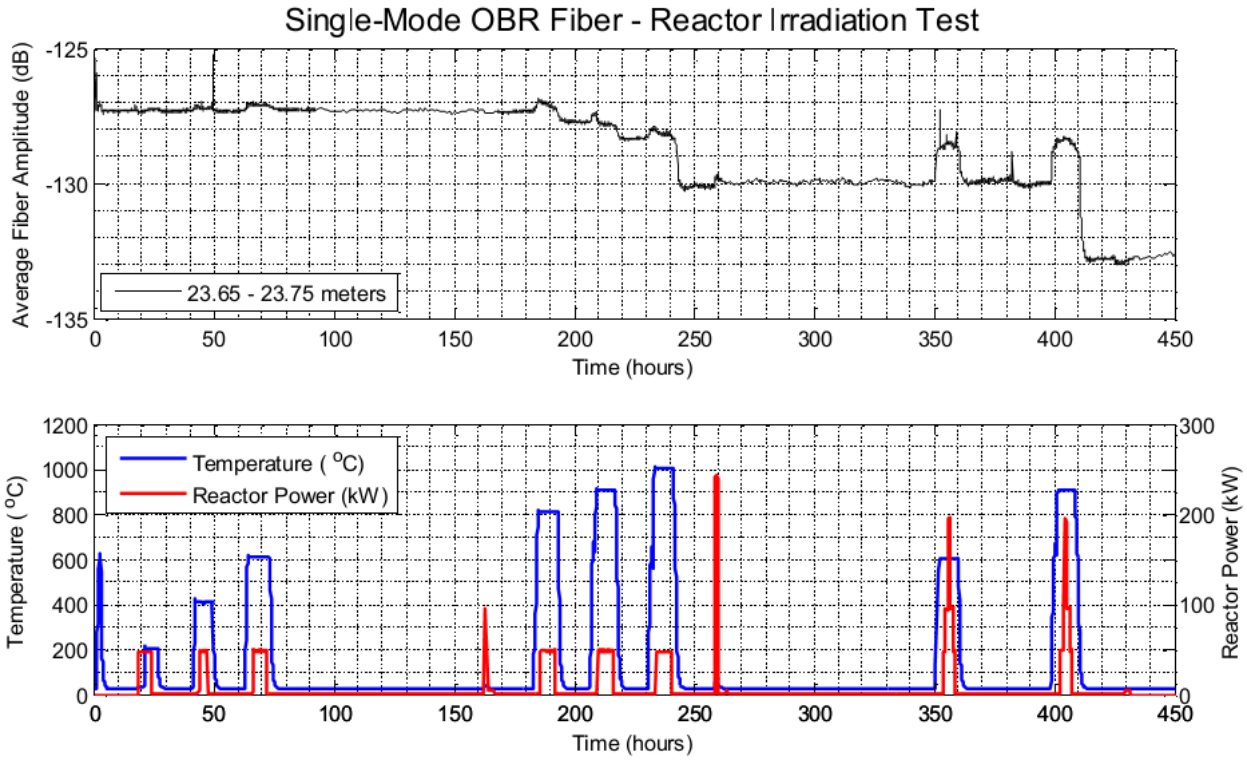

Figure 146: Average Amplitude (dB) for Channel 2 in OBR Reactor Irradiation Experiment

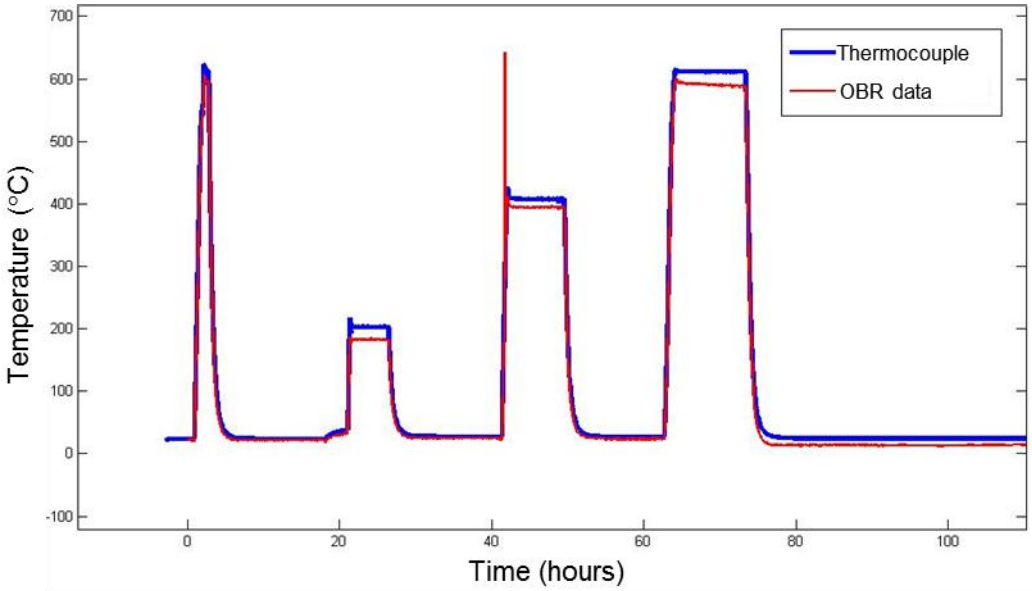

Figure 147: OBR Reactor Experiment Data Reprocessed for Temperature

The OBR data collected during the high temperature reactor experiments was later reprocessed into temperature units. The reprocessed data collected during the first week of reactor experiments is shown in Figure 147. Calibration coefficients determined from the thermal-only experiments were used in the reprocessing. The temperature measured with the OBR follows the

thermocouple measurement up to 600°C. After the data shown in Figure 147, the next temperature step was 800°C. As was observed in previous experiments, after the optical fiber was heated to 800°C, changes to the intrinsic defect distribution in the optical fiber prevent the OBR from correctly calculating temperature change from the initial reference scan. After the optical fiber was exposed to 800°C, the data collected by the OBR with the Corning SMF-28e+ could not be correctly reprocessed into temperature measurements.

Chapter 10. Task J

10.1 Deliverable

Process data and comparison of experimental results with calculations.

10.2 Data Processing

The data collected during these experiments was processed by several individuals and the processed results were presented in the appropriate Task in this report. Additional information can be found in David's dissertation [2], Harish's thesis [10], and Bryan's thesis [97]. Visualization of the results from the transmission testing of the multimode fibers was difficult because of the dependence on time, wavelength, temperature, and dose. To improve visualization, the results from the transmission testing have been post-processed into easily viewable movies that have been posted publicly on the internet [1].

10.3 Comparison of Experimental Results with Calculations

Radiation induced attenuation in glasses has been studied experimentally and theoretically for decades. Previous researchers have studied attenuation caused by activation of pre-existing structural defects, added attenuation caused by additional radiation exposure, and attenuation as a function of time, annealing temperature, dose rate, radiation type, etc. Several researchers have worked to develop predictive models for radiation induced optical attenuation in silica optical fibers. Nearly all of these models were developed empirically with limited experimental data for a specific wavelength and a specific optical fiber in a specific radiation environment at room temperature. The curve fitting parameters used were not always physically meaningful and, until recently, these models did not address temperature dependence.

Because these models do not directly consider the fundamental damage mechanisms that lead to radiation induced attenuation or the mechanisms leading to annealing of the damage, they have limited predictive capability. The difference in radiation induced damage in high-OH and low-OH silica is well known in the literature but the effect of stoichiometry has received less attention. Some of the more recently proposed models consider the effect of temperature on the annealing of radiation induced damage but ignore temperature dependent changes to the silica such as hydrogen diffusion. Because these models are not based on fundamental principles, we did not find a model that could be extended to the attenuation data developed in this project.

The best model we found was proposed by Griscom [120] and was modified slightly by Gilard et al. [121] in 2010. We developed codes to fit our attenuation data by iteratively matching the coefficients in Griscom's model. We had limited success with this approach and it shows that additional development is needed in this area.

10.3.1 Griscom's Fractal Kinetics Model

Griscom proposed a βth order dispersive kinetic model in an attempt to explain the dynamic effects of radiation on the attenuation of optical fibers [120]. This model was slightly modified by Gilard et al. a few years later [121]. The equations for this model are shown in Equation 13, Equation 14, and Equation 15. This model assumes that the concentration of a given defect, or color center, is governed by a constant defect generation term and a temperature dependent annihilation term. The optical attenuation at the wavelength corresponding to the peak attenuation is assumed to be proportional to the color center density, and therefore the model assumes that the attenuation at that wavelength is due to a single color center. The model also assumes that defects are only generated by gamma photons activating pre-existing structural defect sites.

$$\frac{dN_D}{dt} = gN_p\dot{D} - \frac{\alpha}{\tau^\alpha}t^{\alpha-1}N_D{}^\beta$$

where:

N_D = color center density

N_p = pre-existing structural defect density

A = attenuation = $-10\log_{10}(\frac{I}{I_0})$

$A = \varepsilon N_D$

I = optical intensity (wavelength dependent)

I_0 = initial reference intensity

Equation 13: Griscom's Fractal Kinetics Model for Radiation Induced Attenuation

$$\frac{dA}{dt} = \varepsilon g N_p \dot{D} - \frac{\alpha}{\tau^\alpha}\varepsilon^{1-\beta}t^{\alpha-1}A^\beta = B\dot{D} - \frac{\alpha}{\mu^\alpha}t^{\alpha-1}A^\beta$$

$B = \varepsilon g N_p$ $\qquad\qquad$ $\mu = \tau\varepsilon^{\frac{\beta-1}{\alpha}}$

where:

ε = proportionality constant

$\dot{D}$ = dose rate

α = a number between 0 and 1

τ = characteristic decay time

g = a constant

β = order of fit ($1<\beta<2$)

Equation 14

$$\frac{1}{\tau} = \nu e^{-\frac{E_a}{k_B T}}$$

where:

ν = frequency factor

E_a = activation energy of the color center recombination mechanism

k_B = Boltzmann constant

T = temperature of the material (K)

Equation 15

10.3.2 Parameter Matching

A Simulink model was developed in MATLAB to solve Equation 13, Equation 14, and Equation 15. In combination with a MATLAB script, ranges of parameters varied and the calculated attenuation was compared to experimental data. An error reducing algorithm was used to find best fit parameters for a specific experimental dataset. The attenuation observed in the gamma irradiated high-OH fiber shows a distinct attenuation peak centered near 2.07eV (600nm), as shown in Figure 148. The attenuation peak at 600nm was attributed to the NBOHC defect and it is probably acceptable to assume this single defect is responsible for most of the attenuation at that wavelength. Because this dataset met more of the assumptions of Griscom's model, we decided to explore Griscom's model using the time dependent attenuation at 600nm from this dataset.

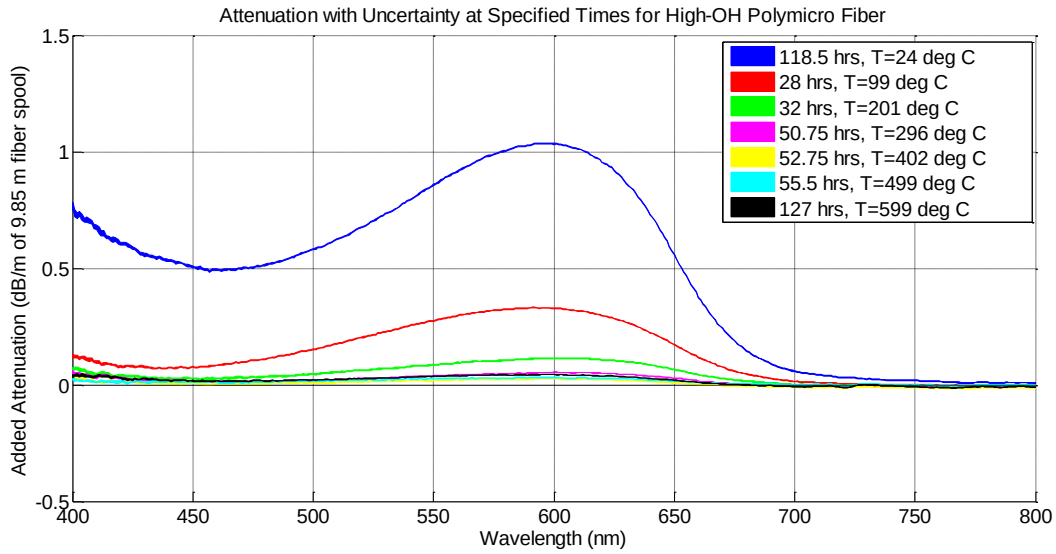

Figure 148: Attenuation at Specified times for high-OH Polymicro Fiber in Gamma Experiment

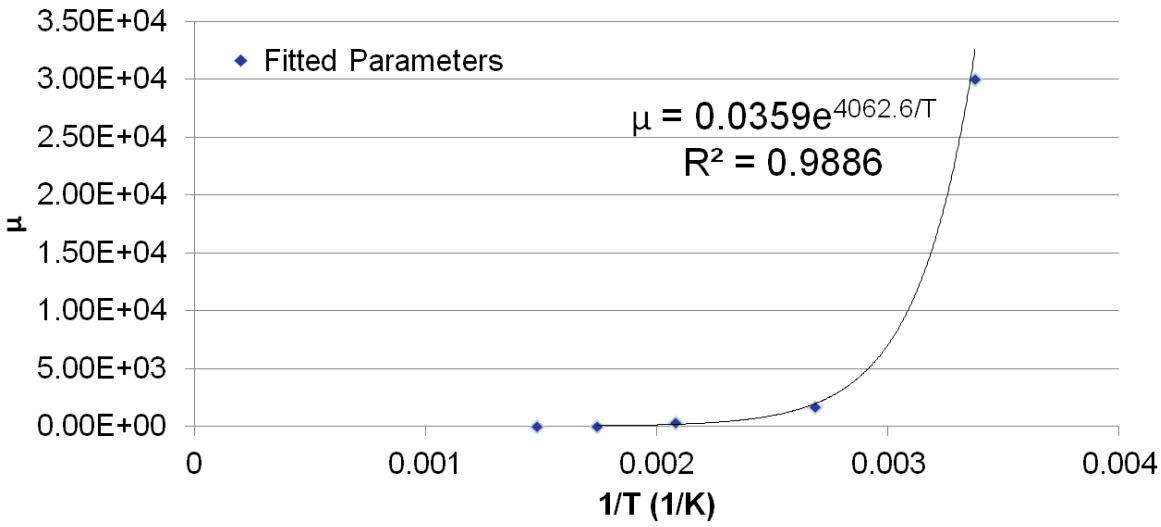

Figure 149: Plot of μ vs. Inverse Temperature for Parameter Fitting

The fractal dimension for fused silica specified in the literature was $\alpha = 0.67$. β, B, and μ were systematically varied for each constant temperature data set until a good fit was obtained. A plot of μ versus the inverse of temperature (1/K) is well approximated by an exponential fit as shown in Figure 149. This shows that the temperature dependence of μ (and τ) is well characterized by an Arrenhius fit, which was expected. If the defect generation parameter, B, was allowed to vary over time, the experimental attenuation at 600nm (shown in Figure 148) is well approximated using the dispersive kinetic model, as shown in Figure 150. However, allowing B to vary physically means that over the course of the experiment, the defect generation rate changed. This is difficult to explain because the gamma dose rate was effectively constant over the course of the experiment.

One possible explanation for varying B is a variable hydrogen concentration in the fiber which could be caused by the increased mobility of hydrogen at high temperatures. Variable hydrogen concentration would change the number of potential defect sites because NBOHCs are generated by breaking OH bonds. The high-OH fiber was manufactured with a high concentration of hydrogen and, based on previous thermal tests, the hydrogen concentration decreased due to high temperature exposure. Even though the curve fit shown in Figure 150 looks good, it is unlikely that the fitting parameters used were physically meaningful.

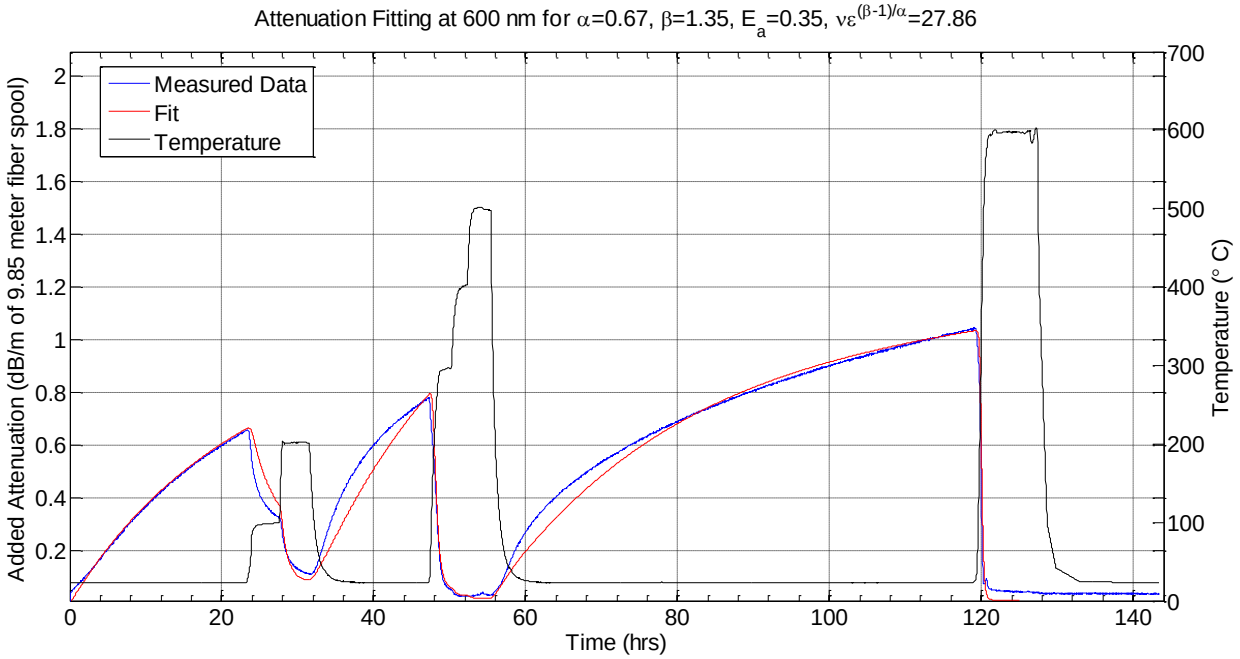

Figure 150: Attenuation Fit at 600nm for α=0.67, β=1.35, E_a=0.35, $\nu\varepsilon^{(\beta-1)/\alpha}$=27.86

10.3.3 Problems with Griscom's Fractal Kinetics Model

A large amount of time was spent fitting parameters from Griscom's model to match our experimental data. Gaussian decomposition was used on other datasets in an attempt to separate attenuation contributions from multiple defects. Unfortunately the spectral data collected in this experiment does not extend far enough into the UV range to identify specific defects. Additional modeling was done to try and make the parameters in Griscom's equation more physical and to enable the parameters to be calculated using other data found in the literature. Through these efforts we came to several conclusions.

First, Griscom's model was conceived for defects that cause attenuation through electronic absorption. Except for the NBOHC defect that causes attenuation around 620nm, all of the other electronic defects absorb photons in the UV range, as shown in Figure 18. Commercially available optical instrumentation, including the OBR, operates at wavelengths in the infrared region, specifically 1300nm and 1550nm. For the goals of this project, creating a predictive model of the optical attenuation in the UV and visible regions is not very helpful because commercial optical instrumentation utilizes the infrared spectrum. Instead of trying to modify the model ourselves, we decided a better course of action would be to publish this work and make our data available to other authors.

Next, Harish spent a great deal of time modeling and investigating radiation induced defects that cause optical absorption through electronic excitations in silica. His results matched with literature, which is good. Unfortunately, vibrational excitations of Si-OH are the primary contributor to optical attenuation at the wavelengths important to commercial optical instrumentation. In this project, we were not well equipped to develop a hydrogen transport model in silica. Fortunately though, there may be ways of mitigating the hydrogen problem instead of trying to model it.

Chapter 11. Conclusions & Future Work

11.1 Conclusions from Reactor Experiments

11.1.1 Multimode Transmission Conclusion

In-situ broadband optical transmission measurements were made through silica optical fibers exposed to radiation from a nuclear reactor while simultaneously being heated to temperatures up to and including 1000°C. Through a series of experiments, the combined effect of high temperature and radiation on the attenuation in several silica optical fiber types was determined, for the first time, in this work. The results from this work have been post-processed into easily viewable movies that have been posted publicly on the internet [1].

The commercially available silica optical fibers irradiated in this work survived optically and mechanically in the high temperature radiation environments tested. In this project, fast neutron fluence of 1.27E+16n/cm^2 was accumulated at temperatures from ambient to 1000°C. The resulting attenuation increase at 1550nm was around 0.5dB/m for the two low-OH fibers tested. Cooke et al. exposed a similar low-OH fiber to a fast fluence of 1.1E19n/cm^2 at ~300°C. The resulting attenuation increase at 1550nm was around 2dB/m [122]. These results are promising for the extension of commercially available optical instrumentation to high temperature reactor environments.

Structural defects accumulate in silica irradiated with fast neutrons at room temperature. The defect accumulation resulting from fast fluences around 1E20n/cm^2 leads to a densification of the silica and reduced optical transmission. Irradiation of silica at high temperature may promote structural rearrangements in the damaged silica that reduce the accumulated damage and prevent or slow the transition to the metamict state. As future work, results from the reactor irradiations can be analyzed for any evidence for or against this hypothesis.

At high temperature, without radiation, optical attenuation in the silica fibers remained low in several wavelength regions and can be used continuously to 900°C with intermittent use to 1000°C. Below 900°C, the primary cause of increased attenuation in the low-OH fibers was diffusion of hydrogen into the silica increasing the Si-OH concentration and the associated Si-OH attenuation. At 1000°C, there was a steady broadband attenuation increase in the Polymicro fibers that would limit the continuous use of the tested Polymicro fibers to 900°C. The cause of this attenuation increase was not isolated but may be caused by fluorine diffusion or crystallization of the fiber [55] [27]. At 1000°C the CeramOptec fiber did not exhibit the same broadband attenuation increase, possibly because of the different dopants used in the fiber. Additional investigation of the Polymicro and CeramOptec fibers at 1000°C is suggested as future work.

Gamma induced attenuation primarily affects wavelengths below 800nm by creation of localized point defects and trapped charge carriers. The recombination rate of point defects and trapped charge carriers increases with increasing temperature resulting in reduced attenuation below 800nm at higher temperatures. Even at room temperature, the gamma induced attenuation at 1300nm and 1550nm was minimal in the tested low-OH fibers at 47.6kRad/hr. Gamma induced attenuation in low-OH silica optical fibers should not limit the use of optical instrumentation operating at 1300nm or 1550nm in high temperature gamma radiation environments. Development of radiation hard optical sensors for high temperature environments is suggested as future work.

Both low-OH and high-OH silica fibers were tested in this project but much of the discussion was focused on low-OH fibers because the intrinsic attenuation in these fibers is more suitable for commercially available optical instrumentation. The high-OH Polymicro fiber tested in this project showed excellent radiation resistance in the heated gamma experiments. Even during room temperature gamma irradiation, the added attenuation between 700nm and 1100nm was nearly

zero. Throughout the reactor irradiations, the added attenuation at 850nm and 1050nm was less than 0.2dB/m. For optical applications in this wavelength range, excluding wavelengths around the 950nm Si-OH peak, high-OH fiber looks promising.

11.1.2 OBR Conclusion

Even though the increase in optical attenuation caused by radiation and thermal effects can probably be accommodated, the intrinsic or extrinsic optical features used to make measurements must also survive in this harsh environment. The OBR uses a reference scan of the intrinsic defect distribution in an optical fiber to calculate change in strain in the fiber. The OBR can calculate quantities other than strain using appropriate calibration coefficients. If the intrinsic defect distribution changes as a result of high temperature or radiation damage, the OBR is unable, with the current data processing techniques, to use the reference scan to correctly process the collected data into strain or temperature. The Corning SMF-28e+ singlemode fiber that we tested worked well, as a distributed sensor, with the OBR up to 700°C. At 750°C, this optical fiber continued to work as an optical waveguide but stopped working as an intrinsic distributed sensor. It is likely that the high temperature exposure was the primary cause of the degradation of the sensing ability of this fiber.

11.2 Future Work

Several directions exist to continue the work accomplished in this project. First, from an applications perspective, it appears that silica optical fibers can survive in high temperature radiation environments. Survivability of optically based sensors needs to be demonstrated in a high temperature radiation environment. Existing commercial sensors may need modified to operate acceptably in this environment. New sensors may need to be designed to measure quantities of interest to nuclear engineers, such as neutron flux and gamma dose rate.

Second, the fluorine doped clad pure silica core Polymicro fibers tested in this work exhibited a steady broadband increase in attenuation when operated at 1000°C in the absence of radiation. The cause of this attenuation increase was not determined but two possibilities include fluorine diffusion out of the clad and the beginning stages of crystallization in the silica. Explicitly determining the degradation mechanism affecting the Polymicro fibers at 1000°C would be useful. In addition, the fluorine doped clad germanium doped core CeramOptec fiber did not exhibit the same broadband attenuation increase when operated at 1000°C. Determining whether or not the CeramOptec fiber can operate continuously at 1000°C would be useful.

Regardless, the nominal useable temperature range around 900°C makes silica optical instrumentation appropriate for the proposed peak operating temperature of most GenIV reactor concepts. Silica instrumentation may not, however, survive peak temperatures during accident conditions. Sapphire has a melting temperature above 2000°C and single crystal sapphire optical fibers are commercially available. Temperature sensors using these fibers have been tested to 1600°C and it would be useful to determine the high temperature performance of this material in a radiation environment.

Thirdly, the fast fluence achieved in this work was 1.27E+16n/cm^2, which is low compared to the room temperature irradiations completed by Cooke et al. [122] and Cheymol [117] et al. High temperature operation reduces the radiation induced attenuation below 800nm caused by point defects and trapped charge carriers. The effect of high temperature operation on the buildup of structural damage in silica has not been determined, and probably cannot be determined with the results of this experiment. It may be possible, however, to determine this computationally.

Finally, the existing models for radiation induced attenuation in silica need to be improved, most importantly by considering the effects of elevated temperature. The existing radiation induced damage models were developed empirically from experimental data. The models do not directly

consider the fundamental damage mechanisms that lead to radiation induced attenuation or the mechanisms leading to annealing of the attenuation. The difference in radiation induced damage in high-OH and low-OH silica is well known in the literature but the effect of stoichiometry has received less attention. Some of the more recently proposed models consider the effect of temperature on the annealing of radiation induced damage but ignore temperature dependent changes to the silica such as hydrogen diffusion.

A more comprehensive model of radiation induced attenuation in silica could be developed, starting from fundamental principles and including more physics than existing models. Experimental data is used to determine coefficients in existing empirical models [120] [121] developed to calculate radiation induced attenuation at one wavelength assuming one optically active defect creation and defect removal mechanism. A better approach would involve tracking the concentrations of multiple defects and summing the resulting optical absorption over the affected wavelengths. Radiation induced defects can recombine into a correct silica structure, restructure into a different defect type, or interact with hydrogen depending on the temperature and availability of hydrogen. In addition, the chemical kinetics of the silica needs to be considered because defect concentrations can change at high temperature in the absence of radiation [39].

Bibliography

[1] D. Hawn, "Fiber Irradiation Data: Processed Videos," Google Drive, 25 June 2012. [Online]. Available: https://docs.google.com/folder/d/0B20QFvfOuXdlMGVMOTFhSDAwQUU/edit.

[2] D. P. Hawn, "The Effects of High Temperature and Nuclear Radiation on the Optical Transmission of Silica Optical Fibers," The Ohio State University, Columbus, 2012.

[3] J. Rempe, H. MacLean, R. Schley, D. Hurley, J. Daw, S. Taylor, J. Smith, J. Svoboda, D. Kotter, D. Knudson, S. C. Wilkins, M. Guers, L. Bond, L. Ott, J. McDuffee, E. Parma and G. Rochau, "New In-Pile Instrumentation to Support Fuel Cycle Research and Development," Idaho National Laboratory, 2011.

[4] U.S. Nuclear Regulator Commission, "Instrumentation and Controls in Nuclear Power Plants: An Emerging Technologies Update (NUREG/CR-6992)," Office of Nuclear Regulatory Research, 2009.

[5] E. J. Friebele and D. L. Griscom, "Radiation Effects in Glass," in *Treatise on Materials Science and Technology, Volume 17: Glass II*, Academic Press, 1979, pp. 257-346.

[6] A. W. Snyder and J. D. Love, Optical Waveguide Theory, New York: Chapman & Hall, 1983.

[7] Micron Optics, Inc., "Micron Optics: Sensing Solutions: Products," [Online]. Available: www.micronoptics.com/sensors_products.php. [Accessed 26 October 2011].

[8] National Instruments Corporation, "Optical Sensor Interrogator for Fiber Bragg Gratings," [Online]. Available: http://sine.ni.com/nips/cds/view/p/lang/en/nid/209012. [Accessed 26 October 2011].

[9] Polymicro Technologies, "Quartz/Silica Characteristics - Typical Thermal Properties," [Online]. Available: www.polymicro.com/catalog/A_9.htm. [Accessed 28 11 2011].

[10] H. Govindarajan, "Atomic-Scale Modeling of the Effects of Irradiation on Silica Optical Fibers," The Ohio State University, Columbus, 2011.

[11] J. W. D. Callister, Materials Science and Engineering an Introduction, Wiley, 2000.

[12] Polymicro Technologies, "E-Mail from Don Doize (don.doize@molex.com) to David Hawn on 5/2/2012 with batch specific fiber attenuation data.," May 2, 2012.

[13] Polymicro Technologies, "Products: Optical Fibers," [Online]. Available: http://www.polymicro.com/products/products.htm. [Accessed 4 July 2012].

[14] C. Winkler, J. D. Love and A. K. Ghatak, "Loss Calculations in Bent Multimode Optical Waveguides," *Optical and Quantum Electronics,* vol. 11, pp. 173-183, 1979.

[15] C. Petrie, D. Hawn, T. E. Blue and W. Windl, "In-Situ Performance of Silica Optical Fibers Heated to 1000°C," *Transactions of the American Nuclear Society,* vol. 106, pp. 616-617, 2012.

[16] A. J. Ikushima, T. Fujiwara and K. Saito, "Silica glass: A material for photonics," *Applied Physics Reviews,* vol. 88, no. 3, pp. 1201-1212, 2000.

[17] D. K. Gifford, B. J. Soller, M. S. Wolfe and M. E. Froggatt, "Distributed Fiber-Optic Temperature Sensing using Rayleigh Backscatter," *Luna Technologies.*

[18] J. Schroeder, "Light Scattering of Glass," in *Treatise on Materials Science and Technology, Volume 12, Glass I: Interaction with Electromagnetic Radiation*, Academic Press, 1977, pp. 157-222.

[19] M. E. Lines, "Scattering losses in optic fiber materials, a new parametrization," *Journal of Applied Physics,* vol. 55, no. 11, pp. 4052-4057, 1984.

[20] D. A. Pinnow, T. C. Rich, F. W. Ostermayer, Jr. and M. DiDomenico, Jr., "Fundamental optical attenuation limits in the liquid and glassy state with application to fiber optic waveguide materials," *Applied Physics Letters,* vol. 22, no. 10, pp. 527-529, 1973.

[21] M. Lancry, E. Regnier and B. Poumellec, "Fictive temperature in silica-based glasses and its application to optical fiber manufacturing," *Progress in Materials Science,* vol. 57, pp. 63-94, 2012.

[22] A. Yablon, "Optical and Mechanical Effects in Frozen-in Stresses and Strains in Optical Fibers," *IEEE Journal of Selected Topics in Quantum Electronics,* vol. 10, no. 2, pp. 300-311, 2004.

[23] G. Ghosh, M. Endo and T. Iwasaki, "Temperature-Dependent Sellmeier Coefficients and Chromatic Dispersions for Some Optical Fiber Glasses," *Journal of Lightwave Technology,* vol. 12, no. 8, pp. 1338-1342, 1994.

[24] J. H. Wray and J. T. Neu, "Refractive Index of Several Glasses as a Function of Wavelength and Temperature," *Journal of the Optical Society of America,* vol. 59, no. 6, pp. 774-776, 1969.

[25] D. L. Kim and M. Tomozawa, "Fictive temperature of silica glass optical fibers - re-examination," *Journal of Non-Crystalline Solids,* vol. 286, pp. 132-138, 2001.

[26] H. Wakabayashi and M. Tomozawa, "Diffusion of Water into Silica Glass at Low Temperature," *Journal of the American Ceramic Society,* vol. 72, no. 10, pp. 1850-1855, 1989.

[27] A. H. Rose, "Devitrification in Annealed Optical Fiber," *Journal of Lightwave Technology,* vol. 15, no. 5, pp. 808-814, 1997.

[28] T. C. Rich and D. A. Pinnow, "Total Optical Attenuation in Bulk Fused Silica," *Applied Physics Letters,* vol. 20, no. 7, pp. 264-266, 1972.

[29] J. A. Bucaro and H. D. Dardy, "High-temperature Brillouin scattering in fused quartz," *Journal of Applied Physics,* vol. 45, no. 12, pp. 5324-5329, 1974.

[30] A. Polian, D. Vo-Thanth and P. Richet, "Elastic Propertis of a-SiO2 up to 2300K from Brillouin scattering measurements," *Europhysics Letters,* vol. 57, no. 3, pp. 375-381, 2002.

[31] N. P. Bansal and R. H. Doremus, Handbook of Glass Properties, Academic Press, 1986.

[32] K. Saito and A. J. Ikushima, "Absorption edge in silica glass," *Physical Review B,* vol. 62, no. 13, pp. 8584-8587, 2000.

[33] I. T. Godmanis, A. N. Trukhin and K. Hubner, "Exiton-Phonon Interaction in Crystalline and Vitreous SiO2," *Physica Status Solidi b,* vol. 116, no. 1, pp. 279-287, 1983.

[34] O. Humbach, H. Fabian, U. Grzesik, U. Haken and W. Heitmann, "Analysis of OH Absorption Bands in Synthetic Silica," *Journal of Non-Crystalline Solids,* vol. 203, pp. 19-26, 1996.

[35] S. R. Nagel, J. B. MacChesney and K. L. Walker, "Modified Chemical Vapor Deposition," in *Optical Fiber Communications: Volume 1 - Fiber Fabrication*, Academic Press, 1985, pp. 1-59.

[36] L. Skuja, M. Hirano, H. Hosono and K. Kajihara, "Defects in oxide glasses," *Physica Status Solidi (c),* vol. 2, no. 1, pp. 15-24, 2005.

[37] L. Skuja, "Optically active oxygen-deficiency-related centers in amorphous silicon dioxide," *Journal of Non-Crystalline Solids,* vol. 239, pp. 16-48, 1998.

[38] A. H. Cherin, An Introduction to Optical Fibers, New York: McGraw-Hill, 1983.

[39] A. R. Silin and L. A. Lace, "Influence of stoichiometry on high temperature intrinsic defects in fused silica," *Journal of Non-Crystalline Solids,* vol. 149, pp. 54-61, 1992.

[40] D. L. Griscom, "Defect Structures of Glasses," *Journal of Non-Crystalline Solids,* vol. 73, pp. 51-77, 1985.

[41] E. J. Friebele, G. H. Sigel and D. L. Griscom, "Drawing-induced defect centers in a fused silica core fiber," *Applied Physics Letters,* vol. 28, no. 9, pp. 516-518, 1976.

[42] E. L. Williams, "Diffusion of Oxygen in Fused Silica," *Journal of The American Ceramic Society,* vol. 48, no. 4, pp. 190-194, 1965.

[43] T. Takahashi, S. Fukatsu and M. K. Itoh, "Self-diffusion of Si in thermally grown SiO2 under equilibrium conditions," *Journal of Applied Physics,* vol. 93, no. 6, pp. 3674-3676, 2003.

[44] A. H. Rose and T. J. Bruno, "The observation of OH in annealed optical fiber," *Journal of Non-Crystalline Solids,* vol. 231, pp. 280-285, 1998.

[45] S. Berger and M. Tomozawa, "Water diffusion into a silica glass optical fiber," *Journal of Non-Crystalline Solids,* vol. 324, pp. 256-263, 2003.

[46] E. Vella, G. Buscarino, G. Vaccaro and R. Boscaino, "Structural organization of silanol and silicon hydride groups in the amorphous silicon dioxide network," *The European Physics Journal B,* vol. 83, pp. 47-52, 2011.

[47] N. V. Tkachenko, Optical Spectroscopy: Methods and Instrumentations, Amsterdam: Elsevier, 2006.

[48] G. E. Walrafen and S. R. Samanta, "Infrared absorbance spectra and interactions involving OH gropus in fused silica," *Journal of Chemical Physics,* vol. 69, no. 1, pp. 493-495, 1978.

[49] M. Bredol, D. Leers, L. Bosselaar and M. Hutjens, "Improved Model for OH Absorption in Optical Fibers," *Journal of Lightwave Technology,* vol. 8, no. 10, pp. 1536-1540, 1990.

[50] T. Izawa and N. Shibata, "Optical attenuation in pure and doped fused silica in the ir wavelength region," *Applied Physics Letters,* vol. 31, no. 1, pp. 33-35, 1977.

[51] Y. Morimoto, T. Igarashi, H. Sugahara and S. Nasu, "Analysis of gas release from vitreous silica," *Journal of Non-Crystalline Solids,* vol. 139, pp. 35-46, 1992.

[52] J. Kirchhof, S. Unger, K. F. Klein and B. Knappe, "Diffusion behavior of fluorine in silica glass," *Journal of Non-Crystalline Solids,* vol. 181, pp. 266-273, 1995.

[53] M. V. Minke and K. A. Jackson, "Diffusion of germanium in silica glass," *Journal of Non-Crystalline Solids,* vol. 351, pp. 2310-2316, 2005.

[54] W. Hermann, A. Raith and H. Rau, "Diffusion of Fluorine in Silica," *Berichte der Bunsengesellschaft für physikalische Chemie,* vol. 91, no. 1, pp. 56-58, 1987.

[55] B. C. Gibson, S. T. Huntington, J. D. Love, T. G. Ryan, L. W. Cahill and D. M. Elton, "Controlled Modification and Direct Characterization of Multimode-Fiber Refractive-Index Profiles," *Applied Optics,* vol. 42, no. 4, pp. 627-633, 2003.

[56] B. C. Gibson, "E-Mail exchange with Brant Gibson (b.gibson@unimelb.edu.au)," July 19 & 22, 2012.

[57] G. Schötz, J. Vydra, G. Lu and D. Fabricant, "New Silica Fiber for Broad-Band Spectroscopy," in *Fiber Optics in Astronomy III, ASP Conference Series*, Puerto de la Cruz, Canary Islands, 1998.

[58] M. Tomozawa, "Phase Separation in Glass," in *Treatise on Materials Science and Technology Volume 17 Glass II*, Academic Press, 1979, pp. 71-110.

[59] E. Dooryhee, J. Duraud and R. Devine, "Radiation-Induced Defects and Structural Modifications," in *Structure and Imperfections in Amorphous and Crystalline Silicon Dioxide*, Wiley, 2000, pp. 349-421.

[60] Korea Atomic Energy Research Institute, "Table of Nuclides," 2000. [Online]. Available: http://atom.kaeri.re.kr/index.html. [Accessed February 2012].

[61] F. Berghmans, B. Brichard, A. Fernandez, A. Gusarov, M. Van Uffelen and S. Girard, "An Introduction to Radiation Effects on Optical Components and Fiber Optic Sensors," in *Optical Waveguide Sensing and Imaging*, Springer, 2008, pp. 127-165.

[62] K. Kajihara, L. Skuja and M. Hirano, "Formation and decay of nonbridging oxygen hole centers in SiO2 gasses induced by F2 laser irradiation: In situ observation using a pump and probe technique," *Applied Physics Letters,* vol. 79, no. 12, pp. 1757-1759, 2001.

[63] A. C. Wright and R. N. Sinclair, "Neutron and X-Ray Scattering Studies of Vitreous Silica," in *Structure and Imperfections in Amorphous and Crystalline Silicon Dioxide*, Wiley, 2000, pp. 121-150.

[64] F. Mota, M. Caturla, J. Perlado, J. Molla and A. Ibarra, "Molecular dynamics study of structural transformation and H effects in irradiated silica," *Journal of Nuclear Materials,* Vols. 386-388, pp. 75-78, 2009.

[65] S. Demos, L. Sheehan and M. Kozlowski, "Spectroscopic investigation of SiO2 surfaces of optical materials for high-power lasers," in *Proc. SPIE 3933, Laser Applications in Microelectronic and Optoelectronic Manufacturing V, 316*, San Jose, CA, 2000.

[66] F. Mota, M. Caturla, J. M. Perlado, A. Ibarra, M. Leon and J. Molla, "Identification and characterization of defects produced in irradiated fused silica through molecular dynamics," *Journal of Nuclear Materials,* Vols. 367-370, no. Part A, pp. 344-349, 2007.

[67] K. Yamahara, K. Okazaki and K. Kawamura, "Molecular Dynamics study of the thermal behavior of silica glass/melt and cristobalite," *Journal of Non-Crystalline Solids,* vol. 291, no. 1-2, pp. 32-42, 2001.

[68] X. Ying-Mei, Q. Ji, H. De-Min, W. Dong-Mei, C. Hui-Ying, G. Jun and Z. Qiu-Min, "Preparation of Amorphous Silica from Oil Shale Residue and Surface Modification by Silane Coupling Agent," *Oil Shale,* vol. 27, no. 1, pp. 37-46, 2010.

[69] P. Johnson, A. C. Wright and R. N. Sinclair, "Neutron scattering from vitreous silica II. Twin-axis diffraction experiments," *Journal of Non-Crystalline Solids,* vol. 58, pp. 109-130, 1983.

[70] F. Mota, M. J. Caturla, J. Perlado, J. Molla and A. Ibarra, "Molecular dynamics study of structure transformation and H effects in irradiated silica," *Journal of Nuclear Materials,* Vols. 368-388, pp. 75-78, 2009.

[71] J. Hopcroft and R. Tarjan, "Efficient planarity testing," *Journal of the Association for Computing Machinery,* vol. 21, no. 4, pp. 549-568, 1974.

[72] S. Munetoh, T. Motooka, K. Moriguchi and A. Shintani, "Interatomic potential for Si–O systems using Tersoff parameterization.," *Computational Materials Science,* vol. 39, no. 2, pp. 334-339, 2007.

[73] "Crystal and Molecular Structures: Visualization and Diffraction," CrystalMaker Software, [Online]. Available: www.crystalmaker.com. [Accessed 4 November 2011].

[74] S. Girard, Origlio, Marcandella, Boukenter, Richard, Baggio, Paillet, Cannas, Bisutti, Meunier and Boscaino, "Radiation Effects on Silica-Based Preforms and Optical Fibers-I: Experimental Study with Canonical Samples," *IEEE Transactions on Nuclear Science,* vol. 55, no. 6, pp. 3473-3482, 2008.

[75] J. Sauer, "Molecular Models in ab Initio Studies of Solids and Surfaces: From Ionic Crystals and Semiconductors to Catalysts," *Chemical Reviews,* vol. 89, pp. 199-255, 1989.

[76] S. Agnello, R. Boscaino, G. Buscarino, M. Cannas and F. M. Gelardi, "Structural relaxation of Eγ′ centers in amorphous silica," *Physical Review B,* vol. 66, 2002.

[77] D. L. Griscom and M. Cook, "29-Si superhyperfine interactions of the E′ center: a potential probe of range-II order in silica glass," *Journal of Non-Crystalline Solids,* vol. 182, pp. 119-134, 1995.

[78] Y. Laudernet, N. Richard, S. Girard, L. Martin-SAmos, A. Boukenter, Y. Ouerdane and J. Meunier, "Ab initio molecular dynamics simulations of oxygen-deficient centers in pure and Ge-doped silica glasses: Structure and optical properties.," *Journal of Non-Crystalline Solids,* vol. 352, pp. 2596-2600, 2006.

[79] E. O'Reilly and J. Robertson, "Theory of defects in vitreous silicon dioxide.," *Physics Review B,* vol. 27, pp. 3780-3795, 1983.

[80] A. H. Edwards, "Theory of intrinsic defects in a-SiO2," *Materials Research Society Symposia Proceedings,* vol. 61, pp. 3-20, 1985.

[81] D. L. Griscom, "The natures of point defects in amorphous silicon dioxide," in *Defects in SiO2 and Related Dielectrics*, Kluwer, 2000, pp. 117-160.

[82] R. A. B. Devine and J. M. Francou, "Extrinsic and intrinsic defect creation in amorphous silica," *Physics Review B,* vol. 41, 1990.

[83] D. L. Griscom, "Optical properties and structures of defects in silica glass," *Journal of the Ceramic Society of Japan,* vol. 99, no. 1154, pp. 923-942, 1991.

[84] L. Skuja, "Optical Properties of point defects in silica," in *Defects in SiO2 and Related Dielectrics*, Kluwer, 2000.

[85] S. Girard, Richard, N., Y. Ouerdane, G. Origlio, A. Boukenter, L. Martin-Samos, P. Paillet, J. Meunier, J. Baggio, M. Cannas and R. Boscaino, "Radiation Effects on Silica-Based Preforms and Optical Fibers-II : Coupling Ab initio Simulations and Experiments," *IEEE Transactions On Nuclear Science,* vol. 55, pp. 3508-3514, 2008.

[86] L. Martin-Samos, Y. Limoge, N. Richard, Crocombette, Roma, Anglada and Artacho, "Oxygen neutral defects in silica: Origin of the distribution of the formation energies," *Europhysics Letters (EPL),* vol. 66, no. 5, pp. 680-686, 2004.

[87] L. Martin-Samos, G. Roma, P. Rinke and Y. Limoge, "Charged Oxygen Defects in SiO2 : Going beyond Local and Semilocal Approximations to Density Functional Theory," *Physical Review Letters,* vol. 104, no. 7, pp. 2-5, 2010.

[88] "VASP ver.5.2," [Online]. Available: http://cms.mpi.univie.ac.at/vasp/.

[89] "OSC's High Performance Computing Systems," [Online]. Available: https://www.osc.edu/supercomputing/hardware#opt.

[90] "Optical properties and density functional perturbation theory (PT)," [Online]. Available: http://cms.mpi.univie.ac.at/vasp/vasp/Optical_properties_density_functional_perturbation_theory_PT.html.

[91] S. Pantelides and W. Harrison, "Electronic structure, spectra, and properties of 4:2-coordinated materials. I. Crystalline and amorphous SiO 2 and GeO 2," *Physical Review B,* vol. 13, no. 6, pp. 2667-2691, 1976.

[92] A. Anedda, "Vacuum ultraviolet absorption of silica samples," *Journal of Non-Crystalline Solids,* vol. 245, pp. 183-189, 1999.

[93] G. Roma, Y. Limoge and L. Martin-Samos, "Aspects of point defects energetics and diffusion in SiO 2 from first principles simulations," *Nuclear Instruments and Methods in Physics Research Letters B,* vol. 250, no. 1-2, pp. 54-56, 2006.

[94] R. Mishra, O. Restrepo, P. Woodward and W. Windl, "First-Principles Study of Defective and Nonstoichiometric Sr2FeMoO6," *Chemistry of Materials,* vol. 22, pp. 6092-6102, 2010.

[95] P. Sushko, S. Mukhopadhyay, A. Mysovsky, V. Sulimov, A. Taga and A. Shluger, "Structure and properties of defects in amorphous silica: new insights from embedded cluster calculations," *Journal of Physics: Condensed Matter,* vol. 17, no. 21, pp. S2115-S2140, 2005.

[96] Y. Jin and K. J. Chang, "Mechanism for the Enhanced Diffusion of Charged Oxygen Ions in SiO2," *Physical Review Letters,* vol. 86, no. 9, pp. 1793-1796, 2001.

[97] B. P. Blake, "Initial Testing of Single-Mode Optical Fibers Interrogated with an Optical Backscatter Reflectometer at High Temperatures and in Radiation Environments for Advanced Instrumentation in Nuclear Reactors," The Ohio State University, Columbus, 2012.

[98] D. P. Hawn, C. Petrie, T. E. Blue and R. Winningham, "Design and Analysis of a High-Temperature Low-Activation Furnace," *Transactions of the American Nuclear Society,* vol. 103, pp. 302-303, 2010.

[99] D. P. Hawn, B. Blake, C. Petrie and T. E. Blue, "Initial Testing of a High-Temperature Low-Activation Furnace," *Transactions of the American Nuclear Society,* vol. 104, pp. 308-309, 2011.

[100] ASTM International, "E1614-94: Standard Guide for Procdure for Measuring Ionizing Radiation-Induced Attenuation in Silica-Based Optical Fibers and Cables for Use in Remote Fiber-Optic Spectroscopy and Broadband Systems," ASTM International, 2004.

[101] I Squared R Element Co., Inc., "Type SEU, Silicon Carbide Heating Elements," Ackron, New York, 2008.

[102] Momentive, "Chemical Composition of Fused Quartz," [Online]. Available: www.momentive.com/WorkArea/DownloadAsset.aspx?id=25473. [Accessed February 2012].

[103] The Ohio State University, "Glassblowing Laboratory," Departments of Chemistry and Biochemistry, [Online]. Available: http://chemistry.osu.edu/rss/glassblowing. [Accessed 23 January 2012].

[104] Zircar Ceramics, "Rigid Materials," [Online]. Available: www.zircarceramics.com/pages/rigidmaterials/index.htm. [Accessed 23 January 2012].

[105] 3M, "Nextel Woven Fabric 312," [Online]. Available: www.3m.com/market/industrial/ceramics/materials/fabric_312.html. [Accessed 2012 January 23].

[106] Thermostatic Industries, Inc., "Gaskets & Seals," [Online]. Available: www.thermostatic.com/gaskets.shtml. [Accessed 23 January 2012].

[107] Micropyretics Heaters International, Inc., "Robust Radiator Modules," [Online]. Available: www.mhi-inc.com/PG3/robust-radiator.html. [Accessed 23 January 2012].

[108] Watlow Electric Manufacturing Company, "DIN-A-MITE C," [Online]. Available: www.watlow.com/products/controllers/din-a-mite-c-power-controller.cfm. [Accessed 24 January 2012].

[109] Sony, "ILX511: 2048-pixel CCD Linear Image Sensor (B/W) Datasheet".

[110] Goodrich, "InGaAs Linear Photodiode Array Datasheet," Princeton, NJ, 2009.

[111] Newport Corporation, "918D-IS-1 Universal Fiber Optic Detector," [Online]. Available: http://search.newport.com/?x2=sku&q2=918D-IS-1. [Accessed 2 February 2012].

[112] Polymicro Technologies, "Polyimide Physical Properties," [Online]. Available: www.polymicro.com/techsupport/techsupport_polyimidephysicalprop.htm. [Accessed November 2011].

[113] Micron Optics, "Sensing Solutions: Products: Sensors: Serialized array of five FBGs in polyimide coated fiber," 2012. [Online]. Available: www.micronoptics.com/uploads/library/documents/Datasheets/Micron%20Optics%20-%20os1200.pdf. [Accessed 21 July 2012].

[114] Luna Technologies, "Products: Fiber Sensing Solutions: Optical Distributed Sensor Interrogator," [Online]. Available: http://www.lunatechnologies.com/products/ODiSI/ODiSI.html. [Accessed 21 July 2012].

[115] D. Hawn, C. Petrie, T. E. Blue and W. Windl, "In-Situ Performance of Optical Fibers Heated to 600°C during Gamma Irradiation," *Transactions of the American Nuclear Society,* vol. 106, pp. 614-615, 2012.

[116] CeramOptec Industries, Inc., "E-mail from Kevin Bakhshpour (kevin.bakhshpour@ceramoptec.com)," 2012.

[117] G. Cheymol, H. Long, J. F. Villard and B. Brichard, "High Level Gamma and Neutron Irradiation of Silica Optical Fibers in CEA OSIRIS Nuclear Reactor," *IEEE Transactions on Nuclear Science,* vol. 55, no. 4, pp. 2252-2258, 2008.

[118] C. M. Petrie, T. E. Blue and J. A. Kulisek, "Modeling High Temperature Radiation Damage to Optical Fibers," *Transactions of the American Nuclear Society,* vol. 104, pp. 269-270, 2011.

[119] A. Kauffman, D. Miller, T. Radcliff, K. Maupin, D. Mills and M. Penrod, "High-Temperature Test Facility for Reactor In-Core Sensor Testing," *Nuclear Technology,* vol. 140, no. 2, pp. 222-232, 2002.

[120] D. Griscom, "Fractal kinetics of radiation-induced point-defect formation and decay in amorphous inslators: Application to color centers in silica-based optical fibers," *Physical Review B,* vol. 64, p. 174201, 2001.

[121] O. Gilard, M. Caussanel, H. Duval, G. Quandri and F. Reynaud, "New Model for Accessing Dose, Dose Rate, and Temperature Sensitivity of Radiation-Induced Absorption in Glasses," *Journal of Applied Physics,* vol. 108, 2010.

[122] D. W. Cooke, B. L. Bennett and E. H. Farnum, "Optical Absorption of Neutron-Irradiated Silica Fibers," *Journal of Nuclear Materials,* vol. 232, pp. 214-218, 1996.

[123] S. Music, N. Filipović-Vinceković and L. Sekovanic, "Precipitation of amorphous SiO2 particles and their properties," *Brazilian Journal of Chemical Engineering,* vol. 28, no. 1, 2011.